Journal of Heat Transfer

Published Monthly by ASME

VOLUME 130 • NUMBER 6 • JUNE 2008

RESEARCH PAPERS

Conduction

Evaporation, Boiling, and Condensation

Experimental Techniques

Forced Convection

Heat Exchangers

Heat and Mass Transfer

Jets, Wakes, and Impingement Cooling

Micro/Nanoscale Heat Transfer

(Contents continued on inside back cover)

This journal is printed on acid-free paper, which exceeds the ANSI Z39.48-1992 specification for permanence of paper and library materials. ∞™
♻ 85% recycled content, including 10% post-consumer fibers.

Editor, **YOGESH JALURIA (2010)**
Assistant to the Editor, **S. PATEL**

Associate Editors
Yutaka Asako, Tokyo Metropolitan University, Japan (2010)
Gautam Biswas, Indian Inst. of Tech., Kanpur (2009)
Louis C. Burmeister, Univ. of Kansas (2008)
Cho Lik Chan, The University of Arizona (2010)
Louis C. Chow, University of Central Florida (2010)
Minking Chyu, Univ. of Pittsburgh (2009)
A. Haji-Sheikh, Univ. of Texas at Arlington (2008)
Anthony M. Jacobi, Univ. of Illinois (2008)
Yogendra Joshi, Georgia Inst. of Tech. (2008)
Satish G. Kandlikar, Rochester Inst. of Tech. (2010)
Sung Jin Kim, KAIST, Korea (2010)
Sai C. Lau, Texas A&M Univ. (2009)
Ben Q. Li, Univ. of Michigan, Dearborn (2009)
Raj M. Manglik, Univ. of Cincinnati (2009)
Jayanthi Y. Murthy, Purdue University (2010)
Roger R. Schmidt, IBM Corporation (2010)
Jamal Seyed-Yagoobi, Illinois Inst. of Tech. (2009)
S. A. Sherif, University of Florida (2010)
Bengt Sunden, Lund Inst. of Tech., Sweden (2008)
Peter Vadasz, Northern Arizona University (2010)
Walter W. Yuen, Univ. of California–Santa Barbara (2008)

Past Editors
V. DHIR
J. R. HOWELL
R. VISKANTA
G. M. FAETH
K. T. YANG
E. M. SPARROW

HEAT TRANSFER DIVISION
Chair, **T. W. TONG**
Vice Chair, **C. H. OH**
Past Chair, **R. W. DOUGLASS**

PUBLICATIONS COMMITTEE
Chair, **BAHRAM RAVANI**

OFFICERS OF THE ASME
President, **SAM Y. ZAMRIK**
Executive Director,
VIRGIL R. CARTER
Treasurer,
THOMAS D. PESTORIUS

PUBLISHING STAFF

Managing Director, Publishing
PHILIP DI VIETRO

Manager, Journals
COLIN McATEER

Production Coordinator
JUDITH SIERANT

Transactions of the ASME, Journal of Heat Transfer (ISSN 0022-1481) is published monthly by The American Society of Mechanical Engineers, Three Park Avenue, New York, NY 10016. Periodicals postage paid at New York, NY and additional mailing offices. POSTMASTER: Send address changes to Transactions of the ASME, Journal of Heat Transfer, c/o THE AMERICAN SOCIETY OF MECHANICAL ENGINEERS, 22 Law Drive, Box 2300, Fairfield, NJ 07007-2300. **CHANGES OF ADDRESS** must be received at Society headquarters seven weeks before they are to be effective. Please send old label and new address.

STATEMENT from By-Laws. The Society shall not be responsible for statements or opinions advanced in papers or ... printed in its publications (B7.1, Para. 3).
COPYRIGHT © 2008 by The American Society of Mechanical Engineers. For authorization to photocopy material for internal or personal use under those circumstances not falling within the fair use provisions of the Copyright Act, contact the Copyright Clearance Center (CCC), 222 Rosewood Drive, Danvers, MA 01923, tel: 978-750-8400, www.copyright.com. Request for special permission or bulk copying should be addressed to Reprints/Permission Department.

Canadian Goods & Services Tax Registration #126148048

Journal of Heat Transfer **Volume 130, Number 6** **JUNE 2008**

TECHNICAL BRIEFS

The ASME Journal of Heat Transfer is abstracted and indexed in the following:

Applied Science and Technology Index, Chemical Abstracts, Chemical Engineering and Biotechnology Abstracts (Electronic equivalent of Process and Chemical Engineering), Civil Engineering Abstracts, Compendex (The electronic equivalent of Engineering Index), Corrosion Abstracts, Current Contents, E & P Health, Safety, and Environment, Ei EncompassLit, Engineered Materials Abstracts, Engineering Index, Enviroline (The electronic equivalent of Environment Abstracts), Environment Abstracts, Environmental Engineering Abstracts, Environmental Science and Pollution Management, Fluidex, Fuel and Energy Abstracts, Index to Scientific Reviews, INSPEC, International Building Services Abstracts, Mechanical & Transportation Engineering Abstracts, Mechanical Engineering Abstracts, METADEX (The electronic equivalent of Metals Abstracts and Alloys Index), Petroleum Abstracts, Process and Chemical Engineering, Referativnyi Zhurnal, Science Citation Index, SciSearch (The electronic equivalent of Science Citation Index), Theoretical Chemical Engineering

On the Numerical Modeling of the Thermomechanical Contact for Metal Casting Analysis

Michele Chiumenti
e-mail: michele@cimne.upc.edu

Carlos Agelet de Saracibar

Miguel Cervera

Universidad Politécnica de Cataluña (UPC),
Modulo C1,
Campus Norte, C/Gran Capitán s/n,
08034 Barcelona, Spain

The paper shows the intrinsic difficulties found in the numerical simulation of industrial casting processes using finite element (FE) analysis. Up until now, uncoupled pure thermal simulations have been mostly considered to model solidification and cooling phenomena. However, a fully coupled thermomechanical analysis provides a more complete insight of the casting process and the final outcome regarding the quality of the part. In this type of analysis, the thermomechanical model used plays a role of paramount importance, as the problem is coupled both ways through contact between part and mould. The paper presents the full statement of the problem regarding contact, and it considers the difficulties associated with FE mesh generation and time integration strategy. It also reviews soft and hard algorithms for mechanical contact presenting some new alternatives. Evaluation of coefficients used for thermal contact is also discussed, and a new proposal is presented. Finally, some numerical applications are presented to assess the performance of the proposed strategies both in benchmark and industrial problems.

[DOI: 10.1115/1.2897923]

Keywords: thermomechanical contact, metal casting analysis, heat conduction, heat convection, heat radiation, finite element method

Introduction

The aim of this study is to show the intrinsic difficulties found and the strategy adopted to simulate a *foundry process*.

Up until now, mostly purely thermal simulations have been considered to study the evolution of the solidification and cooling phenomena. This is mainly due to the fact that this strategy is easier and less costly and, therefore, more convenient for large-scale industrial simulations. On the other hand, the *fully coupled thermomechanical analysis* is the natural framework to represent the heat flow exchange, the final shape of the casting part, as well as the evolution of the residual stresses induced by the manufacturing operations. The accurate modeling of both stresses and deformations of the part during the solidification and the cooling phases is crucial to capture the thermal pattern (temperature and solidification evolution) in aluminum casting or, more generally, when a permanent mould is used. In fact, the thermal deformation of both part and mould modifies the original interfacial heat transfer among all the casting tools involved in the process. The relationship between the heat transfer coefficient and mechanical quantities such as the open air gap or the contact pressure has been experimentally proved. Hence, the mechanical analysis coupled with the thermal simulation is mandatory to produce a reliable casting numerical model.

More specifically, this work will focus on the description of the *thermomechanical contact model* necessary to study the interaction among all the casting tools during the solidification and cooling processes. This is possibly the key point in a casting simulation, playing an extremely important role and coupling the thermomechanical problem in both ways.

Governing Equations

The system of partial differential equations governing the coupled thermomechanical problem is defined by the momentum and energy balance equations, restricted by the inequalities arising from the second law of thermodynamics. This system must be supplemented by suitable constitutive equations and prescribed boundary and initial conditions.

Strong Form of the Governing Equations. Using a mixed $\mathbf{u}/p$ displacement/pressure formulation, the strong forms of the *momentum* and *energy balance equations* are given by

$$\boldsymbol{\nabla}\cdot\mathbf{s}+\boldsymbol{\nabla}p+\mathbf{b}=\mathbf{0} \tag{1}$$

$$\dot{E}=\boldsymbol{\sigma}:\dot{\boldsymbol{\varepsilon}}+\dot{Q} \tag{2}$$

where $\mathbf{s}$ is the deviatoric part of Cauchy's stress tensor defined as $\boldsymbol{\sigma}=p\mathbf{1}+\mathbf{s}$, $\mathbf{b}$ is the vector of forces per unit of volume, $\dot{E}$ is the rate of the internal energy per unit of volume, and $\dot{Q}=\dot{R}-\boldsymbol{\nabla}\cdot\mathbf{Q}$ is the heat supplied to the system per unit of volume due to the internal sources per unit of volume $\dot{R}$ and input heat flow through the boundary $-\boldsymbol{\nabla}\cdot\mathbf{Q}$.

On the other hand, the second law of thermodynamics limits the direction of the energy transformations and it postulates that there exists a state function called enthalpy H so that $\dot{H}=\dot{Q}+\dot{D}$, where $\dot{D}\geq 0$ is the thermomechanical dissipation and it represents the energy dissipated (transformed in heat) for an irreversible process.

Weak Form of the Balance of Momentum Equation. Let $\delta\boldsymbol{\eta}$ and δq be the test functions associated with the displacement and pressure fields $\mathbf{u}$ and p, respectively. The weak form of the balance of momentum equation in the hypothesis of a quasistatic process can be expressed in the mixed format as

$$\int_{\Omega}(\boldsymbol{\nabla}^{S}\boldsymbol{\delta\eta}\mathbf{s})dV+\int_{\Omega}(\boldsymbol{\nabla}\cdot\boldsymbol{\delta\eta}p)dV$$
$$=\int_{\Omega}(\boldsymbol{\delta\eta}\mathbf{b})dV+\int_{\partial\Omega}(\boldsymbol{\delta\eta}\bar{\mathbf{t}})dS+\int_{\partial\Omega}(\boldsymbol{\delta\eta}\mathbf{t}_{c})dS$$

Contributed by the Heat Transfer Division of ASME for publication in the JOURNAL OF HEAT TRANSFER. Manuscript received February 6, 2007; final manuscript received January 25, 2008; published online April 23, 2008. Review conducted by Ben Q. Li.

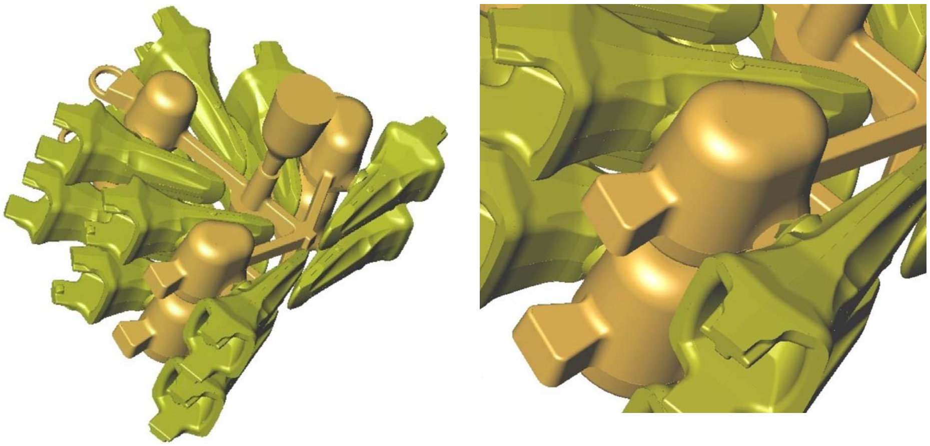

Fig. 1 Sand gravity casting; CAD geometry of the foundry system

$$\int_\Omega \delta q\left(\nabla\cdot\mathbf{u}+\frac{p}{K}-e^\theta\right)dV=0 \qquad (3)$$

where K is the bulk modulus, e^θ is the thermal (volumetric) deformation, and $\overline{\mathbf{t}}$ and $\mathbf{t}_c$ are the prescribed and contact tractions, respectively. Observe that for a liquidlike behavior, $K\rightarrow\infty$ and $e^\theta=0$, the second equation reads

$$\int_\Omega (\delta q\,\nabla\cdot\mathbf{u})dV=0 \qquad (4)$$

stating (in weak form) the incompressibility condition $\nabla\cdot\mathbf{u}=0$. Hence, a stabilization technique becomes necessary to ensure stability. It can be proved that neither standard P1 nor P1/P1 mixed elements pass the Babuska–Brezzi stability condition [1]. An attractive alternative to circumvent such condition can be achieved introducing a stabilizing term in the continuity equation. A first possibility is the so called Galerkin least-squares (GLS) method, which introduces an element-by-element stabilization term based on the residual of the momentum balance equation or as an attractive alternative the *orthogonal subgrid scale* (OSGS) approach [2–6].

Weak Form of the Balance of Energy Equation. Let $\delta\vartheta$ be the test function associated with the temperature field T. The weak form of the balance of energy equation reads

$$\int_\Omega (\delta\vartheta\dot{H})dV+\int_\Omega [\nabla(\delta\vartheta)k\,\nabla T]dV=\int_{\partial\Omega}(\delta\vartheta Q_c)dS \qquad (5)$$

where Fourier's law has been introduced as $\mathbf{Q}=-k\nabla T$, being k the conductivity coefficient. Observe that for casting application the dissipation term $\dot{D}$ is negligible and usually does exist neither as the source term $\dot{R}$ nor any prescribed heat flux at the boundary. The only driving force that moves the problem is Q_c, which is the heat flux at the boundary interfaces due to the thermal contact interaction.

This term is possibly the most important one for this kind of applications and, as it will be shown in the next sections, it is responsible for the coupling between the mechanical and the thermal problems. On one hand, all the mechanical properties, that is, the material behavior, depend on the temperature field; on the other hand, it will be shown that the heat flux at the contact interfaces Q_c depends on mechanical quantities such as the normal contact pressure or the thermal shrinkage of all the foundry components.

Given this, it is not possible to uncouple the problem so that both thermal and mechanical solutions must be obtained at each time step. In this work, the authors chose a staggered solution strategy based on the fractional step method. Interested readers can refer to Refs. [7,8] for further details.

Geometry and FE Mesh

Once the equations to be solved are defined, the main difficulty to be taken into account when modeling a casting process is the geometrical definition of all the casting tools involved in the manufacturing process. The complexity of such geometries makes the meshing operation really difficult. Figure 1 shows the intricacy of the sand casting system used to manufacture excavator teeth.

The high number of casting tools involved in the simulation such as part, molds, cores, cooling channels, chillers, etc., requires an important computer-aided design (CAD) effort, which turns into much greater meshing troubles.

Generally, only a tetrahedral finite element (FE) mesh can be generated. The small thickness of many parts, especially in the case of either low-pressure or high-pressure die-casting processes, is a strong constraint when meshing. Very few elements are placed within the thickness of the casting part, posing difficulties for the numerical description of temperature gradients as well as the evolution of the thermal contraction or the stress field.

The artificial stiffening due to a very coarse mesh discretization is possibly the major difficulty to achieve the result accuracy needed. Figure 2 shows the original CAD geometry and the FE mesh used for a high pressure die-casting (HPDC) analysis. The mesh generated, including mould and filling system, is about 1×10^6 of linear elements, which is the current practical limit in a standard personal computer (PC) platform. However, just one linear element is placed through the thickness of the part.

The artificial stiffening of the discrete model induced by a coarse mesh is increased by the element technology used to respect the volumetric incompressibility constraints as introduced in the previous section. Mechanical contact algorithms particularly suffer such numerical stiffening and, therefore, a very robust contact algorithm must be used to prevent spurious penetrations and numerical locking of the solution.

The discretization of the contact surface is another problem induced by the FE mesh. Surface curvature results in a nonsmooth surface definition, leading to a nonsmooth contact reaction field. The direction of the normal vector at each node of the surface is not univocally defined: There are different possibilities according to the algorithm selected. All these possibilities should converge refining the mesh but if this is not possible (i.e., a large industrial analysis), the choice can seriously affect the final result.

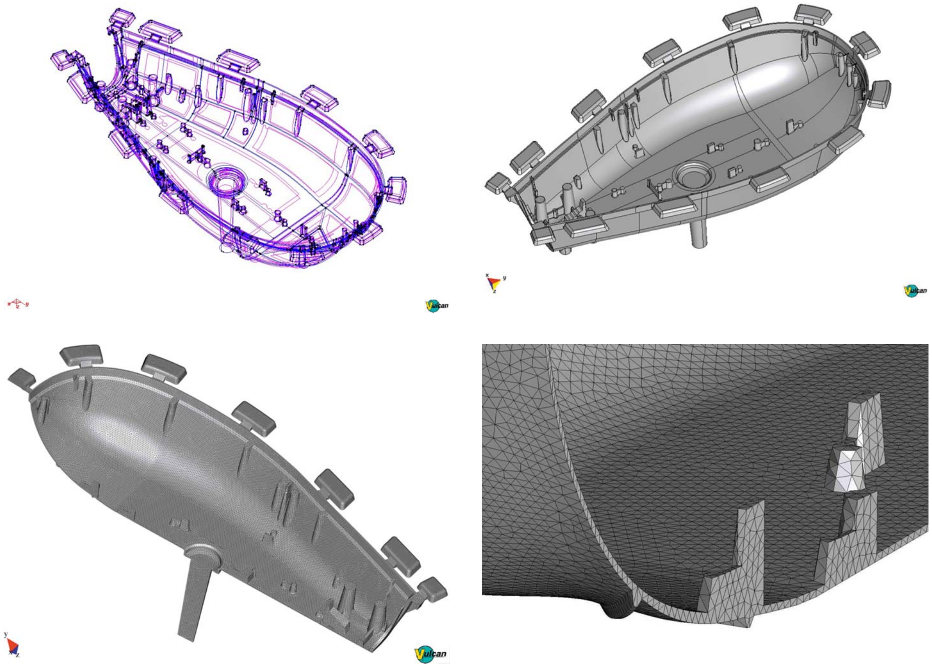

Fig. 2 HP die-casting process: CAD geometry and FE mesh generated

Thermomechanical Contact Algorithms

On foundry processes, the numerical simulation of the mechanical interaction among casting tools such as part, mould, cores, etc., is an extremely important issue to be taken into account. Looking at the definition of heat conduction and heat convection laws, it is clear how important is an accurate definition of the contact pressure as well as the prediction of the open air gaps between casting part and mould surfaces. The relationship between heat transfer coefficients and open air gap has been experimentally proved [9,10], especially in the case of low-pressure as well as HPDC processes, which use permanent moulds.

In the literature, it is possible to find many different algorithms to study the mechanical contact between deformable bodies [11,12]. In a solidification process, the shrinkage of the casting material is of order of 3–5% of the original volume and no other movements are allowed, so that it is possible to assume a small displacement contact algorithm. This hypothesis reduces the cost associated with the so called *closest-point-projection* procedure, which is commonly used when large slips can occur [13]. A simpler node-to-node or face-to-face contact algorithm can be assumed without loss of accuracy. Therefore, coincident surface meshes are generated such that the location of the boundary nodes of the mould matches the location of the casting nodes. Observe, as great advantage of such strategy, that neither spurious initial penetrations nor fictitious open gaps are allowed at the beginning of the simulation.

Once the contact zone is identified and discretized, two different typologies of contact algorithms can be applied to prevent the penetration establishing the contact constraints. On one hand, the so called *soft contact* algorithms are based on penalization techniques, such as the *penalty* method or the *augmented Lagrangian* algorithm, among others [14,15,13]. On the other hand, the so called *hard contact* algorithms based on the computation of the contact reactions totally prevent the penetration at the contact interface, such as the *Lagrange multiplier* method [11].

In a penalty approach, the final penetration is not zero and it depends on the value of the penalty parameter selected. This is a major problem in the case of casting analysis because it is really difficult to select the appropriate penalty value. In practice, this value is usually taken as a function of the stiffness and element sizes of the contacting bodies. It is also a fact that during both the solidification and the cooling processes, casting stiffness drastically changes, leading to a hard choice of the penalty. Some authors propose a temperature dependent parameter according to the temperature evolution at the casting interface [16,17]. Even if the results achieved are better, the use of fairly large values of the penalty parameter to prevent the penetration of one boundary through the other is still problematic.

It must also be observed that the use of iterative solvers, such as a conjugate gradient or GMRES iterative solvers, is a really attractive alternative for the solution of large-scale industrial problems. The number of iterations necessary to achieve the solution is a function of the condition number of the matrix of the system. By adding the contact contributions to the assembled matrix (which depend on the value of the penalty parameter used), the number of iterations required by the solver to converge increases, and as a direct consequence, the total CPU time. High values of the penalty parameter lead to a matrix ill conditioning up to the limit case of solver locking.

A possibility to reduce the matrix ill conditioning, without losing result quality, is the augmented Lagrangian method [14]. The drawback is the terrible CPU time increase.

As a third possibility, proposed here by the authors, a block-iterative solution can be considered. The basic idea consists of using a penalty method together with the decomposition of the final system of equations into casting, mold, and contact equations, such as

$$\begin{bmatrix} \mathbf{A}_{\text{cast}} & \mathbf{0} & \mathbf{A}_{c,\text{cast}} \\ \mathbf{0} & \mathbf{A}_{\text{mold}} & \mathbf{A}_{c,\text{mold}} \\ \mathbf{A}_{c,\text{cast}} & \mathbf{A}_{c,\text{mold}} & \mathbf{A}_{c} \end{bmatrix} \begin{Bmatrix} d\mathbf{u}_{\text{cast}} \\ d\mathbf{u}_{\text{mold}} \\ d\mathbf{u}_{c} \end{Bmatrix} = \begin{Bmatrix} \mathbf{r}_{\text{cast}} \\ \mathbf{r}_{\text{mold}} \\ \mathbf{r}_{c} \end{Bmatrix} \tag{6}$$

where the contact equations are those associated with the nodes at the contact interface. As a result, an arrow shaped system of equations is obtained. An iterative solution of such a system is proposed in the form

$$\mathbf{A}_{\text{cast}} d\mathbf{u}_{\text{cast}}^{i+1} = \mathbf{r}_{\text{cast}} - \mathbf{A}_{c,\text{cast}} d\mathbf{u}_{c}^{i}$$

$$\mathbf{A}_{\text{mold}} d\mathbf{u}_{\text{mold}}^{i+1} = \mathbf{r}_{\text{mold}} - \mathbf{A}_{c,\text{mold}} d\mathbf{u}_{c}^{i}$$

Table 1 Typical convergence performance obtained using the standard penalty method, the augmented Lagrangian algorithm, and the proposed block-iterative method

Penalty method	Convergence ratio	Augmented Lagrangian	Convergence ratio	Block-iterative method	Convergence ratio
Iter=1	1.000000E+3	Iter=1	1.000000E+3	Iter=1	1.00000E+3
Iter=2	2.245836E+2	Iter=2	8.957635E+2	Iter=2	6.84654E+1
Iter=3	2.093789E+2	Iter=3	7.846474E+0	Iter=3	8.57626E−2
Iter=4	7.473996E+1	Iter=4	6.735237E−3	Block-iter	
Iter=5	5.873453E+1	New augm		Iter=4	2.97468E+1
Iter=6	9.986438E+0	Iter=5	5.734238E+1	Iter=5	4.845342E−2
Iter=7	3.762686E−2	Iter=6	6.723579E−3	Block-iter	
Iter=8	2.125986E−4	New augm		Iter=6	4.734127E−3
		Iter=7	3.946447E−3		

$$\mathbf{A}_c d\mathbf{u}_c^{i+1} = \mathbf{r}_c - \mathbf{A}_{c,\mathrm{cast}} d\mathbf{u}_{\mathrm{cast}}^{i+1} - \mathbf{A}_{c,\mathrm{mold}} d\mathbf{u}_{\mathrm{mold}}^{i+1} \tag{7}$$

where index (i) stands for the iteration counter within the block-iterative solution.

The advantages of such procedure are manifold. First, the local matrices that solve each of the subproblems generated are much better conditioned, leading to a much better performance of any iterative solver chosen. Second, the partial problems to be solved are smaller and consequently faster to solve and, finally, the proposed structure can be easily parallelized so that casting and mold can be assembled and solved using different processors. Observe that the only information to be transferred is the vector of nodal unknowns. As a drawback of the method, it must be pointed out that the number of iterations required by the block-iterative method proposed depends on the penalty parameter used. Therefore, even if a better control on the global solution is achieved, the performance still depends on the conditioning of the original matrix.

In Table 1, it is possible to observe the typical Newton–Raphson convergence evolution for the three methods described. The augmented Lagrangian method shows a faster convergence evolution if compared to the standard penalty algorithm. On the other hand, the total number of iterations necessary to solve the time step is higher, leading to a longer CPU time. Looking at the block-iterative method, it is possible to judge the good performance of the Newton–Raphson convergence even if the total number of iterations is still high.

Note that the block-iterative procedure gives a solution even if the iterative loop is not fully converged, allowing the solution of the following time step without stopping the full simulation process due to a loss of convergence of the global analysis.

Thermal Contact Model

Accurate knowledge of the interfacial heat transfer coefficient between the solidifying casting and the surrounding mould is essential to produce a realistic solidification model. Hence, a reliable thermal contact model must be considered taking into account the heat transfer when the surfaces are in contact or when it exists as an open air gap [16].

Closed-Gap Thermal Contact Model. We refer to *closed-gap* thermal contact model Q_{closed} when the casting surface is in contact with the mould surface. In such case, standard Fourier's law cannot describe the heat transfer phenomena because the contacting surfaces do not physically match perfectly, leading to different temperatures at the casting and the mould surfaces (see Fig. 3). A heat resistance due to the gas trapped among the surface asperities can be experimentally observed. This resistance reduces as the contact pressure increases because the *effective* contact area extends.

The heat flux is computed as the product of a heat transfer coefficient, h_{close}, multiplied by the thermal gap, $g_\theta = T_{\mathrm{cast}} - T_{\mathrm{mould}}$, existing between the casting and mould surfaces in the form

$$Q_{\mathrm{closed}} = h_{\mathrm{closed}}(t_n)(T_{\mathrm{cast}} - T_{\mathrm{mould}}) \tag{8}$$

It must be observed that the h_{closed} is the inverse of the heat resistance coefficient, meaning that high values of the h_{closed} result into small values of the heat resistance. As a limit, an infinite value of the h_{closed} means that there is no heat resistance and Fourier's law governs the heat flux between the two bodies.

As it was commented above, the heat transfer coefficient can be

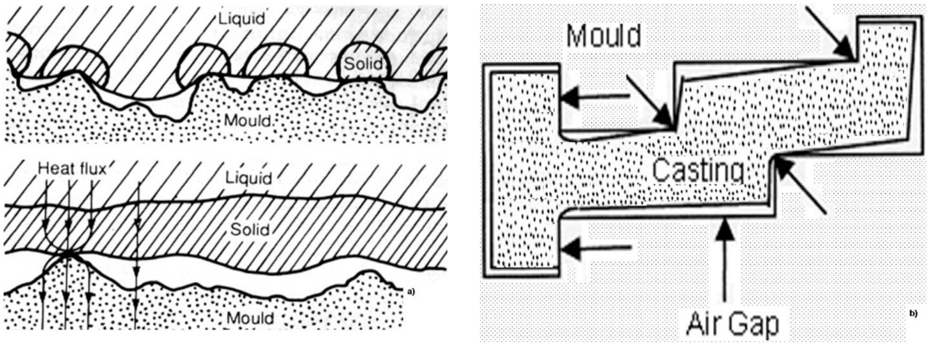

Fig. 3 Thermal contact model. (*a*) The heat conduction coefficient is a function of the effective contact area, which depends on the contact pressure. (*b*) Depending on the casting shrinkage, thermal conduction or thermal convection must be considered.

assumed as a function of the normal contact pressure, t_n, between the two contacting surfaces. The model proposed computes a thermal resistance, R_{closed}, due to the air trapped in between the mould and the casting surfaces and induced by the roughness values measured on those surfaces. In addition, the thermal resistance due to the mould coating is also accounted so that the total thermal resistance can be expressed by

$$R_{\text{closed}} = \frac{R_z}{k_{\text{air}}} + \frac{\delta_{\text{coat}}}{k_{\text{coat}}} \tag{9}$$

where $R_z = 0.5\sqrt{R_{z,\text{cast}}^2 + R_{z,\text{mould}}^2}$ is the mean peak-to-valley height of the rough surfaces, δ_{coat} is the effective thickness of the coating, and k_{air} and k_{coat} are the thermal conductivities of the gas trapped and the coating, respectively.

The effect induced by contact pressure is modeled according to the experimental evidence using the following expression:

$$h_{\text{closed}}(t_n) = \frac{1}{R_{\text{closed}}}\left(\frac{t_n}{H_e}\right)^b \tag{10}$$

where H_e is the Vickers hardness and $0.6 \leq b \leq 1.0$ is a constant exponent [9,10]. Observe that the model assumes a h_{close} proportional to the normal contact pressure as a measure for the effective contact surface interaction.

Open-Gap Thermal Contact Model. Heat convection between two bodies appears when they separate one from the other due to the thermal shrinkage effect. The model considered by the authors does not pretend to describe the air convection between the two surfaces: The surrounding air is neither discretized nor studied. The model only looks for the *effects* on the heat transfer between the two bodies. An *open-gap* heat flux Q_{open} is assumed to describe this phenomenon following the so called *Newton law of cooling*. Such heat flux is defined as a function of a coefficient, h_{open}, multiplied by the thermal gap in the form

$$Q_{\text{open}} = h_{\text{open}}(g_n)(T_{\text{cast}} - T_{\text{mould}}) \tag{11}$$

It can be verified experimentally that the heat transfer coefficient, h_{open}, depends on the open air gap, g_n (the distance between the two surfaces) due to the insulating effect of the gas trapped in the cavity:

$$h_{\text{open}}(g_n) = \frac{k_{\text{air}}}{g_n} \tag{12}$$

On the other hand, it must be observed that the above expression must be limited with the value assumed by the heat transfer coefficient when the gap is close so that

$$h_{\text{open}} = \min\left(\frac{k_{\text{air}}}{g_n}, h_{\text{close}}\right) \tag{13}$$

The model presented above is recommended for permanent mould casting. This is the case of low-pressure and HPDC technologies. The high conductivity of the metallic (steel) mould drops down when an air gap is formed due to the shrinkage of the casting material. Air (trapped gas) conductivity is much lower than the steel conductivity and the insulating effect is evident.

Observe that either the contact pressure (used to compute the heat conduction coefficient) or the gap formation can be taken into account only if a *coupled thermo mechanical simulation* is performed. Both solidification and cooling evolution are driven by the heat flux exchanged through the boundaries and such heat flux is coupled with the mechanical behavior. If a purely thermal model is used to compute the solidification evolution, a lack of information must be assumed and a simplified model for the heat flux exchange must be considered.

In this case, both open-gap and closed-gap heat fluxes can only depend on the temperature field, which is the only nodal variable computed. Both models reduce to

$$Q_{\text{ther}} = h_{\text{ther}}(T_{\text{cast}} - T_{\text{mould}}) \tag{14}$$

where the heat transfer coefficient, h_{ther}, can be only a function of the temperature field. Proposals introduced by different authors assume as driving variables the temperature of the casting surface, or the temperature of the mould surface, or even an average (air) temperature field.

In our opinion, the temperature field at the contact surface is not representative of the heat flux behavior and it is not possible to distinguish between open-gap and closed-gap heat behaviors because the mechanical gap is not computed. It is easy to observe, experimentally as well as numerically, that the surface temperature of the casting material drops very rapidly when coming in contact with the mould. The surface skin becomes solid even if the casting volume is still mainly liquid. As a consequence, the temperature field on the surface is not representative of the solidification evolution of the part (thermal shrinkage).

To overcome this problem, we propose a heat transfer coefficient as a function of the percentage of solidified casting material, $h_{\text{ther}}(F_S)$, where F_S takes into account the evolution of the solidification as

$$F_S = \frac{1}{V}\int f_S(T)dV \tag{15}$$

where $0 \leq f_S(T) \leq 1$ is the solid fraction function computed at each point of the casting volume. As a result, the heat flux is defined as a function of the volumetric contraction of the casting that is an average open air gap all around the part. Given this, the heat transfer coefficient is computed as

$$h_{\text{ther}}(F_S) = F_S\bar{h}_{\text{open}} + (1 - F_S)\bar{h}_{\text{close}} \tag{16}$$

where $\bar{h}_{\text{close}}$ and $\bar{h}_{\text{open}}$ are average values for the heat conduction and heat convection coefficients, respectively.

Heat Convection Model: The Newton Law of Cooling. Observe that a heat convection model should be considered to study the cooling of the casted part induced by the surrounding environment during the demolding operation. Also, in this case, the FE discretization only studies the thermomechanical behavior of the bodies without considering the air. The proposed model is based on the Newton law of cooling considering the heat flux as the product between a heat transfer coefficient and the thermal gap:

$$Q_{\text{conv,env}} = h_{\text{env}}(T_{\text{env}})(T_{\text{mould}} - T_{\text{env}}) \tag{17}$$

Note that the heat transfer coefficient depends on the casting temperature in contact with the environment $h_{\text{env}}(T_{\text{cast}})$, assuming that the air convection generated is proportional to the existing thermal gap.

Heat Radiation Model. Heat radiation flux between two facing bodies is computed using the Stefan–Boltzmann law:

$$Q_{\text{rad}} = h_{\text{rad}}[(T_{\text{cast}} + 273.16)^4 - (T_{\text{mould}} + 273.16)^4] \tag{18}$$

where the heat radiation coefficient h_{rad} depends on the emissivities of the two bodies, $\varepsilon_{\text{coat}}$ and $\varepsilon_{\text{mould}}$, respectively, and Stefan's constant σ_a as

$$h_{\text{rad}} = \frac{\sigma_a}{(1/\varepsilon_c + 1/\varepsilon_m - 1)} \tag{19}$$

It must be pointed out that, for casting analysis, the two surfaces are coincident so that the view factors can be neglected.

Finally, when the heat is dissipated through the surrounding environment during demolding, the radiation law is expressed in the form

$$Q_{\text{rad,env}} = \sigma_a\varepsilon_{\text{cast}}[(T_{\text{cast}} + 273.16)^4 - (T_{\text{env}} + 273.16)^4] \tag{20}$$

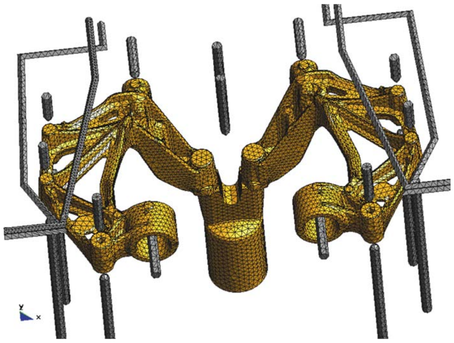

Fig. 4 Automotive part; FE mesh generated for the casting and the cooling system

Numerical Simulations

The formulation presented in previous sections is illustrated here with a number of numerical simulations. The goal is to demonstrate the good performance of the proposed formulation in the framework of infinitesimal strain coupled thermal plasticity for industrial casting analyses and, in particular, for steel mould casting. Computations are performed with the FE code VULCAN developed by the authors at the International Center for Numerical Method in Engineering (CIMNE) in Barcelona, Spain, and commercialized by QUANTECH-ATZ [18]. In all the simulations, the Newton–Raphson method, combined with a line-search optimization procedure, is used to solve the nonlinear system of equations arising from the spatial and temporal discretizations of the weak form of the governing equations. Convergence of the incremental iterative solution procedure was monitored by requiring a tolerance of 0.1% in the residual based error norm.

Penalty Versus Augmented Lagrangian Method. This example is intended to show the important role played by the element size. It is easy to understand that the finer the mesh used is, the more deformable is the body defined in the FE mesh, allowing the use of lower values of the penalty parameter to achieve a good solution. Figures 5(*a*) and 5(*b*) show two different mesh discretizations used to demonstrate the performance of the soft contact formulation. The contact benchmark consists of the upsetting of the upper block pressed against the base block. To increase the difficulty, the material stiffness of the base block is ten times higher compared to the other block.

This benchmark tries to reproduce the situation that one should face when solving a real industrial solidification analysis. Figure 4 shows an automotive casting part and the corresponding FE mesh. Half a million elements are necessary to mesh the full casting system including cooling channels and mould. Even if the mesh looks good and the total number of elements is close to the computational limit in a standard PC, few elements are placed in the thickness of the part. Hence, mechanical contact presents the same problem shown by the coarse mesh in the contact benchmark.

Figures 6(*a*) and 7(*a*) show the convergence of both the contact reaction and the contact penetration when the penalty parameter is increased. Figure 6(*b*) shows what happens when the coarse mesh is used. It is not possible to achieve the converged solution for

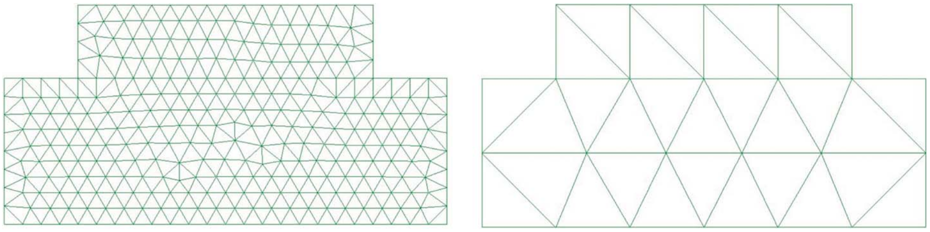

(*a*) (*b*)

Fig. 5 Contact benchmark: (*a*) fine mesh and (*b*) coarse mesh

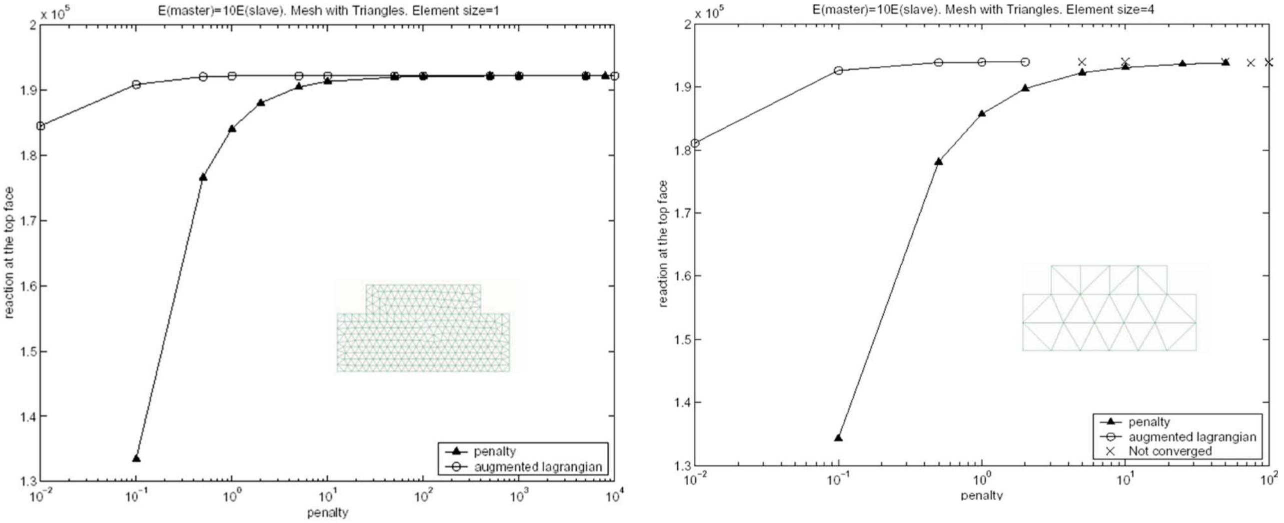

(*a*) (*b*)

Fig. 6 Contact reaction for both the penalty and the augmented Lagrangian methods when increasing the penalty parameter: (*a*) fine mesh and (*b*) coarse mesh

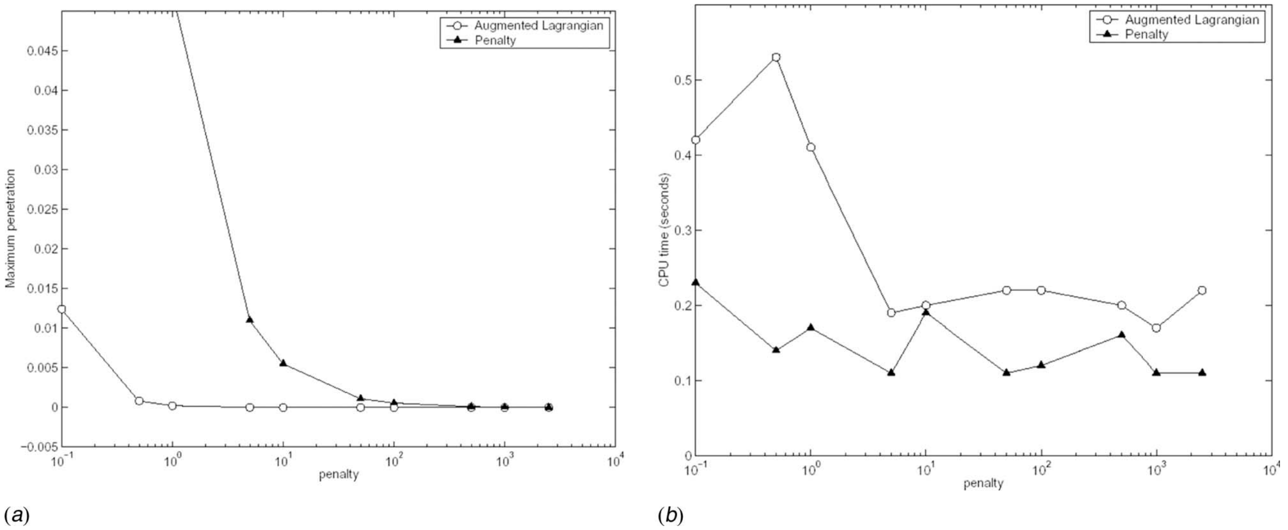

(*a*) (*b*)

Fig. 7 Contact benchmarkcomparison between penalty and the augmented Lagrangian methods: (*a*) convergence of the contact penetration to satisfy contact impenetrability constraint when increasing the penalty parameter and (*b*) CPU time

high values of the penalty parameter due to locking of the analysis. The convergence to the final solution is slower and often it cannot be achieved. In fact, locking of the solution is the main drawback of the penalized methods. Roughly speaking, if a penetration is detected, then a contact element is generated. The stiffness of such element in the direction normal to the surface is set to a very high value compared to the material stiffness of the contacting bodies. Observe that, to get zero penetration and fully satisfy the impenetrability constraint imposed by the contact condition, an infinite value should be given to the penalty parameter. This is not possible and it can be demonstrated that the maximum value that can be used corresponds to the maximum eigenvalue of the final system of equations to be solved. In many occasions, this value is not large enough to prevent penetration and if one tries to increase it, then locking of the solution occurs.

The augmented Lagrangian algorithm is possibly the most used solution to overcome this problem, enabling the use of lower values for the original penalty parameter. It can be observed in Figs. 6(*a*) and 7(*a*) how the augmented Lagrangian method has a better performance to achieve the converged solution using lower values for the penalty parameter. On the other hand, Fig. 7(*b*) clearly presents the weakness of the method in terms of CPU time. Augmented Lagrangian is two or three times slower than the standard penalty method. Hence, even if the choice of a correct penalty parameter is less problematic, the CPU time increases significantly. According to the experience of the authors, this method is not efficient for large-scale computations.

Thermomechanical Solidification Benchmark. This example is concerned with the solidification process of a cylindrical aluminum specimen in a steel mould. The main goal of this benchmark is to show the accuracy of the full coupled thermomechanical contact model proposed for a solidification analysis. The numerical results have been compared to the experimental values in Ref. [19]. The experiment consists of the solidification of commercially pure aluminum into an instrumented mould. Thermocouples have been placed in the mould wall and in the mould cavity. The thermocouple locations are shown in Fig. 8. Two quartz rods were inserted into the mould to measure both the displacement of the solidifying cylinder and the mould expansion. The geometry of the problem is shown in Fig. 8. The starting conditions assumed for the numerical simulation consider a completely filled mould with aluminum in the liquid state at a uniform temperature of 670°C, and an initial temperature of the mould was set to 200°C. A thermoelastic constitutive model has been used to simulate the material behavior of both the aluminum casting and the steel mould. The external surfaces of the mould as well as the upper surface of the casting metal have been assumed perfectly insu-

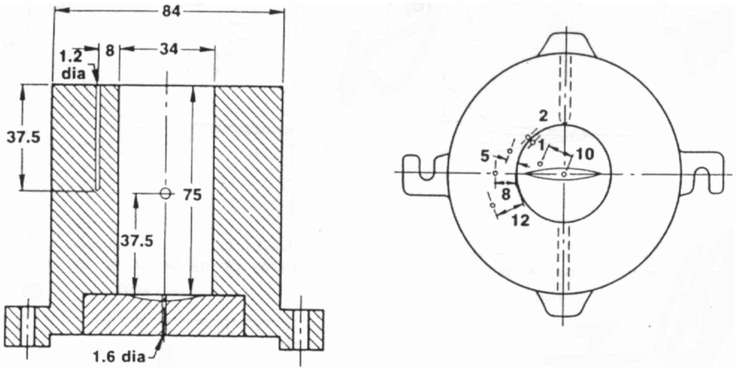

Fig. 8 Cylindrical aluminum solidification test; geometry of the experimental apparatus and location of both thermocouple and displacement transductors

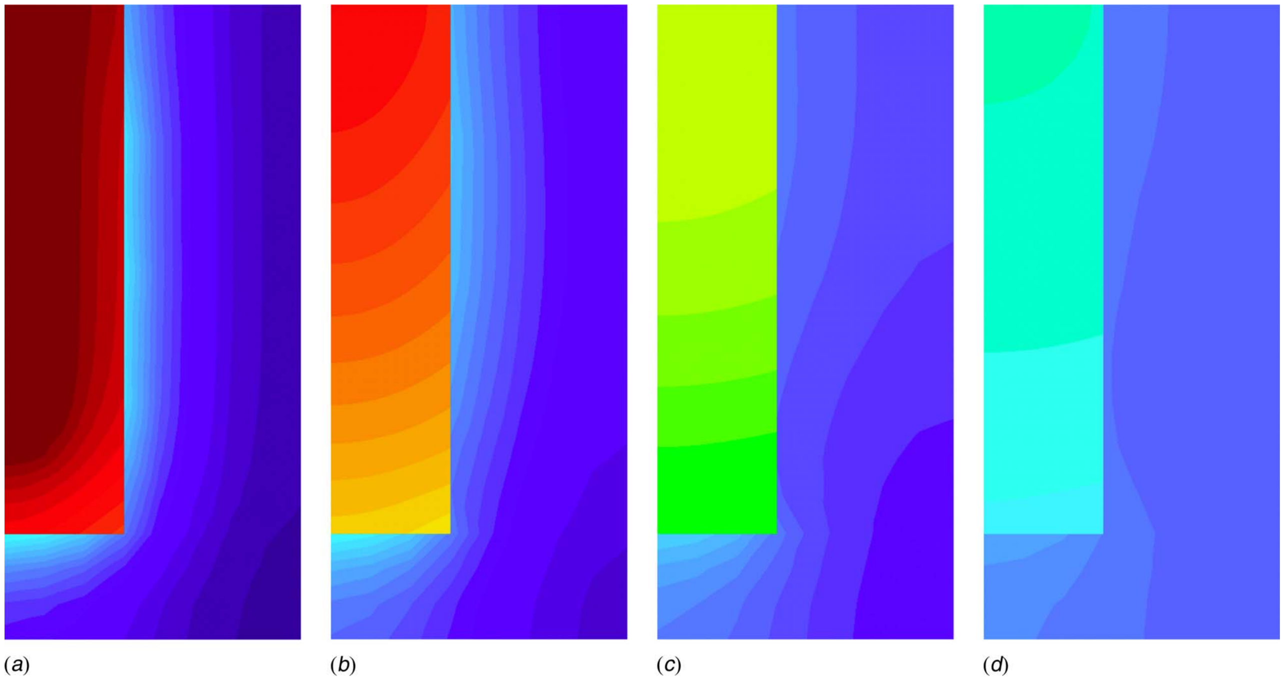

Fig. 9 Cylindrical aluminum solidification test; temperature evolution: (*a*) 10 s, (*b*) 20 s, (*c*) 40 s, and (*d*) 90 s

lated. A constant heat transfer coefficient by conduction $h_{\mathrm{cond}} = 2300\ \mathrm{W/m^2\,s}$ has been assumed as the limit value of the convection-radiation heat flux existing between the aluminum part and the steel mould as a function of the open air gap (Fig. 9).

Figure 10 shows the temperature evolution at the casting center, casting surface, and mould surface compared to the experimental

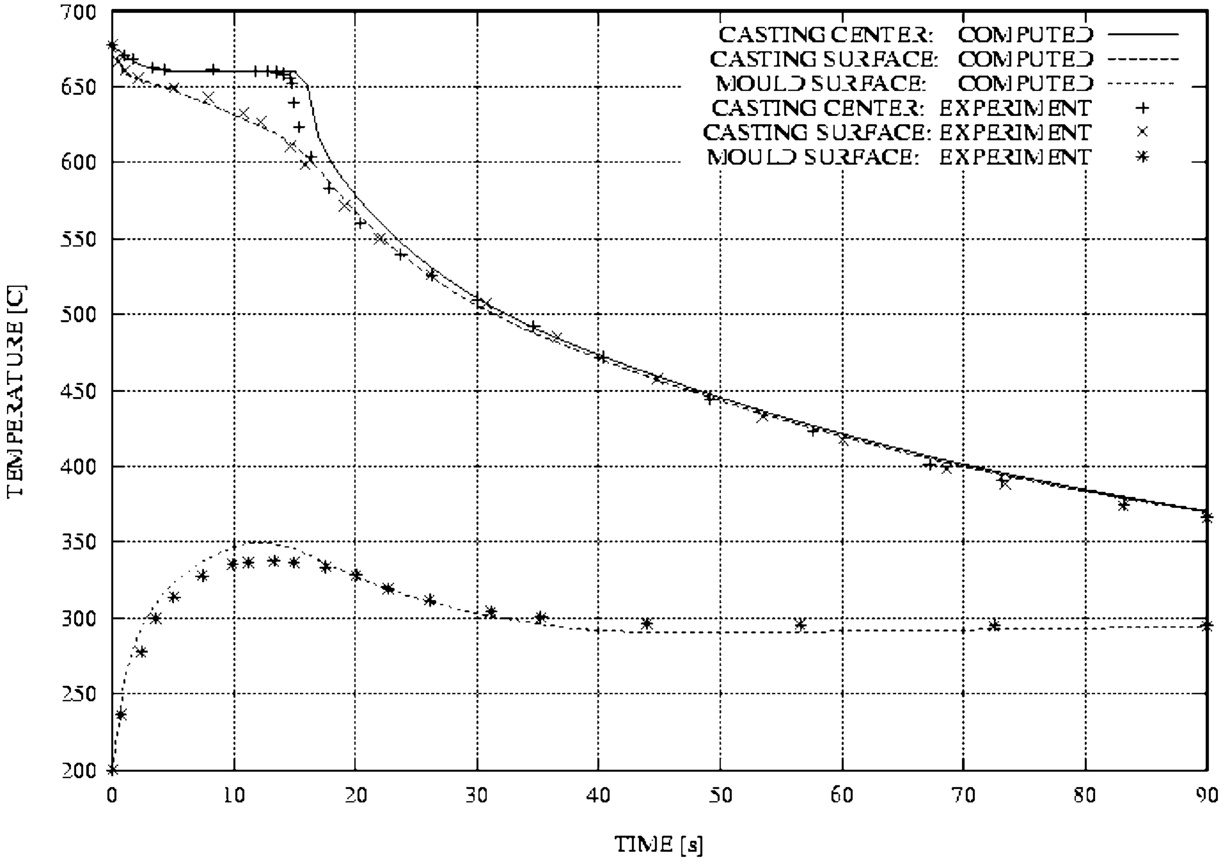

Fig. 10 Comparison between computed and experimental values of the temperature at the casting center, casting surface, and mould surface, respectively

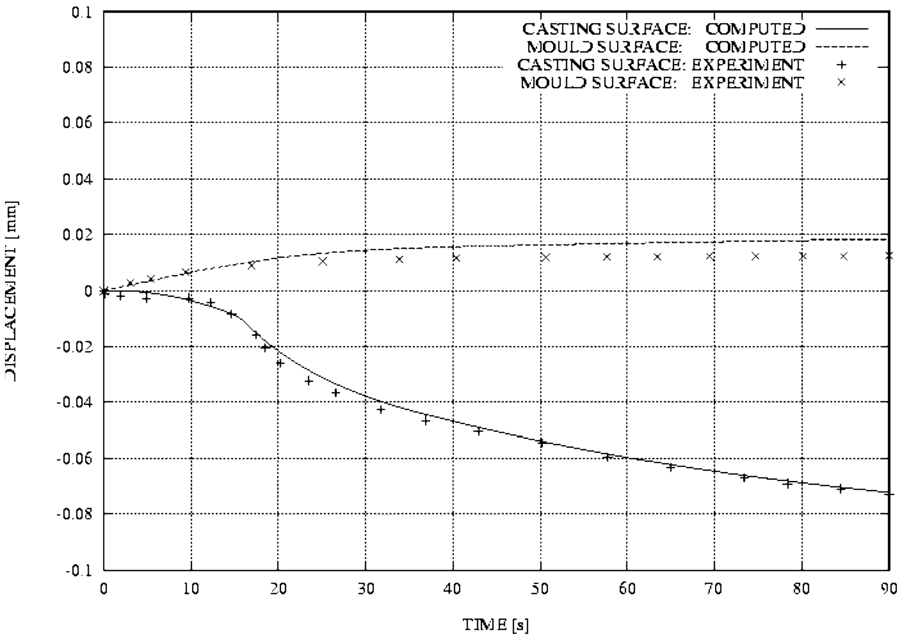

Fig. 11 Comparison between computed and experimental values of the radial displacement on the casting surface and mould surface, respectively

data. Figure 11 shows the evolution of the radial displacements for both casting and mould surfaces. The difference between the two curves corresponds to the evolution of the open air gap. Temperature and air gap evolutions predicted by the model compare very well with the experimental results demonstrating the accuracy of the thermomechanical model presented [20,21].

Foundry Simulation of an Aluminum Motor Block. The final numerical simulation is concerned with the solidification process of an aluminum motor block in a steel mould. Geometrical and material data were provided by the TEKSID Aluminum Foundry Division. The full mesh, including the mould, consists of 580.000 tetrahedral elements. The aluminum material behavior has been modeled by the fully coupled thermoviscoplastic model, while the steel mould behavior has been modeled by a simpler thermoelastic model. The initial temperature is 700°C for the casting and is 300°C for the mould. The cooling system has been kept at 20°C. The temperature evolution as well as thermal shrinkage during solidification are shown in Fig. 12. Figure 13 shows the temperature, von Mises deviatoric stresses, and equivalent plastic strain distributions.

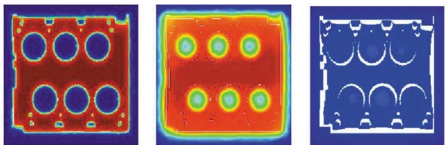

Fig. 12 Temperature and shrinkage evolution (plane *xy*)

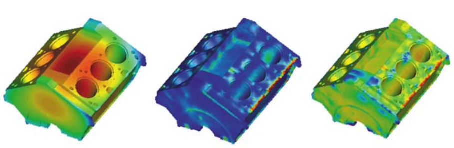

Fig. 13 (*a*) Temperature, (*b*) J2 von Mises, and (*c*) plastic strain distributions

Concluding Remarks

In a foundry analysis, many casting tools must be represented. Nowadays, the mesh discretization that can be adopted for the computation in a standard PC is, unfortunately, generally too coarse. Very few elements can be placed in the thickness of the casting, especially if HPDC processes must be simulated. The low capability to capture the high temperature gradients, the solidification process, as well as the contact interaction makes an accurate simulation difficult to achieve. Moreover, the complexity of the CAD geometry obliges the use of tetrahedral elements inducing high numerical stiffening in the solution. This problem is augmented when the incompressibility constraint is enforced as in the case of liquidlike behavior or J2-plasticity constitutive law.

The nonsmooth description of the contacting surfaces is another consequence introduced by the mesh discretization: The normal vector to the surface is nonunivocally defined and in the case of coarse meshes, the contact reaction field is not uniformly spread.

Furthermore, the use of large time steps as well as the loss of constraint induced by the shrinkage effect of the casting make the analysis highly nonlinear.

The thermomechanical contact plays an extremely important role in a casting analysis, driving the solidification and the following cooling phase. A novel definition of the heat transfer coefficient for purely thermal analysis has been proposed. On the other hand, the dependency on mechanical quantities such as the contact pressure or the open air gap makes the difference when selecting the contact algorithm to correctly represent the mechanical constraint.

Nomenclature

$\boldsymbol{\sigma}$ = stress tensor
$p, \mathbf{s}$ = hydrostatic and deviator parts of the stress tensor
H = enthalpy
Q_{rad} = heat flux by radiation
$Q_{\text{closed}}, Q_{\text{open}}$ = heat flux at the contact interface (closed- and open-gap models)
$h_{\text{closed}}, h_{\text{open}}$ = heat transfer coefficients (closed- and open-gap models)

T_{mould}, T_{cast}, T_{env} = mold, casting, and environment temperatures
t_n = contact pressure
g_n = normal gap (open air gap)

References

[1] Brezzi, F., and Fortin, M., 1991, *Mixed and Hybrid Finite Element Methods*, Springer, New York.
[2] Agelet de Saracibar, C., Chiumenti, M., Valverde, Q., and Cervera, M., 2006, "On the Orthogonal Subgrid Scale Pressure Stabilization of Finite Deformation J2 Plasticity," Comput. Methods Appl. Mech. Eng., **195**, pp. 1224–1251.
[3] Cervera, M., Chiumenti, M., Valverde, Q., and Agelet de Saracibar, C., 2003, "Mixed Linear/Linear Simplicial Elements for Incompressible Elasticity and Plasticity," Comput. Methods Appl. Mech. Eng., **192**, pp. 5249–5263.
[4] Chiumenti, M., Valverde, Q., Agelet de Saracibar, C., and Cervera, C., 2002, "A Stabilized Formulation for Elasticity Using Linear Displacement and Pressure Interpolations," Comput. Methods Appl. Mech. Eng., **191**, pp. 5253–5264.
[5] Chiumenti, M., Valverde, Q., Agelet de Saracibar, C., and Cervera, C., 2004, "A Stabilized Formulation for Incompressible Plasticity Using Linear Triangles and Tetrahedral," Int. J. Plast., **20**, pp. 1487–1504.
[6] Codina, R., 2000, "Stabilization of Incompressibility and Convection Through Orthogonal Sub-Scales in Finite Element Methods," Comput. Methods Appl. Mech. Eng., **190**, pp. 1579–1599.
[7] Cervera, M., Agelet de Saracibar, C., and Chiumenti, M., 1999, "Thermo-Mechanical Analysis of Industrial Solidification Processes," Int. J. Numer. Methods Eng., **46**, pp. 1575–1591.
[8] Chiumenti, M., Agelet de Saracibar, C., and Cervera, M., 1999, "Constitutive Modelling and Numerical Analysis of Thermomechanical Phase-Change Systems," CIMNE, Monograph M48, Barcelona.
[9] Hallam, C. P., Griffiths, W. D., and Butler, N. D., 2000, "Modelling of the Interfacial Heat Transfer Between an Al-Si Alloy Casting and a Coated Die Steel," *Proceedings of IX International Conference on Modelling of Casting, Welding and Advanced Solidification Processes*.
[10] Ransing, R. S., and Lewis, R. W., 1998, "Thermo-Elasto-Visco-Plastic Analysis for Determining Air Gap and Interfacial Heat Transfer Coupled With the Lewis-Ransing Correlation for Optimal Feeding Design," *Proceedings of VIII International Conference on Modelling of Casting, Welding and Advanced Solidification Processes*, San Diego, CA.
[11] Wriggers, P., 2002, *Computational Contact Mechanics*, Wiley, New York.
[12] Wriggers, P., and Zavarise, G., 1993, "Thermomechanical Contact: A Rigorous but Simple Numerical Approach," Comput. Struct., **46**, pp. 47–53.
[13] Laursen, T. A., and Simo, J. C., 1993, "A Continuum-Based Finite Element Formulation for the Implicit Solution of Multibody, Large Deformation Frictional Contact Problems," Int. J. Numer. Methods Eng., **36**, pp. 3451–3485.
[14] Agelet de Saracibar, C., 1998, "Numerical Analysis of Coupled Thermo-Mechanical Frictional Contact Problems. Computational Model and Applications," Arch. Comput. Methods Eng., **5**, pp. 243–301.
[15] Ju, J. W., and Taylor, R. L., 1998, "A Perturbed Lagrange Formulation for the Finite Element Solution of Non-Linear Frictional Contact Problems," Journal of Theoretical and Applied Mechanics, **7**, pp. 1–14.
[16] Jaouen, O., and Bellet, M., 1998, "A Numerical Mechanical Coupling Algorithm for Deformable Bodies: Application to Part/Mold Interaction in Casting Process," *Proceedings of VIII International Conference on Modelling of Casting, Welding and Advanced Solidification Processes*, San Diego, CA.
[17] Nour-Omid, B., and Wriggers, P., 1987, "A Note on the Optimum Choice for Penalty Parameter," Commun. Appl. Numer. Methods, **3**, pp. 581–585.
[18] VULCAN, Software for Simulation of Casting Processes, QUANTECH-ATZ, http://www.quantech.es/QuantechATZ/Vulcan.html
[19] Nishida, Y., Droste, W., and Engler, S., 1986, "The Air-Gap Formation Process at the Casting-Mould Interface and the Heat Transfer Mechanism Through the Gap," Metall. Trans. B, **17B**, pp. 833–844.
[20] Agelet de Saracibar, C., Cervera, M., and Chiumenti, M., 2001, "On the Constitutive Modelling of Coupled Thermomechanical Phase Change Problems," Int. J. Plast., **17**, pp. 1565–1622.
[21] Agelet de Saracibar, C., Cervera, M., and Chiumenti, M., 1999, "On the Formulation of Coupled Thermoplastic Problems With Phase-Change," Int. J. Plast., **15**, pp. 1–34.

Flow Boiling of R134a and R134a/Propane Mixtures at Low Saturation Temperatures Inside a Plain Horizontal Tube

A. Rabah[1]
e-mail: rabahss@hotmail.com

S. Kabelac

Institut für Thermodynamik,
Helmut-Schmidt Universität,
Universität der Bundeswehr–Hamburg,
Holstenhofweg 85,
22043 Hamburg, Germany

Local heat transfer coefficients for flow boiling of pure 1,1,1,2-tetrafluoroethane (R134a) and binary mixtures of propane (R290) and R134a were measured. The experimental setup employed a vapor heated plain horizontal tube ($d_i = 10$ mm, $d_o = 12$ mm, $L = 500$ mm). The measurements covered a wide range of saturation temperatures ($233 \leq T_s \leq 278$ K), mass fluxes ($100 \leq \dot{m} \leq 300$ kg/m^2 s), qualities ($0 \leq \dot{x} \leq 1$), and concentrations ($0 \leq \tilde{z} \leq 0.65$). In the zeotropic region of R134a/R290 mixtures, the measured local heat transfer coefficient was found to show a maximum decrease by a factor of 2 relative to that for pure R134a. At the azeotropic point (65% R290), it was found to increase by a factor of 1.2. The measured local heat transfer coefficients for both R134a and R134a/R290 were compared with a number of correlations.
[DOI: 10.1115/1.2897345]

Keywords: flow boiling, R134a, propane, mixture

1 Introduction

The reduction in chlorofluorocarbon (CFC) and hydrochlorofluorocarbon (HCFC) production and the scheduled phaseout of these ozone depleting refrigerants prompted the development and characterization of new environmentally safe refrigerants for use in air-conditioning and refrigeration equipments. The most successful, to date, has been the development of 1,1,1,2-tetrafluoroethane (R134a) as a substitute for dichlorodifluoromethane (R12). R134a has similar saturation pressure and coefficient of performance (COP) as R12 [1]. Several zeotropic and azeotropic mixtures resulting in vapor pressure and COP similar to R22 have been identified. Among them, propane (R290)/R134a mixture is a possible substitute to R22 [2]. R134a/R290 mixture possesses an azeotropic point at 65 mol % R290 [3]. The azeotropic mixture of R134a/R290 has a higher COP and capacity than R22. Incorporation of a natural fluid typically has the additional advantage of making mixture soluble for mineral oil. Of course, the disadvantage of using high percentage of hydrocarbon in any mixture is that it is likely to be flammable. Besides environmental and safety considerations and thermodynamic properties, flow boiling heat transfer characteristics play an important role in the selection of the substitute refrigerant. That is to say, if the heat transfer characteristic of an alternative refrigerant does not deviate too much from that of a reference fluid, a maximum retrofitting would be possible without major changes in the component design and the manufacturing process.

Experimental data and calculation methods are available for thermodynamic properties, but there is a limited number of publications on heat transfer characteristics of newly developed refrigerants and their mixtures.

Kattan et al. [4] carried out extensive measurements on flow boiling of R134a, R502 (azeotropic mixture of R22 and R115), R404A (near-azeotropic mixture of R125/R134a/R143a), and R402A (azeotropic mixture of R22/R290/R125) at a saturation pressure of 0.27 MPa. They employed water as a heating medium. They used their data and developed a flow pattern map and a correlation for the prediction of heat transfer coefficient.

Wettermann [5] measured the local heat transfer coefficients of R134a, R846, and R134a/R846 mixtures at moderate to high saturation pressure (0.4–3.24 MPa) on electrically heated plain copper and nickel horizontal tubes. His study aimed to investigate the influence of mass flux, heat flux, pressure, flow patterns, and other parameters on the flow boiling heat transfer coefficient. Other investigations on R134a include among others the work of Eckels et al. [6] at moderate saturation pressure.

With reference to predictive models for pure component heat transfer coefficient, there exist a number of empirical and semi-empirical correlations. These include the models of Steiner [7], Shah [8], Gungor and Winterton [9], Kandlikar [10], and Kattan et al. [11], to mention a few. All these correlations were developed based on superimposition of two main flow boiling mechanisms, namely, nucleate boiling and forced convection [12].

Figure 1 shows comparison between a number of predictive models for the heat transfer coefficient and previous experimental data.

In contrary to the flow boiling of pure substances, there exist only limited works in the open literature in the field of flow boiling of mixtures. These works are not listed in the present work; nevertheless, reference is to be made to Collier and Thome [13]. The existing works were on horizontal and vertical tubes of copper, nickel, and stainless steel. As in the case for pure substances, most of the available experimental works are for mixtures of old refrigerants. Furthermore, most of the available pure component predictive models are used for mixtures with some modifications.

2 Experimental Setup

Figure 2(*a*) shows a schematic representation of the experimental setup. It composed of three loops, namely, a test loop carrying the tested refrigerant, secondary evaporator providing the hot utility, and refrigeration cycle for cold utility.

2.1 Test Loop. The locus of the test loop is indicated by the thick solid line in Fig. 2(*a*). It consisted of test section (TS),

---

[1] Corresponding author.

Contributed by the Heat Transfer Division of ASME for publication in the JOURNAL OF HEAT TRANSFER. Manuscript received February 5, 2007; final manuscript received July 17, 2007; published online April 23, 2008. Review conducted by Yogesh Jaluria.

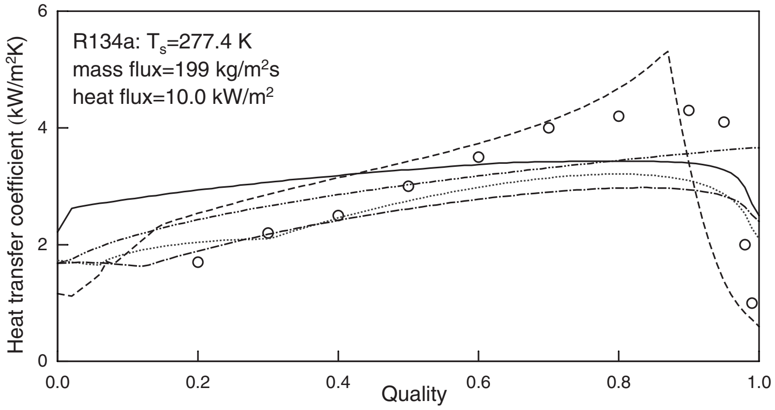

Fig. 1 Comparison of five different correlations with the experimental data of Kattan et al. [4]. Legend: ······, Shah [8]; –··–, Gungor and Winterton [9]; –·–·–, Kandlikar [10]; – – –, Kattan et al. [11]; —, Steiner [7]; ○, Kattan et al. [4] experimental data.

condenser (HE1), storage tank (T1), second condenser (HE2), positive-displacement pump (P1), two sets of preheaters (H1,…,6 and H7,…,10), and two sight glasses (SG1 and SG2). The refrigerant (in liquid state) in the storage tank T1 was pumped into the test loop using positive-displacement pump P1. At the negative suction side of the pump, a plate-type subcooler HE2 was installed. This was made to avoid cavity. The pump produced a constant volume flow of refrigerant. To control the flow rate into the test loop as well as to provide the minimum flow rate necessary for cooling and lubrication the pump, a bypass line was installed. The bypass line diverted a certain portion of flow and returned back to the storage tank T1. At the upstream of the first set of preheaters H1,…,6, the temperature, pressure, and mass flow rate of the incoming subcooled refrigerant were measured. Knowledge of these parameters facilitates the calculation of enthalpy at the inlet of the test loop, which is required for the determination of vapor quality. Heat was added to refrigerant as it passed through the two sets of preheaters, H1,…,6 and H7,…,10. This was made to bring the refrigerant to the desired vapor quality, temperature, and pressure at the inlet of the test section. Before it entered into the test section, the temperature, and pressure of the refrigerant were measured. At the outlet of the test section, the temperature and pressure drop were also measured. Parallel to the temperature and pressure measurements, the prevailing flow patterns at the inlet and outlet of the test section were observed at sight glasses SG1 and SG2. The two phase refrigerant leaving the test section was then condensed and returned to storage tank. The condenser HE1 was a plate-type heat exchanger. The cold utility needed for condensation and subsequent subcooling of the refrigerant leaving the test section was realized by a two-stage vapor compression refrigeration cycle with R507 as a working refrigerant. The refrigeration unit has a cooling rate in the range from 10 kW (223 K) to 25 kW (273 K). The thermal losses to the surrounding from the pipes and apparatus except the sight glasses were minimized using Armaflex foam as insulation.

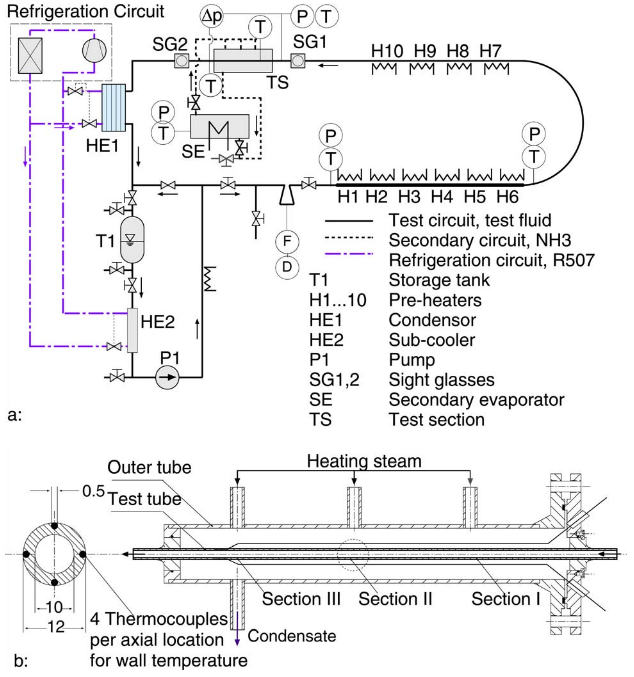

Fig. 2 (*a*) Experimental setup and (*b*) test section

The test section consisted of two horizontal concentric pipes (Fig. 2(*b*)), similar in configuration to double pipe heat exchanger. The inner tube was made of stainless steel (d_i=10 mm, d_o=12 mm, L=500 mm). It was instrumented with a number of nickel-chrome thermocouples along its length at three axial locations (Sections I, II, III in Fig. 2(*b*)). At each axial location, thermocouples were distributed at the top, bottom, left, and right hand sides of the tube. The thermocouple was soldered in a 0.5 mm deep groove at the external surface of the tube.

The outer tube was provided with three inlet ports for the incoming vapor (hot utility) and one port at the bottom for the condensate leaving the test section. The refrigerant temperature and pressure at the inlet and outlet of the test section as well as the pressure drop across the test section were measured.

2.2 Secondary Evaporator. The purpose of the secondary evaporator was to provide the necessary hot utility for evaporating the test refrigerant. Figure 3 shows a schematic presentation of the secondary evaporator. Ammonia vapor, being having high latent heat of evaporation λ relative to other refrigerants, was used as a hot utility. It was generated in a cylindrical-shaped stainless steel container ($300\times\oslash 71.0$ mm), with a liquid charge of more than 50 vol %. The liquid container was equipped with two 1 kW rod-type electric immersion heaters. The power to the electric heaters was supplied from a variable resistance regulated transformer. The ammonia vapor was condensed at the external of tube and returned as liquid to the boiler by gravity.

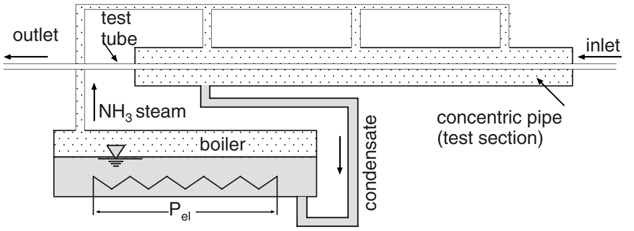

Fig. 3 Secondary evaporator loop for heating the test section

3 Measurements and Uncertainties

The standard uncertainty is the positive square root of the estimated variance. The individual standard uncertainties are combined to obtain the expanded uncertainty. The expanded uncertainty is calculated from the low of propagation of uncertainty. All measurement uncertainties are reported for a 95% confident interval except where specified otherwise.

The nickel-chrome thermocouples were calibrated against a standard platinum resistance thermometer (SPRT). SPRT was calibrated by Physikalisch Technischen Bundesanstalt (PTB) to an expanded uncertainty of 1.5 mK. For the reference junction temperature, a quartz thermometer, which was calibrated with a distilled ice bath, agreed with SPRT to within 0.004 K. The measured thermocouple electromotive force (EMF) was regressed to the reference SPRT temperature as

$$T = a + bV \tag{1}$$

The standard uncertainty U_T is calculated from the law of propagation of error as

$$U_T = \sqrt{A_T^2 + C_T^2 + P_T^2} \tag{2}$$

where A_T is the data acquisition error, C_T is the calibration error, which is the SPRT error, and P_T is the precision error, which is defined in accordance with DKD [14] as

$$P_T = \frac{t_{\lambda,95\%}\sigma}{\sqrt{N}} \tag{3}$$

where t is the student test at 95% confidence, σ is the standard deviation, N is the number of data points, and λ is the degree of freedom $\lambda = N-1$.

Example 1. The calibration equation of one of temperature sensor used in this work was

$$T = -0.501147 + 1.009014V \tag{4}$$

with $\sigma = 0.083$ K and $N = 18$.

- Estimation of precision error P_T. Using Adunka's [15] table, the student test was estimated $t_{17,95\%} = 2.11$. Hence, Eq. (3) yields $P_T = 42.422$ mK.
- Data acquisition error A_T. The data acquisition error was taken as that supplied by the manufacturer of the corresponding multimeter, "hybridrecorder Yokogawa HR 3760." It has a "quoted" uncertainty of $\pm(0.05\%$ of reading $+2$ mV) for $V \leq 50$ V. This was converted, in accordance with 95% confidence limit for an output voltage of 40.139 V, which corresponds to 313 K (DKD [14]), into

$$A_V = \frac{0.05 \times 40.139 \times 10^{-2} + 2 \times 10^{-3}}{\sqrt{3}} \text{V} = 12.742 \text{ mV} \tag{5}$$

hence,

$$A_T = \frac{\partial T}{\partial V} A_V \tag{6}$$

With the partial derivative $\partial T/\partial V$ evaluated using Eq. (4), the data acquisition error A_T is 12.857 mK.

- Calibration error C_T. The calibration error was taken as that for SPRT error $C_T = 1.5$ mK.
- Standard uncertainty U_T,

$$U_T = \sqrt{42.422^2 + 12.857^2 + 1.5^2} = 44.353 \text{ mK} \tag{7}$$

The pressure was measured using a high precision DMS (dehnungsmesstreifen (strain-gauge)) pressure transducer with an uncertainty of 0.1%. The pressure drop was also measured with a DMS-differential pressure transducer with an uncertainty of 0.1%. The voltage was measured using Keithley voltmeter with an error of 0.2% according to manufacturer.

4 Data Reduction

For flow boiling in a horizontal tube, the local heat transfer coefficient at the axial position z is

$$h(z) = \frac{\dot{q}_i(z)}{T_{wi}(z) - T_s(z)} \tag{8}$$

where $T_s(z)$ is the saturation temperature for pure refrigerant or the bubble point temperature for mixture at the axial position z. The local heat flux is

$$\dot{q}_i(z) = \frac{\dot{Q}(z)}{A_i} \tag{9}$$

where A_i is the heat transfer area based on the inside diameter.

In the present study, measurement of the local heat flux was not possible. Therefore, $\dot{q}(z)$ was calculated using Nusselt's theory of film condensation. However, to compensate for Nusselt's idealization, the heat flux predicted using Nusselt model was corrected as

$$\dot{q}(z) = \dot{q}_{\text{Nu}}(1 + az) \tag{10}$$

where $\dot{q}_{\text{Nu}}$ is the arithmetic mean of the local heat fluxes at Sections I, II, III in Fig. 2(*b*). They were calculated using Nusselt theory. The constant a was determined by balancing the calculated heat load with the measured one. The total heat load supplied to the test tube is

$$\dot{Q}_{\text{tot}} = \pi d_o \int_0^L \dot{q}(z) dz \tag{11}$$

Hence

$$a = \frac{2\dot{Q}_{\text{tot}}}{\pi d_o \dot{q}_{\text{Nu}} L^2} - \frac{2}{L} \tag{12}$$

where

$$\dot{Q}_{\text{tot}} = P_{\text{el}} - \dot{Q}_{\text{loss}} \tag{13}$$

where P_{el} is the electrical power supplied to vaporize ammonia. The heat loss to the surrounding was estimated to be less than 5%.

The inside wall temperature was calculated from the measured outside wall temperature $T_{wo}(z)$ utilizing a one dimensional steady state conduction equation as

$$T_{wi}(z) = T_{wo}(z) - \frac{r_o}{k}\dot{q} \ln\left[\frac{r_o}{r_i}\right] \tag{14}$$

where r_i is the inside radius of the tube and r_o is the outside radius of the tube taking into account the thermocouple thickness. k is the thermal conductivity of the tube. $T_{w,o}(z)$ was taken as the arithmetic mean of the four measured outside wall temperatures around the tube at the axial location z [16].

It should be noted that the above conduction model is for homogeneous material, while in the present work, a thermocouple was embedded in the pipe wall and the thermal conductivity of the thermocouple is different from the base tube (inhomogeneous). The error due to heat conduction in the thermocouple is generally estimated to be well below 0.01 mK [17,18].

For pure R134a and azeotropic R134a/R290 mixtures, the saturation temperature was calculated using the fundamental equation of state of Tillner-Roth and Baehr [19] and Tillner-Roth [20], respectively. The quality at the inlet of the test section was calculated assuming thermodynamic equilibrium as

$$\dot{x}_i = \frac{h(p_i,T_i) - h_f(T_i)}{h_g(T_i) - h_f(T_i)} \tag{15}$$

where the subscript i signifies the inlet of the test section. h_f and h_g are the saturated liquid and vapor enthalpies, respectively. They were calculated using the above mentioned fundamental equation of states. The bulk enthalpy at the inlet of the test section $h(p_i,T_i)$ was obtained from the first law of thermodynamics applied to steady state flow process with negligible potential and kinetic energy as

$$h(p_i,T_i) = h(T_1,p_1,\tilde{z}) + \sum_{i=1}^{10} \dot{Q}_i/\dot{M} \tag{16}$$

where $\dot{Q}_i$ is the heat supplied to the preheater i. $\dot{M}$ is the mass flow rate. T_1, p_1, and $\tilde{z}$ are the temperature, pressure, and concentration at the inlet of the first preheater, respectively. To be remembered is that the fluid condition at the inlet of the first preheater in the test loop was at a subcooling state. The change in the vapor quality across the test section is

$$\Delta\dot{x} = \frac{\dot{Q}_{\text{tot}}}{\dot{M}\lambda} \tag{17}$$

The quality at the axial position z in the test tube was calculated assuming linear variation as

$$\dot{x}(z) = \dot{x}_i + \frac{z}{L}\Delta\dot{x} \tag{18}$$

For the case of zeotropic mixture, the vapor quality as well as the molar compositions were calculated using flash model coupled with bubble point calculation. The present formulation for the prediction of molar compositions was validated, as shown in Fig. 4. Here, the symbols represent vapor liquid equilibrium (VLE) data of Kleiber [21], and the solid lines represent the calculated bubble point using the above mentioned fundamental equation of state. The results give an average deviation of 0.017 vapor mole fraction $\tilde{y}_{\text{R290}}$.

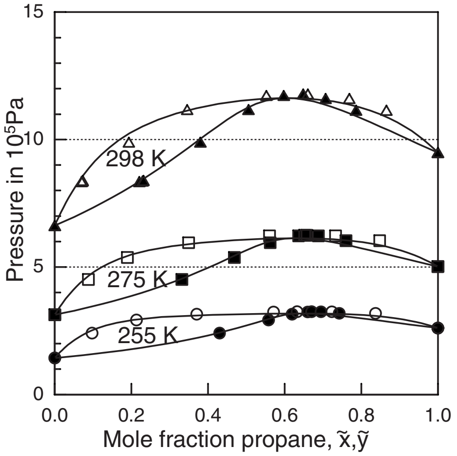

Fig. 4 A phase diagram for the system R134a/R290 mixtures (open and closed symbols represent measured data for dew and bubble points, respectively)

5 Results

5.1 Heat Transfer Coefficient

5.1.1 Pure R134a. Local heat transfer coefficients are reported for pure R134a. Figure 5 depicts the flow boiling data for R134a at $\dot{m}$=200 kg/m^2 s and T_s=of 263 K (0.2 MPa) for a wide range of vapor qualities ($0 \leq \dot{x} \leq 1$). The observed flow pattern parallel to the measured local heat transfer coefficient is shown schematically in the lower part of Fig. 5. Also shown are the "theoretical" convective and nucleate boiling heat transfer coefficients and their combined contribution. Both the convective h_c and the nucleate boiling h_n heat transfer coefficients were predicted using Steiner [7] correlation (Appendix). Their combined contribution was calculated using the asymptotic model of Steiner [7] as

$$h = \sqrt[3]{h_c^3 + h_n^3} \tag{19}$$

The following observations are drawn from Fig. 5.

1. The measured local heat transfer coefficient increases with vapor quality until it reaches a peak Point E followed by a sharp falloff. The variation of the slope of the local heat transfer coefficient with respect to the vapor quality may be attributed to the change in the flow patterns and the different boiling mechanisms (nucleate and convective) encountered in evaporation.
2. In the early stage of evaporation ($\dot{x} < 0.1$), the measured heat transfer coefficient matches very well with the predicted nucleate boiling curve (centered line) and deviates widely from the convective curve (dotted line). As can be seen in the lower part of Fig. 5, the observed flow pattern that corresponds to this region is identified as bubbly flow. In the bubbly flow pattern region, nucleate boiling is generally known to be the dominant mechanism of flow boiling.
3. In the region $0.1 \leq \dot{x} \leq 0.65$, the measured local heat transfer coefficient matches very well with the calculated combined contribution of nucleate and convective boiling (solid line). In this region, the observed flow patterns varied from stratified wavy to annular flow pattern. Under these flow patterns, both boiling mechanisms (convective and nucleate) are known to be active.
4. In the region near to the dryout, just before the onset of the dryout (Point E) causes a deterioration, the heat transfer coefficient shows an enhancement by a factor of 1.1–1.25. This factor is defined as the ratio between the measured local heat transfer coefficient and the ideal one at the vapor quality $\dot{x}_E$. The ideal heat transfer coefficient is defined as that it would have been obtained if the slope of the measured local heat transfer coefficient remained constant up to Point E.
5. Beyond Point E, the local heat transfer coefficient drops sharply. This is due to the partial dryout. That is to say, the convective local heat transfer coefficient, averaged around the perimeter of the tube, is lower than that if the entire perimeter were covered by liquid.

Similar results are shown in Fig. 6 at various mass fluxes, heat fluxes, and saturation temperatures. The overall trend of the measured local heat transfer coefficient for a wide range of vapor qualities $0 \leq \dot{x} \leq 1$ is in line with the earlier investigations reported by Kattan et al. [4] (see Fig. 1), Kabelac and de Buhr [16], and Wettermann [5].

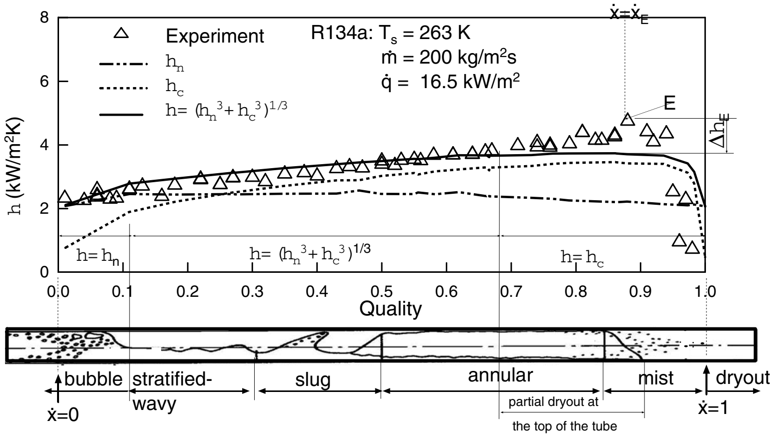

Fig. 5 The influence of the vapor quality on the local heat transfer coefficient of pure R134a

5.1.2 Mixture. Figure 7 shows the local heat transfer coefficient for R134a/R290 mixtures at $\dot{m}=100\ \mathrm{kg/m^2\,s}$, $\dot{x}=0.2$, and $p=2$ bars. As an illustration, a $T-\tilde{x},\tilde{y}$ phase diagram and a concentration difference diagram are shown in the left hand side and the upper part of Fig. 7, respectively. Also shown are the theoretical convective and nucleate boiling heat transfer coefficients and their combined contribution. The nucleate boiling was calculated using Schluender [22] model, which is

$$\frac{h_n}{h_{n,\mathrm{id}}} = \left\{ 1 + \frac{h_{n,\mathrm{id}}}{\dot{q}} (\tilde{y}_1 - \tilde{x}_1) \left[1 - \exp\left(- \frac{B_o \dot{q}}{\rho_L \beta_L \lambda} \right) \right] \right\}^{-1} \tag{20}$$

Due to the fact that R134a/R290 mixture possesses liquid-liquid immiscibility at low temperatures, the diffusion effect was also considered in the convective boiling. Thus, the convective boiling was modeled similar to the nucleate boiling (Eq. (20)) with h_c replaces h_n. The combined heat transfer coefficient h was calculated using Eq. (19).

It can be seen (Fig. 7) that both the concentration and the concentration difference have strong influence on the local heat transfer coefficient. That is to say, in the region prior to the azeotropic point, the local heat transfer coefficient decreases with increasing concentration until it reaches a minimum point, then increases toward the azeotropic point. The same cycle is repeated in the region beyond the azeotropic point. The minimum corresponds to the point where the concentration difference $|\tilde{y}-\tilde{x}|$ is maximum. Schluender [22] postulated that the reduction in the mixture heat

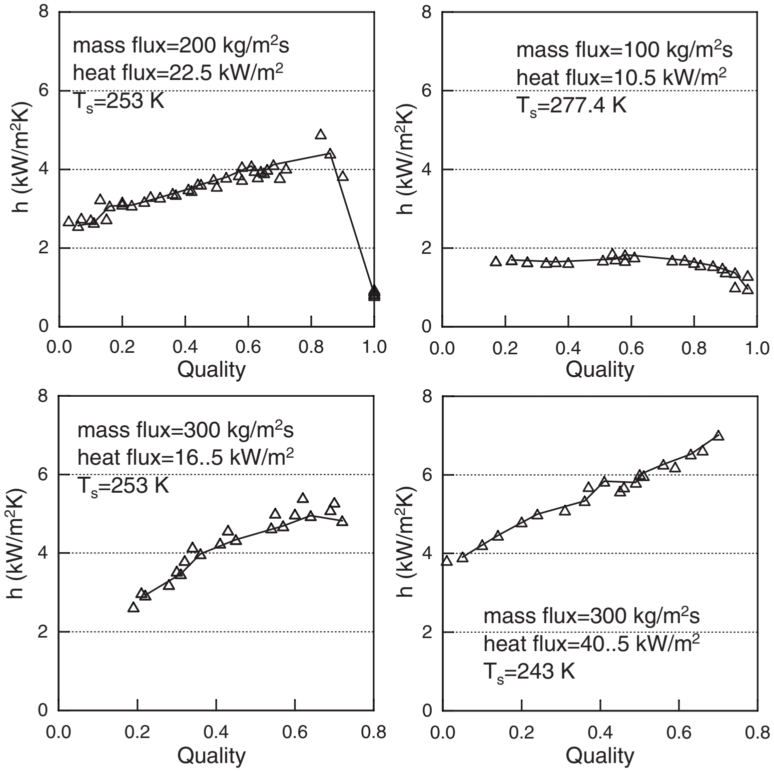

Fig. 6 The influence of the vapor quality on the local heat transfer coefficient of pure R134a

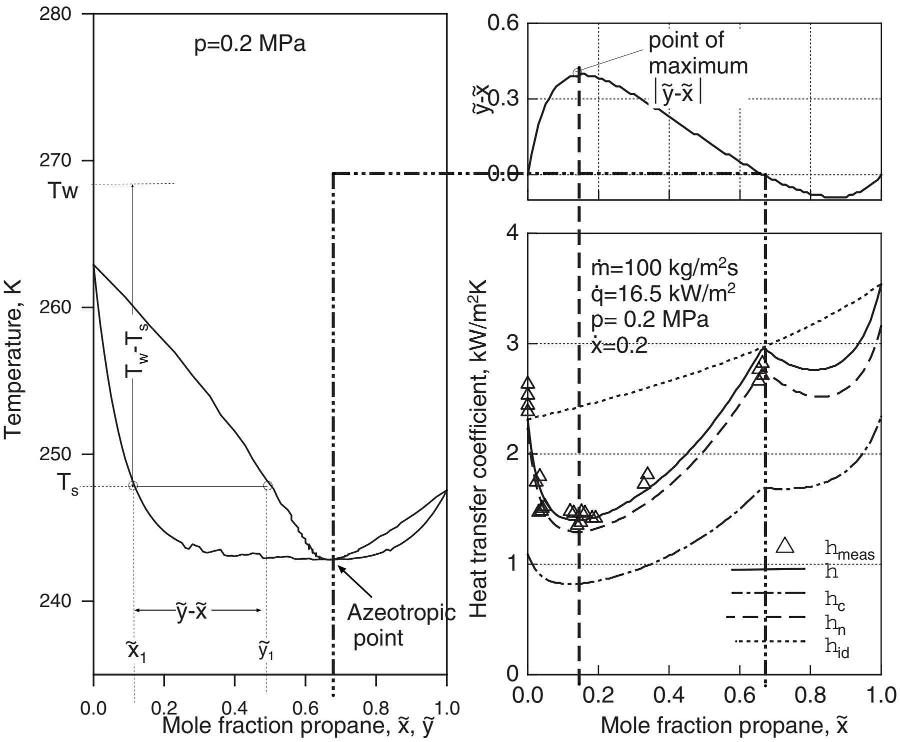

Fig. 7 The influence of the concentration on the local heat transfer coefficient for R134a/R290 mixtures

transfer coefficient relative to that for pure components of the mixture is caused by the additional resistance of mass transfer. The resistance to mass transfer is represented by the concentration difference $|\tilde{y}-\tilde{x}|$. The preferential evaporation of the more volatile component R290 is an additional factor to degrade the mixture heat transfer coefficient.

Besides the strong influence of concentration and concentration difference on the local heat transfer coefficient of R134a/R290, further observations may be drawn from Fig. 7.

1. The mixture local heat transfer coefficient is smaller than the ideal heat transfer coefficient. The ideal heat transfer coefficient is indicated by the dotted line in Fig. 7. In the ideal case, the heat transfers only by two mechanisms (convective and nucleate); however, in reality, there is additional resistance due to mass transfer (diffusion). As the concentration difference increases, the diffusion resistance increases, yielding lower heat transfer coefficient relative to the ideal one.
2. The maximum concentration difference $|\tilde{y}-\tilde{x}|$ occurs at a mole fraction of 12% R290. At this point, the mixture heat transfer coefficient decreases by a factor of 2 relative to that for pure R134a and by a factor of 2.5 relative to the theoretical value of pure R290. This is attributed to the maximum diffusion resistance and preferential evaporation of the more volatile component R290 as explained above.
3. The local heat transfer coefficient increases toward the azeotropic point. At this point, it is enhanced by a factor of 1.2 relative to that for R134a. However, it is degraded by a factor of 1.2 relative to the theoretical value of R290. This may be attributed to the fact that at the azeotropic point, the mass diffusion diminishes $|\tilde{y}-\tilde{x}|\rightarrow 0$ (similar to pure component) and hence the resistance to heat transfer decreases. In addition, there is no preferential evaporation at the azeotropic point.
4. The measured local heat transfer coefficient for R134a/R290 mixture (triangle symbol) matches very well with the locus of the calculated local heat transfer coefficient (solid line). However, it lays slightly away from the locus of the nucleate boiling curve (dashed line) and wide away from the locus of the convective boiling curve (centered line). This suggests that for this particular set of data, the local heat transfer coefficient may not be convective dominated boiling. It may be either for nucleate dominated boiling or a combination (interaction) of both boiling mechanisms. Bearing in mind that this particular set of data was obtained at relatively low mass flux (100 $\text{kg/m}^2\text{ s}$) and quality (0.2), hence low Reynolds number. Additionally, most of the observed flow patterns, at this particular set of data, were identified with stratified to wavy flow patterns. Under these flow boiling conditions, the domination of the nucleate boiling may be justified.

Figure 8 shows the influence of mass flux on the local heat transfer coefficient for R134a/R290 mixtures. The solid line represents the calculated local heat transfer coefficients by Eq. (19). It is clear that there is a significant effect of the mass flux on the local heat transfer coefficient; the local heat transfer coefficient increases with mass flux. Furthermore, the influence of mass flux on the local heat transfer coefficient increases with the mole fraction of more volatile component R290. For example, at a mole fraction of 18% R290, the difference between the local heat transfer coefficients at 200 $\text{kg/m}^2\text{ s}$ and 100 $\text{kg/m}^2\text{ s}$ does not exceed 0.5 $\text{kW/m}^2\text{ K}$ and that at the point of azeotropic is about 1.0 $\text{kW/m}^2\text{ K}$. This is attributed to the dependency of mass transfer coefficient on mass flux, analogous to heat transfer coefficient.

5.2 Comparison With Correlations. As indicated in the literature review, R134a is a widely accepted substitute for R12, and R134a/R290 mixture is a possible substitute for R22. Therefore, the validity of the existing correlations for the prediction of the local flow boiling heat transfer coefficient for pure R134a and R134a/R290 mixture needs to be tested.

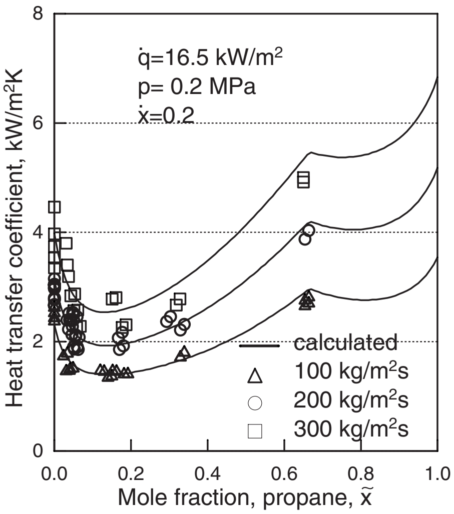

Fig. 8 The influence of mass flux on the local heat transfer coefficient

5.2.1 Pure R134a. In the present work, five correlations were fitted to R134a experimental data. These are Steiner [7], Kattan et al. [11], Kandlikar [10], Gungor and Winterton [9], and Schrock and Grossmann [23] correlations. It should be noted that these correlations are valid only in the region prior to the point of dryout, prior to critical quality $\dot{x}_c$. Thus, all data points at dryout and beyond $(\dot{x} \geq \dot{x}_c)$ are excluded. Table 1 summarizes the mean error and the standard deviation associated with each correlation. Additionally, the number of data points that falls within an error band of $\pm 30\%$ is also indicated. The total number of data points is around 3×330 (i.e., 330 test runs at each of the heat transfer coefficient were measured at three axial positions along the test tube). All correlations predict R134a data with a mean error of less than 30%. However, Gungor and Winterton [9] and Schrock and Grossman [23] predict less number of data points (data points within a band of error of less than 30%) relative to other correlations. This may be attributed to low saturation temperatures [24]. As an illustration, Fig. 9 shows the result of comparison between the calculated and the measured R134a data.

5.2.2 R134a/R290 Mixtures. In the present study, three correlations were fitted to the experimental data. These are Steiner [7], Jung et al. [25], and Kandlikar [26] correlations. Table 2 summarizes the deviation associated with each correlation. The total number of data points is around 3×800.

Figure 10 shows comparison between the measured and the calculated local heat transfer coefficient for R134a/R290 mixtures using Steiner [7] correlation as an illustration. Generally, the correlations give a higher error for mixture relative to pure components, while Steiner [7] correlation gives the best fit to R134a/R290 data. This may be attributed to the fact that the correlations are basically developed for pure components and modified for mixtures. That is to say, the diffusion effect was not taken into account in the original formulation. In addition, some of the correlations do not account for the diffusion effect in the convective part particularly for liquid-liquid immiscible mixture as R134a/R290.

Table 1 Comparison of five different correlations with flow boiling experimental data of pure R134a

Correlation	Mean error (%)	Standard deviation (%)	Data points within an error band of 30%
Steiner [7]	15.48	28.05	89.20
Kattan et al. [11]	21.58	32.56	70.53
Kandlikar [10]	17.99	25.50	80.50
Gungor and Winterton [9]	20.96	28.85	69.71
Schrock and Grossmann [23]	28.54	35.48	50.62

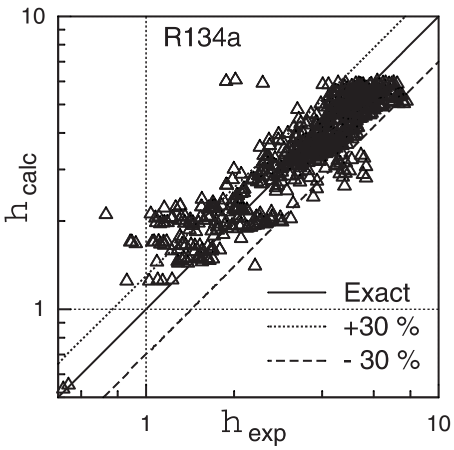

Fig. 9 Comparison of experimental data with Steiner [7] correlation for pure R134a

More detailed comparison is also made by dividing the data into zeotropic region and azeotropic point, as shown in Fig. 11. Clearly, Steiner [7] correlation gives a better accuracy for azeotropic $(\tilde{z}=0.65)$ data than the zeotropic one $(0<\tilde{z}<0.65)$. This may be attributed to the complete suppression of the diffusion effect at the azeotropic point. The relatively high mean error associated with Steiner's correlation in the zeotropic region may be attributed to the high level of uncertainty associated with the prediction of the mixture transport properties.

6 Conclusion

Flow boiling heat transfer coefficients for R134a and R134a/R290 were measured for a wide range of parameters.

- For R134a, the results of the measurements were found to

Table 2 Comparison of three different correlations with experimental data of R134a/R290 mixtures

Correlation	Mean error (%)	Standard deviation (%)	Data points within an error band of 30%
Steiner [7]	24.39	27.61	76.43
Jung et al. [25]	37.63	54.35	55.53
Kandlikar [26]	39.63	30.55	42.62

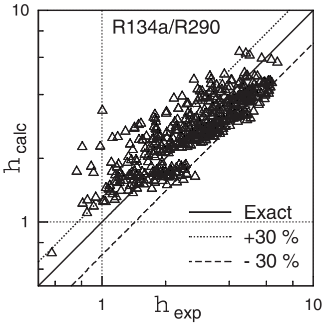

Fig. 10 Comparison of Steiner correlation with the experimental data for R134a/R290 mixtures

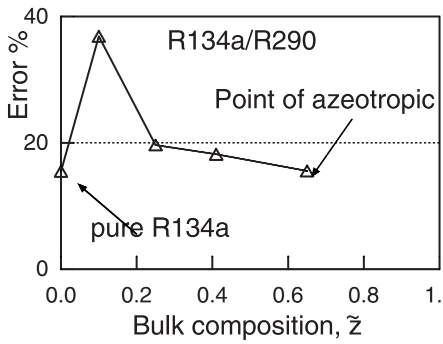

Fig. 11 Variation of the mean error with the bulk composition of R134a/R290 mixtures

confirm the dependency of the local heat transfer coefficient on vapor quality, mass flux, heat flux, saturation temperature, and flow patterns.

- For R134a/R290 mixtures, the results of the measurements revealed a significant effect of concentration, concentration difference, and mass flux on local heat transfer coefficient.
- It was found that the addition of a small amount of propane (12%) to R134a caused the local heat transfer coefficient to decrease by a factor of 2 relative to that for pure R134a (see Fig. 7). The local heat transfer coefficient of azeotropic mixture was found to increase by a factor of 1.2 relative to that for pure R134a. This was attributed to the preferential evaporation of more volatile component R290, hence increasing the bubble point of mixture relative to that for pure R134a.
- Most of the available correlations fitted R134a data with a mean error of less than 30%.
- For R134a/R290 mixtures, the correlations produced a higher mean error relative to pure R134a.

Acknowledgment

The authors acknowledge the grant by the German Academic Exchange Service (DAAD) for Ali Rabah.

Nomenclature

A = area (m^2), constant
c_p = isobar specific heat (J/kg K)
d = diameter (m)
h = enthalpy (J/kg), heat transfer coefficient (W/m^2 K)
k = thermal conductivity (W/m K)
L = length (m)
$\dot{M}$ = mass flow rate (kg/s)
$\dot{m}$ = mass flux (kg/m^2 s)
p = pressure (Pa)
$\dot{Q}$ = heat flow rate (W)
$\dot{q}$ = heat flux (W/m^2)
T_s = saturation temperature (K)
T_w = wall temperature (K)
U = overall heat transfer coefficient (W/m^2 K)
$\dot{x}$ = quality
$\tilde{x}$ = liquid mole fraction
$\tilde{y}$ = vapor mole fraction
z = axial coordinate (m)
$\tilde{z}$ = bulk mole fraction

Greek Symbols

β = mass transfer coefficient (m/s)
λ = latent heat of evaporation (J/kg K)
Φ = scaling parameter
ρ = density (kg/m^3)
σ = standard deviation
ε = void fraction
φ = angle (deg)

Subscripts

c = convective, critical
calc = calculated value
el = electrical
exp = experimental value
f = saturated liquid
g = saturated vapor or gas
h = hydraulic
i = inside
id = ideal
lm = logarithmic mean
n = nucleate
o = outside, reference state
r = reduced
s = saturated
tot = total

Superscript

° = degree

Appendix: Steiner Correlation

Steiner [7] considered the two phase heat transfer coefficient h as a combination of convective and nucleate part using an asymptotic model as

$$h = (h_c^3 + h_n^3)^{1/3} \tag{A1}$$

where h_c and h_n are the convective and nucleate boiling heat transfer coefficients, respectively.

1 Convective Boiling Heat Transfer Coefficient

The convective boiling heat transfer coefficient for a completely wetted tube (i.e., all types of flow patterns except stratified and stratified-wavy flow) is calculated as

$$\frac{h_c}{h_L} = \left\{ \left[(1-\dot{x}) + 1.2\dot{x}^{0.4}(1-\dot{x})^{0.01}\left(\frac{\rho_f}{\rho_g}\right)^{0.37} \right] + \left[\frac{h_G}{h_L}\dot{x}^{0.01}\left(1 + 8(1-\dot{x})^{0.7}\left(\frac{\rho_f}{\rho_g}\right)^{0.67}\right) \right]^{-2} \right\}^{-0.5} \tag{A2}$$

The heat transfer coefficients h_L and h_G are those of single phase flow, assuming that the total mass velocity is pure liquid or pure vapor, respectively. They are calculated in the case of a fully developed turbulent flow using Gnielinski [27] model

$$\text{Nu} = \frac{(f/8)(\text{Re} - 1000)\text{Pr}}{1 + 12.7(f/8)^{0.5}(\text{Pr}^{2/3} - 1)} \tag{A3}$$

where

$$\text{Nu} = \frac{hd}{k} \tag{A4}$$

$$\text{Re} = \frac{\dot{m}d}{\mu} \tag{A5}$$

$$\text{Pr} = \frac{c_p\mu}{k} \tag{A6}$$

$$f = (1.82 \log \text{Re} - 1.62)^{-2} \tag{A7}$$

For partial wetting of the tube (stratified or stratified-wavy flow), the average heat transfer coefficient at the tube circumference under the thermal boundary condition of a constant wall temperature is given as

$$h_c = h_{\mathrm{wet}}(1-\Phi) + h_G\Phi \tag{A8}$$

where Φ is the scaling parameter, h_{wet} is the convective boiling heat transfer coefficient at the wetted part of the tube and it is calculated using Eq. (A2), and h_G is the heat transfer coefficient in the dry part of the tube (nonwetted). It is calculated using Eq. (A3) with Re and Nu defined as

$$\mathrm{Re}_G = \frac{\dot{m}\dot{x}d_h}{\epsilon\mu_g} \tag{A9}$$

and

$$\mathrm{Nu} = \frac{h_G d_h}{k_g} \tag{A10}$$

The void fraction ε is calculated using Rauhani [28] model as

$$\varepsilon = \frac{\dot{x}}{\rho_g}\left\{[1+0.12(1-\dot{x})]\left(\frac{\dot{x}}{\rho_g} + \frac{1-\dot{x}}{\rho_L}\right) + \frac{1.18(1-\dot{x})[g\sigma(\rho_f-\rho_g)]^{1/4}}{\dot{m}\rho_f^{1/2}}\right\}^{-1} \tag{A11}$$

The hydraulic diameter of the vapor-occupied part of the tube cross section is

$$d_h = d\left(\frac{\varphi - \sin\varphi}{d + 2\sin(\varphi/2)}\right) \tag{A12}$$

where φ is the stratified angle calculated iteratively from the following relationship:

$$\varphi = 2\pi\varepsilon + \sin\varphi \tag{A13}$$

With the assumption that no bubbles in the liquid phase and no entrainment (holdup) in the vapor phase, the scaling parameter Φ can be calculated as

$$\Phi = \frac{\varphi}{2\pi} \tag{A14}$$

2 Nucleate Boiling Heat Transfer Coefficient

The nucleate boiling heat transfer coefficient h_n is

$$\frac{h_n}{h_o} = \psi C_f\left(\frac{\dot{q}}{\dot{q}_o}\right)^{n(pr)} F(p_r)F(R_a)F(d)F(\dot{m},\dot{x}) \tag{A15}$$

where

$$F(p_r) = 2.692p_r^{0.43} + \left(\frac{1.6p_r^{6.5}}{1-p_r^{4.4}}\right) \tag{A16}$$

$$F(\dot{m},\dot{x}) = \frac{\dot{m}}{\dot{m}_o}^{0.25}\left[1 - p_r^{0.1}\left(\frac{\dot{q}}{q_{\mathrm{cr},n}}\right)^{0.3}\dot{x}\right] \tag{A17}$$

$$\dot{q}_{\mathrm{cr},n} = 2.79\dot{q}_{\mathrm{cr},0.1}p_r^{0.4}(1-p_r) \tag{A18}$$

$$\dot{q}_{\mathrm{cr},0.1} = 0.13\lambda_o\rho_{g,o}^{0.5}[\sigma_o g(\rho_{f,0}-\rho_{g,o})]^{0.25} \tag{A19}$$

$$F(R_a) = (R_a/R_{ao})^{0.133} \tag{A20}$$

$$F(d) = (d_o/d)^{0.5} \tag{A21}$$

$$n(p_r) = 0.9 - 0.3p_r^{0.3} \tag{A22}$$

$$C_f = 0.789\left(\frac{\widetilde{M}}{\widetilde{M}_{H_2}}\right)^{0.11} \tag{A23}$$

where $\widetilde{M}$ is the molecular weight and $\widetilde{M}_{H_2}$=2.016.

$$\psi = \begin{cases} 0.86 & \text{stratified flow} \\ 1 & \text{all other types of flow pattern} \end{cases}$$

The reference parameters for the nucleate boiling heat transfer coefficient for R134a and R290 are

	h_o (W/m^2 K)	$\dot{q}_o$ (W/m^2)	R_{ao} (m)	d_o (m)
R134a	3500	20,000	10^{-6}	0.01
R290	4000	20,000	10^{-6}	0.01

References

[1] Granryd, E., 2001, "Hydrocarbons as Refrigerant-An Overview," Int. J. Refrig., **24**, pp. 15–24.

[2] Morrison, G., and McLinden, M. O., 1993, "Azeotropy in Refrigerant Mixture," Int. J. Refrig., **16**(2), pp. 129–138.

[3] Didion, D. A., and Bivens, D. B., 1990, "Role of Refrigerant Mixtures as Alternative to CFCs," Int. J. Refrig., **13**, pp. 163–175.

[4] Kattan, N., Thome, J. R., and Favrat, D., 1998, "Flow Boiling in Horizontal Tubes: Part 2-New Heat Transfer Data for Five Refrigerants," ASHRAE Trans., **120**, pp. 148–155.

[5] Wettermann, M., 1999, "Wärmeübergang beim Sieden von Gemischen bei Zwangskonvektion im Horizontalen Verdampferrhor," Fortschritt-Berichte VDI-Reihe 3, No. 625.

[6] Eckels, S. J., Doerr, T. M., and Pate, M. B., 1998, "A Comparison of the Heat Transfer and Pressure Drop for R-134a and Lubricant Mixture in Different Diameter Smooth Tubes and Nicro Fin Tubes," ASHRAE Trans., **104**(A), pp. 376–386.

[7] Steiner, D., 1997, *Strömungssieden Gesättiger Flüssigkeiten*, VDI-Wärmeatlas VDI-Verlag, Berlin, Auflage 8.

[8] Shah, M. M., 1982, "Chart Correlation for Saturated Boiling Heat Transfer: Equation and Further Studies," ASHRAE Trans., **88**(1), pp. 80–89.

[9] Gungor, K. E., and Winterton, R. H. S., 1986, "General Correlation for Flow Boiling in Tubes and Annuli," Int. J. Heat Mass Transfer, **26**, pp. 351–358.

[10] Kandlikar, S. G., 1990, "A General Correlation for Two-Phase Flow Boiling Heat Transfer Inside Horizontal and Vertical Tubes," Int. J. Heat Mass Transfer, **112**, pp. 219–228.

[11] Kattan, N., Thome, J. R., and Favrat, D., 1998, "Flow Boiling in Horizontal Tubes: Part 3-Development of a new Heat Transfer Model Based on Flow Pattern Map," ASHRAE Trans., **120**, pp. 156–165.

[12] Zhang, W., 2005, "Correlation for Boiling Heat Transfer at Low Liquid Reynolds Number in Small Diameter Channels," ASME J. Heat Transfer, **127**(11), pp. 1214–1221.

[13] Collier, J. G., and Thome, J. R., 1994, *Convective Boiling and Condensation*, 3rd ed., Oxford University Press, Oxford, UK.

[14] Der Deutsche Kalibrierdienst (DKD), 1991, *Ermittlung von Meßunsicherheiten (DKD-3)*, Physikalisch-Technische-Bundesanstlt, Braunschweig, Germany.

[15] Adunka, A., 2000, *Meßunsicherheiten: Theorie und Praxis*, Vulkan-Verlag, Essen, Auflage 2.

[16] Kabelac, S., and de Buhr, H. J., 2001, "Flow Boiling of Ammonia in a Plain and Low Finned Horizontal Tube," Int. J. Refrig., **24**, pp. 41–50.

[17] Eckert, E. R. G., and Goldstein, R. J., 1979, *Measurement in Heat Transfer*, 2nd ed., Hemisphere, Washington.

[18] Kedzierski, M. A., 2003, "Improved Thermal Boundary Layer Parameter for Semi-Theoretical Refrigerant/Lubricant Pool Boiling Model," International Congress of Refrigeration, IRC0504, pp. 1–8.

[19] Tillner-Roth, R., and Baehr, H. D., 1994, "An International Standard Formulation of the Thermo-Dynamic Properties of, 1,1,1,2-Tetraflouroethane (HFC-134a) Covering Temperatures From 170 K to 455 K at Pressure up to 70 MPa," J. Phys. Chem. Ref. Data, **23**, p. 657.

[20] Tillner-Roth, R., 1998, *Fundamental Equation of State*, Shaker-Verlag, Aachen.

[21] Kleiber, M., 1994, "Vapor-Liquid Equilibria of Binary Refrigerant Mixtures Containing Propylene or R134a," Fluid Phase Equilib., **92**, pp. 149–194.

[22] Schluender, E. U., 1982, "Über den Wärmeübergang bei der Blasenverdampfung von Gemischen," Verfahrenstechnik, **16**(9), pp. 692–698.

[23] Schrock, V. E., and Grossman, L. M., 1962, "Forced Convection in Tubes," Nucl. Sci. Eng., **12**, pp. 474–481.

[24] Park, C. Y., and Hrnjak, P. S., 2005, "Flow Boiling Heat Transfer of CO_2 at Low Temperatures in a Horizontal Smooth Tube," ASME J. Heat Transfer, **127**(12), pp. 1305–1312.

[25] Jung, D. S., McLinden, M., Radermacher, R., and Didion, D., 1989, "Horizontal Flow Boiling Heat Transfer Experiments With a Mixture of R22/R114," Int. J. Heat Mass Transfer, **32**, pp. 131–145.

[26] Kandlikar, S. G., 1998, "Boiling Heat Transfer With Binary Mixtures: Part II-Flow Boiling in Plain Tubes," Transaction of ASME, **120**, pp. 388–394.

[27] Gnielinski, V., 1976, "New Equation for Heat and Mass Transfer in Turbulent Pipe and Channel Flow," Int. Chem. Eng., **16**, pp. 359–368.

[28] Rauhani, S. Z., 1969, "Subcooled Void Fraction," Technical Report No. AE-RTV 841.

Simultaneous Retrieval of Total Hemispherical Emissivity and Specific Heat From Transient Multimode Heat Transfer Experiments

G. Venugopal
Research Scholar

M. Deiveegan
Research Scholar

C. Balaji
Associate Professor

S. P. Venkateshan[1]
Professor
e-mail: spv@iitm.ac.in

Heat Transfer and Thermal Power Laboratory,
Department of Mechanical Engineering,
Indian Institute of Technology Madras,
Chennai 600 036, India

Transient cooling experiments of a heated vertical aluminum plate with an embedded heater, in quiescent air, were conducted for the simultaneous estimation of total hemispherical emissivity and specific heat of the plate material. During cooling, the heat loss from the hot plate by natural convection and radiation was taken into account. During the experiments, plate temperatures were recorded at several locations using a data acquisition system. A numerically computed transient response of the plate is then compared with the experimentally known transient response to estimate the residual, the minimization of which using Levenberg–Marquardt's iterative procedure retrieves the parameters pertinent to the problem. The experiments were conducted for three different surface emissivities of the plate obtained by using suitable surface treatment. A consistency test for the present approach was also done by conducting transient heating experiments using the retrieved values of parameters and a comparison of simulated and calculated natural convection heat transfer coefficients as a function of temperature. The experiments have been performed over a temperature range of 320–430 K and a Rayleigh number range of 2×10^6–2×10^7. The emissivity values are in good agreement with previous reported results. [DOI: 10.1115/1.2891221]

Keywords: emissivity, specific heat, simultaneous estimation, Levenberg–Marquardt's iterative procedure, multimode heat transfer

Introduction

The thermophysical properties, specific heat, and emissivity have significant roles in determining the thermal response in numerous important engineering applications. Both these properties, though dependent on temperature, have been assumed to be constants in the modeling of many applications because information concerning the variation of these properties with temperature is not always available.

Many different techniques are available for the measurement of specific heat of solids; among these, calorimetry based methods are widely employed, because such methods are simple and inexpensive. An accurate knowledge of total hemispherical emissivity (hereafter referred to as emissivity) is a prerequisite for estimating radiative heat transfer in applications such as solar energy utilization, aerospace systems, and so on. The emissivity is dependent on the wavelength, the temperature, and also on the chemical and physical state of the surface. The emissivity of surfaces can be measured either directly or indirectly. The direct measurement method requires measurement of the radiation emitted from a sample at known temperatures. The indirect method, however, employs a measurement of the surface reflectivity that uses an external source of radiation, and the emissivity is deduced by the use of Kirchhoff's law [1]. Numerous articles are available on emissivity measurement by conventional techniques. These are expensive and also require sophisticated instruments. Moreover, a major requirement of many of these techniques is the maintenance of vacuum to eliminate other modes of heat transfer. However, recently, Krishnan et al. [2] proposed a novel method for estimation of emissivity by conducting experiments on a system cooling in quiescent air, subjected to multimode heat transfer.

A few studies have been reported [3–5] on simultaneous measurement of specific heat and emissivity, and these studies were based on the transient calorimetric method, which inherently demands large investment in terms of money and infrastructure. A method based on pulse self-resistive heating was reported by Cezairliyan [3] for the multiple measurements of thermophysical properties of electrically conducting solid metallic substances in the range from 1500 K to the melting point of the sample. Masuda and Higano [4] described a transient radiation calorimetric technique for the measurement of total hemispherical emissivity. Sasaki et al. [5] extended the same technique for the simultaneous estimation of specific heat and total hemispherical emissivity, deduced from the temperature time curve of two specimens, one of which is a standard metallic material whose specific heat and emissivity have been measured accurately and the other one is the metallic material whose property values are to be estimated. More recently, Tanda and Misale [6] used the principle of transient calorimetry to estimate emissivity from energy balance at steady state and the specific heat from the transient response of the sample while cooling. From the viewpoint of the physics of the problem, transient radiation calorimetric technique is simple to handle due to the presence of only one mode of heat transfer but requires heavy expenditure in view of the requirement of a vacuum. However, in a transient cooling method involving more than one mode of heat transfer, the simultaneous estimation of specific heat and emissivity is much more difficult to resolve, unless the variation of problem specific parameters, other than specific heat and emis-

---

[1] Corresponding author.

Contributed by the Heat Transfer Division of ASME for publication in the JOURNAL OF HEAT TRANSFER. Manuscript received January 12, 2007; final manuscript received June 10, 2007; published online April 23, 2008. Review conducted by A. Haji-Sheikh.

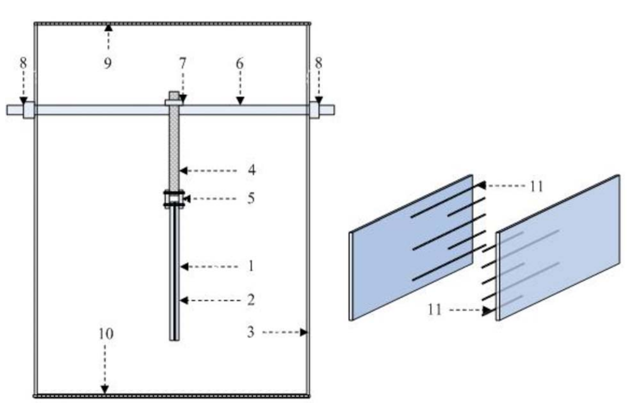

Fig. 1 Schematic of the experimental setup for the transient multimode heat transfer experiments. 1-heated vertical plate; 2-electric heater; 3-side wall of test section (wood); 4-Teflon rod; 5-Steel strip; 6-stainless steel rod; 7-adjusting nut; 8-adjusting nut; 9-perforated wooden panel; 10-wire mesh; 11-stainless steel sheathed thermocouples.

sivity, with temperature is carefully taken into account. This paper presents a simple and efficient method for the simultaneous retrieval of emissivity and specific heat of metallic substances from multimode transient heat transfer experiments by an effective and judicious combination of experimental and numerical techniques.

Experimental setup

The experimental setup essentially consists of a heated vertical plate (hereafter called test plate) freely suspended from two parallel stainless steel rods (6 mmϕ), arranged across the test section, using two Teflon® rods (3 mmϕ) attached to both ends of the top edge of the test plate. The use of Teflon® rods minimizes the conduction losses from the test plate. With a nut and screw arrangement made on both ends of each stainless steel rod, the test plate can be positioned exactly along the longitudinal midplane of the test section. The upper end of each Teflon® rod carries a similar arrangement by which perpendicularity of the test plate with respect to the horizontal plane can be achieved. The test plate is attached to the lower end of the Teflon® rods through small 1 mm thickness steel strips. The test plate is made of an assembly of two aluminum plates of dimensions 150 × 250 × 3 mm with a flat heater sandwiched between them. The flat heater is formed by winding a Nichrome wire over a mica sheet and the same is electrically insulated from the unexposed side of the aluminum plates by using mica sheets. The two halves of the test plate are joined together by means of fastening screws and nuts. Proper seating of fastening screws and nuts is ensured by countersinking the holes, and thus any possibility of occurrence of local turbulence due to protrusions is eliminated. The chamfering operation done on the bottom edge of the test plate ensures smooth and free gliding of freestream air over the test plate. The volume ratio of the test plate to the test section is 9×10^{-5}, and therefore the test plate is treated as a small object placed in a large enclosure. With a view to ensure a disturbance free environment inside the test section, the test section is provided with a wire mesh and perforated wooden panel, respectively, at the inlet and exit of the test section. The wire mesh and the perforated wooden panel are arranged at distances of 30 cm and 45 cm, respectively, from the bottom and top edge of the test plate.

The temperatures at different locations of the test plate (Fig. 1) are recorded by using ten "K-type" (36 AWG) stainless steel sheathed thermocouples, five on each aluminum plate, fixed to the plates, using highly conducting copper cement. The ambient temperature is measured by a separate K-type thermocouple kept inside the test section. All thermocouples are calibrated before fixing them into the grooves machined in the plates and they are connected to a personal computer (PC) based data acquisition system (Model No. 34970A, Agilent Technologies Ltd.) through compensating wires. The power input to the heater is supplied from a regulated dc power source (Aplab Systems Ltd., India, Model No. H0615), which has a range of 30–600 V and 0–1.5 A. The test plate can be heated to different temperature levels by controlling the input to the heater. The power input to the heater is calculated by measuring the voltage and current using a digital multimeter. The details of the experimental setup are depicted in Fig. 1.

Experimental Procedure

The test plate is given a definite amount of electrical power, and the electrical power is switched off after the steady state is reached. Steady state is assumed to be reached when the temperature of the test plate is observed to vary within $\pm 0.1^\circ\mathrm{C}$ in 10 min. The transient response of the system while cooling the plate is recorded using the data acquisition system and this is done at regular intervals of 30 s for a period of half an hour. The experiments are repeated for several power inputs to the heater, simulating natural convection environment inside the test section, subject to an ambient temperature variation of $\pm 0.4^\circ\mathrm{C}$ during an experiment. The experiments are done for three types of surfaces, viz, polished aluminum, aluminum paint coated polished aluminum, and blackboard paint (Manufacturer: Asian Paints Ltd., India) coated polished aluminum. The polished surface was obtained by a buffing operation. The surface roughness of the buffed plate is measured using a surface texture measuring instrument (Make: Perthometer S2-Mahr GMBH, Germany), and the surface roughness (R_a) is estimated as 0.083 μm.

Mathematical Modeling and Data Analysis

The governing equation for the transient cooling of the isothermal plate is

$$-mc_p\frac{dT_h}{dt} = \varepsilon\sigma A_s(T_h^4 - T_\infty^4) + hA_s(T_h - T_\infty) + Q_L \qquad (1)$$

The left-hand side of Eq. (1) represents the rate of depletion of energy stored in the plate at time t. The first and second terms on the right-hand side of Eq. (1) represent, respectively, the radiative and convective heat transfer rates. The third term on the right-hand side of Eq. (1) stands for small correction term for the heat loss by conduction through the thermocouple wires attached to the test plate. Since the fractional heat loss Q_L will be a small quantity, in the present study, this quantity is neglected. The convective heat transfer coefficient can be replaced in terms of the convective Nusselt number. For laminar natural convection from an isothermal vertical plate, the Churchill correlation for an average value of Nusselt number [7] is used and this is given by

$$\overline{\mathrm{Nu}}_L = 0.68 + \frac{0.670\mathrm{Ra}_L^{1/4}}{[1+(0.492/\mathrm{Pr})^{9/16}]^{4/9}}, \quad \mathrm{Ra}_L \leqslant 10^9 \qquad (2)$$

With this, Eq. (1) takes the form

$$-mc_p\frac{dT_h}{dt} = \varepsilon\sigma A_s(T_h^4 - T_\infty^4) + \left(0.68 + \frac{0.670\mathrm{Ra}_L^{1/4}}{[1+(0.492/\mathrm{Pr})^{9/16}]^{4/9}}\right) \times \frac{k_f}{L}A_s(T_h - T_\infty) \qquad (3)$$

Equation (3) is the mathematical representation of the problem under consideration. The important point of this experiment is that the thermal equilibration of the plate as it loses heat must be almost instantaneous, and such an assumption is truly valid for materials with high thermal conductivity. Experience tells us that the value of average heat transfer coefficient for this class of problems is approximately 6 $\mathrm{W/m^2\,K}$ and if an equal contribution is expected in respect to radiation heat transfer, the overall heat

Table 1 Retrieved values of emissivity and specific heat for a polished surface for various initial temperatures (for $\phi=0$)

	Emissivity			Specific heat (J/kg K)		
T_i (K)	a	b	$\varepsilon(T)$	c	d	$c_p(T)$
327.85	0.04817	$4.75E-06$	0.05	740.159	0.4696	894.12
335.75	0.04783	$1.47E-05$	0.053	741.338	0.4736	900.35
346.81	0.04286	$2.1E-06$	0.044	745.675	0.4875	914.75
354.86	0.04232	$1.1E-05$	0.043	743.644	0.4845	915.57
358.79	0.03979	$3.12E-06$	0.041	740.084	0.4759	910.83
370.34	0.04294	$2.66E-06$	0.044	744.671	0.4861	924.70
383.96	0.04083	$4.5E-06$	0.043	743.815	0.4867	930.69
400.96	0.04432	$7.55E-06$	0.047	741.072	0.4801	933.57
407.15	0.04206	$7.14E-06$	0.045	743.974	0.4853	941.56
428.54	0.04176	$2.97E-06$	0.043	741.072	0.4955	953.41

transfer coefficient is estimated to be 12 $\mathrm{W/m^2\,K}$. The characteristic length based on the volume to surface area ratio is calculated as 2.82 mm, and the thermal conductivity of aluminum is taken as 240 W/m K. The Biot number calculated for the present transient problem turns out to be 1.41×10^{-4}, and hence the lumped capacity formulation is justified. The mass of the test plate assembly, inclusive of the mass of the heater, was measured using an electronic mass balance machine having a resolution of 0.001 kg and the value was determined to be 0.698 kg. The mass of the heater was separately weighed and recorded as 0.057 kg. This shows that the percentage ratio of the mass of the heater to the mass of the test plate is 8%, and hence the error in the estimation of specific heat due to inclusion of the mass of the heater is not negligible. In the present study, the test plate is modeled as an isotropic composite medium. In principle, two transient experiments may be made with different plate thickness using the same heater. From these, it is possible to estimate the specific heat of the plate material alone.

The computation of the transient response of the system by solving Eq. (3) for a given initial condition, known ambient temperature, and known values of system parameters is the conventional direct heat transfer problem. Traditionally, this is known as the forward model in the parlance of parameter estimation using the inverse method. The present study aims at the estimation of the parameters, emissivity, and specific heat, from a knowledge of measured transient response of the system using a parameter estimation algorithm. Basically, parameter estimation from the experimentally known transient response of the system is an inverse problem, and, in the present study, parameter estimation is done by treating the problem as an optimization problem, requiring the minimization of the square of the residuals between the experimental and simulated temperatures. Though the problem as such is a two parameter one, in the present case, this is considered as four parameter model by expressing emissivity and specific heat as linear functions of temperature. Parameter estimation in heat conduction by solving inverse problems is well established (see, for example, Ref. [8]). As regards an inverse problem with the simultaneous estimation of more than one parameter, estimation of thermal conductivity and specific heat in a two dimensional orthotropic solid medium is reported by Sawaf et al. [9] using Levenberg–Marquardt's iterative procedure. However, the present study is concerned with the estimation of a radiative (surface) property along with a thermophysical property. The experimentally known transient response of the system is compared with the numerically computed transient response, by solving the forward problem with initial guess values for all the parameters, to compute the residual. Minimization of this residual using Levenberg–Marquardt's iterative procedure retrieves the optimum values of parameters.

Solution Procedure

Let Eq. (3) be represented as

$$\frac{dT_h^{\mathrm{num}}}{dt}=f(\varepsilon,A_s,t,m,c_p,T_h,T_\infty,\mathrm{Ra}_L,k_f,L) \qquad (4)$$

The solution of the above initial-value problem, subject to the initial condition $T_h=T_i$ at $t=0$, provides the temperature time history. Equation (4) represents the forward problem in the solution procedure and to solve this initial-value problem for ordinary differential equation, a sixth-order Runge–Kutta method is used.

Inverse Problem

The inverse problem considered here is concerned with the simultaneous estimation of the surface emissivities and specific heat of solid metallic substance from measured temperatures. The emissivity and specific heat are assumed as linear functions of temperature such as $\varepsilon(T)=a+bT$ and $c_p(T)=c+dT$. The constants a, b, c, and d are to be retrieved. In the present work, the Levenberg–Marquardt method [10,11] is used to minimize the difference between the simulated and measured temperatures.

The formulation of the inverse problem considered here is similar to that of the direct problem except that the surface emissivities and specific heat are unknown. Instead, the measured temperature of the plate ($T_h^{\exp}$) is available. The inverse problem consists then of utilizing the measured data ($T_h^{\exp}$) to determine the four elements of the unknown vector $\mathbf{X}$ defined as

$$R=\sum_{i=1}^{N_{\mathrm{data}}}[T_h^{\exp}-T_h^{\mathrm{num}}(\mathbf{X})]^2 \qquad (5)$$

where T_h^{num} is the simulated data. All of the arguments of $\mathbf{X}$ will be referred to as parameters. The Levenberg–Marquardt algorithm is used to minimize the norm R, with respect to each of the unknown parameters $\mathbf{X}=\{a,b,c,d\}$. In Levenberg–Marquardt algorithm, the steepest descent method is initially followed. Thereafter, Newton's method is adopted. The Levenberg–Marquardt algorithm, like other numeric minimization algorithms, is an iterative procedure that starts with an initial guess for the vector of unknowns, $\mathbf{X}^0$. In each iteration step, the parameter vector $\mathbf{X}^k$ is replaced with $\mathbf{X}^{k+1}$, defined as $\mathbf{X}^{k+1}=\mathbf{X}^k+\Delta\mathbf{X}^k$. For a fuller discussion on the algorithm, see Ref. [12].

Results and Discussion

The results obtained from the present study are summarized in the tables presented below. The results presented here are for a commercial aluminum, the metallurgical compositions of which observed using scanning electron microscope (Make: FEI-Czech

Table 2 Retrieved values of emissivity and specific heat for aluminum paint for various initial temperatures (for $\phi=0$)

	Emissivity			Specific heat (J/kg K)		
T_i (K)	a	b	$\varepsilon(T)$	c	d	$c_p(T)$
321.18	0.2090	$3.56E-05$	0.22	741.529	0.4731	893.48
326.15	0.2102	$2.25E-05$	0.218	740.512	0.4703	893.90
335.42	0.2094	$2.41E-05$	0.217	740.700	0.4717	898.92
345.14	0.2079	$1.96E-05$	0.215	742.892	0.4786	908.07
350.46	0.2062	$4.30E-06$	0.208	744.894	0.4850	914.87
361.57	0.2069	$8.14E-06$	0.210	740.195	0.4730	911.22
373.14	0.2078	$2.37E-05$	0.217	740.682	0.4743	917.66
385.58	0.2060	$1.05E-05$	0.210	741.417	0.4785	925.92
396.52	0.2060	$7.06E-06$	0.209	741.846	0.4806	932.41

Republic, Model: QUANTA 200) are Al K (95.4 wt %) and O K (4.6 wt %). Both emissivity and specific heat are obtained as linear functions of temperature such that $\varepsilon(T)=a+bT$ and $c_p(T)=c+dT$. The values of the constants obtained for each case are listed in Tables 1–3.

Estimation of Emissivity. Table 1 indicates the results of emissivity measurements done for a polished surface prepared by the polishing process mentioned earlier. The mean value of the constants and standard deviation of the retrieved values are shown in Table 4. A look at the order of constant b implies that the temperature dependency of emissivity is not significant in the range of temperatures encountered in the present study. The present study establishes the observation made by Zhang et al. [13] that emissivity is a weak function of temperature. A comparison of the present results with the results reported by Tanda and Misale, [6], Masuda and Higano [14], Rammohan Rao and Venkateshan [15], and Krishnan et al. [2] shows good agreement. Tables 2 and 3 show the values of emissivity for two more cases, i.e., test plate with aluminum paint and blackboard paint coating, respectively, and the results are also compared with the results available in Refs. [2,15]. The value of emissivity of blackboard paint coating in Ref. [15] was reported as 0.85 ± 0.01 and that of aluminum paint coating in Ref. [2] was reported as 0.31 ± 0.01. The comparison shows that there are small differences between the results of the present study and those reported in Refs. [2,15]. This is due to the difference in surface conditions of the test plate, paints, and the thickness of paint coating that were used in the respective studies. Furthermore, in the problem of simultaneous estimation of thermophysical properties, the effect of the variation of specific heat with temperature can be a reason for a small change in the estimated values of emissivity from those reported in references that assumed values reported in literature for the specific heat.

Estimation of Specific Heat. The specific heat of the test plate material, modeled as a composite medium inclusive of the heater and the fastening screws, is simultaneously estimated from the three test cases, and the predicted values of constants c and d are shown in Tables 1–3. It is important to note that constant d indicates the temperature dependency of specific heat in the range of temperature of experiments. The result negates the assumption of a constant value of specific heat that has been used widely in many of the previously reported studies on emissivity measurement. In the present study, the specific heat variation with temperature was expected to follow a linear relation, in the temperature range of experiments, and similar trends have been reported for materials chromel and alumel by Sasaki et al. [5] and aluminum alloy (anticoradal 6063) by Tanda [6]. Also, the retrieved value of specific heat of the test plate material is very close to those reported in Ref. [16] for a wide variety of aluminum based alloys.

In general, it is observed that the spread of retrieved values of emissivity and specific heat around the linear fit (based on the mean values of constants in respective cases) in the low emissivity case is larger when compared with intermediate and high emissivity case. The discrepancy observed is attributed to the uncertainty induced by different levels of cooling rates experienced by the test plate for different surface emissivities. For instance, slow cooling rate at low surface emissivity leads to larger errors in the measurement of temperature and heat loss estimation, which in turn obviously causes wide scatter of data around the best fit. On the other hand, for the case of high emissivity, the rapid cooling rate

Table 3 Retrieved values of emissivity and specific heat for blackboard paint for various initial temperatures (for $\phi=0$)

	Emissivity			Specific heat (J/kg K)		
T_i (K)	a	b	$\varepsilon(T)$	c	d	$c_p(T)$
327.75	0.8164	$3.18E-05$	0.826	740.172	0.4693	893.99
333.36	0.8148	$1.52E-05$	0.819	741.422	0.4734	899.24
340.35	0.8148	$2.44E-06$	0.816	741.196	0.4735	902.35
348.97	0.8149	$7.36E-06$	0.817	740.668	0.4729	905.70
355.62	0.8168	$3.75E-06$	0.818	739.780	0.4705	907.10
369.54	0.8121	$7.84E-06$	0.815	741.180	0.4765	917.27
378.37	0.8059	$4.36E-06$	0.806	746.409	0.490	931.81
386.15	0.8156	$7.76E-06$	0.819	738.795	0.4711	920.71
387.84	0.8146	$1.9E-05$	0.822	739.675	0.4735	923.32
396.15	0.8122	$1.36E-05$	0.818	740.751	0.4769	929.68
405.75	0.8149	$6.12E-06$	0.817	738.146	0.4713	929.38
418.40	0.8055	$6.13E-06$	0.808	742.408	0.4852	945.42

Table 4 Estimated mean and uncertainty associated with the retrieved parameters (for $\phi=0$)

	c	d
Specific heat $c_p(T)=c+dT$	741.59 ± 2.036	0.478 ± 0.007
Emissivity $\varepsilon(T)=a+bT$	a	b
Polished surface	0.043 ± 0.003	$6.05\times10^{-6} \pm 4.11\times10^{-6}$
Aluminum paint	0.208 ± 0.002	$2.34\times10^{-5} \pm 2.23\times10^{-5}$
Blackboard paint	0.813 ± 0.004	$1.04\times10^{-5} \pm 8.36\times10^{-6}$

induces a larger uncertainty in heat loss estimation. It is observed from the tabulated results that consistent values have been obtained for the test plate coated with aluminum paint. Figures 2 and 3 show, respectively, the variation of emissivity and specific heat with temperature. For the specific heat, a least squares fit for data that consider specific heat estimates from experiments with all the three surfaces considered in this study is also included in Fig. 3 to compare with the linear fit, based on the mean values, used to represent the variation of specific heat with temperature. It is obvious from the comparison that the difference in the calculated values of specific heat between the two fits is marginal. Figure 4 shows a comparison of the measured and simulated temperature versus time curve for the test plate coated with aluminum paint. As stated earlier, the emissivity and specific heat were estimated using the temperature history of the test plate during cooling. However, as a test of consistency of the present approach, an inverse estimation was also carried out for retrieving the convective heat transfer coefficient for the transient heating of the test plate using the retrieved values of emissivity and specific heat obtained from transient cooling experiments. The modeling of the transient heating experiment is similar to the transient cooling problem except that the heat generation term, which appears in the energy balance equation, is incorporated in the form of power input to the heater. The inverse estimation was done for heating of the test plate of polished surface and aluminum paint coated surface. A comparison of the numerically computed heat transfer coefficient with heat transfer coefficient calculated directly using Churchill correlation was made, and the result is represented in the form of parity plot shown in Fig. 5. It is evident from the parity plot that the Churchill correlation slightly overpredicts the heat transfer coefficient. This bias is expected to occur due to the following reasons. The heat transfer coefficient calculated using Churchill correlation is expected to represent the total heat transfer coefficient taking into account for radiation heat transfer also, as no details about the heat loss from the part of radiation mode are mentioned in Ref. [7]. This reasoning is arrived at from the observation that for low emissivity case, the maximum error between the heat transfer coefficient obtained by employing the Churchill correlation and the retrieved heat transfer coefficient is about 1% only, whereas for the higher emissivity case, the error goes up to 4%. The convective heat transfer, calculated after deducting the radiation heat loss from the total heat input, that has

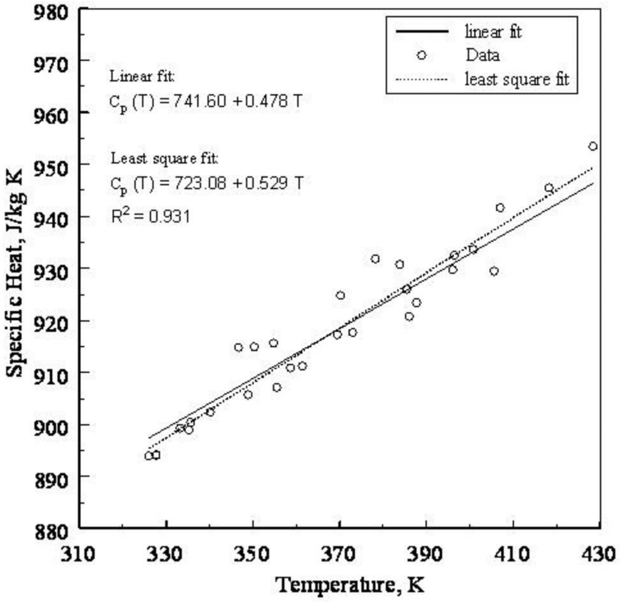

Fig. 3 Retrieved value of specific heat as a function of temperature

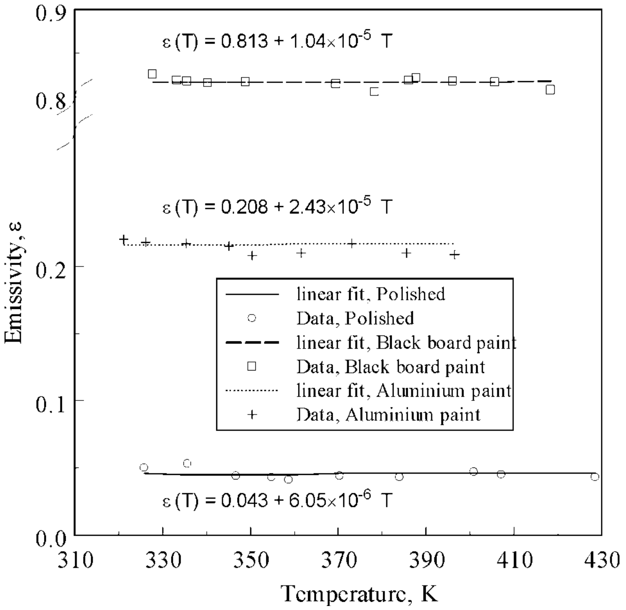

Fig. 2 Retrieved values of emissivity as a function of temperature for three samples

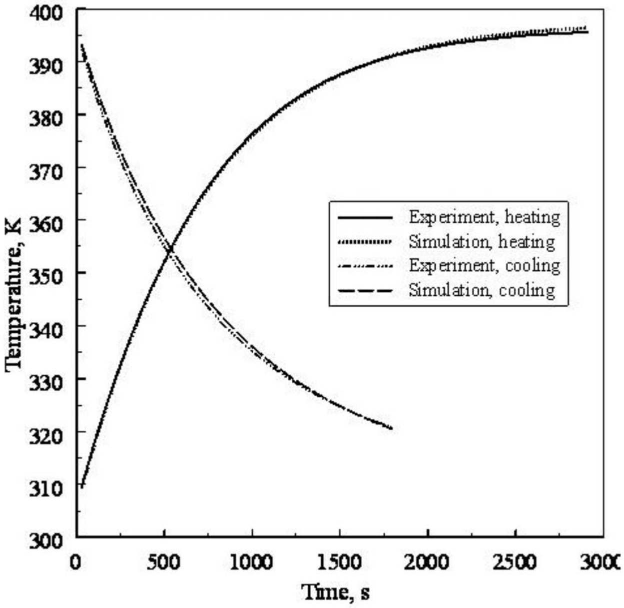

Fig. 4 Comparisons of experimental and simulated temperature time curves for aluminum paint coated surface

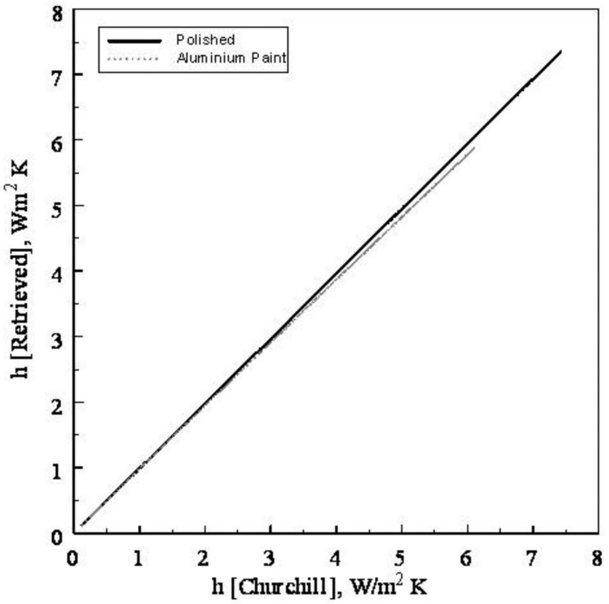

Fig. 5 Comparison of retrieved and calculated heat transfer coefficients using the Churchill correlation

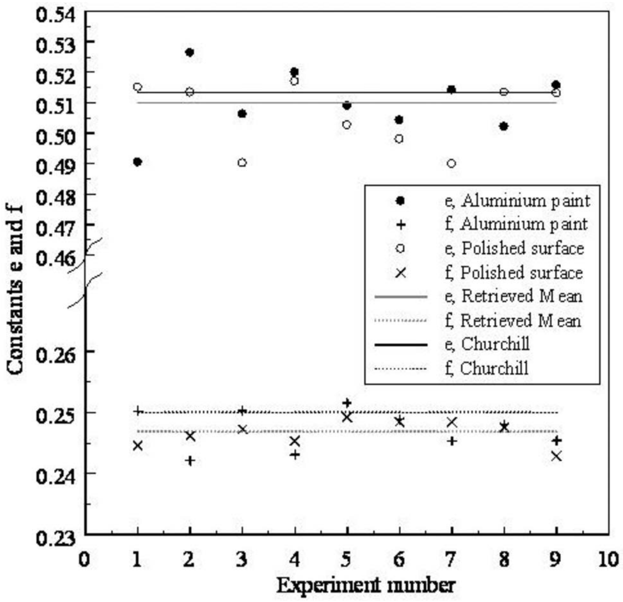

Fig. 6 Comparison between constants retrieved and constants specified in the Churchill correlation

taken care of the unaccountable heat losses can also be another reason for the slightly higher value of the convective heat transfer coefficient calculated using the Churchill correlation, as compared to the retrieved value of the heat transfer coefficient. The retrieved values of the heat transfer coefficient indicate that the concept of instantaneous Rayleigh number works well for transient heating or cooling of lumped systems, and therefore the transient heating experiments are equally good for the retrieval of emissivity and specific heat, provided accurate measurement of power input is possible. Additionally, the present study once again establishes the strength of Churchill correlation in calculating the heat transfer coefficient for a heat transfer problem involving natural convection. As a final validation exercise, the values of the coefficient and power of Rayleigh number term encountered in the Churchill correlation were also retrieved by Levenberg–Marquardt's method, and the retrieved values match well with the respective values reported in the said correlation. In the case of natural convection in air, Prandtl number varies very little with temperature and so the coefficient of Rayleigh number divided by the denominator term in the Churchill correlation can be represented as an another constant and the Churchill correlation takes the simple form $\overline{\mathrm{Nu}}_L = 0.68 + e\mathrm{Ra}_L^f$. The mean and standard deviation of the retrieved parameters e and f, respectively, are obtained as 0.508 ± 0.01 and 0.247 ± 0.003. For the retrieval of parameters e and f from the transient heating experiments, the retrieved values of emissivity and specific heat from transient cooling experiments have been used. A representative comparison of the retrieved values and the values reported in the correlation is shown in Fig. 6.

Experimental Uncertainty

The physical quantities measured during the experiments are power input to the heater, linear dimensions of the test plate, mass of the test plate, and temperature of the test plate, and the corresponding uncertainties are ±0.014 W, ±0.02 mm, ±0.001 kg, and ±0.3°C, respectively. For the case of retrieved parameters, the mean value, has been taken as the best value and standard deviation among the values was taken to be error in the estimation. The uncertainty in the estimation of emissivity and specific heat was determined according to the method described in Ref. [17] and estimated as ±0.003 and ±3.708 J/kg K, respectively. The uncertainties reported here are for experiments without measurement errors ($\phi=0$). The uncertainties encountered in the retrieved parameters are shown in Table 4.

Finally, to estimate the error propagation due to expected random errors in the temperature measurement, the parameters are reestimated after perturbing the measured temperatures with Gaussian noise. The effect of noise is taken into account artificially by the following relation:

$$T_i^{\mathrm{correct}} = T_i^{meas} + \phi\omega \qquad (6)$$

where T_i^{correct} is the corrected temperature, T_i^{meas} is the measured temperature, ϕ is the standard deviation of measurement errors, and ω is a random number. Two cases with random noise level $\phi=0.1$ and 0.3 were considered. The value of ω is randomly generated and chosen over the range $-2.576 < \omega < 2.576$, which represents the 99% confidence bound for the temperature measurement. The error analysis is carried out for the polished aluminum surface, and the estimated values of emissivity and specific heat for the cases considered are, respectively, shown in Figs. 7 and 8. For each experimental trial, the measured temperatures are perturbed with the random errors assigning different standard deviation values mentioned earlier. The results show that, among all the experimental trials, even for the worst case, the maximum deviations are observed as 22% and 1.21%, respectively, for the emissivity and specific heat with respect to the respective values predicted by the linear fit. As another validation test, a single experiment is chosen (corresponding to the tenth row of Table 1) and 15 test cases were run for $\phi=0.3$. The mean value of the specific heat is estimated as 948.402 J/kg K with a standard deviation of ±2 J/kg K. The corresponding values predicted by linear fit are 946.43 J/kg K and ±3.708 J/kg K, respectively. Also, to compute the deviation of the estimated results from the zero error measurement result, the average relative errors for the retrieved parameters are expressed as follows:

$$\frac{1}{N}\sum_{i=1}^{N}\left|\frac{\varepsilon(T_i)-\bar{\varepsilon}(T_i)}{\bar{\varepsilon}(T_i)}\right| \times 100 \qquad (7)$$

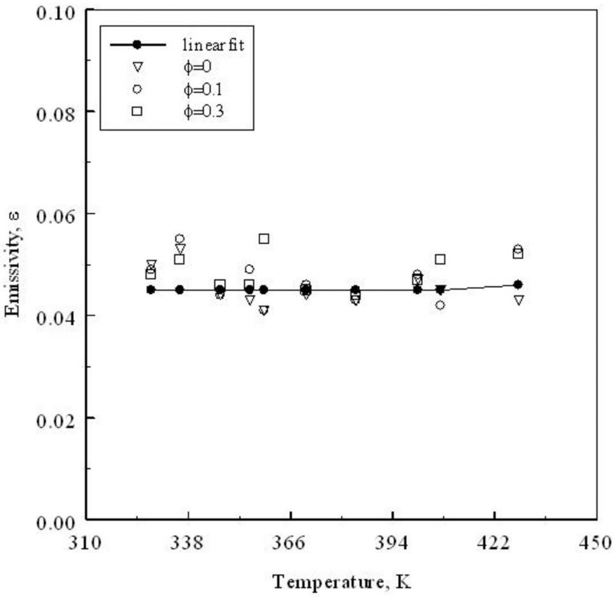

Fig. 7 The estimated emissivity for polished aluminum surface $\varepsilon(T)$ when ϕ=0.0, 0.1, and 0.3

$$\frac{1}{N}\sum_{i=1}^{N}\left|\frac{C_p(T_i)-\overline{C_p}(T_i)}{\overline{C_p}(T_i)}\right|\times 100 \tag{8}$$

where $\varepsilon(T)$ and $\overline{\varepsilon}(T)$ stand for the estimated values of emissivity with and without measurement error (i.e., $\phi=0$). A similar definition is also applicable for the specific heat. The average relative errors of emissivity and specific heat computed with standard deviation of measurement error $\phi=0.1$ are obtained as 4% and 0.12%, respectively, whereas with $\phi=0.3$, the average relative errors of emissivity and specific heat are 7.67% and 0.31%, respectively. The error analysis shows that the estimated errors associated with the retrieved parameters are within the accepted range, which also indicates the robustness of the temperature measurement in the present experimental study.

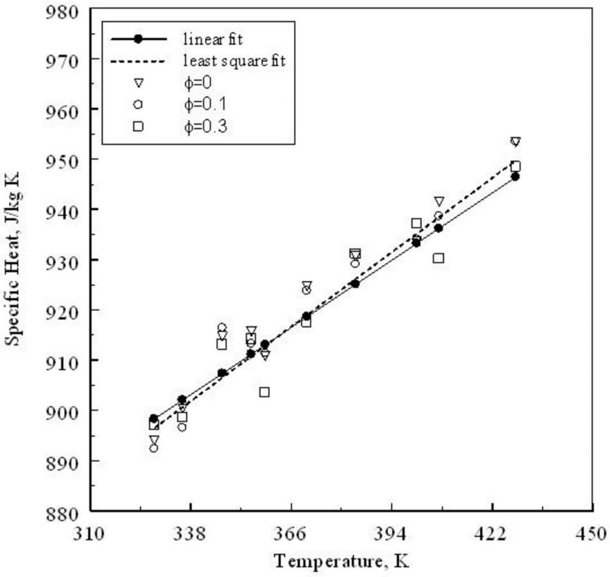

Fig. 8 The estimated specific heat $c_p(T)$ when ϕ=0.0, 0.1, and 0.3

Conclusions

A new approach for the simultaneous estimation of emissivity and specific heat of metallic substances by a judicious combination of experimental and numerical techniques has been discussed. The applicability of the present approach has been established for the simultaneous determination of thermophysical properties from the transient cooling of a lumped system in still air by laminar natural convection and surface radiation. The present method is simple, less expensive, and has the advantage of greater rapidity in obtaining results. The temperature dependency of emissivity is not significant in the temperature range of 325–425 K for the three surface conditions studied. On the other hand, specific heat increases significantly with temperature, and therefore the variation of specific heat with temperature should be accounted for, particularly in transient experiments, even over a narrow temperature range. The results of transient heating experiments provide additional information about the efficacy of the present approach.

Nomenclature

A_s = surface area of the test plate, m^2
c_p = specific heat capacity of the test plate assembly, J/kg K
h = average heat transfer coefficient, $\mathrm{W/m^2\,K}$
k_f = thermal conductivity of fluid (air), W/m K
L = length of the test plate, m
N = total number of experiments
m = mass of the test plate assembly, kg
Nu_L = average convective Nusselt number, hL/k_f
Pr = Prandtl number
R = residual
R_a = surface roughness parameter
Ra_L = Rayleigh number based on the length of the test plate, $g\beta(\Delta T)L^3/(\nu\alpha)$
T = temperature, K
t = time, s

Greek Symbols

ε = total hemispherical emissivity
σ = Stefan–Boltzmann constant, $5.67\times10^{-8}\ \mathrm{W/m^2K^4}$
ϕ = standard deviation of measurement errors
ω = random number

Subscripts

i = initial
h = hot test plate
∞ = ambient

Superscripts

exp = experimental
num = numerical
correct = corrected
meas = measured

References

[1] Kribus, A., Vishnevetsky, I., Rotenberg, E., and Yakir, D., 2003, "Systematic Errors in the Measurement of Emissivity Caused by Directional Effects," Appl. Opt., **42**, pp. 1839–1846.
[2] Krishnan, A. S., Balaji, C., and Venkateshan, S. P., 2003, "A Synergistic Approach to Parameter Estimation in Multimode Heat Transfer," Int. Commun. Heat Mass Transfer, **40**, pp. 515–524.
[3] Cezairliyan, A., 1984, "A Dynamic Technique for Measurements of Thermo Physical Properties at High Temperatures," Int. J. Thermophys., **5**, pp. 177–193.
[4] Masuda, H., and Higano, M., 1988, "Measurement of Total Hemispherical Emissivities of Metal Wires by Using Transient Calorimetric Technique," ASME J. Heat Transfer, **110**, pp. 166–172.
[5] Sasaki, S., Masuda, H., Higano, M., and Hishinuma, N., 1994, "Simultaneous

Measurement of Specific Heat and Total Hemispherical Emissivity of Chromel and Alumel by a Transient Calorimetric Technique," Int. J. Thermophys., **15**, pp. 547–565.

[6] Tanda, G., and Misale, M., 2006, "Measurement of Total Hemispherical Emittance and Specific Heat of Aluminum and Inconel 718 by a Calorimetric Technique," ASME J. Heat Transfer, **128**, pp. 302–306.

[7] Churchill, S. W., and Chu, H. H. S., 1975, "Correlating Equations for Laminar and Turbulent Free Convection From a Vertical Plate," Int. J. Heat Mass Transfer, **18**, pp. 1323–1329.

[8] Beck, J. V., Blackwell, B., and St. Clair, Jr., C. R., 1985, *Inverse Heat Conduction*, Wiley, New York.

[9] Sawaf, B., Ozisik, M. N., and Jarny, Y., 1995, "An Inverse Analysis to Estimate Linearly Temperature Dependent Thermal Conductivity Components and Heat Capacity of an Orthotropic Medium," Int. J. Heat Mass Transfer, **38**, pp. 3005–3010.

[10] Levenberg, K. A., 1944, "Method for the Solution of Certain Non-Linear Problems in Least Squares," Q. Appl. Math., **2**, pp. 164–168.

[11] Marquardt, D. W., 1963, "An Algorithm for Least-Squares Estimation of Nonlinear Parameters," J. Soc. Ind. Appl. Math., **11**, pp. 431–441.

[12] Deiveegan, M., Balaji, C., and Venkateshan, S. P., 2006, "Comparison of Various Methods for Simultaneous Retrieval of Surface Emissivities and Gas Properties in Gray Participating Media," ASME J. Heat Transfer, **128**, pp. 829–837.

[13] Zhang, B., Redgrove, J., and Clark, J., 2004, "A Transient Method for Total Emissivity Estimation," Int. J. Thermophys., **25**, pp. 423–438.

[14] Masuda, M., and Higano, M., 1985, "Transient Calorimetric Technique for Measuring Total Hemispherical Emissivities of Metals With Rigorous Evaluation of Heat Loss Through Thermocouple Leads," J. Opt. Soc. Am. A, **2**, pp. 1877–1882.

[15] Rammohan Rao, V., and Venkateshan, S. P., 1991, "Parameter Estimation—Imbedding Technique Verses Least Square Residual Method," *Heat and Mass Transfer, Proceedings of the 11th National Heat and Mass Transfer Conference*, Madras, India, Tata McGraw-Hill, New Delhi, pp. 303–308.

[16] ASM Metals Handbook, 1990, "Properties of Wrought Aluminum and Aluminum Alloys," ASM International Hand Book Committee, 10th ed., Vol. 2, pp. 62–122.

[17] Holman, J. P., 2001, *Experimental Methods for Engineers*, 7th ed., McGraw-Hill, New York.

James Geer
Professor Emeritus
Watson School of Engineering
and Applied Science,
Binghamton University,
Binghamton, NY 13902

John Fillo
Associate Dean for Research and External Affairs
Watson School of Engineering
and Applied Science,
Binghamton University,
Binghamton, NY 13902

Finite Difference Schemes for Diffusion Problems Based on a Hybrid Perturbation–Galerkin Method

A new technique for the development of finite difference schemes for diffusion equations is presented. The model equations are the one space variable advection diffusion equation and the two space variable diffusion equation, each with Dirichlet boundary conditions. A two-step hybrid technique, which combines perturbation methods based on the parameter $\rho = \Delta t/(\Delta x)^2$ *with the Galerkin method, provides a systematic way to develop new finite difference methods, referred to as hybrid equations. The main contributions of this paper include the (1) recovery of classical explicit or implicit finite difference schemes using only the perturbation terms; (2) development of new finite difference schemes, referred to as hybrid equations, which have better stability properties than the classical finite difference equations, permitting the use of larger values of the parameter* ρ*; and (3) higher order accurate methods, with either* $O((\Delta x)^4)$ *or* $O((\Delta x)^6)$ *truncation error, formed by convex linear combinations of the classical and hybrid equations. The solution of the hybrid finite difference equations requires only a tridiagonal equation solver and, hence, does not lead to excessive computational effort.*

[DOI: 10.1115/1.2891135]

Keywords: finite difference equations, diffusion/advection equations, perturbation methods, stability, truncation error

1 Introduction

The numerical solution by finite difference methods of partial differential equations (PDEs), which allows quantification of fluid dynamic and heat transfer problems, has matured over the past 30–40 years to such a degree as to raise the question of the need for new approaches in finite difference methods. When one looks at the success of the work of Patankar [1] and his students, as well as others, it causes one to stop and take serious note of this question.

The issues that have challenged those carrying out computations and those developing computational methods have centered on three key issues: stability of the computational method, accuracy as quantified by truncation error, and computational costs, which include "production-run" costs and development costs [2]. In addition, the question of how well the physics of the problem has been captured by the model PDEs has likewise been of concern as, for example, in the modeling of advection terms and in how the pressure is treated in the Navier–Stokes equations.

The approach we adopt addresses these numerical issues by treating the formulation of finite difference schemes for diffusion equations by utilizing a two-step hybrid analysis technique, which combines perturbation techniques and the Galerkin method. Here, the perturbation parameter is $\rho=\Delta t/(\Delta x)^2$, where Δt is the time step and Δx is the spatial step. As will be shown, this combination of techniques leads to the formulation of higher order finite difference equations with improved truncation error and improved stability. (The results presented here differ from those of Ref. [3] primarily in the way the time derivative term is treated.)

The hybrid perturbation–Galerkin technique has been applied as an analytical (as opposed to a purely numerical) approach to the solution of several classes of two point boundary value problems for ordinary differential equations (ODEs) [4–6], boundary value problems for elliptical PDEs [7], and resonant frequency calculations [8,9] and to the analysis of nonlinear heat conduction problems [10–12]. The hybrid method has also been applied successfully to the numerical solution of second order linear ODEs [13]. This paper addresses the problem of applying the hybrid technique to the numerical solution of PDEs.

The hybrid method itself may be viewed either as a technique to improve the accuracy of perturbation expansions or as a technique to generate a small number of good coordinate functions for a Galerkin-type approximation. In particular, the examples discussed in Refs. [3–13] illustrate that the perturbation coordinate functions appear to be exceptionally good trial functions to be used in a Galerkin approximation and that (at least) reasonably accurate approximate solutions can be obtained by using only a small number of these functions. In Ref. [3], it was observed that the hybrid method bears some resemblance to the finite analytic method [14].

The hybrid method is presented in Sec. 2 and applied to the first model problem in Sec. 3. Composite schemes are presented in Sec. 4, while the stability of these schemes is discussed in Sec. 5. The schemes presented for the first model problem are illustrated in Sec. 6 for two test cases. The method is then applied to the second model problem (diffusion in two space variables) in Sec. 7. In Sec. 8, our results are summarized, and various extensions of our techniques are discussed briefly, including necessary modifications for the case of Neumann or mixed boundary conditions.

2 Description of the Method

To prepare to apply the hybrid method (to be described shortly), the spatial region of the problem of interest is decomposed into a number of small elements. The method of lines [15] is employed, so that the time derivative is retained in a differential form, while

---

Contributed by the Heat Transfer Division of ASME for publication in the JOURNAL OF HEAT TRANSFER. Manuscript received March 14, 2006; final manuscript received January 30, 2008; published online April 21, 2008. Review conducted by Yogesh Jaluria.

the terms involving spatial derivatives are approximated by finite difference expressions. This reduces the problem to a system of first order ODEs in time.

In the first step of the hybrid method, the solution to the system of ODEs is expanded as a regular perturbation series, using ρ as the perturbation parameter. This perturbation solution is in the form of a series of perturbation coordinate functions, each multiplied by ρ raised to an integer power. The perturbation coordinate functions are expressed in an analytical form. When the perturbation solution is evaluated at an interior node, an algebraic equation relating interior nodal values is obtained, reproducing some classical finite difference schemes.

The second step of the hybrid method is to construct a new approximation to the solution of the ODEs, which is a linear combination of a finite subset of the perturbation coordinate functions, each multiplied by an unknown amplitude, δ_j. These amplitudes are determined by requiring that the residual formed by substituting this approximation into the governing ODEs is orthogonal to each coordinate function used in the approximation. This results in a tridiagonal system of linear algebraic equations for the amplitudes $\{\delta_j\}$. Once these amplitudes are determined, the hybrid solution is evaluated at an interior node, resulting in a new set of finite difference equations.

3 First Model Problem

To illustrate the method, consider first the problem of finding $u=u(x,t)$ satisfying the advection diffusion equation

$$u_t = u_{xx} - Vu_x, \quad 0 < x < 1, \quad t > 0 \tag{1}$$

the boundary conditions

$$u(0,t) = g(t) \quad \text{and} \quad u(1,t) = h(t) \quad \text{for all } t \geqslant 0 \tag{2}$$

and the initial condition

$$u(x,0) = f(x), \quad 0 < x < 1 \tag{3}$$

Here, $g(t)$, $h(t)$, and $f(x)$ are specified functions, while V is a specified constant, which we may assume as positive.

3.1 Method of Lines. Define $\Delta t > 0$ and let n be a positive integer. Then, define

$$\begin{gathered}\Delta x = \frac{1}{n+1}, \quad x_i = i\Delta x, \quad i = 0,1,\ldots,n+1 \\ t_j = j\Delta t, \quad j = 0,1,2,\ldots, \quad u_{i,j} = u(x_i,t_j)\end{gathered} \tag{4}$$

Then, for $t_j \leqslant t \leqslant t_{j+1}$ and $0 \leqslant i \leqslant n+1$, define

$$t = t_j + \Delta t\eta \quad \text{and} \quad u(x_i,t) = u_{i,j} + \Delta t\nu_i(\eta) \tag{5}$$

for $0 \leqslant \eta \leqslant 1$. Using definitions (4) and (5) and the boundary conditions (2), we note that

$$\nu_0(\eta) = \frac{g(t_j + \Delta t\eta) - g(t_j)}{\Delta t}, \quad \nu_{n+1}(\eta) = \frac{h(t_j + \Delta t\eta) - h(t_j)}{\Delta t} \tag{6}$$

Hence, these quantities are *known*, while each $v_i = v_i(\eta)$, $i = 1,2,\ldots,n$, is *unknown* and must be determined.

To determine these quantities, we approximate the right side of Eq. (1) at $x=x_i$, $1 \leqslant i \leqslant n$, by a second order finite difference formula for u_{xx} and a finite difference formula for u_x, i.e.,

$$u_{xx}(x_i,t) = \frac{u(x_{i-1},t) - 2u(x_i,t) + u(x_{i+1},t)}{(\Delta x)^2} + 0((\Delta x)^2)$$

$$u_x(x_i,t) = \frac{(1-\xi)(u(x_{i+1},t) - u(x_i,t)) + (1+\xi)(u(x_i,t) - u(x_{i-1},t))}{2\Delta x} + O(\xi\Delta x) + O((\Delta x)^2)$$

(Here, we note that setting $\xi=0$ yields the central difference approximation for u_x, while setting $\xi=1$ yields the upwind approximation to u_x.) Inserting these expressions into Eq. (1) evaluated at $x=x_i$, ignoring the $O(\xi\Delta x)$ and $O((\Delta x)^2)$ error terms, and then using Eqs. (5), Eq. (1) yields the relations

$$\nu_i' = \alpha_i + \rho\{c\nu_{i-1} + a\nu_i + b\nu_{i+1}\} \tag{7}$$

where $i = 1,2,\ldots,n$ and where we have defined

$$\begin{gathered}\alpha_i \equiv \frac{1}{(\Delta x)^2}\{cu_{i-1,j} + au_{i,j} + bu_{i+1,j}\} \\ a = -2\left(1 + \frac{V\Delta x}{2}\xi\right), \quad b = 1 - \frac{V\Delta x}{2}(1-\xi), \quad c = 1 + \frac{V\Delta x}{2}(1+\xi)\end{gathered} \tag{8}$$

Equations (7) is a system of n (tridiagonal) first order ODEs for the n unknowns $\{v_i(\eta)\}$, which must be solved subject to the initial conditions

$$\nu_i(0) = 0, \quad i = 1,2,\ldots,n \tag{9}$$

which follow from definitions (4) and (5).

To solve for the functions $\{v_i(\eta)\}$, it is first convenient to write Eq. (7) in matrix-vector form as

$$\mathbf{v}' = \boldsymbol{\alpha} + \boldsymbol{\rho}\boldsymbol{\beta} + \boldsymbol{\rho}\mathbf{A}\mathbf{v} \tag{10}$$

where the n-component vectors $\mathbf{v}$, $\boldsymbol{\alpha}$, and $\boldsymbol{\beta}$ are defined by

$$\mathbf{v} = \begin{pmatrix}\nu_1 \\ \nu_2 \\ \cdot \\ \cdot \\ \cdot \\ \nu_n\end{pmatrix}, \quad \boldsymbol{\alpha} = \begin{pmatrix}\alpha_1 \\ \alpha_2 \\ \cdot \\ \cdot \\ \cdot \\ \alpha_n\end{pmatrix}, \quad \boldsymbol{\beta} = \begin{pmatrix}c\nu_0 \\ 0 \\ \cdot \\ \cdot \\ 0 \\ b\nu_{n+1}\end{pmatrix} \tag{11}$$

and the $n \times n$ matrix $\mathbf{A}$ is defined by

$$\mathbf{A} = \begin{pmatrix} a & b & 0 & 0 & \cdot & \cdot & 0 \\ c & a & b & 0 & \cdot & \cdot & 0 \\ \cdot & \cdot & \cdot & \cdot & \cdot & \cdot & \cdot \\ \cdot & \cdot & \cdot & \cdot & \cdot & \cdot & \cdot \\ \cdot & \cdot & \cdot & \cdot & \cdot & \cdot & \cdot \\ 0 & 0 & 0 & \cdot & c & a & b \\ 0 & 0 & 0 & \cdot & 0 & c & a \end{pmatrix} \tag{12}$$

Then, the solution to Eq. (10) subject to initial conditions (9) is

$$\mathbf{v} = \int_0^\eta e^{\rho A\cdot(\eta - s)}(\boldsymbol{\alpha} + \rho\boldsymbol{\beta}(s))ds \tag{13}$$

3.2 Perturbation Solution for $\boldsymbol{\nu}$ When $\boldsymbol{\rho}$ is Small. We now formally expand the solution for $\mathbf{v}$ given by Eq. (13) for small values of ρ and write, for any positive integer N,

$$\mathbf{v} = \mathbf{v}^{(0)} + \rho\mathbf{v}^{(1)} + \rho^2\mathbf{v}^{(2)} + \cdots = P^{(N)}(\eta,\rho) + 0(\rho^N) \tag{14}$$

where

$$P^{(N)}(\eta,\rho) = \sum_{j=0}^{N-1} \rho^j \mathbf{v}^{(j)}(\eta) \tag{15}$$

with

$$\begin{gathered}\mathbf{v}^{(0)} = \int_0^\eta \alpha ds = \boldsymbol{\eta} \cdot \boldsymbol{\alpha} \\ \mathbf{v}^{(k)} = \frac{\boldsymbol{\eta}^{k+1}}{(k+1)!}A^k\boldsymbol{\alpha} + \int_o^\eta \frac{(\eta - s)^{k-1}}{(k-1)!}A^{k-1}\boldsymbol{\beta}(s)ds, \quad k = 1,2,\ldots\end{gathered} \tag{16}$$

In particular,

$$\mathbf{v}^{(1)} = \frac{\eta^2}{2}A\boldsymbol{\alpha} + \int_0^{\eta} \boldsymbol{\beta}(\mathrm{s})ds$$

$$\mathbf{v}^{(2)} = \frac{\eta^3}{6}A^2\boldsymbol{\alpha} + \int_0^{\eta} A\boldsymbol{\beta}(\mathrm{s})(\eta - s)ds \tag{17}$$

In the special case when $g(t)$ and $h(t)$ are constants, $\beta(s) \equiv 0$, and these expressions simplify to

$$\mathbf{v}^{(0)} = \eta \cdot \boldsymbol{\alpha}, \quad \mathbf{v}^{(1)} = \frac{\eta^2}{2}A\boldsymbol{\alpha}, \quad \mathbf{v}^{(2)} = \frac{\eta^3}{6}A^2\boldsymbol{\alpha} \tag{18}$$

3.3 Finite Difference Formulas Based on the Perturbation Solution for v. We now use the definitions in Eqs. (4), (5), and (14) to write, for $j=0,1,2,\ldots,$

$$u_{i,j+1} = u_{i,j} + \Delta t v_i(1) = u_{i,j} + \Delta t\{P_i^{(N)}(1,\rho) + O(\rho^N)\}$$

or, ignoring the $O(\rho^N)$ error term, we define

$$u_{i,j+1}^{(N)} = u_{i,j} + \Delta t P_i^{(N)}(1,\rho), \quad N = 1,2,\ldots \tag{19}$$

(Here, $u_{i,0}=f(x_i)$, $i=0,1,\ldots,n+1$, are known from Eq. (3).) Setting $N=1$ in Eq. (19) and using Eqs. (15) and (16), we find that

$$u_{i,j+1}^{(1)} = \rho c u_{i-1,j} + (1 + \rho a)u_{i,j} + \rho b u_{i+1,j} \tag{20}$$

which is the classical explicit finite difference scheme. In particular, using Taylor's theorem and Eqs. (20) and (1), we find that the leading order terms $T_{i,j}^{(1)}$ in the local truncation error for this scheme is

$$\begin{aligned} T_{i,j}^{(1)} = &- \frac{V\xi\Delta x}{2}u_{xx}(x_i,t_j) + (\Delta x)^2\left\{ \frac{(6\rho - 1)}{12}u_{xxxx}(x_i,t_j) \right. \\ &\left. + \frac{V}{6}(1 - 6\rho)u_{xxx}(x_i,t_j) + \frac{\rho V^2}{2}u_{xx}(x_i,t_j) \right\} \\ &- \frac{V\xi(\Delta x)^3}{24}u_{xxxx}(x_i,t_j) + 0((\Delta x)^4) \end{aligned} \tag{21}$$

3.4 Hybrid Perturbation–Galerkin Solution for v. For any positive integer N, we now construct a new approximate solution $\tilde{v}^{(N)}$ for $\mathbf{v}$ in the form

$$\tilde{v}_i^{(N)} = \sum_{j=0}^{N-1} \delta_i^{(N,j)} v_i^{(j)}, \quad i = 1,2,\ldots n, \quad N = 1,2,\ldots \tag{22}$$

Here, $\tilde{v}_i^{(N)}$ is defined by replacing the coefficient ρ^j of $v_i^{(j)}$ in the definition of $P_i^{(N)}$ by a new (unknown) "amplitude" $\delta_i^{(N,j)} = \delta_i^{(N,j)}(\rho)$. (Here, we also define $\tilde{v}_0^{(N)}=v_0$ and $\tilde{v}_{n+1}^{(N)}=v_{n+1}$. Hence, these quantities are known.) To determine these new amplitudes, we require that the residual obtained by substituting $\{\tilde{v}_i^{(N)}\}$ into the governing differential equation (Eq. (7)) be orthogonal to each of an appropriate set of test functions $\{\psi_{i,k}, i=1,\ldots,n, k=0,1,\ldots,N-1\}$, i.e.,

$$\int_0^1 R_i \cdot \psi_{i,k} d\eta = 0, \quad i = 1,2,\ldots,n, \quad k = 0,1,\ldots,N-1$$

$$R_i \equiv (\tilde{v}_i^{(N)})' - \alpha_i - \rho(c\tilde{v}_{i-1}^{(N)} + a\tilde{v}_i^{(N)} + b\tilde{v}_{i+1}^{(N)}) \tag{23}$$

Equations (23) are a system of nN (linear) algebraic equations for the nN unknowns $\{\delta_i^{(N,j)}\}$. For example, if we set $\psi_{i,k}=v_i^{(k)}(\eta)$, i.e., we choose the perturbation coordinate functions $\{v_i^{(k)}(\eta)\}$ as the test functions, then Eqs. (23) are the usual Bubnov–Galerkin conditions. If we set $\psi_{i,k}=\partial R_i/\partial\delta_i^{(N,k)}$, then Eqs. (23) are equivalent to requiring that the L_2 norm of each residual R_i is a minimum, i.e., the usual least-squares criteria.

Setting $N=1$ in Eqs. (23) with $\psi_{i,k}=v_i^{(k)}(\eta)$ and using the solution for $\mathbf{v}^{(0)}$ in Eq. (16), Eqs. (23) yield the tridiagonal system of equations

$$- \varepsilon c\gamma_{i-1}^{(1,0)} + (1 - a\varepsilon)\gamma_i^{(1,0)} - \varepsilon b\gamma_{i+1}^{(1,0)} = \alpha_i \tag{24}$$

$i=1,2,\ldots,n$, where we have defined

$$\varepsilon = \frac{2\rho}{3}, \quad \gamma_i^{(1,0)} = \alpha_i\delta_i^{(1,0)}, \quad i = 1,2,\ldots,n$$

$$\gamma_0^{(1,0)} = 3\int_0^1 v_o(\eta)\eta d\eta, \quad \gamma_{n+1}^{(1,0)} = 3\int_0^1 v_{n+1}(\eta)\eta d\eta \tag{25}$$

Equation (24) is tridiagonal and, hence, can be solved in a very efficient manner (see, e.g., Ref. [16]). For later reference, we note that it follows from Eq. (24) that as $\Delta x \rightarrow 0$,

$$\begin{aligned} \gamma_i^{(1,0)} = &\, u_{xx} - Vu_x + \frac{V\xi}{2}\Delta x u_{xx} + \left\{ \frac{2\rho V^2}{3}u_{xx} - \frac{1 + 8\rho}{6}Vu_{xxx} \right. \\ &\left. + \frac{1 + 8\rho}{12}u_{xxxx} \right\}(\Delta x)^2 + 0(\xi(\Delta x)^3) + 0((\Delta x)^4), \\ &i = 1,2,\ldots,n \end{aligned} \tag{26}$$

where it is understood that the partial derivatives of u are evaluated at (x_i,t_j).

3.5 Finite Difference Formulas Based on the Hybrid Solution for v. Once the quantities $\{\delta_i^{(N,j)}\}$ have been determined, we define

$$\tilde{u}_{i,j+1}^{(N)} = u_{i,j} + \Delta t \cdot \tilde{v}_i^{(N)}(1), \quad i = 1,2,\ldots,n \tag{27}$$

In particular, setting $N=1$ in Eq. (27), we find

$$\tilde{u}_{i,j+1}^{(1)} = u_{i,j} + \Delta t\gamma_i^{(1,0)}, \quad i = 1,2,\ldots,n \tag{28}$$

where the quantities $\{\gamma_i^{(1,0)}\}$ are determined from Eq. (24), In fact, using Eq. (24), Eqs. (28) can be written as

$$(I - \varepsilon A)\tilde{\mathbf{u}}_{\mathbf{j+1}} = \left(I + \frac{\varepsilon}{2}A\right)\tilde{\mathbf{u}}_{\mathbf{j}} + \mathbf{d}_j \tag{29}$$

where $\mathbf{d}_\mathbf{j}$ is a known vector. Then, using Taylor's theorem, it follows that the leading order term $\tilde{T}_{i,j}^{(1)}$ in the local truncation error for this scheme is

$$\begin{aligned} \tilde{T}_{i,j}^{(1)} = &- \frac{V\xi\Delta x}{2}u_{xx} - \frac{(\Delta x)^2}{12}\{2\rho V^2 u_{xx} - 2(1 + 2\rho)Vu_{xxx} \\ &+ (1 + 2\rho)u_{xxxx}\} + 0(\xi(\Delta x)^3) + 0((\Delta x)^4) \end{aligned} \tag{30}$$

4 Composite Solutions

The form of the truncation errors for the explicit method (Eq. (21)) and for the hybrid scheme with $N=1$ (Eq. (30)) suggests that a more accurate scheme can be constructed by considering a convex linear combination of these two schemes. For this purpose, it is convenient to consider separately two cases, depending on whether or not V is zero.

4.1 Case I: $V=0$ (Pure Diffusion). We begin by forming a convex linear combination of the explicit scheme (Eq. (20)) and the hybrid scheme (Eq. (28)) (both with $V=0$) and write

$$u_{i,j+1} = \theta(\rho c u_{i-1,j} + (1 + \rho a)u_{i,j} + \rho b u_{i+1,j}) + (1 - \theta)(u_{i,j} + \Delta t\gamma_i^{(1,0)}) \tag{31}$$

where θ is an arbitrary parameter. Using expressions (21) and (30) for the truncation errors of these two schemes, as well as Eqs. (26), it follows that the $O((\Delta x)^2)$ term in the local truncation error for this composite scheme vanishes if we set $\theta=(1+2\rho)/8\rho$. Inserting this value into Eq. (31), we define the composite approximation

$$u^C_{i,j+1} = \left(\frac{1+2\rho}{8}\right)u_{i-1,j} + \left(\frac{3-2\rho}{4}\right)u_{i,j} + \left(\frac{1+2\rho}{8}\right)u_{i+1,j} + \frac{(6\rho-1)}{8}(\Delta x)^2\gamma_i^{(1,0)} \tag{32}$$

$i=1,2,\ldots,n$ and find that the leading order term $T^C_{i,j}$ in the local truncation error for this scheme is

$$T^C_{i,j} = \left(\frac{2-5\rho-30\rho^2}{180}\right)u_{ttt}(x_i,t_j)(\Delta x)^4 \tag{33}$$

Another classical finite difference formula with a similar truncation error is given by the (implicit) Douglas scheme

$$(1-6\rho)u_{i-i,j+1} + (10+12\rho)u_{i,j+1} + (1-6\rho)u_{i+1,j+1} = (1+6\rho)u_{i-i,j} + (10-12\rho)u_{i,j} + (1+6\rho)u_{i+1,j} \tag{34}$$

$i=1,2,\ldots,n$ where the leading order term $T^D_{i,j}$ in the local truncation error is given by

$$T^D_{i,j} = \left(\frac{1-20\rho^2}{240}\right)u_{ttt}(x_i,t_j)(\Delta x)^4 \tag{35}$$

The form of the errors in Eqs. (33) and (35) suggests that we consider the “superconvex” linear combination

$$u^S_{i,j+1} = \theta u^C_{i,j+1} + (1-\theta)u^D_{i,j+1} \tag{36}$$

where $u^C_{i,j+1}$ is defined by Eq. (32), $u^D_{i,j+1}$ is defined by Eqs. (34), and θ is a constant. Using Eqs. (33) and (35), we see that the term proportional to $(\Delta x)^4$ in the truncation error of this scheme can be eliminated by choosing $\theta=-3(1-20\rho^2)/(5-20\rho-60\rho^2)$. With this value for θ, Scheme (36) becomes

$$u^S_{i,j+1} = \frac{1}{(5-20\rho-60\rho^2)}(3(20\rho^2-1)u^C_{i,j+1} + 4(2-5\rho-30\rho^2)u^D_{i,j+1}) \tag{37}$$

which has a truncation error proportional to $(\Delta x)^6$.

4.2 Case II: $V \neq 0$ (Advection and Diffusion). To construct composite schemes for this case, we first observe that by setting $\xi=\rho V\Delta x$ in the explicit scheme (Eq. (20)), its truncation error (Eq. (21)) becomes

$$T^{(1)}_{i,j} = (\Delta x)^2\frac{(1-6\rho)}{12}\{2Vu_{xxx}(x_i,t_j) - u_{xxxx}(x_i,t_j)\} + O((\Delta x)^4) \tag{38}$$

In a similar manner, by setting $\xi=-\rho V\Delta x/3$ in the hybrid scheme (Eq. (28)), its truncation error (Eq. (30)) becomes

$$\widetilde{T}^{(1)}_{i,j} = (\Delta x)^2\frac{(1+2\rho)}{12}\{2Vu_{xxx}(x_i,t_j) - u_{xxxx}(x_i,t_j)\} + O((\Delta x)^4) \tag{39}$$

The form of these truncation errors suggests that we form the convex linear combination

$$\theta\{\text{explicit}(\xi=\rho V\Delta x)\} + (1-\theta)\{\text{hybrid}(\xi=-\rho V\Delta x)/3\}$$

with $\theta=(1+2\rho)/8\rho$. With this choice of θ, the $O((\Delta x)^2)$ terms from $T^{(1)}_{i,j}$ and $\widetilde{T}^{(1)}_{i,j}$ cancel, leaving an $O((\Delta x)^4)$ truncation error for the composite scheme,

$$u^C_{i,j+1} = \theta u^{(1)}_{i,j+1}\big|_{\xi=\rho V\Delta x} + (1-\theta)\widetilde{u}^{(1)}_{i,j+1}\big|_{\xi=-\rho V\Delta x/3}, \quad \theta = \frac{1+2\rho}{8\rho} \tag{40}$$

where $u^{(1)}_{i,j+1}$ is defined in Eq. (20) with $\xi=\rho V\Delta x$ and $\widetilde{u}^{(1)}_{i,j+1}$ is defined in Eq. (28) with $\xi=-\rho V\Delta x/3$.

5 Stability

To investigate the stability of the numerical schemes we have just introduced, we first write each of them in the form

$$\mathbf{u}_{j+1} = B\mathbf{u}_j + \mathbf{d}_j, \quad j=0,1,2,\ldots \tag{41}$$

where $\mathbf{u}_{j+1}=(u_{i,j+1})$, $\mathbf{u}_j=(u_{i,j})$, and $\mathbf{d}_j=(d_{i,j})$ are each n-component vectors, and $B=(b_{i,j})$ is a known $n\times n$ matrix of constants. Here, each of the constants $d_{i,j}$ is known in terms of the boundary or initial conditions of the problem. Then, we shall say that the scheme described by Eqs. (41) is *stable* if and only if *each of the eigenvalues* λ *of* B *satisfies the condition that* $|\lambda| \leq 1$[16].

5.1 Case I: $V=0$ (Pure Diffusion). We first consider the hybrid scheme defined by Eqs. (28). To write these equations in the form of Eq. (41), we first note that the quantities $\{\gamma_i^{(1,0)}\}$ are determined from Eqs. (24), which we write in the form

$$C\vec{\gamma}^{(1,0)} = \frac{1}{(\Delta x)^2}A\mathbf{u}_j + \frac{1}{(\Delta x)^2}\boldsymbol{\omega}_j \tag{42}$$

where A and C are tridiagonal matrices, with A defined by Eq. (12) and $C=I-\varepsilon A$, and $\boldsymbol{\omega}_j=(u_{0,j},0,0,\ldots,0,u_{n+1,j})^t$. (Here, I is the $n\times n$ identity matrix.) We now multiply the vector form of Eqs. (28) by C (use Eq. (42)) and then multiply the resulting expression by C^{-1} to obtain

$$B = (I-\varepsilon A)^{-1}\left(I + \frac{\varepsilon}{2}A\right) \tag{43}$$

where we have used the definition $\varepsilon=2\rho/3$. Since the eigenvalues μ_s of A are (see, e.g., Ref. [16])

$$\mu_s = -4\sin^2\left(\frac{s\pi}{2(n+1)}\right), \quad s=1,2,\ldots,n \tag{44}$$

it follows from Eq. (43) that the eigenvalues of B for this scheme are

$$\lambda_s = \frac{1-2\varepsilon\sin^2\left(\frac{s\pi}{2(n+1)}\right)}{1+4\varepsilon\sin^2\left(\frac{s\pi}{2(n+1)}\right)}, \quad s=1,2,\ldots,n \tag{45}$$

From Eqs. (45), it follows that $|\lambda_s| \leq 1$ for all $\varepsilon > 0$; hence, the scheme is *unconditionally stable* for all $\rho > 0$.

A similar sequence of manipulations for the composite scheme described by Eq. (32) shows that matrix $B=B^C$ for this scheme is given by

$$B^C = \left(I - \frac{2\rho}{3}A\right)^{-1}\left(I + \frac{\rho}{3}A - \frac{\rho(1+2\rho)}{12}A^2\right)$$

Hence, the eigenvalues of B^C are given by

$$\lambda_s = \frac{1-(4\rho/3)S^2 - (4\rho(1+2\rho)/3)S^4}{1+(8\rho/3)S^2}, \quad S \equiv \sin\left(\frac{s\pi}{2(n+1)}\right) \tag{46}$$

From Eqs. (46), it follows that $|\lambda_s| \leq 1$ for all s only for $\rho < \sqrt{3}/2 = 0.866025$. Thus, this composite scheme is only *conditionally* stable.

For the supercomposite scheme described by Eq. (37), the matrix $B=B^S$ is given by

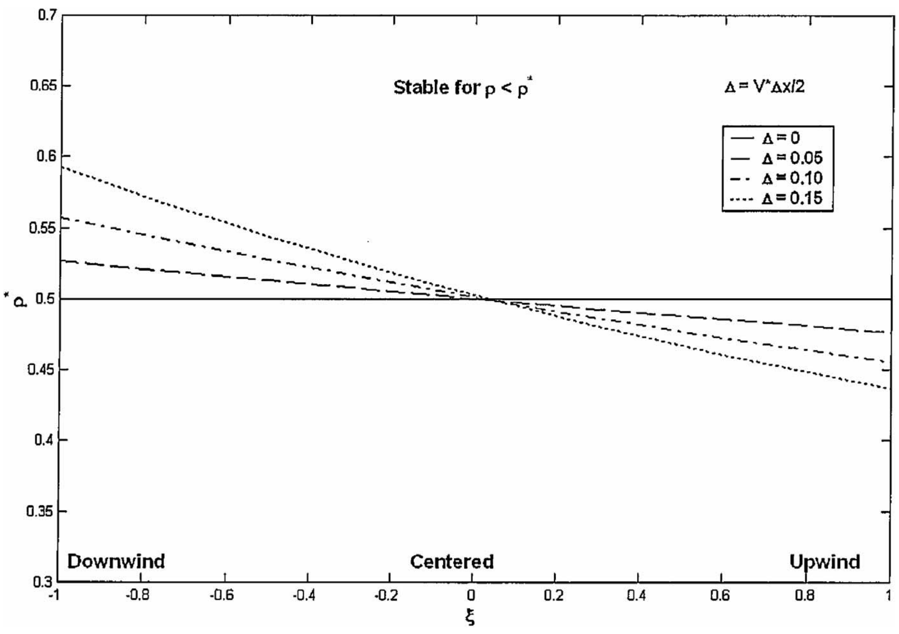

Fig. 1 Critical values ρ^* of ρ plotted as a functionf of ξ for several values of $\Delta = V\Delta x/2$ for the explicit scheme (Eq. (20)) for the first model problem. As the plot indicates, the scheme is (somewhat) more stable for negative values of ξ than for positive values of ξ.

$$B^S = (1-b)\{(I+\varepsilon_1 A)^{-1}(I+\varepsilon_2 A)\} + b(I+\varepsilon A) + b\varepsilon_3(I-\varepsilon_4 A)^{-1}A \tag{47}$$

where we have defined $\varepsilon=(1+2\rho)/8$, $\varepsilon_1=(1-6\rho)/12$, $\varepsilon_2=(1+6\rho)/12$, $\varepsilon_3=(6\rho-1)/8$, $\varepsilon_4=2\rho/3$, and $b=-3(1-20\rho^2)/(5-20\rho-60\rho^2)$. Hence, the eigenvalues of B^S are given by

$$\lambda_s = \frac{45 - 15(1-2\rho)S^2 - 40\rho(1+6\rho)S^4 - 12\rho(1-20\rho^2)S^6}{5(3-(1-6\rho)S^2)(3+8\rho S^2)} \tag{48}$$

where S is defined in Eq. (46). From Eq. (48), it follows that $|\lambda_s| \leq 1$ for all s only for $\rho < 1+3/\sqrt{5}=2.34164$. Thus, this super-composite scheme is also only conditionally stable, but is stable for larger values of ρ than the composite scheme (Eq. (32)).

5.2 Case II: $V \neq 0$ (Diffusion and Advection). The eigenvalues λ_s of the matrix $B=B_{\text{exp}} \equiv I+\rho A$ corresponding to the explicit scheme (Eq. (20)) are given by

$$\lambda_s = 1+\rho\mu_s, \quad \mu_s = -2(1+\Delta\xi) + 2\sqrt{(1+\Delta\xi)^2-\Delta^2}\cos\left(\frac{s\pi}{n+1}\right) \tag{49}$$

$s=1,2,\ldots,n$, with $\Delta = V\Delta x/2$. In Fig. 1, the critical value of ρ^* of ρ for which max $|\lambda_s|=1$ is plotted as a function of ξ for several values of Δ. As the plot illustrates, the scheme is stable for (somewhat) larger values of ρ when ξ is negative (corresponding to downwind schemes) than when ξ is positive.

The eigenvalues λ_s of the matrix $B=B_{\text{hyb}} \equiv (I-\varepsilon A)^{-1}(I+(\varepsilon/2)A)$, with $\varepsilon=2\rho/3$, corresponding to the hybrid scheme (Eq. (29)) are given by

$$\lambda_s = \frac{1+(\varepsilon/2)\mu_s}{1-\varepsilon\mu_s}, \quad \varepsilon = \frac{2\rho}{3} \tag{50}$$

$s=1,2,\ldots,n$, where μ_s is defined in Eq. (49). From expression (50), it follows that for $-1 \leq \xi \leq 1$ and all $V>0$, $\lambda_s \leq 1$ for all $\rho > 0$; hence, the scheme is unconditionally stable.

The matrix $B=B_{\text{com}}$ corresponding to the composite scheme (Eq. (40)) is given by

$$B_{\text{com}} = \theta B_{\text{exp}_{|\xi=2\rho\Delta}} + (1-\theta)B_{\text{hyb}_{|\xi=-2\rho\Delta/3}}, \quad \theta = \frac{1+2\rho}{8\rho} \tag{51}$$

Although we do not, as yet, have usable analytical expressions for the eigenvalues of B_{com}, they can be computed numerically in a straightforward manner. A typical result is shown in Fig. 2, where the critical values of ρ (corresponding to max$|\lambda|=1$) are plotted as a function of V for a specified value of Δx. Typically, the critical values of ρ for the composite scheme are about 75% larger than those for the explicit scheme on which it is based.

6 Test Problems

We now illustrate the various schemes we have mentioned with several test problems.

Test problem 1. For the first test problem, we set $V=0$ in Eq. (1), $g(t)=h(t)=0$ in Eq. (2), and $f(x)=\sin(\pi x)$ in Eq. (3). Thus, the exact solution is given by

$$u(x,t) = e^{-\pi^2 t}\sin(\pi x)$$

Then, letting $u_{i,j}$ denote the approximation for $u(x_i,t_j)$ defined by a finite difference scheme, we define the relative error $e_{i,j}$ by

$$e_{i,j} = \frac{u_{i,j}-u(x_i,t_j)}{u(x_i,t_j)}, \quad i=1,2,\ldots,n$$

In particular, for *odd* values of n, we define $m=(1+n)/2$, so that $x_m=0.5$; hence, the relative error $e_{m,j}$ at the midpoint in x becomes

$$e_{m,j} = e^{\pi^2 t_j}u_{m,j} - 1$$

In Figs. 3 and 4, we have plotted $e_{m,j}$ as a function of time (t_j) for the different schemes we have discussed, with two different values of ρ.

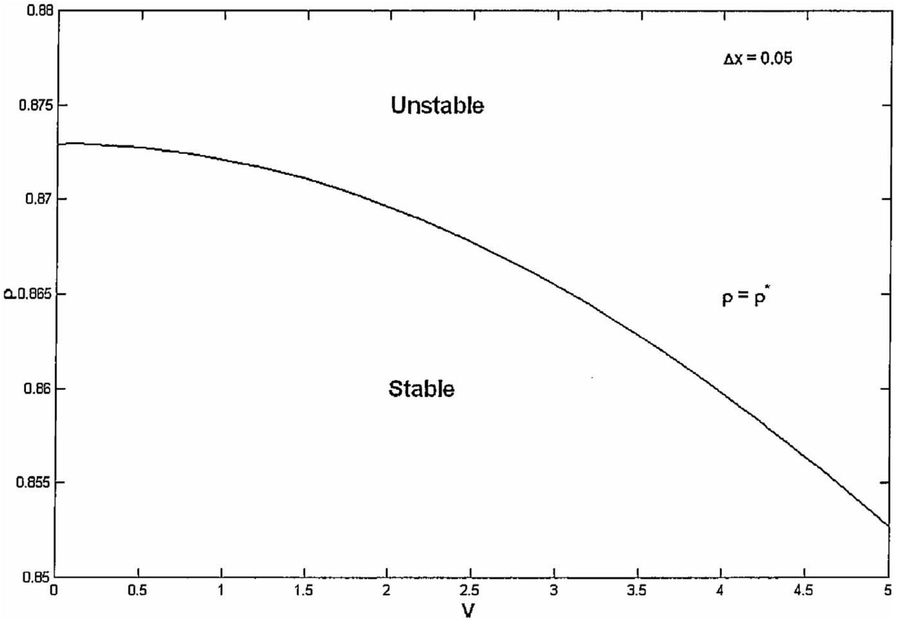

Fig. 2 Critical values ρ^* of ρ plotted as a function of V for $\Delta x=0.05$ for the composite scheme (Eq. (40)) for the first model problem. These critical values are about 75% larger than the corresponding values for the explicit scheme (see Fig. 1).

Test problem 2. For the second test problem, we let V in Eq. (1) be arbitrary, set $g(t)=h(t)=0$ in Eq. (2), and $f(x)=e^{Vx/2}\sin(\pi x)$ in Eq. (3). The exact solution for this case is given by

$$u(x,t)=e^{-(\pi^2+(V/2)^2)t+Vx/2}\sin(\pi x)$$

Again, letting $u_{i,j}$ denote the approximation for $u(x_i,t_j)$ defined by a finite difference scheme, the relative error $e_{m,j}$ at the midpoint in x becomes

$$e_{m,j}=e^{(\pi^2+(V/2)^2)t_j-V/4}u_{m,j}-1$$

In Fig. 5, we have plotted $e_{m,j}$ as a function of time (t_j) for the different schemes we have discussed with $\rho=1/3$.

7 Two Space Dimensions

We now extend some of the ideas just discussed to the case of two space dimensions.

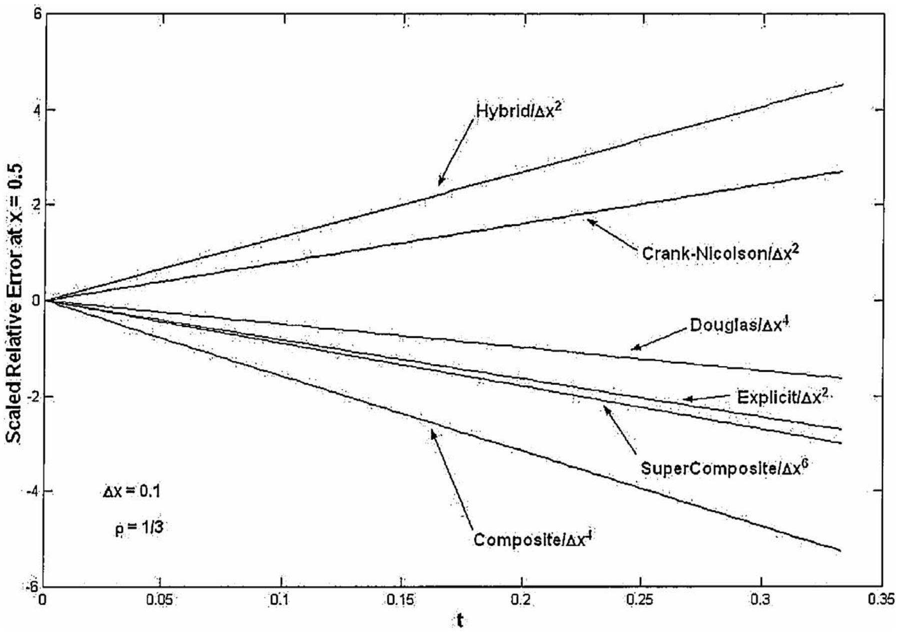

Fig. 3 Scaled relative error at $x=0.5$ plotted as a function of time for test problem 1 using various numerical schemes, with $\Delta x=0.1$ and $\rho=1/3$. Note that the $O((\Delta x)^4)$ error of the composite scheme (Eq. (32)) and the $O((\Delta x)^6)$ error of the supercomposite scheme (Eq. (36)) are clearly illustrated.

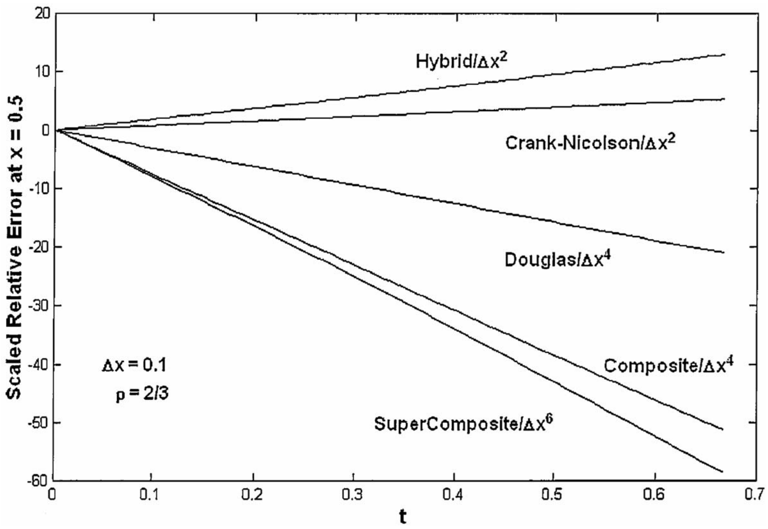

Fig. 4 Scaled relative error at $x=0.5$ plotted as a function of time for test problem 1 using various numerical schemes, with $\Delta x=0.1$ and $\rho=2/3$. Note that the $O((\Delta x)^4)$ error of the composite scheme (Eq. (32)) and the $O((\Delta x)^6)$ error of the supercomposite scheme (Eq. (36)) are clearly illustrated. Also, the explicit method is not used here since $\rho>\rho^*=1/2$ for this method.

7.1 Model Problem. Find $u=u(x,y,t)$, satisfying

$$u_t = u_{xx} + u_{yy}, \quad 0 < x < a, \quad 0 < y < b, \quad t > 0 \tag{52}$$

the boundary conditions

$$u(0,y,t) = g_0(y,t), \quad u(a,y,t) = g_a(y,t)$$

$$u(x,0,t) = h_0(x,t), \quad u(x,b,t) = h_b(x,t), \quad \text{for all } t \geq 0 \tag{53}$$

and the initial condition

$$u(x,y,0) = f(x,y), \quad 0 < x < a, \quad 0 < y < b \tag{54}$$

Following the preliminary steps as in the one-dimensional case, we define $\Delta t > 0$ and let n and m be positive integers. Then, we define

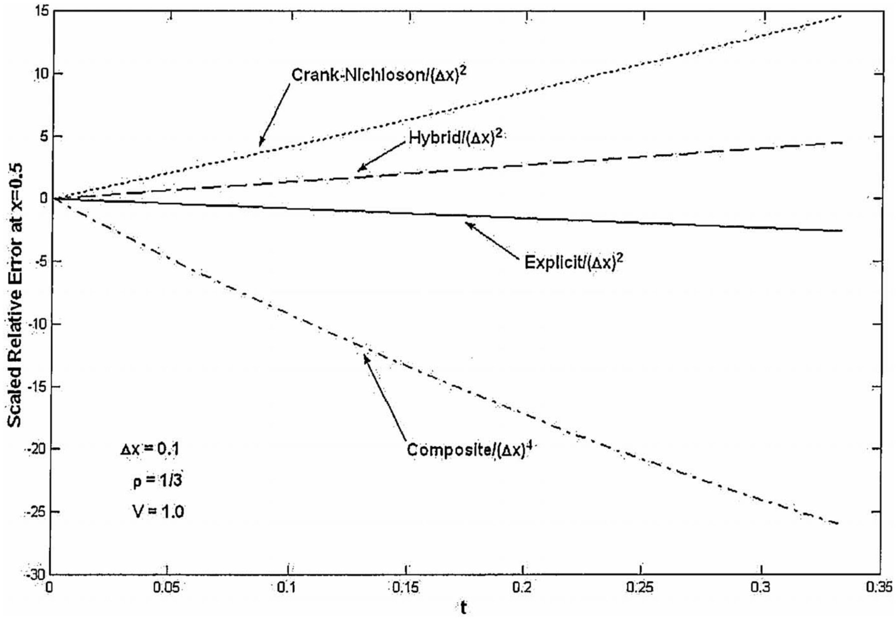

Fig. 5 Scaled relative error at $x=0.5$ plotted as a function of time for test problem 2 using various numerical schemes, with $\Delta x=0.1$, $\rho=1/3$, and $V=1$. Note that the $O((\Delta x)^4)$ error of the composite scheme (Eq. (40)) is clearly illustrated.

$$\Delta x = \frac{a}{n+1}, \quad x_i = i\Delta x, \quad i = 0,1,\ldots,n+1$$

$$\Delta y = \frac{b}{m+1}, \quad y_j = j\Delta y, \quad j = 0,1,\ldots,m+1 \tag{55}$$

$$t_k = k\Delta t, \quad k = 0,1,2,\ldots, \quad u_{i,j,k} = u(x_i,y_j,t_k)$$

For simplicity of exposition, we shall assume that $\Delta x = \Delta y$.

Suppose now that u is known at time t_k. We shall now advance the solution from $t=t_k$ to $t=t_{k+2}$ in two distinct steps. Following the ideas of the classical ADI method, see, e.g., Ref. [17].

7.2 Step 1: $t=t_k$ to $t=t_{k+1}$.

For $t_k \leqslant t \leqslant t_{k+1}$ and $0 \leqslant i \leqslant n+1$, $0 \leqslant j \leqslant m+1$, define

$$t = t_k + \Delta t\eta \quad \text{and} \quad u(x_i,y_j,t) = u_{i,j,k} + \Delta t v_{i,j}(\eta) \tag{56}$$

for $0 \leqslant \eta \leqslant 1$. We note that using definitions (55) and (56) and boundary conditions (53),

$$v_{0,j}(\eta) = \frac{g_0(y_j,t_k+\Delta t\eta) - g_0(y_j,t_k)}{\Delta t},$$
$$v_{n+1,j}(\eta) = \frac{g_a(y_j,t_k+\Delta t\eta) - g_a(y_j,t_k)}{\Delta t} \tag{57}$$

with similar expressions holding for $v_{i,o}(\eta)$ and $v_{i,m+1}(\eta)$. Hence, these quantities are known. However, each $v_{i,j}=v_{i,j}(\eta)$, $i=1,2,\ldots,n$, $j=1,2,\ldots,m$, is unknown and must be determined. To determine these quantities, we evaluate Eq. (52) at $x=x_i$ and $y=y_j$ and approximate the terms u_{xx} and u_{yy} on the right side by the usual second order finite difference formulas and write

$$u_t(x_i,y_j,t) = \frac{u(x_{i-1},y_j,t) - 2u(x_i,y_j,t) + u(x_{i+1},y_j,t)}{(\Delta x)^2} + 0((\Delta x)^2) + \frac{u(x_i,y_{j-1},t) - 2u(x_i,y_j,t) + u(x_i,y_{j+1},t)}{(\Delta y)^2} + 0((\Delta y)^2) \tag{58}$$

Ignoring the $O((\Delta x)^2)$ and $O((\Delta y)^2)$ error terms, approximating the term corresponding to u_{yy} by its value at $t=t_k$, and then using Eq. (56), Eq. (58) yields the relations

$$v'_{i,j} = \alpha_{i,j,k} + \rho(v_{i-1,j} - 2v_{i,j} + v_{i+1,j}) \quad i = 1,2,\ldots,n, \quad j = 1,2,\ldots,m \tag{59}$$

where we have defined

$$\alpha_{i,j,k} \equiv \frac{u_{i-1,j,k} - 2u_{i,j,k} + u_{i+1,j,k}}{(\Delta x)^2} + \frac{u_{i,j-1,k} - 2u_{i,j,k} + u_{i,j+1,k}}{(\Delta y)^2},$$
$$\rho \equiv \frac{\Delta t}{(\Delta x)^2} \tag{60}$$

For each fixed value of j, $1 \leqslant j \leqslant m$, Eqs. (59) are a system of n (tridiagonal) first order ODEs for the n unknowns $\{v_{i,j}(\eta)\}$, which must be solved subject to the initial conditions

$$v_{i,j}(0) = 0, \quad i = 1,2,\ldots,n \tag{61}$$

which follow from definitions (55) and (56).

The form of Eqs. (59) is exactly the same as the form of the equations for the quantities $\{v_i\}$ in the one space dimension case. In particular, for small values of ρ, we have $v_{i,j}=\alpha_{i,j,k}\eta+0(\rho)$. Hence, to leading order, setting $\eta=1$ in Eq. (56) yields the relations

$$u_{i,j,k+1} = u_{i,j,k} + \Delta t\alpha_{i,j,k} \quad 1 \leqslant i \leqslant n, \quad 1 \leqslant j \leqslant m \tag{62}$$

which are the usual first order accurate explicit formulas. Also, the hybrid perturbation–Galerkin approximation $\tilde{v}_{i,j}^{(N)}$ for $v_{i,j}$ is computed using the same ideas as in the one space dimension case. In particular, for $N=1$, we set $\tilde{v}_{i,j}^{(1,0)}=\delta_{i,j}^{(1,0)}\alpha_{i,j,k}\eta$ and find that $\gamma_{i,j}^{(1,0)} \equiv \delta_{i,j}^{(1,0)}\alpha_{i,j,k}$ satisfies Eq. (24), with α_i replaced by $\alpha_{i,j,k}$ Thus, the corresponding hybrid finite difference equations, using Eqs. (56) with $v_{i,j}$ replaced by $\tilde{v}_{i,j}^{(1,0)}$ and with $\eta=1$, are

$$u_{i,j,k+1} = u_{i,j,k} + \Delta t\gamma_{i,j}^{(1,0)}, \quad 1 \leqslant i \leqslant n, \quad 1 \leqslant j \leqslant m$$

where $\{\gamma_{i,j}^{(1,0)}\}$ are determined by Eq. (24), with α_i replaced by $\alpha_{i,j,k}$, $a=-2$, and $b=c=1$.

7.3 Step 2: $t=t_{k+1}$ to $t=t_{k+2}$.

For $t_{k+1} \leqslant t \leqslant t_{k+2}$ and $0 \leqslant i \leqslant n+1$, $0 \leqslant j \leqslant m+1$, define

$$t = t_{k+1} + \Delta t\eta \quad \text{and} \quad u(x_i,y_j,t) = u_{i,j,k+1} + \Delta t v_{i,j}(\eta) \tag{63}$$

We again evaluate Eq. (52) at $x=x_i$ and $y=y_j$ and approximate the terms u_{xx} and u_{yy} on the right side by the finite difference formulas (Eq. (58)). Ignoring the $O((\Delta x)^2)$ and $O((\Delta y)^2)$ error terms, approximating the term corresponding to u_{xx} by its value at $t=t_{k+1}$, and then using Eq. (63) yield the relations

$$v'_{i,j} = \alpha_{i,j,k+1} + \rho(v_{i,j-1} - 2v_{i,j} + v_{i,j+1}), \quad j = 1,2,\ldots,m,$$
$$i = 1,2,\ldots,n \tag{64}$$

For each fixed value of i, $1 \leqslant i \leqslant n$, Eqs. (64) are a system of m (tridiagonal) first order ODEs for the m unknowns $\{v_{i,j}(\eta)\}$, which must be solved subject to the initial conditions (Eq. (61)).

The form of Eqs. (64) is again exactly the same as the equations for the quantities $\{v_i\}$ in the one space dimension case. Hence, the leading order perturbation solution yields the explicit formula

$$u_{i,j,k+2} = u_{i,j,k+1} + \Delta t\alpha_{i,j,k+1}, \quad 1 \leqslant i \leqslant n, \quad 1 \leqslant j \leqslant m \tag{65}$$

Also, the hybrid perturbation–Galerkin approximation $\tilde{v}_{i,j}^{(N)}$ for $v_{i,j}$ is computed using the same ideas as in the one space dimension case. In particular, for $N=1$, we set $\tilde{v}_{i,j}^{(1)}=\delta_{i,j}^{(1,0)}\alpha_{i,j,k+1}\eta$ and find that $\gamma_{i,j}^{(1,0)} \equiv \delta_{i,j}^{(1,0)}\alpha_{i,j,k+1}$ satisfies Eq. (24), with α_i now replaced by $\alpha_{i,j,k+1}$. Thus, the corresponding hybrid finite difference equation, using Eqs. (63) with $v_{i,j}$ replaced by $\tilde{v}_{i,j}^{(1,0)}$ and with $\eta=1$, is

$$u_{i,j,k+2} = u_{i,j,k+1} + \Delta t\gamma_{i,j}^{(1,0)}$$

where $(\gamma_{i,j}^{(1,0)})$ are again determined by Eq. (24), with α_i now replaced by $\alpha_{i,j,k+1}$, $a=-2$, and $b=c=1$.

To illustrate these results, we consider two more test problems.

Test problem 3. We set $a=b=1$ and $g_0\ (y,t)=g_a(y,t)=h_0(x,t)=h_b(x,t)=0$ in Eq. (53), and $f(x,y)=\sin(\pi x)\sin(\pi y)$ in Eq. (54), so that the exact solution is

$$u(x,y,t) = e^{-2\pi^2 t}\sin(\pi x)\sin(\pi y)$$

In Fig. 6, we have plotted the scaled relative error at the midpoint $x=y=1/2$ as a function of t using the explicit scheme (Eq. (62)), the classical ADI method, and the hybrid method defined above for the case when $\Delta x=0.05$ and $\rho=0.25$. As the figure illustrates, for this example (with homogeneous boundary conditions), the error for both the explicit and ADI methods is $O((\Delta x)^2)$, while the error for the hybrid scheme is $O((\Delta x)^4)$.

Test Problem 4. We again set $a=b=1$ and $g_0\ (y,t)=g_a(y,t)=h_0(x,t)=0$, but let $h_b(x,t)=\sin(\pi x)$ in Eq. (53) and $f(x,y)=\sin(\pi x)\ \{\sin(\pi y)+\sinh(\pi y)/\sinh(\pi)\}$ in Eq. (54), so that the exact solution is

$$u(x,y,t) = \sin(\pi x)\left\{\frac{\sinh(\pi y)}{\sinh(\pi)} + e^{-2\pi^2 t}\sin(\pi y)\right\}$$

In Fig. 7, we have plotted the scaled relative error at the midpoint $x=y=1/2$ as a function of t using the explicit scheme (Eq. (62)), the classical ADI method, and the hybrid method defined above for the case when $\Delta x=0.05$ and $\rho=0.25$. As the figure illustrates,

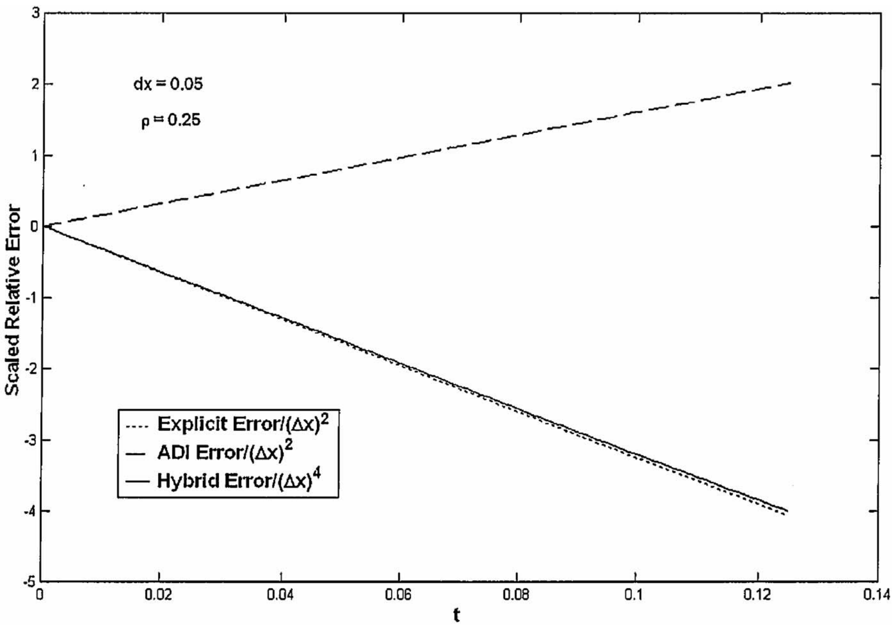

Fig. 6 Scaled relative error at $x=y=0.5$ plotted as a function of time for test problem 3 using various numerical schemes, with $\Delta x=0.05$ and $\rho=1/4$. Note that the $O((\Delta x)^4)$ error of the hybrid method (Sec. 7) is clearly illustrated.

for this example (with nonhomogeneous boundary conditions), all three errors are $O((\Delta x)^2)$.

8 Summary and Discussion

A two-step hybrid analysis technique, which combines perturbation techniques with the Galerkin method, has been used to provide a systematic way to develop new finite difference schemes. These new schemes, referred to as hybrid equations, have been shown to have better stability properties than the classical (explicit) schemes on which they are based and can be combined with classical schemes to form higher order accurate methods. The solution of the hybrid finite difference equations requires only a tridiagonal equation solver and, hence, can be solved in a very efficient manner.

The basic method we have presented for deriving hybrid finite difference equations can be extended in several directions. For example, higher order perturbation solutions $P_i^{(N)}(\eta,\rho)$ for v_i, with $N>1$ (see Eqs. (15) and (16)), could be used in formulas (19).

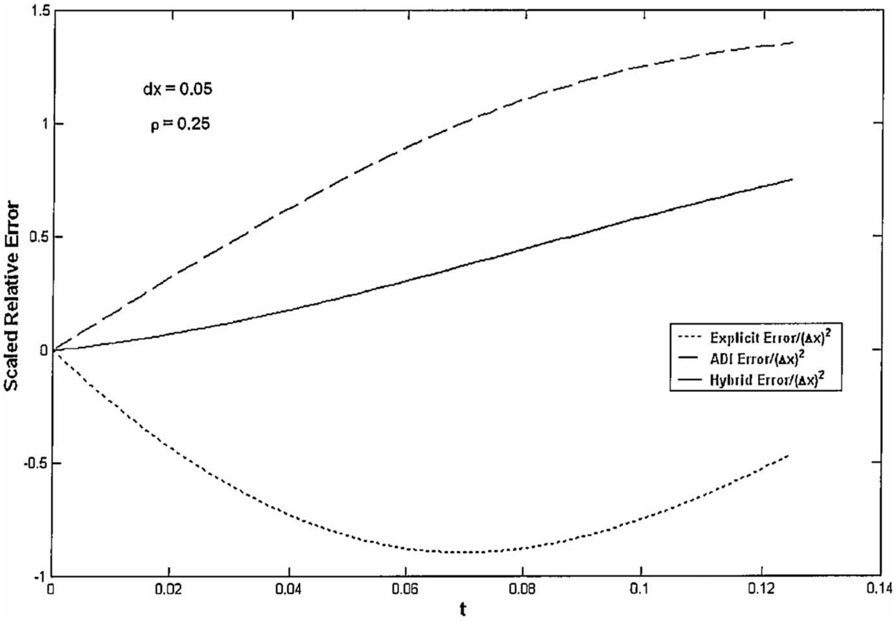

Fig. 7 Scaled relative error at $x=y=0.5$ plotted as a function of time for test problem 4 using various numerical schemes, with $\Delta x=0.05$ and $\rho=1/4$. Note that the error of the hybrid method (Sec. 7) changes from $O((\Delta x)^4)$ to $O((\Delta x)^2)$ due to the nonhomogeneous boundary conditions.

However, the resulting equations for $u_{i,j+1}$, corresponding to Eq. (20), and the subsequent hybrid equations, corresponding to Eq. (24), would have increased bandwidth. In particular, the resulting equations are no longer tridiagonal in nature, and also present the usual problems of applying such schemes near boundaries (see, e.g., Ref. [16]).

The basic method we have used was formulated formally in Sec. 3 in such a manner that as $\rho \to 0$, the leading order perturbation solution for $\mathbf{v}$ led to the classical *explicit* scheme for $u_{i,j+1}$. However, a similar formulation could have been presented, which, as $\rho \to 0$, would lead to the classical *implicit* scheme for $u_{i,j+1}$.

In particular, the definitions in Eqs. (5) could be replaced by

$$t = t_{j+1} - \Delta t \eta \quad \text{and } u(x_i,t) = u_{i,j+1} - \Delta t v_i(\eta) \tag{66}$$

for $0 \leq \eta \leq 1$. In this case, the resulting equations for $\{v_i\}$ are very similar to Eq. (7), but with j replaced by $j+1$ in the definition of α_i in Eq. (8). Consequently, setting $\eta=1$ in Eq. (66), i.e., by requiring that $u_{i,j}=u_{i,j+1}-\Delta t v_i$ (1), and using the leading order perturbation solution for v_i lead (in place of Eq. (20)) to the classical implicit scheme

$$-\rho c u_{i-1,j+1} + (1-\rho a)u_{i,j+1} - \rho b u_{i+1,j+1} = u_{i,j}$$

Of course, taking a convex linear combination of definitions (5) and (66) would lead to Crank–Nicolson-type schemes as the leading order approximation.

Derivative boundary conditions can be handled by the method we have presented by incorporating rather straightforward modifications. One technique (see, e.g., Ref. [16]) is to assume that the differential equation holds at the boundary and use a finite difference approximation to the derivative boundary condition to eliminate the "fictitious" point that lies outside the spatial region of interest. This simply increases the size, but not the bandwidth, of the equations that need to be solved. These extensions, as well as others, and the derivation of hybrid schemes for other PDEs are currently being investigated.

With regard to the time needed to carry out computation using the hybrid method, there is an added computational step solving the finite difference equations based on the hybrid solution. Solving for the "amplitude" functions requires solving a tridiagonal matrix, but there are fast solvers to do so. To quantify the actual cost and better represent this measure requires more extensive calculations, which have yet to be done. The computational cost for improved stability is likewise tied to the point just made about the added hybrid solution step. The extension of the new scheme to three dimensions is straightforward and is based on what was done for the two-dimensional case.

Nomenclature

A = $n \times n$ matrix
B = $n \times n$ matrix of constants
a,b,c = coefficients in finite difference equations
$\mathbf{d}$ = n-component vector dependent on boundary conditions
e = relative error
$f(x)$ = initial condition
g,h = dimensionless boundary conditions
T = local truncation error
t = dimensionless time
u = dimensionless "temperature"
V = dimensionless velocity
x,y = dimensionless coordinate
$\Delta x, \Delta y$ = grid spacing

Greek Symbols

α = advection/diffusion parameter
δ = amplitude function
ε, ρ = perturbation parameters
λ = eigenvalue
η = dimensionless independent time
v = general dependent value
Θ = arbitrary parameter
ξ = determines central difference (=0) and upwind (=1) approximations to u_x

Subscripts

exp = explicit scheme
i = indices of grid point
J = index of time step

References

[1] Patankar, S., 1980, *Numerical Heat Transfer and Fluid Flow*, Hemisphere, New York.
[2] Roache, P., 1972, *Computational Fluid Dynamics*, Kenmore Publishers, Albuquerque, NM.
[3] Fillo, J., and Geer, J., 1999, "A New Numerical Technique for the Solution to the Heat Equation Based on a Hybrid Perturbation Galerkin Method," *Proceedings of the 33rd National Heat Transfer Conference*, Albuquerque, NM.
[4] Anderson, C. M., and Geer, J. F., 1991, "Investigating a Hybrid Perturbation Galerkin Technique Using Computer Algebra," J. Symb. Comput., **12**, pp. 695–714.
[5] Geer, J. F., and Andersen, C. M., 1989, "A Hybrid Perturbation Galerkin Technique for Differential Equations Containing a Parameter," Appl. Mech. Rev., **42**(11), pp. 569–577.
[6] Geer, J. F., and Andersen, C. M., 1990, "A Hybrid Perturbation-Galerkin Technique that Combines Multiple Expansions," SIAM J. Appl. Math., **50**, pp. 1474–1495.
[7] Geer, J. F., and Andersen, C. M., 1991, *Asymptotic Analysis and the Numerical Solution of Partial Differential Equations*, Lecture Notes in Pure Applied Mathematics, Vol. 130, Marcel Dekker, New York.
[8] Geer, J. F., and Andersen, C. M., 1991, "Resonant Frequency Calculations Using a Hybrid Perturbation Galerkin Technique," Appl. Mech. Rev., **44**(11), pp. S76–S88.
[9] Geer, J. F., and Dadfar, M. B., 1990, "Nonresonant Excitation of the Forced Duffing Equation," *Proceedings of the International Conference on Control and Modelling*, Tehran, Iran, pp. 69–73.
[10] Noor, A. K., and Balch, C. D., 1984, "Hybrid Perturbation/Bubnov-Galerkin Technique for Nonlinear Thermal Analysis," AIAA J., **22**(2), pp. 287–294.
[11] Geer, J. F., and Fillo, J., 1996, "Hybrid Perturbation-Galerkin Technique for Nonlinear Heat Conduction Problems I: Steady Problems," Numer. Heat Transfer, Part B, **29**, pp. 61–73.
[12] Fillo, J., and Geer, J., 1996, "Hybrid Perturbation-Galerkin Technique for Nonlinear Heat Conduction Problems II: Partial Differential Equations," Numer. Heat Transfer, Part B, **29**, pp. 75–89.
[13] Geer, J., and Fillo, J., 1999, "A New Numerical Solution Technique for Differential Equations Containing a Small Parameter," *Applied Mechanics in the Americas*, Vol. 6, Rio de Janeiro, Brazil.
[14] Chen, J. C., 1988, *Finite Analytic Method: Handbook of Numerical Heat Transfer*, W. J. Minkowyz, ed., Wiley, New York.
[15] Golub, G., and Ortega, J., 1991, *Scientific Computing and Differential Equations: An Introduction to Numerical Methods*, Academic, New York.
[16] Smith, G. D., 1978, *Numerical Solution of Partial Differential Equations: Finite Difference Methods*, Clarendon, Oxford.
[17] Peaceman, D. W., and Rachford, H. H., 1955, "The Numerical Solution of Parabolic and Elliptic Differential Equations," J. Soc. Ind. Appl. Math., **3**(1), pp. 28–41.

Shyy Woei Chang[1]
Professor
Thermal Fluids Laboratory,
Department of Marine Engineering,
National Kaohsiung Marine University,
No. 142, Haijhuan Road,
Nanzih District,
811 Kaohsiung, Taiwan, R.O.C.
e-mail: swchang@mail.nkmu.edu.tw

Tong-Minn Liou
Professor
Department of Power Mechanical Engineering,
National Tsing Hua University,
300 Hsinchu, Taiwan, R.O.C.

Shyr Fuu Chiou
Lecturer
Thermal Fluids Laboratory,
National Kaohsiung Marine University,
No. 142, Haijhuan Road, Nanzih District,
81143 Kaohsiung, Taiwan, R.O.C.

Shuen Fei Chang
MS Student
Department of Marine Engineering,
National Kaohsiung Marine University,
No. 142, Haijhuan Road,
Nanzih District,
811 Kaohsiung, Taiwan, R.O.C.

Heat Transfer in High-Speed Rotating Trapezoidal Duct With Rib-Roughened Surfaces and Air Bleeds From the Wall on the Apical Side

An experimental study of heat transfer in a radially rotating trapezoidal duct with two opposite walls roughened by 45 deg staggered ribs and bleed from the apical side wall is performed. Centerline heat transfer variations on two rib-roughened surfaces are measured for radially outward flows with and without bleeds at test conditions of Reynolds number (Re), rotation number (Ro), and density ratio ($\Delta\rho/\rho$) in the ranges of 15,000–30,000, 0–0.8, and 0.04–0.31, respectively. Geometrical configurations and rotation numbers tested have considerably extended the previous experiences that offer practical applications to the trailing edge cooling of a gas turbine rotor blade. A selection of experimental data illustrates the individual and interactive influences of Re, Ro, and buoyancy number (Bu) on local heat transfer with and without bleeds. Local heat transfer results are generated with the influences of bleeds on the apical side examined to establish heat transfer correlations with Re, Ro, and Bu as the controlling flow parameters for design applications. The rotation of present trapezoidal duct with rib-roughened surfaces and air bleeds on the apical side worsens the impairing heat transfer impacts due to bleeds. Within the Ro range of 0.1–0.8, bleeds on the apical side of the rotating channel respectively produce 25–50% and 25–40% of heat transfer reductions from the rotational no-bleed references along the leading and trailing centerlines. Such heat transfer reductions due to the combined bleeds and Ro-Bu impacts need design precautions for turbine rotor blades. [DOI: 10.1115/1.2891217]

Keywords: 45 deg angled and staggered ribs, bleeds on the apical side, high rotating number, turbine rotor blade cooling

1 Introduction

Gas turbine rotor blades are cooled by means of film, impingement, and multipass channel cooling with airflows circulating through several 180 deg sharp turns that connect straight channels with various cross-sectional shapes. These internal coolant channels are fitted with a variety of surface ribs or pin fins to promote the cooling performances. The internal coolant channel at the trailing edge of a gas turbine rotor blade is typically trapezoidal with a low channel aspect ratio, which usually bleeds airflows through the discrete holes along its apical sidewall to cool the downstream static blades. As the occasion demands, the coolant is also bled from these internal cooling channels to facilitate the external film cooling. Bleeds from either the rib floor or from the apical sidewall of a trapezoidal duct modify the flow structures, the boundary layer developments, and, therefore, the heat transfer distributions over all constituent surfaces of the bleed channel. Experimental evidences confirmed the considerable impacts of one-wall bleeds on the flow and heat transfer in a ribbed *static* channel [1–5]. Extractions of a coolant from the bleed holes through the ribbed wall elevate the local heat transfer coefficients in the vicinity of bleed holes [2]. With 20–25% of the drawing coolant flow from the bleed holes in a two-pass square channel roughened by a variety of surface ribs, Ekkad et al. demonstrated that the regionally averaged heat transfer levels with bleeds were similar as that for a rib-roughened surface without bleeds [3]. Thurman and Poinsatte [4] examined the detailed heat transfer distributions for a triple-pass channel roughened by transverse ribs at the different bleed conditions of uniform bleed, increasing and decreasing bleed flow rates per hole, or no bleed. The uniform bleed condition generally provided the better heat transfer enhancement among the various bleed conditions studied in Ref. [4]. Chanteloup and Bölics [5] performed the detailed particle image velocimetry (PIV) flow measurements in a two-pass channel roughened by staggered 45 deg ribs with bleeds from one ribbed wall of the second passage. As the coolant flow is ejected from *one* ribbed wall, the rib-induced secondary flow cells adjacent to the bleed wall have almost diminished with its counter-rotating secondary flow cells to be enlarged in the entire test channel.

As the internal coolant channels rotate with the turbine rotor blade, the rotation manifesting effects interact with the modified flow structures triggered by bleeds to provide synergistic influences on the flow and heat transfer in a rotating channel with bleeds. The rotation induced Coriolis forces generate the secondary flows that interact with the rib triggered flows to produce a rich mode of secondary flow patterns in a rotating ribbed channel. The turbulence intensity is promoted on the unstable side but suppressed on the stable side of an orthogonally rotating channel with the spanwise roll cells generated as the relative strengths of Coriolis forces reach beyond the critical ratios [6]. The buoyancy-type alteration to the flow field driven by the centrifugal acceleration in

---

[1] Corresponding author.

Contributed by the Heat Transfer Division of ASME for publication in the Journal of Heat Transfer. Manuscript received January 7, 2007; final manuscript received August 17, 2007; published online April 22, 2008. Review conducted by Minking Chyu.

the order of up to 50,000 g considerably affects the cooling performance of the internal coolant channel in a gas turbine rotor blade [7]. However, the operating temperatures of a gas turbine rotor blade, the complex internal cooling configurations, as well as the extremely high rotational speed have combined to oppose the progress in acquiring the laboratory scale heat transfer data with a realistic simulation of engine conditions. Many previous studies for the turbine rotor blade cooling were confined to low Ro with simplified channel geometries. Studies in Refs. [8–18] focus on the geometrical parameters relevant to the cooling performance of a rotating channel that include the configuration of the rib floor, the channel orientation and cross-sectional shape, the type of surface roughness such as pin fin and dimple, and the multipass channels connected by 180 deg turns. Reductions of Reynolds number to elevate the rotational number also became a long term, but inadequate, approach for such laboratory scale experiments. This approach comprises the opportunity to stimulate the turbulence structures at the conditions of high Re ($\mathrm{Re} > 15{,}000$), which undermines the reflection of realistic rotational effects on turbulence structures for laboratory scale experiments. In general, the typical gas turbine engine speed falls in the range of 3000–20,000 rpm with the maximum Re of 100,000 for the internal coolant flow that gives the Ro range of 0–2 [19]. There is a strategic need to extend the experimental data in order to emulate more closely the realistic engine conditions by extending the ranges of Re and Ro simultaneously. A touch of the realistic engine conditions that simultaneously satisfy the conditions of $\mathrm{Re} \geqslant 10{,}000$ and $\mathrm{Ro} \geqslant 0.45$ are those studies preformed at high pressures [20–26]. To acquire such laboratory scale heat transfer data, with Re, Ro, and $\Delta\rho/\rho$ simultaneously reaching the engine conditions, the rotating tests are performed with large hydraulic diameters of test channels at high pressures. Our preliminary studies using this approach have acquired two sets of heat transfer data in the range of $\mathrm{Re} \times \mathrm{Ro} \leqslant 13{,}500$ and $\mathrm{Ro} \leqslant 1.8$ [25,26]. The present study adopts the similar experimental approach but elevates Re to the range of 15,000–30,000, which gives the rotation number up to 0.8. Although it has been a common practice to bleed a coolant on the apical side of the rotating trapezoidal duct at the trailing edge of a gas turbine rotor blade, there is no previously published heat transfer data from the rotating trapezoidal rib-roughened duct with bleeds on the apical side. In particular, the lack of heat transfer data obtained at high Re ($\mathrm{Re} > 15{,}000$) and high Ro ($\mathrm{Ro} > 0.5$) has been a long term problem for cooling applications to turbine rotor blades. The originality of the present work is to generate the heat transfer data at high Re ($15{,}000 \leqslant \mathrm{Re} \leqslant 30{,}000$) and high Ro ($0.1 \leqslant \mathrm{Re} \leqslant 0.8$) for a set of rotating trapezoidal rib-roughened ducts with and without air bleeds on the apical side. The parametric analysis based on local Nusselt number ratios between two rotating ducts with and without bleeds is also the first time presentation that reveals the influences of bleeds on heat transfer performances in the rotating trapezoidal duct fitted with 45 deg staggered ribs.

2 Experimental Details

2.1 Parameters in the Experimental Study. The heat transfer characteristic in a rotating channel is parametrically controlled by Reynolds (Re), rotation (Ro), and buoyancy (Bu) numbers that respectively quantify the relative strengths of forced convection, Coriolis secondary flows, and buoyancy effects in their own rights. The buoyancy number (Bu) in the dimensionless form of $\Delta\rho/\rho\,\mathrm{Ro}^2(R/d)$ quantifies the relative strength of the rotating buoyancy effect. This experimental study is aimed at disclosing the functional relationship of Eq. (1) for the present trapezoidal rotating duct with bleeds from its apical sidewall,

$$\mathrm{Nu} = \Psi\{\mathrm{Re}, \mathrm{Ro}, \mathrm{Bu}, X\} \tag{1}$$

The experimentally defined Nusselt number (Nu) in Eq. (1) is calculated as

$$\mathrm{Nu} = qd/[k(T_w - T_b)] \tag{2}$$

Determinations of q and T_b in Eq. (1) for this particular channel geometry with bleeds from the wall on the apical side draw precautions in the stages of test-channel design and data reduction. The convective heat flux q in Eq. (2) is obtained by subtracting the external heat loss from the total heat flux supplied. The extent and characteristics of the external heat loss are acquired by means of a series of static and rotating heat-loss calibration tests that are individually performed. Functional relationships between the external heat-loss flux and the wall-to-ambient temperature difference at five different rotational speeds are acquired. The equation that evaluates the local heat-loss flux is incorporated into the data processing program to account for the local convective heat flux (q) at each axial station where T_w is measured. For this class of experiment, the maximum heat loss is about 9.7% of the total heat flux supplied.

It is impractical to perform the direct measurement of fluid temperature (T_f) without disturbing the flow field in the test channel. In order to determine the fluid bulk temperature (T_b), the local enthalpy balance is accounted at each T_w measurement spot for the entire channel at the test conditions with no bleed. In the channel with bleeds, the coolant extractions from the discrete bleed holes along the channel axis reduce the mass flow rate of the coolant in a stepwise manner along the test channel. As the test results acquired from the channel without bleed indicate that the heat transfer distributions in the flow region after the seventh rib consistently resemble the so-called repeated Nu profiles, the present trapezoidal test channel is designed, with the first bleed commencing after the airflow traverses seven sets of staggered ribs. This developed flow assumption after the seventh rib in the trapezoidal ribbed channel enables the adoption of Eq. (3) to evaluate the axial gradient of T_b in the bleed section of the test channel using the axial gradient of T_f evaluated from the temperature measurements at the exits of bleed holes,

$$\partial T_b/\partial x \cong \partial T_f/\partial x \tag{3}$$

Having acquired the axial gradient of T_b approximated from Eq. (3), the fluid bulk temperatures in the bleed section of the test channel are accordingly evaluated. The process of T_b evaluations for the test channels with and without bleed is constantly checked by comparing the calculated fluid bulk temperature with the actual temperature measurement at the exit plane of the test channel. The measured T_b value at the exit plane of the test channel is obtained by averaging the temperature measurements at three different spanwise locations with an equal interval. Data batches are accepted when the differences between the calculated and measured T_b values are less than 8%. All the fluid properties required to define the dimensionless parameters in Eq. (1) are evaluated at the calculated T_b values.

With a predefined coolant mass flow rate ($\dot{m}$) for a specified Reynolds number, the reduction of mean flow velocity is attempted by increasing the pressure of airflow inside the rotating channel, which increases Ro and Bu accordingly. The channel pressure for all the static and rotational tests with and without bleeds is fixed at 2.5 bars, which fixes the channel-to-ambient pressure ratio at the value well above the pressure ratio for the choke flow through each bleed hole. This measure is attempted to obtain the fixed amount of coolant extraction from each bleed hole at each set of Re-Ro condition so that the airflow rate of total bleed extraction is basically controlled for both sets of static and rotational tests. The result of this attempt is demonstrated in Fig. 1, which depicts the variations of total coolant extraction in terms of $\dot{m}_{\mathrm{bleed}}$ and $\dot{m}_{\mathrm{bleed}}/\dot{m}$ versus Re in the static channel with bleeds. As shown in Fig. 1, the total coolant extraction ($\dot{m}_{\mathrm{bleed}}$) is approximately independent of Re for the present choked bleed flows at the condition of constant channel pressure. As the airflow rate fed into the test channel ($\dot{m}$) increases as Re increases, ratios of $\dot{m}_{\mathrm{bleed}}/\dot{m}$ decrease with the increase of Re. In the rotating channel,

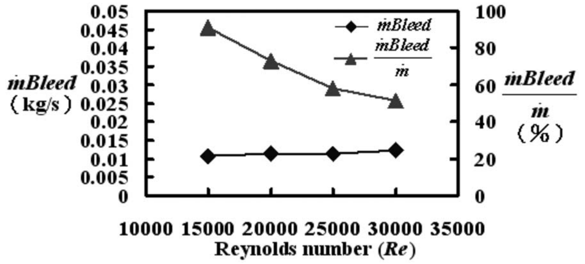

Fig. 1 Variations of the total coolant extraction ($\dot{m}_{\text{bleed}}$) and fraction ($\dot{m}_{\text{bleed}}/\dot{m}$) versus Re in the static channel with bleeds

the coolant extraction also operates at the choked condition, with the channel pressure fixed at the constant level the same as the pressure level inside the static channel. The data trends revealed in Fig. 1 are likely to be followed by that from a rotating channel with bleeds, which reassembles the basically uniform bleed condition. This uniform bleed condition is reconfirmed by measuring the pressure drops across the static test channels with bleeds at all the Re tested. The pressure drops across the rib-roughened duct fall in the range of 4.5–21 mm H_2O heights, so that the pressures inside the entire static and rotating channels with bleeds remain well above the critical levels for the choked nozzle condition. Heat transfer results generated from the present study using the channel with bleeds from the wall on apical side are subject to the bleed condition featured in Fig. 1. Table 1 summarizes the parametric ranges of experimental tests. The maximum Re and Ro in Table 1 are not simultaneously attainable. With the Re range of 15,000–30,000, the present Ro and Bu ranges are considerably extended from the past research experiences [7–18].

2.2 Experimental Setup. A detailed description of this rotating test rig as well as the instrumentation and data acquisition systems has been previously reported [25,26]. The rotating radius (R) from the center of rotation to the midspan of the test section is 247 mm, which is equivalent to 8.23 hydraulic diameters of the test channel. As the properties of coolant, such as viscosity and density, vary with the fluid temperature, the airflow rate entering the test section is constantly adjusted to compensate such temperature induced property variations, so that the variances, of Re and Ro at the flow entrance of the test section are controlled within ±1% of the targeting values.

The test module with airflow in the radially outward direction is depicted in Fig. 2. The test section itself is trapezoidal with a channel length of 340 mm and made up of leading (1) and trailing (2) Teflon walls, together with the apical (3) and bottom (4) Teflon sidewalls. The widths of the apical and bottom sidewalls are 10 mm and 30 mm, respectively. After seven pairs of skewed ribs from the flow entrance, five bleed holes with a diameter of 1.5 mm are sequentially positioned at the midrib locations along the centerline of the apical side wall, as indicated in Fig. 2. These bleed holes drill through the 5 mm thick apical side wall with the exit flow temperature to be measured by a thermocouple penetrating into each bleed passage (5) in the apical side wall (see Fig. 2). The leading, trailing, and side walls are physically held together by means of a series of axial bolts to form the trapezoidal-sectioned test channel with a hydraulic diameter (d) of 30 mm. Heat transfer measurements and electrical heating power are only provided over two opposite leading (6) and trailing (7) rib floors. Each of these two ribbed heating foils ((6) and (7)) are produced by forging a continuous 63 mm wide and 0.1 mm thick stainless-steel foil. The heating foil gives an active heating length of 340 mm. Periodical surface ribs with an attack angle of 45 deg are arranged in the staggered manner on two opposite leading and trailing walls. Geometric features of each rib floor are characterized by four dimensionless parameters: rib angle of attack $\alpha = 45$ deg, rib height e (3 mm)/channel hydraulic diameter d (30 mm)=0.1, rib pitch P (30 mm)/rib height e (3 mm)=10, and rib land 1 (3 mm)/rib height e (3 mm)=1.

Table 1 Range of experimental nondimensional parameters

Dimensionless parameter	Range
Reynolds number (Re)	15,000–30,000
Rotation number (Ro)	0–0.8
Buoyancy number (Bu)	0.16–1.54
Density ratio ($\Delta\rho/\rho$)	0.04–0.31

Tested Re at each rotation number

Ro	Re	Ro	Re
0.8	15,000	0.4	20,000, 25,000, 30,000
0.6	20,000	0.3, 0.2	15,000, 20,000, 25,000, 30,000
0.5	15,000, 20,000, 25,000	0.1	

Surface areas of all the skewed ribs are taken into account for the heating area as the realistic heat flux is evaluated. The high-current, low-voltage dc electrical power is connected in a series to heat two ribbed foils ((6) and (7)), which generates the basically uniform heat flux heating conditions on two opposite leading and trailing walls. The apical and bottom sidewalls of the trapezoidal test channel are thermally adiabatic. For the present test-section simulation, the distributions of heat flux over the top and two side surfaces of each skewed rib remain uniform.

The electrical heating power is supplied and adjusted with the power consumption measured by a wattmeter. Two rib-roughened heating foils ((6) and (7)) are clamped between the top and bottom Teflon flanges ((8) and (9)) in which two 3 mm thick copper plates sandwich the heating foils to complete the electrical circuit. Along the centerline of each leading or trailing rib floor, nine K-type thermocouples (10) with equal intervals are sparkle welded on the back of the stainless-steel heating foil ((6) and (7)) to measure the centerline wall temperatures. The coordinate system and the locations of these thermocouples with respect to the rib and midrib locations along the centerline of rib floor are indicated in Fig. 2. Although the peripheral temperature variations are expected due to a number of factors such as the bleeds on the apical side, the channel rotation, and the rib-induced secondary flows, this study is limited by the available channels of instrumentation slip-ring unit. As a result, the peripheral heat transfer variations over the rib floors are not investigated by the present study. It is also worth noting that the rotation angle of the present test configuration is 90 deg, which is not representative for the typical trailing edge cooling channel with a rotation angle of around 135 deg but features the asymmetric condition about the axial axis. The main objective of the present study is to reveal the influences of interactive Ro-Bu impacts upon the effects of bleeds on heat transfer for the rotating trapezoidal duct roughened by 45 deg ribs.

A cylindrical plenum chamber (16) consolidates with the bottom end flange (9) within which several layers of fine meshes (11) are installed. The complete set of the test section is tightened between the top and bottom flanges ((8) and (9)) by four draw bolts (12). A convergent channel of 150 mm length is fitted on the top end flange (8) where an exhaust valve (13) is attached at the exit end to adjust the pressure level inside the test section.

The fluid temperature at the flow entrance is measured by a type-K thermocouple (14) penetrating into the entry plenum chamber. The fluid properties required to evaluate Re and Ro when the heat transfer test is performed are calculated based on this measured air inlet temperature. The fluid temperature from each bleed hole (T_f) in Eq. (3) is detected by the thermocouple (5) penetrating into the core of each bleed passage. The local fluid bulk temperature (T_b) at each measurement station is accordingly defined using Eq. (3). At the exit plane of the test channel, three

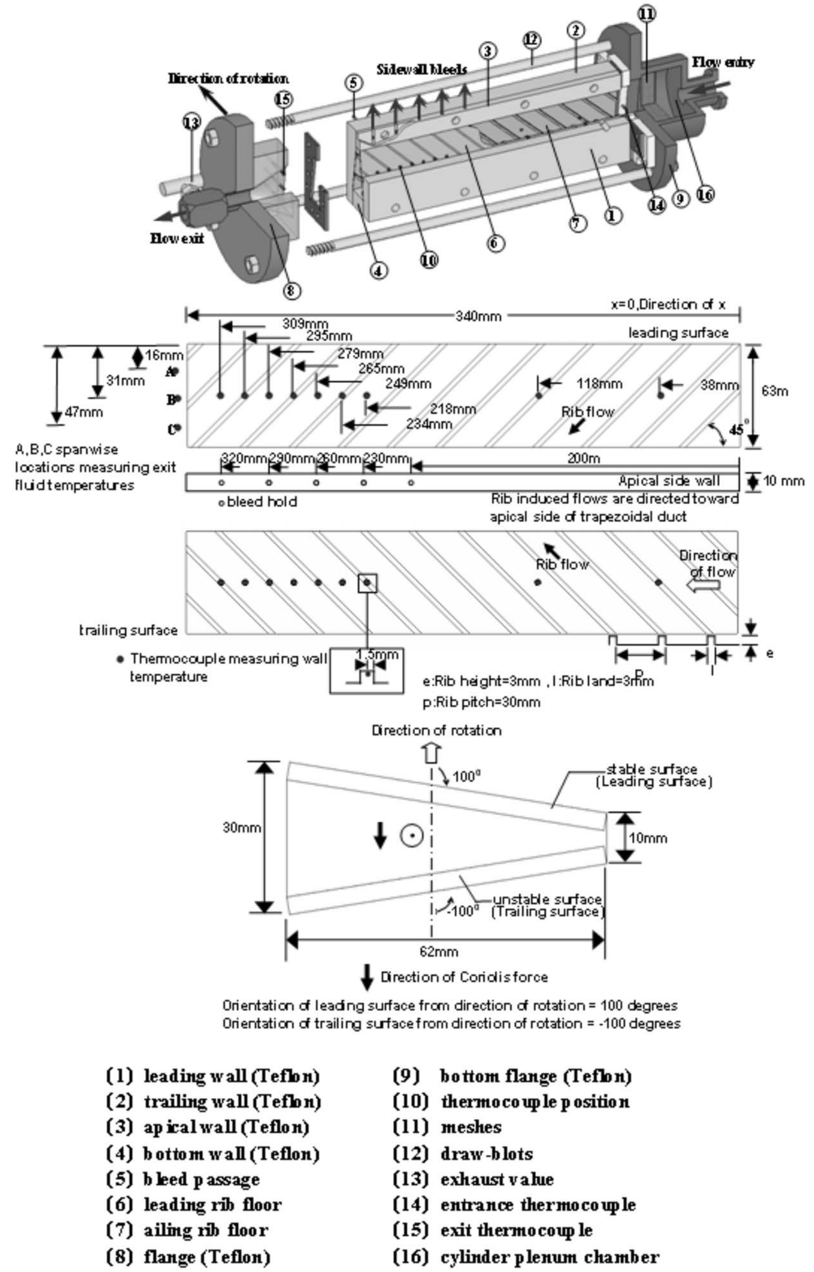

Fig. 2 Heat transfer test module

type-K thermocouples (15) penetrate into the test channel at three different spanwise locations, as indicated in Fig. 2. Depending on the parametric conditions examined, the ranges of variation shown in these three thermocouples at the exit of the test channel are about 10–30%.

2.3 Experimental Procedures. Initially, the static and rotating heat transfer tests for the channel without bleed are performed to generate the database against which the heat transfer results for the channel with bleeds are compared. To investigate the rotating buoyancy effect, four ascending heater powers to raise the highest T_w levels to 348 K, 373 K, 403 K, and 433 K are used for each selected Re-Ro combination. The dimensionless data generated in the phase of rotating experiments are analyzed to examine the influences of rotation on heat transfer for the channel with bleeds from the wall on the apical side. However, it is impractical to eliminate the influences of rotating buoyancy on heat transfer as the finite wall-to-fluid temperature difference is essential to experimentally define the Nusselt number. As a result, the experimental heat transfer results generated in the series of rotational tests involve certain degrees of buoyancy impacts. The so-called zero-buoyancy heat transfer data are therefore acquired by extrapolating the rotational heat transfer data into the limiting condition of $\mathrm{Bu}=0$. This regression procedure is attempted to define the heat transfer level without the buoyancy interaction, so that the analysis aimed at revealing the isolated Re and Ro effects without the buoyancy interaction is performed using this set of zero-buoyancy heat transfer data.

The majority of experimental uncertainties in calculating the dimensionless groups summarized in Eq. (1) are attributed from the temperature measurements as the fluid properties are estimated in accordance with the local T_b. Also indicated by the uncertainty analysis is the improved accuracy for the tests with the higher heater flux and Reynolds number that result in the larger wall-to-fluid temperature differences. Based on the method of estimating the experimental uncertainty recommended by the editorial board of ASME J. Heat Transfer [27], with the wall-to-fluid bulk temperature differences varying in the range of 37–68 K, the maximum uncertainties for Nu, Re, Ro, and Bu are about 9.8%, 7.6%, 4.1%, and 5.8%, respectively.

3 Results and Discussion

3.1 Heat Transfer at Static Conditions. At zero rotational speed, the acquired wall temperature distributions along two opposite centerlines of leading and trailing rib floors with and without bleeds do not exhibit significant differences but only reflect the differences between the rib and midrib locations due to the rib-induced flow phenomena. The successive bleeds along the apical sidewall reduce the local airflow rate in a stepwise manner when the bulk flow travels along the bleed section. As a result, the axial gradients of T_w and T_b over the bleed section are increased from the counterpart levels in the channel without bleed. Axial T_w profiles in the region after the seventh rib exhibit streamwise zigzag patterns with the lower wall temperatures developed at the rib locations relative to its adjacent downstream midrib spots. As the heating condition over each rib floor corresponds closely to the uniform heat flux, the axial distributions of T_b in the channel without bleed and between two successive bleed holes rise linearly. The axial Nu_0 variation after the airflow traverses seven pairs of skewed ribs shows the mirror image of the zigzag T_w pattern with the higher heat transfer rate at the rib location. This is demonstrated in Fig. 3 where the axial distributions of T_w, T_b, and $\mathrm{Nu}_0/\mathrm{Nu}_\infty$ in the channels with and without bleeds are compared at the Reynolds number of 25,000 with the nominal heat flux of 5000 W m^{-2}. By way of normalizing Nu_0 with the Dittus–Boelter Nusselt number (Nu_∞) [28], the heat transfer enhancement from the smooth-walled tube level is highlighted. The cross examinations of Figs. 3(*a*) and 3(*b*) and Figs. 3(*c*) and 3(*d*) reveal the impacts of bleeds on the axial distributions of T_w and $\mathrm{Nu}_0/\mathrm{Nu}_\infty$, respectively. It is consistently followed by all the static heat transfer results, as typified in Fig. 3, that the reduced $\mathrm{Nu}_0/\mathrm{Nu}_\infty$ ratios are accompanied with the increased T_w levels in the section with bleeds. Unlike the flow scenarios developed in the channels with bleeds from the rib floor [1–4], the present sidewall extractions can neither bleed off the boundary layers over the rib floor nor reduce the extent of flow separation behind each rib. The favorable mechanisms due to the bleeds from the rib floor are absent in the present channel with bleeds on the apical side. However, the strengths of secondary flows induced by the skewed ribs and the downstream flow momentum are likely to be weakened in the static channel due to the bleeds on the apical side. Therefore, at the comparable conditions defined in Fig. 3 for the two static channels with and without bleeds, the increased T_w levels over the bleed section are produced by the twofold impacts of the decreased heat transfer rate and the reduced local airflow rate that need design precautions.

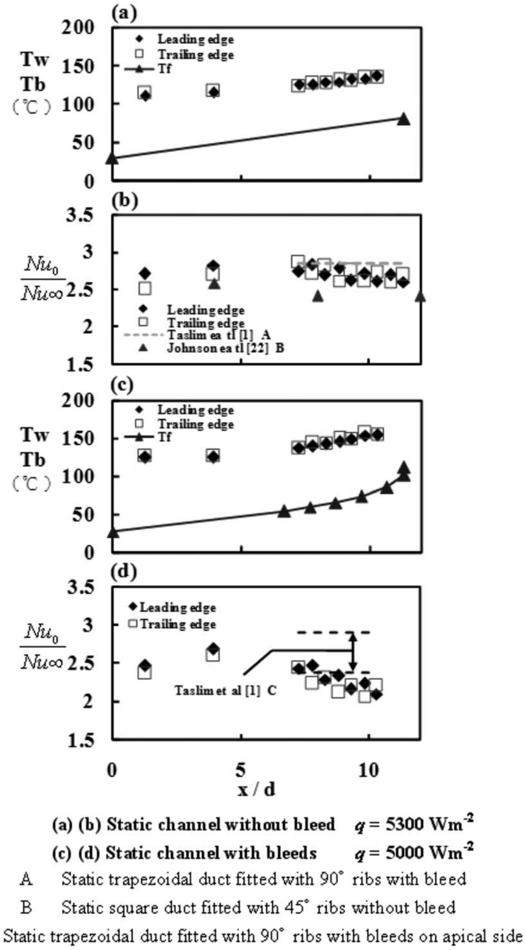

Fig. 3 Axial distributions of T_w, T_b, and $\mathrm{Nu}_0/\mathrm{Nu}_\infty$ in the static channels with and without bleeds at a Reynolds number of 25,000

Also shown in Figs. 3(*b*) and 3(*c*) are the results of Taslim et al. [1] and Johnson et al. [22], which respectively investigate the heat transfer in the static trapezoidal duct roughened by 90 deg ribs with and without bleed on the apical side [1] and in the square sectioned serpentine passages roughened by 45 deg ribs with and without rotation [22]. With Re=25,000, the spatially averaged Nusselt numbers reported in Ref. [1] are normalized by the Dittus–Boelter correlation [27], as indicated by the dashed lines in Figs. 3(*b*) and 3(*d*), while the local Nu_0 values collected from Ref. [22] are divided by $0.0176\mathrm{Re}^{0.8}$, seen as the data points in Figs. 3(*b*) and 4(*b*), in order to match their boundary conditions. As seen in Fig. 3(*b*), the selection of heat transfer data compared in the developed flow region falls in a similar range. The heat transfer levels in the two sets of trapezoidal rib-roughened ducts generated from the present study and from Taslim et al. [1] are slightly higher than those in the square-sectioned passage roughened by 45 deg ribs [22]. In the trapezoidal rib-roughened ducts, the present $\mathrm{Nu}_0/\mathrm{Nu}_\infty$ distributions shown in Fig. 3(*d*) decline in the axial direction that are generally higher than the results reported in Ref. [1]. It is noticed that the present bleeding airflows operate at the choked conditions, which provide bleeding ratios higher than those controlled by Taslim et al. [1] at the unchoked conditions. Therefore, the present data trends displayed in Fig. 3(*d*) decline axially and fall below the data range reported in Ref. [1] due to the high bleeding ratio ($\dot{m}_{\mathrm{bleed}}/\dot{m}$) of about 56% at Re=25,000 (see Fig. 1). Nevertheless, justified by the similar cited range of data points from three different research groups as compared in Fig. 3(*b*), the agreements of present heat transfer data with previous investigations are satisfactory.

As typified in Fig. 3(*b*), the tendency for the so-called zigzag *repeated-rib-type* $\mathrm{Nu}_0/\mathrm{Nu}_\infty$ variation takes place after the seventh rib in the channel without bleed. In the section with bleeds on the apical side, the axial heat transfer variations along two opposite centerlines also follow the zigzag pattern but display an *overall declination*, as shown in Fig. 3(*d*). The so-called repeated rib flow region is not observed in the bleed section of the present ribbed channel at zero rotational speed. In the static ribbed channel, the extent of data scatters at each x/d location driven by varying the $\Delta\rho/\rho$ value in the present test range is small, which indicates the negligible buoyancy impact. Over the Re ranges of 15,000–30,000, the $\mathrm{Nu}_0/\mathrm{Nu}_\infty$ ratios vary in the range of 3.7–2.8, which

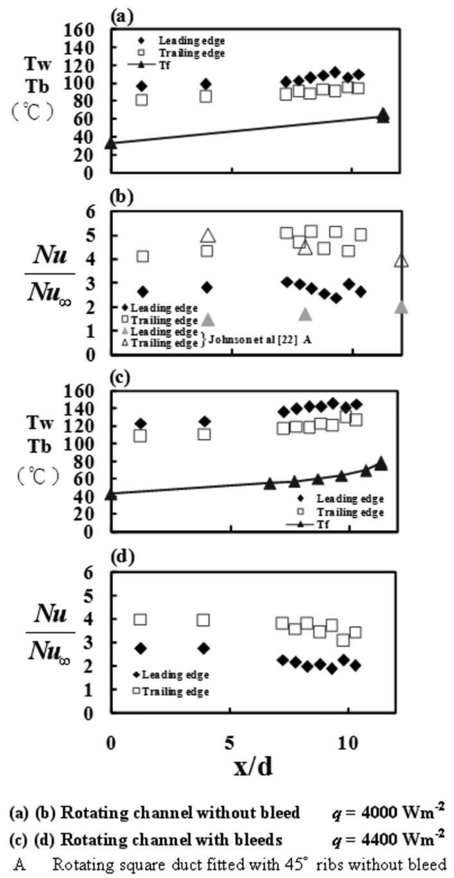

Fig. 4 Axial distributions of T_w, T_b, and $\mathrm{Nu}/\mathrm{Nu}_\infty$ along leading and trailing edges at Re=25,000 and Ro=0.3 for two rotating channels with and without bleed

fall systematically as Re increases. For the static channels with and without bleeds, the Nu_0 versus Re relationships at the rib and midrib locations are individually analyzed using Eq. (4).

$$\mathrm{Nu}_0 = A(x/d) \times \mathrm{Re}^{n(x/d)} \tag{4}$$

Coefficients A and n vary with the axial location (x/d) for both test channels to reflect the effects of ribs, bleeds, and boundary layer developments on heat transfer. Table 2 summarizes the values of A and n along the centerlines of leading and trailing rib floors.

In the Re range of 15,000–30,000, heat transfer enhancements generated by the present rib floors fall in the range of 2.8–3.4 and 3.7–4 times of Nu_∞ levels [28] for the test channels with and without bleed, respectively. Bleeds on the apical side undermine the overall heat transfer performances from the no-bleed references to the extents of 96–50%, which decrease as Re increases. Ratios of $\mathrm{Nu}_0/\mathrm{Nu}_\infty$ in the present no-bleed channel generally agree with the cited ranges reported for the channels with 45 deg ribs [8,22]. Heat transfer results acquired by the present study are deemed to be verified so that the two sets of Nu_0 correlations are taken as the references for assessing the rotational effect on heat transfer for the present channel configurations.

3.2 Heat Transfer at Rotating Conditions.

With rotating radially outward flows, leading-edge wall temperatures constantly operate at higher levels compared to on trailing wall temperatures at any Re-Ro combination. This result assures the generation of Coriolis secondary flows even if the agitated rib flows prevail over the rotating ribbed channel. Figure 4 depicts the axial distributions of T_w, T_b, and $\mathrm{Nu}/\mathrm{Nu}_\infty$ along the centerlines of leading and trailing rib floors at Re=25,000 and Ro=0.3 for two rotating channels with and without bleed, which are both subject to the nominal heat flux of 4000 W m^{-2}. Heat transfer results reported in Ref. [22] for the rotating square passage fitted with 45 deg staggered ribs at the same Re and Ro are comparable with present rotational heat transfer data shown in Fig. 4(*b*), which reveal the influences of the cross-sectional shape of the rotating channel on heat transfer. Coriolis-force effects create the leading-to-trailing T_w differences that result in the higher local Nusselt numbers along the centerline of the trailing wall relative to its leading counterparts for both rotating trapezoidal and square channels. The trailing edge heat transfer levels along the centerline of the present trapezoidal duct depicted in Fig. 4(*b*) are in close agreement with those in the square-sectioned passage. However, the leading-edge heat transfer levels in the trapezoidal duct are generally higher than those in the square-sectioned passage. As the rib-floor configurations between the present study and the study of Johnson et al. [22] are identical and the close agreements in static heat transfer results have been demonstrated in Fig. 3(*b*), such different heat transfer performances along the leading centerline, as shown in Fig. 4(*b*), are caused by the different cross-sectional shapes of these rotating channels.

The influences of bleeds on the axial distributions of T_w, T_b, and $\mathrm{Nu}/\mathrm{Nu}_\infty$ over the bleed section of the rotating channel, as indicated in Figs. 4(*c*) and 4(*d*), generally follow the static results

Table 2 Coefficients *A* and *n* for Nu_0

Location	No-bleed channel				Bleed channel			
	Leading		Trailing		Leading		Trailing	
x/d	A	n	A	n	A	n	A	n
1.3[a]	0.0667	0.8	0.0777	0.78	0.0595	0.81	0.0853	0.77
3.9[a]	0.106	0.76	0.0123	0.74	0.0975	0.76	0.105	0.75
	Rib		Midrib		Rib		Midrib	
7.3[c]	0.542	0.6	0.836	0.55	0.796	0.54	0.509	0.59
7.8 and 8.3[d]	0.542	0.6	0.836	0.55	0.588	0.57	0.829	0.53
8.8 and 9.3[e]	0.542	0.6	0.836	0.55	0.685	0.55	0.875	0.52
9.8 and 10.3[f]	0.542	0.6	0.836	0.55	0.797	0.53	1.01	0.5

[a] x/d=1.3 (rib 1 and midrib 1-2).
[b] x/d=3.9 (rib 4 and midrib 3-4).
[c] x/d=7.3 (rib 8 and midrib 7-8).
[d] x/d=7.8 and 8.3 (rib 9 and midrib 8-9).
[e] x/d=8.8 and 9.3 (rib 10 and midrib 9-10).
[f] x/d=9.8 and 10.3 (rib 11 and midrib 10-11).

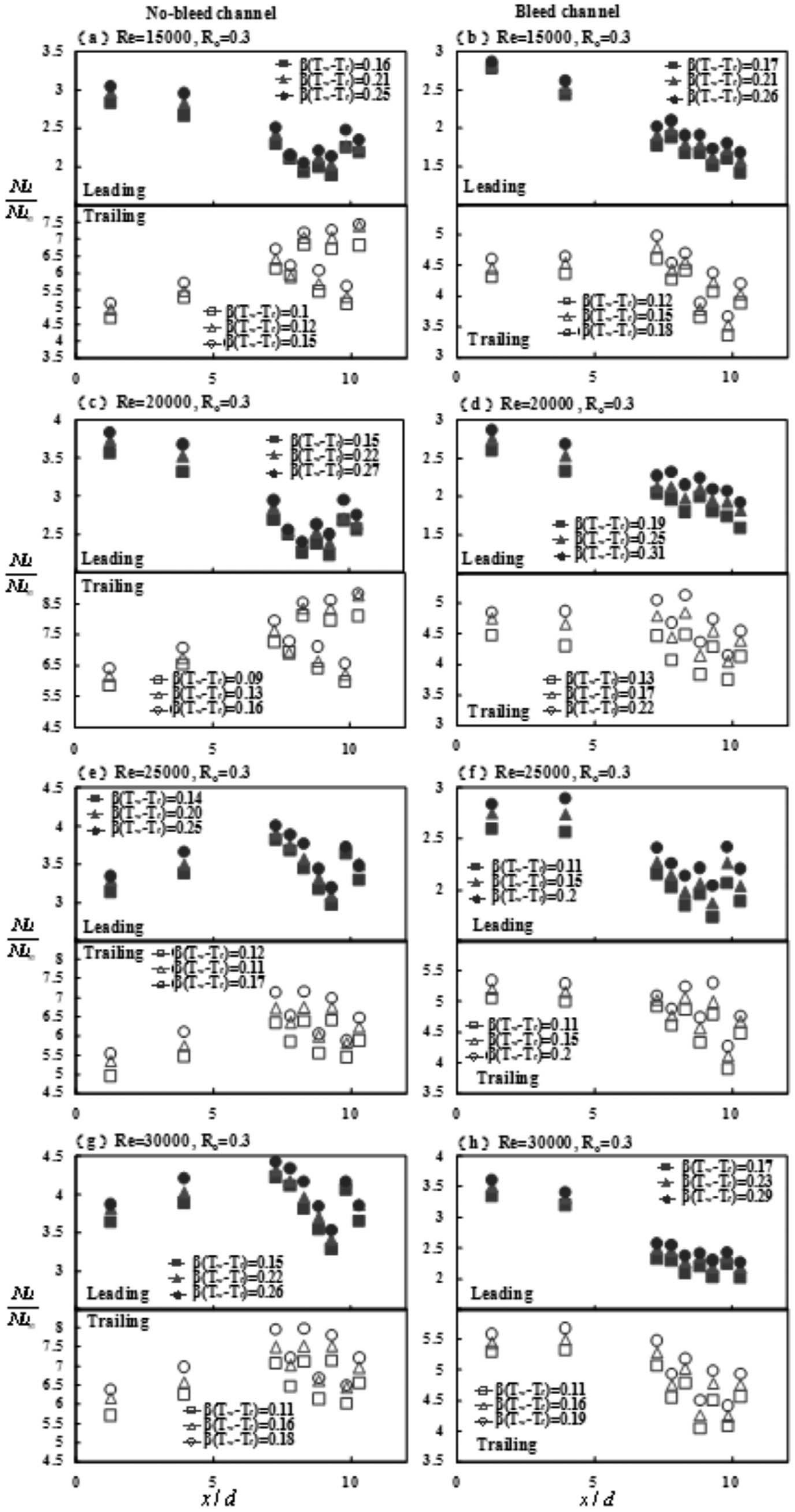

Fig. 5 Axial distributions of Nu/Nu_∞ ratios along leading and trailing centerlines with Re=15,000, 20,000, 25,000, and 30,000 at a rotation number of 0.3 for the rotating channels with and without bleed

demonstrated in Figs. 3(*c*) and 3(*d*). However, the extents of bleed impact on the axial distributions of T_w and $\mathrm{Nu}/\mathrm{Nu}_\infty$ are different between the leading and trailing walls in the rotating channel. As the considerable axial decreases of $\mathrm{Nu}/\mathrm{Nu}_\infty$ ratios still persist over the bleed section along the leading and trailing walls (see Fig. 4(*d*)), the bleeds on the apical side can still affect the vortical structures over two opposite rib floors even if the Coriolis secondary flows are predominant in the rotating channel.

Figure 5 displays the axial distributions of $\mathrm{Nu}/\mathrm{Nu}_\infty$ ratios along the centerlines of leading and trailing walls with Re=15,000, 20,000, 25,000, and 30,000 at a fixed rotation number of 0.3 for the rotating channels with and without bleed. At each Re examined, as shown in each plot of Fig. 5, three sets of distinguishable axial heat transfer distributions driven by three buoyancy levels along the leading or the trailing edge demonstrate the persistent rotating buoyancy effect on heat transfer. The upward $\mathrm{Nu}/\mathrm{Nu}_\infty$ trend driven by increasing $\Delta\rho/\rho$ ratio at each measurement station suggests that the rotating buoyancy effect in isolation improves local heat transfer for both rotating channels. For all the Re tested at each selected rotation number, as exemplified in Fig. 5, data bands driven by varying the $\Delta\rho/\rho$ ratio consistently show the wider range along the leading centerline relative to its trailing-edge result. The stronger rotating buoyancy impacts on heat transfer develop along the leading edge. Clear evidences of relatively high heat transfer levels along the trailing edge to its leading counterparts are reconfirmed for all the rotational results depicted in Fig. 5. In addition to such Coriolis-force manifesting effects, the bleeds on the apical side reduce heat transfer levels along both leading and trailing centerlines from the no-bleed references with predominant impacts on the trailing-edge heat transfer that incur considerable axial heat transfer decays in the bleed section. For the entire test conditions, the $\mathrm{Nu}/\mathrm{Nu}_\infty$ ratios for the rotating ribbed channels with and without bleeds respectively fall in the ranges of 1–3 and 3–5 as the combined effects of Re, Ro, and Bu.

As a major contribution of the present work to this technical community, the influences of bleeds on the apical side of the rotating trapezoidal duct fitted with 45 deg staggered ribs on two bevel walls are parametrically analyzed. Such influences are highlighted by comparing the local Nu measurements between the rotating channels with bleeds ($\mathrm{Nu}_{\mathrm{bleed}}$) and without bleed ($\mathrm{Nu}_{\mathrm{no\ bleed}}$) along the leading and trailing centerlines over the bleed section. Figure 6 displays the axial variations of $\mathrm{Nu}_{\mathrm{bleed}}/\mathrm{Nu}_{\mathrm{no\ bleed}}$ along the leading (a) and trailing (b) edges at Ro=0, 0.1, 0.4, and 0.6 with the nominal Re and density ratio $[\Delta\rho/\rho=\beta(T_w-T_b)]$ of 20,000 and 0.14. As the heat transfer results in static conditions described previously, the lack of heat transfer augmentation mechanism from the scenario with bleeds on the rib floor along with the accumulated losses of airflow rate inside the trapezoidal ribbed duct by extracting the coolant on the apical side result in the streamwise declination of Nu_0 from the no-bleed condition. Such heat transfer impediment due to bleeds on the apical side is followed by all the rotational data trends obtained with Ro=0.1, 0.4, and 0.6, as seen in Fig. 6. With Ro =0, the ratios of $\mathrm{Nu}_{\mathrm{bleed}}/\mathrm{Nu}_{\mathrm{no\ bleed}}$ fall from 0.85 at the first bleed hole to about 0.8 at the fifth bleed hole. Further increases of Ro from 0 to 0.6 systematically reduce the ratios of $\mathrm{Nu}_{\mathrm{bleed}}/\mathrm{Nu}_{\mathrm{no\ bleed}}$ along both leading and trailing centerlines to 0.7 to 0.6 (leading) and 0.68 to 0.48 (trailing) at the first and fifth bleed holes, respectively, as Ro=0.6. This particular result typified in Fig. 6 at Re =20,000 with the bleed ratio ($\dot{m}_{\mathrm{bleed}}/\dot{m}$) of about 70% (see Fig. 1) demonstrates that the impeding heat transfer effects due to bleeds on the apical side are amplified by the combined Ro-Bu impacts that lead to further heat transfer reductions. The orthogonal rotation of present trapezoidal duct worsens the impairing heat transfer impacts due to bleeds on the apical side. Within the Ro range of 0.1–0.8, bleeds on the apical side produce 25–50% and 25–40% of heat transfer reductions from the no-bleed references along the leading and trailing centerlines, respectively. Such further heat transfer reductions due to the increase of Ro, as demonstrated in Fig. 6, are worthy of precautions in the design stage of turbine rotor blades.

(a) Leading edge , βΔT=0.14

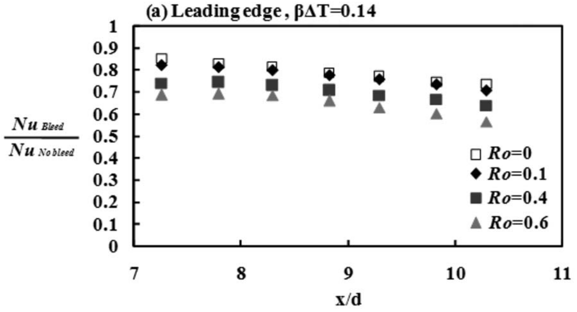

(b) Trailing edge , βΔT=0.14

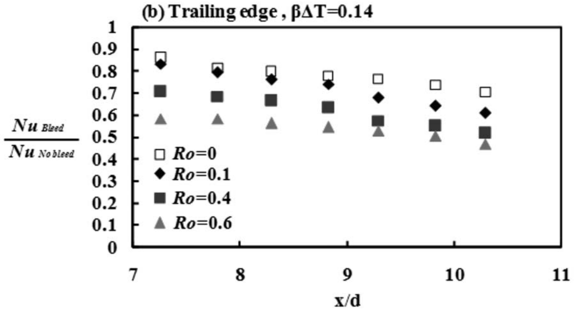

Fig. 6 Axial distributions of $\mathrm{Nu}_{\mathrm{bleed}}/\mathrm{Nu}_{\mathrm{no\ bleed}}$ along (*a*) leading and (*b*) trailing edges of the bleed section at Ro=0, 0.1, 0.4, and 0.6 with nominal Re and $\beta(T_w-T_b)$ of 20,000 and 0.14

3.3 Parametric Study and Data-Fitted Correlations. By way of comparison with the static Nusselt number (Nu_0), the rotational heat transfer data are expressed as the Nusselt number ratio ($\mathrm{Nu}/\mathrm{Nu}_0$), which indexes the rotation induced heat transfer variation from the static reference. As Nu_0 is defined by Eq. (4), which involves the functional component of Re^n, the expression of the $\mathrm{Nu}/\mathrm{Nu}_0$ ratio is attempted to isolate the Re effect from the Ro-Bu impacts via the Re^n relationship. This is testified by comparing the axial distributions of the $\mathrm{Nu}/\mathrm{Nu}_0$ ratio obtained at a fixed rotation number but with different Reynolds numbers of 15,000, 20,000, 25,000, and 30,000. The convergence of different $\mathrm{Nu}/\mathrm{Nu}_0$ ratios obtained from different Reynolds numbers at each measurement station with a fixed rotation number verifies the applicability of isolating Re impacts from the rotational influences via the Re^n relationship. This is demonstrated in Fig. 7 in which the axial distributions of the $\mathrm{Nu}/\mathrm{Nu}_0$ ratio along the leading and trailing edges of the bleed channel with four different Re at the fixed rotation number of 0.1, 0.2, 0.3, 0.4, or 0.5 are compared. The averaged density ratio ($\Delta\rho/\rho$) along the leading or trailing centerline is selected at a nominal value of 0.21 for each four sets of data trend, as shown in Fig. 7. Giving the satisfactory data convergence for each selected rotation number at each axial station, the isolation of Re impacts from the rotation manifesting mechanisms via the Re^n relationship seems to be acceptable. The ratios of $\mathrm{Nu}/\mathrm{Nu}_0$ are constantly above unity along the trailing centerline. The $\mathrm{Nu}/\mathrm{Nu}_0$ ratio can fall to 0.42 at the rotation number of 0.2, which features the worst heat transfer scenario even if the rotating buoyancy effect appears to enhance local heat transfer. Nevertheless, the heat transfer results collected from the rotating channel with bleeds are subject to the modified flow structures triggered by the coolant extractions that reduce the downstream airflow rate in the accumulative manner. The subsequent parametric analysis is therefore individually performed for each measurement location in the bleed section.

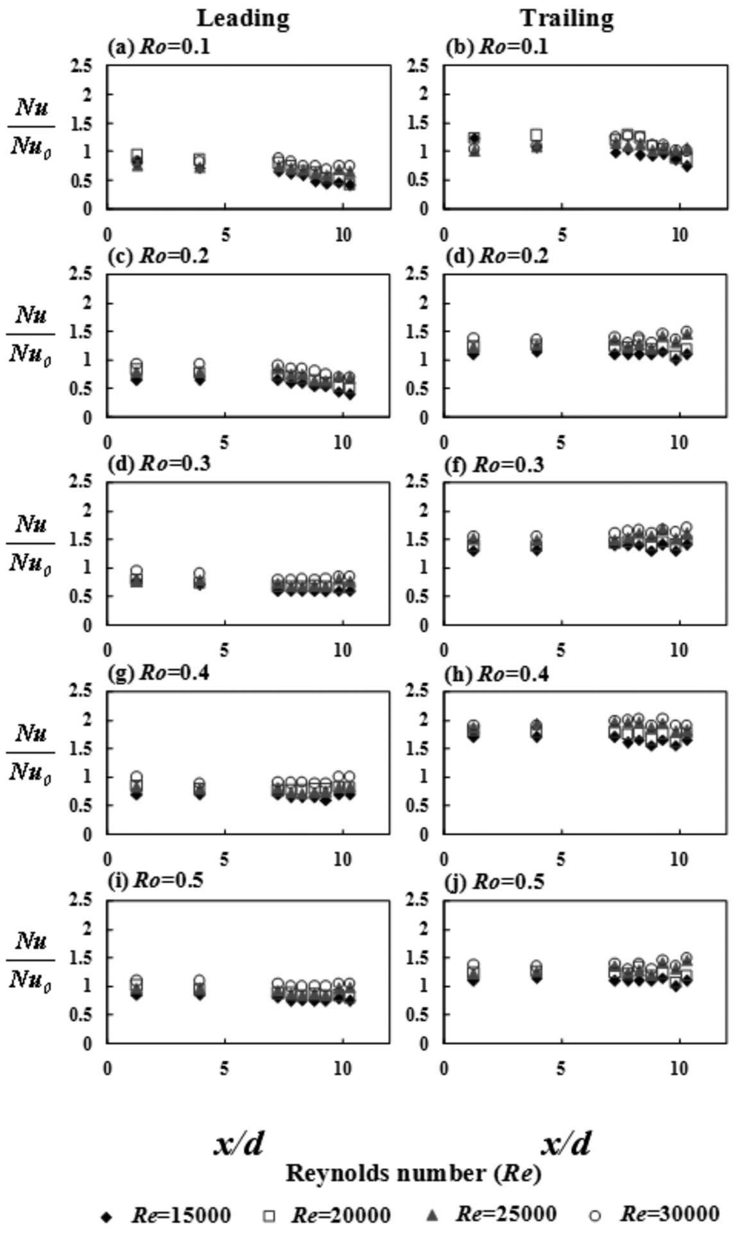

Fig. 7 Axial distributions of the $\mathrm{Nu}/\mathrm{Nu}_0$ ratio along leading and trailing centerlines of the bleed channel with Re=15,000, 20,000, 25,000, and 30,000 at rotation numbers of 0.1, 0.2, 0.3, 0.4, and 0.5

The heat transfer data at the limiting case of $\beta(T_w-T_b)=0$ but $\mathrm{Ro}\neq 0$, which simulates the condition of zero buoyancy in a rotating channel, are generated from the regression analysis. For a set of predefined geometric configurations, the plot of the $\mathrm{Nu}/\mathrm{Nu}_0$ ratio against $\mathrm{Ro}^2\,\beta(T_w-T_b)(R/d)$ is a meaningful way to unravel the rotating buoyancy effect. The regression-type curve fitting for each series of data trend obtained with different Reynolds numbers but at a fixed rotation number leads to the limiting heat transfer solution at zero $\beta(T_w-T_b)$. This process is illustrated in Fig. 8, which produces the rotational zero-buoyancy heat transfer data after extrapolating a series of $\mathrm{Nu}/\mathrm{Nu}_0$ ratios collected from a fixed Ro toward the asymptotic value corresponding to zero Bu. As the converged linearlike increase of the $\mathrm{Nu}/\mathrm{Nu}_0$ ratio driven by the increase of Bu is evident for each Ro controlled data series displayed in Fig. 8, the rotational heat transfer data at each measurement location in the flow region with bleeds on the apical side is correlated by the equation of

$$\frac{\mathrm{Nu}_{L,T}}{\mathrm{Nu}_0}=\phi_1\{\mathrm{Ro},x/d\}+\phi_2\{\mathrm{Ro},x/d\}\times \mathrm{Ro}^2\,\beta(T_w-T_b)(R/d) \quad (5)$$

In Eq. (5), ϕ_1 and ϕ_2 are functions of Ro and the axial location, which absorb the influences of bleeds on heat transfer. While the magnitudes of ϕ_2 functions, which represent the various slopes of the correlating lines shown in Fig. 8, reflect the degrees of rotating buoyancy impact on heat transfer, the functional values of ϕ_1 at various rotation numbers account for the rotational zero-buoyancy heat transfer levels. The plot of the ϕ_1 value against Ro reveals the isolated Ro impacts on local heat transfer without any buoyancy interaction.

Figure 9 typifies the varying manners of the so-called zero-buoyancy heat transfer data against Ro on two opposite rotating rib floors at the axial locations in the section with bleeds on the apical side. Acting by the Coriolis-force effect alone, heat transfer differences between leading and trailing edges increase with the

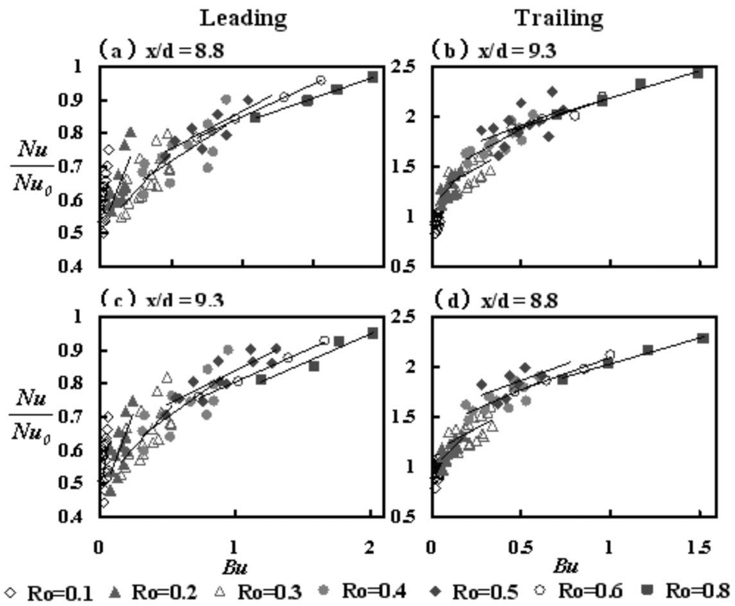

Fig. 8 Variations of the $\mathrm{Nu}/\mathrm{Nu}_0$ ratio against Bu at fixed rotation numbers

increase of Ro due to the growing strength of Coriolis secondary flows. Also compared in each individual plot of Fig. 9 are the extrapolated $\mathrm{Nu}/\mathrm{Nu}_0$ ratios at the zero-buoyancy conditions for the present rotating channel without bleed. It is constantly shown in Fig. 9 that the $\mathrm{Nu}/\mathrm{Nu}_0$ ratios along the leading and trailing centerlines of two rotating channels with and without bleed follow a similar track. Trailing edge heat transfer levels consistently increase with the increase of Ro. Leading-edge heat transfer levels are initially reduced but turned to be recovered as Ro increases from 0 to 0.8 for both rotating channels with and without bleeds. In this respect, the worst heat transfer scenarios develop at the rotation number of 0.2 for all the axial locations along the leading centerline over the bleed section. With such worst heat transfer scenarios, the leading-edge $\mathrm{Nu}/\mathrm{Nu}_0$ ratios fall in the range of 0.4–0.45 over the bleed section of the present rotating channel.

Figure 10 examines the degrees of rotating buoyancy effects on heat transfer by plotting ϕ_2 values against Ro where the results acquired from the rotating channels with and without bleed are compared. Within the parametric range of $0.1 < \mathrm{Ro} < 0.8$, the general data trend that shows that ϕ_2 values decrease as Ro increases is followed by all the data series at each axial station along the leading and trailing centerlines for both rotating channels with and without bleeds. The ϕ_2 values in the rotating channel with bleeds on the apical side are considerably less than the no-bleed references as compared in each plot of Fig. 10. The physical implication of this result is the weakened rotating buoyancy effects on heat transfer due to the bleeds on the apical side. Although the ϕ_2 values always remain positive in the range of $0.1 < \mathrm{Ro} < 0.8$ for both rotating channels, which reconfirms the improved local heat transfer by enhancing the relative strength of rotating buoyancy in isolation, the reduction of ϕ_2 values as Ro increases signifies the weakened heat transfer enhancement attributed from the buoyancy interaction. It is evident that ϕ_2 values are functions of Ro. The existence of coupling effects between Coriolis force and rotational buoyancy is assured.

In the Ro range from 0.1 to 0.8, the zero-buoyancy heat transfer levels in terms of $\mathrm{Nu}/\mathrm{Nu}_0$ ratios along both leading and trailing centerlines can be well correlated by linear functions, as shown in Fig. 9. Evidences of this correlation process are typified in Fig. 9

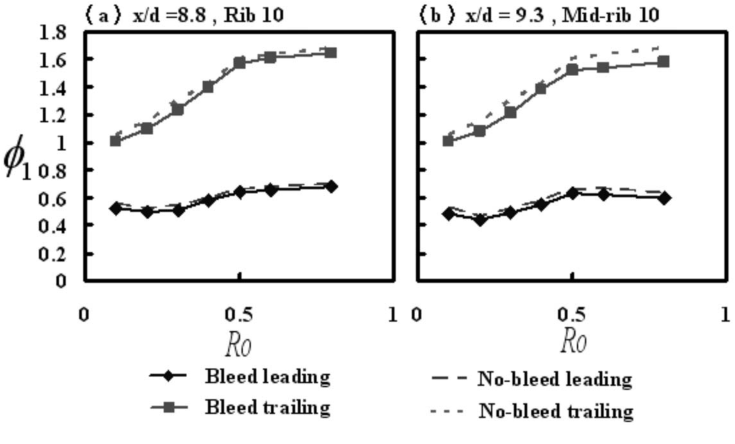

Fig. 9 Variations of the zero-buoyancy heat transfer data against Ro at axial locations in the bleed section

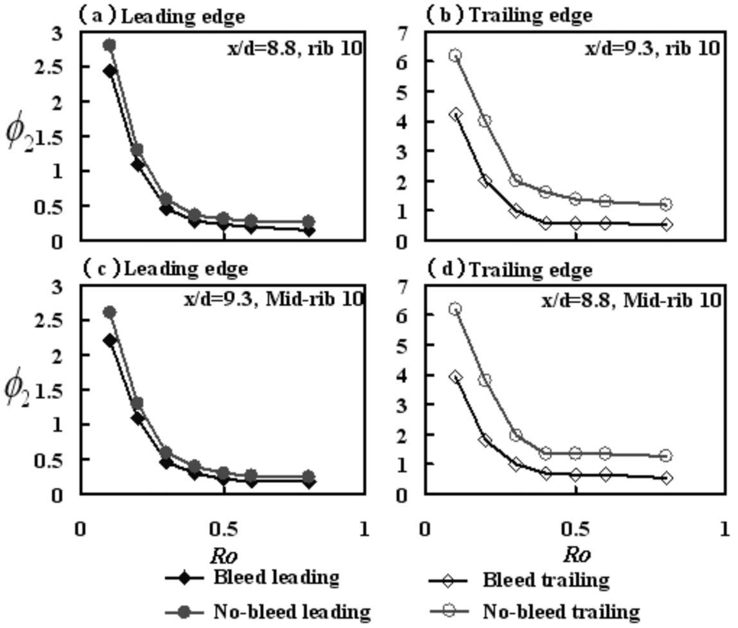

Fig. 10 Variations of the ϕ_2 value against Ro for rotating channels with and without bleed

where the lines shown are the regressive curves of the evaluated zero-buoyancy heat transfer data. Varying manners of ϕ_2 values against Ro are shown in Fig. 10, which follow the general trend of exponential decay for both leading and trailing walls. In combination with the regression results depicted in Figs. 9 and 10, the heat transfer correlations at the measurement stations in the bleed section of the present rotating channel along the leading and trailing centerlines are derived with the functional structure of

$$\mathrm{Nu}/\mathrm{Nu}_0 = (a_1 + a_2 \times \exp(a_3 \times \mathrm{Ro})) + [a_4 + a_5 \times \exp(a_6 \times \mathrm{Ro})]\beta(T_w - T_b)(R/d) \times \mathrm{Ro}^2 \qquad (6)$$

Coefficients a_s in Eq. (6) for the axial locations in the bleed section of the present rotating channel are summarized in Table 3.

The comparison of all the experimental measurements with the correlative predictions from Eqs. (4) and (6) is performed to examine the overall success of the present experimental proposal. Over the entire range of parametric conditions examined, 95% of the present experimental data is found to agree within +30% of the correlation proposed. This is demonstrated in Fig. 11 where the experimental measurements and the correlative evaluations are compared. Consider the complexities induced by the surface ribs, bleeds on the apical side, Coriolis force, and rotating buoyancy. This set of heat transfer correlation can offer a more realistic reference for the design of internal cooling passages in a gas turbine rotor blade with bleeds on the apical side. As shown in Fig. 11, which reviews the entire set of rotational heat transfer results,

Table 3 Correlative coefficients a_s for $\mathrm{Nu}/\mathrm{Nu}_0$

Location x/d	Leading edge					
	a_1	a_2	a_3	a_4	a_5	a_6
7.3	0	0.613	0.1503	0.18	10.9	−12.6
7.8	0	0.5475	0.2983	0.211	9.26	−12.4
8.3	0	0.54	0.3857	0.1191	7.76	−10.1
8.8	0	0.4711	0.4947	0.1541	5.84	−9.41
9.3	0	0.4451	0.4689	0.147	4.89	−8.59
9.8	0	0.4865	0.5608	0.233	11.6	−15.4
10.3	0	0.4511	0.631	0.109	1.94	−5.3

Location x/d	Trailing edge					
	a_1	a_2	a_3	a_4	a_5	a_6
7.3	1.69	−1.04	−3.7	0.35	4.27	−6.32
7.8	1.84	−1.11	−2.52	0.404	5.46	−7.83
8.3	1.85	−1.14	−2.69	0.369	2.44	−4.56
8.8	1.88	−1.07	−1.78	0.533	9.04	−9.77
9.3	1.92	−1.177	−2.05	0.575	9.59	−9.56
9.8	1.77	−0.963	−1.71	0.682	3.57	−8.09
10.3	2.62	−1.84	−1.11	0.533	5.04	−7.6

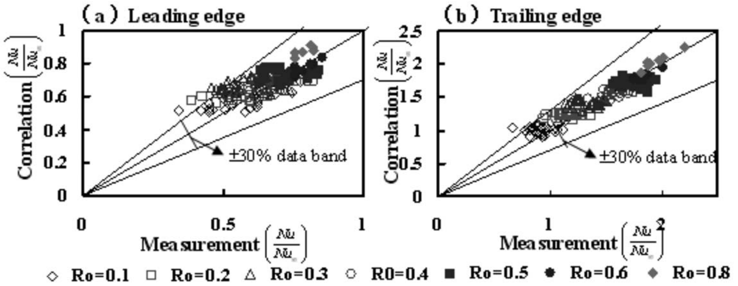

Fig. 11 Comparison of experimental measurements and correlative evaluations of Nu/Nu_0.

the local Nusselt number ratios of Nu/Nu_0 are respectively in the ranges of 0.5–0.9 and 1–2.3 along the centerlines of leading and trailing rib floors over the bleed section. Nevertheless, extrapolations of Eqs. (4) and (6) beyond the present parametric ranges can usually give rise to uncertainties.

4 Conclusions

This experimental study compares heat transfer data between two sets of rotating channels with and without bleeds. Several concluding remarks summarized as follows are obtained from this experimental study.

1. In the Re range of 15,000–30,000, the present rib floors have respectively generated the overall heat transfer enhancements in the ranges of 2.8–3.4 and 3.7–4 times of Dittus–Boelter levels for the static channels with and without bleed. Coolant bleeds from the apical sidewall undermine the static heat transfer performances from the no-bleed references to the extents of 96% to 50%. Twofold impacts of bleeds on the apical side of the trapezoidal duct, namely, the impeded cooling performance and the reduced local airflow rate, result in considerable increases of T_w levels along the bleed section in which the variations of the Nu_0/Nu_∞ ratio along two opposite leading and trailing centerlines follow a zigzag pattern but display an overall declination in the axial direction.
2. Isolated Re impacts on rotational heat transfers over the leading and trailing rib floors in the bleed section are well accounted for by the Re^n relationship for this rotating configuration.
3. As Ro increases, the Coriolis-force effects in isolation cause the trailing edge heat transfer to be consistently increased from the static reference but initially reduce the leading-edge heat transfer from the zero-rotation level that is followed by a subsequent heat transfer recovery at the higher rotation numbers for both rotating channels with and without bleeds. The worst heat transfer scenarios develop at the rotation number of 0.2 along the leading centerline over the bleed section where the Nu/Nu_0 ratios fall in the range of 0.4–0.45.
4. The individual rotating buoyancy effect improves local heat transfer within the present parametric range examined. However, the rotating buoyancy effects decrease rapidly as Ro increases so that the coupling Ro-Bu impacts on local Nu/Nu_0 ratios are demonstrated. Bleeds on the apical side of the rotating trapezoidal duct suppress the degrees of rotating buoyancy effect on heat transfer.
5. The increase of Ro systematically reduces the ratios of $Nu_{\text{bleed}}/Nu_{\text{no bleed}}$ along both leading and trailing centerlines. The impeding heat transfer effects due to bleeds on the apical side at the static conditions are amplified by rotation, which leads to further heat transfer reductions so that the orthogonal-mode rotation of the present trapezoidal duct worsens the impairing heat transfer impacts due to bleeds on the apical side.
6. All the heat transfer data generated by this study are presented by means of a set of heat transfer correlations that permits the evaluations of individual and interactive effects of Re, Ro, and Bu on Nu at the rib and midrib locations along the leading and trailing centerlines. It is well known that the local heat transfer measurements based on limited thermocouple measurements cannot be representative of the full-surface heat transfer of a rotating channel. These reported heat transfer data at the rib and midrib locations along the centerline of the leading and trailing walls are not representative of the overall cooling performance of the coolant channel in the trailing edge of a rotor blade. This set of heat transfer correlations generated on the basis of limited thermocouple measurements cannot be representative of the regional-average heat transfer and, therefore, has very limited applications for blade design but is a measure to evaluate all the heat transfer data generated by this phase of experiments.

Acknowledgment

This research project was financially supported by National Science Council, Taiwan under Grant No. NSC 94-2611-E-022-001.

Nomenclature

English Symbols

A, a_s, n = coefficients
Bu = buoyancy number$=Ro^2\beta(T_w-T_b)(R/d)=Ro^2\beta\Delta T(R/d)$
d = hydraulic diameter of the trapezoidal flow duct (m)
e = rib height (m)
k = thermal conductivity of fluid (W m^{-1} K^{-1})
l = rib land (m)
$\dot{m}$ = mass flow of airflow from channel inlet (kg s^{-1})
$\dot{m}_{\text{bleed}}$ = mass flow of total bleed flow (kg s^{-1})
Nu = Nusselt number$=qd/[k(T_w-T_b)]$
Nu_0 = static Nusselt number
Nu_∞ = Nu value for fully developed turbulent duct flow in stationary channels
P = rib pitch (m)
Pr = Prandtl number$=\mu C_p/k$
q = convective heat flux (W m^{-2})
Re = Reynolds number$=\rho W_m d/\mu$
R = rotating radius at midspan of the test duct from the rotating axis (m)
Ro = rotating number$=\Omega d/W_m$

T_b = fluid bulk temperature (K)
T_f = local fluid temperature (K)
T_w = wall temperature of the test duct (K)
W_m = mean through flow velocity (m s^{-1})
x = axial location (m)
X = dimensionless axial location$=x/d$

Greek Symbols

α = rib angle of attack (deg)
β = thermal expansion coefficient of fluid (K^{-1})
ρ = fluid density (kg m^{-3})
μ = fluid dynamic viscosity (kg s^{-1} m^{-1})
Ω = rotating speed of test duct (rad^{-1})
Ψ, ϕ_1, ϕ_2 = unknown functions

Subscripts

L = centerline of rotating leading edge
T = centerline of rotating trailing edge
0 = nonrotating situation

References

[1] Taslim, M. E., Li, T., and Spring, S. D., 1995, “Experimental Study of the Effects of Bleed Holes on Heat Transfer and Pressure Drop in Trapezoidal Passages With Tapered Turbulators,” ASME J. Turbomach., **117**, pp. 281–289.
[2] Shen, J. R., Wang, Z., Ireland, P., Jones, T. V., and Byerley, A. R., 1996, “Heat Transfer Enhancement With a Turbine Blade Cooling Passage Using Ribs and Combinations of Ribs With Film Cooling Holes,” ASME J. Turbomach., **118**, pp. 428–434.
[3] Ekkad, S. V., Hung, Y., and Han, J. C., 1998, “Detailed Heat Transfer Distributions in Two-Pass Square Channels With Rib Turbulators and Bleed Holes,” Int. J. Heat Mass Transfer, **41**, pp. 3781–3791.
[4] Thurman, D., and Poinsatte, P., 2001, “Experimental Heat Transfer and Bulk Air Temperature Measurements for a Multipass Internal Cooling Model With Ribs and Bleed,” ASME J. Turbomach., **123**, pp. 90–96.
[5] Chanteloup, D., and Bölics, A., 2002, “Flow Characteristics in Two-Leg Internal Coolant Passages of Gas Turbine Airfoils With Film-Cooling Hole Ejection,” ASME J. Turbomach., **124**, pp. 499–507.
[6] Tafti, D. K., and Vanka, S. P., 1991, “A Numerical Study of the Effects of Spanwise Rotation on Turbulent Channel Flow,” Phys. Fluids A, **3**(4), pp. 642–656.
[7] Morris, W. D., and Aythan, T., 1979, “Observations on the Influences of Rotation on Heat Transfer in the Coolant Channels of Gas Turbine Rotor Blades,” Proc. Inst. Mech. Eng., **193**(21), pp. 303–311.
[8] AI-Hadhrami, L., Griffith, T. S., and Han, J.-C., 2003, “Heat Transfer in a Two-Pass Rotating Rectangular Channels (AR=2) With Five Different Orientations of 45-Deg V-Shaped Rib Turbulators,” ASME J. Heat Transfer, **125**, pp. 233–242.
[9] Fann, S., Yang, W.-J., and Zhang, N., 1994, “Local Heat Transfer in a Rotating Serpentine Passage With Rib-Roughened Surface,” Int. J. Heat Mass Transfer, **37**, pp. 217–228.
[10] Ei-Husayni, H. A., Taslim, M. E., and Kercher, D. M., 1994, “Experimental Heat Transfer Investigation of Stationary and Orthogonally Rotating Asymmetric and Symmetric Heated Smooth and Turbulated Channel,” ASME J. Turbomach., **116**, pp. 124–132.
[11] Parsons, J. A., Han, J. C., and Zhang, Y., 1995, “Effect of Model and Wall Heating Condition on Local Heat Transfer in a Rotating Two-Pass Square Channel With Rib Turbulators,” Int. J. Heat Mass Transfer, **38**, pp. 1151–1159.
[12] Dutta, S., and Han, J. C., 1996, “Local Heat Transfer in Rotating and Ribbed Two-Pass Square Channels With Three Channel Orientations,” ASME J. Heat Transfer, **118**, pp. 578–584.
[13] Murata, A., and Mochizuki, S., 2001, “Effect of Centrifugal Buoyancy on Turbulent Heat Transfer in an Orthogonally Rotating Square Duct With Transverse or Angled Rib Turbulators,” Int. J. Heat Mass Transfer, **46**, pp. 3119–3133.
[14] Liou, T.-M., Chen, M.-Y., and Tsai, M.-H., 2002, “Fluid Flow and Heat Transfer in a Rotating Two-Pass Square Duct With In-Line 90-Deg Ribs,” ASME J. Turbomach., **124**, pp. 260–268.
[15] Willett, F. T., and Bergles, A. E., 2002, “Heat Transfer in Rotating Narrow Rectangular Pin-Fin Ducts,” Exp. Therm. Fluid Sci., **25**, pp. 573–582.
[16] Griffith, T. S., AI-Hadhrami, L., and Han, J.-C., 2003, “Heat Transfer in Rotating Rectangular Cooling Channels (AR=4) With Dimples,” ASME J. Turbomach., **125**, pp. 555–563.
[17] Murata, A., and Mochizuki, S., 2003, “Effect of Cross-Sectioned Aspect Ratio on Turbulent Heat Transfer in an Orthogonally Rotating Rectangular Duct With Angled Rib Turbulators,” Int. J. Heat Mass Transfer, **46**, pp. 3119–3133.
[18] Liou, T.-M., Chen, M.-Y., and Wang, Y.-M., 2003, “Heat Transfer, Fluid Flow, and Pressure Measurements Inside a Rotating Two-Pass Duct With Detached 90-Deg Ribs,” ASME J. Turbomach., **125**, pp. 565–574.
[19] Morris, W. D., 1996, “A Rotating Facility to Study Heat Transfer in the Cooling Passage of Turbine Blades,” Proc. Inst. Mech. Eng., Part A: J. Power and Energy, **210**, pp. 55–63.
[20] Iskakov, K. M., and Trushin, V. A., 1985, “The Effect of Rotation on Heat Transfer in the Radial Cooling Channels of Turbine Blades,” Teploenergetika (Moscow, Russ. Fed.), **32**(2), pp. 52–55.
[21] Wagner, J. H., Johnson, B. V., Graziani, B. A., and Yeh, F. C., 1992, “Heat Transfer in Rotating Serpentine Passages With Trips Normal to the Flow,” ASME J. Turbomach., **114**, pp. 847–857.
[22] Johnson, B. V., Wagner, J. H., Steuber, G. D., and Yeh, F. C., 1994, “Heat Transfer in Rotating Serpentine Passages With Trip Skewed to the Flow,” ASME J. Turbomach., **116**, pp. 113–123.
[23] Chang, S. W., and Morris, W. D., 1998, “A Comparative Study of Heat Transfer Between Rotating Circular Smooth-Walled and Square Rib-Roughened Ducts With Cooling Application for Gas Turbine Rotor Blades,” JSME Int. J., Ser. B, **41**(2), pp. 302–315.
[24] Chang, S. W., and Morris, W. D., 2003, “Heat Transfer in a Radially Square Duct Fitted With In-line Transverse Ribs,” Adv. Electron. Electron Phys., Suppl., **42**, pp. 267–282.
[25] Chang, S. W., Yang, T. L., and Wang, W. J., 2006, “Heat Transfer in a Rotating Twin-Pass Trapezoidal-Sectioned Passage Roughened by Skewed Ribs on Two Opposite Walls,” Heat Transfer Eng., **27**(10), pp. 63–79.
[26] Chang, S. W., Liou, T.-M., Yeh, W.-H., and Hung, J.-H., 2007“Heat Transfer in a Radially Rotating Square-Sectioned Duct With Two Opposite Walls Roughened by 45 Degree Staggered Ribs at High Rotation Numbers,” ASME J. Heat Transfer, **129**, pp. 188–199.
[27] JHT Editorial Board of ASME J. Heat Transfer, 1993, “Journal of Heat Transfer Policy on Reporting Uncertainties in Experimental Measurements and Results,” ASME J. Heat Transfer, **115**, pp. 5–6.
[28] Dittus, F. W., and Boelter, L. M. K., 1930, Univ. Calif. Publ. Eng., **2**, p. 443.

Energy Separation in the Wake of a Cylinder

R. J. Goldstein
e-mail: rjg@me.umn.edu

K. S. Kulkarni
e-mail: kaustubh@me.umn.edu

Heat Transfer Laboratory,
Department of Mechanical Engineering,
University of Minnesota,
111 Church St. SE,
Minneapolis, MN 55455

Energy separation is a spontaneous redistribution of total energy (enthalpy) in a fluid without external work or heat flow, resulting in some portion of fluid having higher total energy (enthalpy) and another portion having lower energy (enthalpy) than the surrounding fluid. The present study investigates the mechanism of energy separation in the vortex field behind an adiabatic circular cylinder. Time-averaged velocity and temperature measurements are carried out in the wake of a cylinder in a cross flow of air. The measurements are performed at downstream locations of three, five, seven, and ten diameters, for a Reynolds number, based on upstream velocity and cylinder diameter, of 9.2×10^4 *and freestream Mach number of 0.22. The measured velocity and recovery temperature data are expressed in nondimensional form as an energy separation factor. The distribution of energy separation factor indicates that the main cause of energy separation is the periodic vortex flow in the wake. The vortex strength and the separation effect decrease as the flow moves downstream. However, energy separation is observed even ten diameters downstream.* [DOI: 10.1115/1.2891222]

Keywords: Energy separation, total temperature, moving vortices, recovery factor, turbulence effects, separated flow

1 Introduction

The phenomenon of energy separation was first observed by Ranque [1] in studies of a vortex tube. Extensive numerical and experimental studies have shown the presence of energy separation under different flow conditions including resonance tubes [2], laminar and turbulent boundary layers [3,4], jet impingement flows [5–7], free shear layer [8–10], and vortex streets behind blunt bodies [11,12]. Different mechanisms for energy separation are proposed for these different flow situations. However, the exact mechanism of energy separation is still not completely understood. For free shear flows such as jet flows and blunt body wakes, it is commonly believed that unsteady vortices are the cause of energy separation.

Eckert [13] presented a model of a single vortex rotating clockwise while being convected to the right in explaining energy separation. The model considers that the vortex consists of a viscous core and an inviscid outer layer. It has a swirling velocity of V_w and a freestream convective velocity V_0. To better understand the temperature distribution in the vortex region, consider a dimensionless total temperature inside this vortex represented by $(C_p(T_t-T_{t,\infty})/V_0V_w)$, where $T_{t,\infty}$ is the total temperature of the flow far away from the vortex center. It is then seen that the total temperature T_t in the upper half of the vortex is higher than the freestream total temperature $T_{t,\infty}$ and the reverse is true for the lower half of vortex. Figure 1 shows the velocity field and isotherms for the flow around such a vortex. The total temperature extrema are located at the border between the viscous and inviscid regions.

Kurosaka et al. [14] suggested a similar mechanism for energy separation in a vortex street based on the energy equation for inviscid flow without conduction as given in

$$\rho C_p\frac{DT_t}{Dt}=\rho\frac{Dh_t}{Dt}=\frac{\partial p}{\partial t} \tag{1}$$

The key points of this model are that the total temperature follows the temporal fluctuations in the pressure for an unsteady flow and the pressure in the center of the vortex is lower than outside. Hence, the total temperature of a fluid element following the trochoidal-like path line in a vortex street (Fig. 2) starts to fall as it moves from 12 o'clock to 6 o'clock position since the low pressure vortex center is approaching the fluid element. The pressure rises as the vortex passes by the fluid element for the second half of the cycle and the total temperature of the fluid element rises.

Numerical and experimental studies by Han and Goldstein [8,9] and Seol and Goldstein [10] support the above mechanisms for the case of free jet flows.

1.1 Flow Characteristics in the Wake of Cylinder. The flow over a circular cylinder forms an unsteady laminar wake when the Reynolds number is larger than some relatively small value ($\mathrm{Re}\sim48$) [15]. Friehe's experiments [16] at low Reynolds numbers ($50\leq\mathrm{Re}\leq175$) indicate a constant Strouhal number ($\mathrm{St}=fD/U_\infty$) of ~0.2 for $\mathrm{Re}\geq90$. Other researchers [17–19] showed that St is invariant and equal to ~0.2 up to the critical Reynolds number ($\mathrm{Re}\sim2.0\times10^5$), characterized by a laminar boundary layer on the front of the cylinder surface. A theoretical calculation based on inviscid Orr–Sommerfeld equation (instability analysis) by Triantafyllou et al. [20] indicates $\mathrm{St}=0.21$ at $\mathrm{Re}=1.4\times10^5$. Beyond the critical Re, the flow in the wake is not two dimensional and hence lacks the periodic nature of the vortex shedding [18]. This observation is also confirmed by studies [21,22] for $2.0\times10^5\leq\mathrm{Re}\leq3.5\times10^6$. Bearman [21] found a very high Strouhal number ($\mathrm{St}=0.46$) at $\mathrm{Re}=5.5\times10^5$. However, Roshko [22] found at supercritical range of Reynolds number ($\mathrm{Re}\geq3.5\times10^6$), a harmonic vortex shedding process with $\mathrm{St}=0.27$. Nakagawa [23] used a Mach–Zehnder interferometer to investigate vortex shedding around a circular cylinder with $\mathrm{Re}=1.7\times10^5$ and $M_\infty=0.391$. The density variation captured in the flow visualization shows the separation of total pressure due to the vortex shedding process. The vortex shedding frequency was found to correspond to $\mathrm{St}=0.1848$. He also found St to be independent of Re and M_∞. Nakagawa [24] in a similar experiment ($0.696\times10^5\leq\mathrm{Re}\leq4.137\times10^5$ and $0.1522\leq M_\infty\leq1.9049$) with a square cylinder found that periodic vortex shedding occurs even in the presence of shock waves. The shape of the vortex, however, is deformed by the shock wave.

Contributed by the Heat Transfer Division of ASME for publication in the JOURNAL OF HEAT TRANSFER. Manuscript received January 17, 2007; final manuscript received August 2, 2007; published online April 23, 2008. Review conducted by Sai C. Lau.

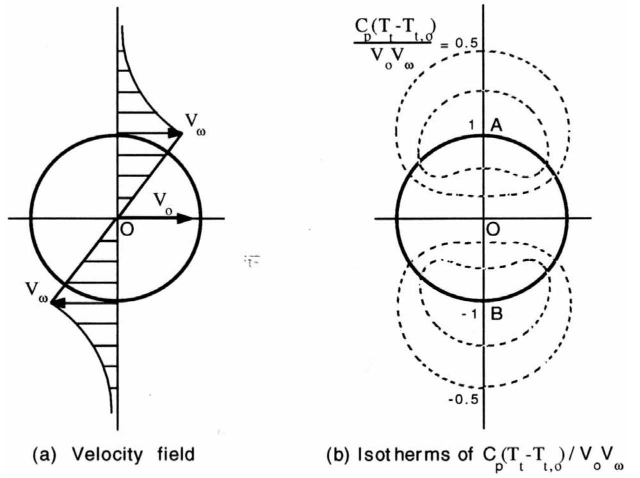

(a) Velocity field (b) Isotherms of $C_p(T_t-T_{t,o})/V_oV_\omega$

Fig. 1 Velocity field and total temperature distribution near a vortex [13]

1.2 Energy Separation in the Wake of Cylinder. To understand the phenomenon of aerodynamic heating, extensive experimentation was done in the late 1930s. Eckert and Weise [3], while studying flow past a circular cylinder, found that the surface temperature of an adiabatic cylinder decreases from the front stagnation line to the rear stagnation line for $\mathrm{Re}=1.4\times10^5$, $M_\infty=0.685$. They found at the rear stagnation line, the surface temperature was less than even the static temperature of the flow. Later Ryan [25] confirmed these experiments finding evidence of this anomalous behavior (which he called "aerodynamic cooling") in the wake of a cylinder. He also found this cooling effect enhanced when vortex shedding was intensified by external acoustics. Thomann [26] repeated the measurements for $6.0\times10^4\leq\mathrm{Re}\leq3.2\times10^5$ and $0.5\leq M_\infty\leq3.0$ and found good agreement with previous researchers.

However, near sonic speeds, the cylinder surface temperature at the rear stagnation line showed no cooling effect. He argued that if vortex shedding is the cause of the energy separation, there should be no vortex shedding at sonic speeds. The Schlieren photographs indeed support this argument. Later, many researchers [12,14,27] confirmed the energy separation on the surface of cylinder and also showed that intensified vortex shedding strengthens the energy separation. Experimental evidence for the mechanism proposed by Kurosaka et al. [14] was found by Ng et al. [28] through time accurate measurements of simultaneous total pressure and total temperature in the wake of a cylinder for $\mathrm{Re}=2.3\times10^5$ and $M_\infty=0.4$. The time traces of total temperature and total pressure in the near wake are quantitatively similar supporting the theoretical arguments.

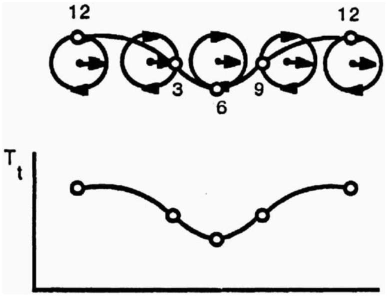

Fig. 2 Variation of total temperature along a path line in a vortex street [14]

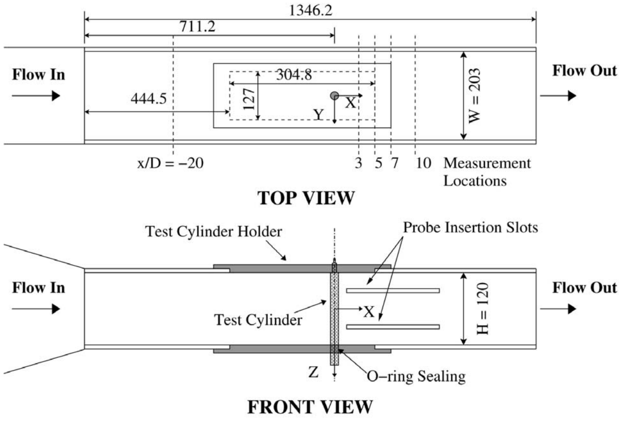

(a) Schematic Diagram of Test Section (All Dimensions in mm)

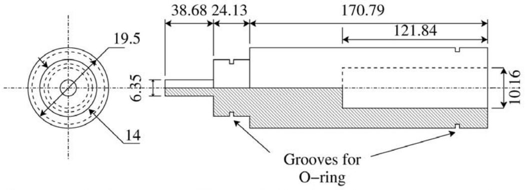

(b) Schematic Diagram of Test Cylinder (All Dimensions in mm)

Fig. 3 Schematic diagram of test apparatus

Few direct measurements of energy separation in the wake of a cylinder are available. Some are restricted to supersonic or transonic flow regimes. The mechanism of energy separation as proposed by Eckert [13] and Kurosaka et al. [14] indicates that energy separation should be evident and measurable even in low speed gas flows. Hence, the objective of the present work is to study the time-averaged energy separation phenomena in the wake of a circular cylinder. It includes measurement of the average total temperature distribution in the wake along with velocity measurements at different downstream locations.

2 Experimental Apparatus and Procedure

2.1 Experimental Facility. A subsonic suction-type wind tunnel is used in the study. Air enters the tunnel through a bellmouth inlet of $609\times609\ \mathrm{mm}^2$ cross section and passes through a flow straightener and air filter. Downstream three wire mesh screens placed 100 mm apart reduce the freestream turbulence level. To achieve the air speed necessary for a sufficiently large dynamic temperature required in the experiment, two flow contractions having area ratios 9:1 and 5:3 are introduced between the screens and the test section. The combined effect of the two contractions allows a maximum speed of 95 m/s in the test section without any obstruction.

The test section is a 1346 mm long rectangular duct made of 19 mm thick Plexiglas sheets with a cross section of 120 mm (height) × 203 mm (width) (Fig. 3(*a*)). Two test windows, 305 × 127 mm, are provided on top and bottom walls of the duct. Holes drilled in the test windows allow insertion of the vertical test cylinder. Two slots of length 300 mm, width 5 mm and 50 mm apart are cut through a sidewall for insertion of temperature and hot wire probes. The adiabatic test cylinder shown in Fig. 3(*b*) is made of phenolic and is partially hollowed with 19 mm outside diameter (o.d.) and 10.2 mm inside diameter (i.d.). The

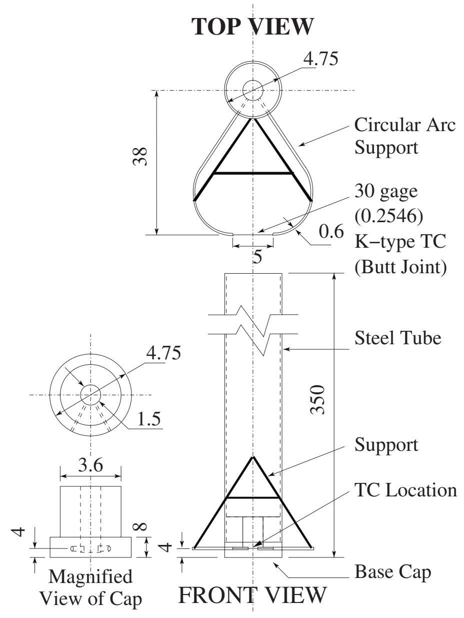

Fig. 4 Schematic diagram of recovery temperature probe (all dimensions in mm)

resultant blockage with the vertical cylinder in the test section is 9.4%.

The total temperature in the wake of the cylinder is measured with a recovery temperature probe and the velocity and turbulent intensity are measured with a hot wire anemometer.

2.2 Recovery Temperature Probe. A thermocouple probe is used to measure the local total temperature in the wake of the cylinder. Initially, a stagnation (total) temperature probe was used [29]. With this, the flow slows down inside a small cylindrical tube (with flow inlet to exit ratio=8:1) and its temperature is measured with a K-type thermocouple junction. The recovery factor of this probe is very close to 1 (~0.99); thus, it measures the stagnation temperature directly. However, due to the tubular structure of the probe and its directional sensitivity, it is not accurate in the near wake region of the cylinder where the flow is highly vortical and two or three dimensional. Hence, a bare wire thermocouple probe is used in the present experiment.

The present recovery temperature probe is based on design ideas of Hottel and Kalitinsky [30] and Moffat [31] for bare wire thermocouple probes (Fig. 4). It consists of a butt-joint K-type thermocouple made from sheathed wires. A small portion of the wire insulation is removed close to the butt joint, which is positioned midway between two circular arc steel tubes 5 mm apart. These tubes carry the thermocouple wires and also act as support for the junction. The support arms join in a plastic base cap attached to a 350 mm long steel tube (5 mm o.d., 3.6 mm i.d.). Additional supports (as shown in Fig. 4) from the circular arc tubes to this steel tube reduce vibration of the thermocouple junction.

The flow near the thermocouple junction should be unaffected by the support structure of the probe. Hence, the circular arc tubes are chosen to be of sufficient length such that the junction is far from the front stagnation line of the support tube (approximately eight diameters of support tube o.d.). Potential flow theory is used to calculate the minimum distance between the support tube and the thermocouple junction.

The choice of a K-type thermocouple is based on the thermal analysis of the probe. The relatively low conductivity of alumel and chromel helps minimize the conduction error. Also, a butt-joint thermocouple junction (in comparison with a bead joint) exposed to cross flow shows stable recovery factor characteristics for different freestream velocities [30]. Smaller diameter wire reduces conduction error but also reduces structural strength. Thirty gauge (0.2546 mm diameter) K-type thermocouple wires with a butt-joint junction are the reasonable compromise chosen for the recovery temperature probe.

2.3 Experimental Procedure. An automated traversing system moves the recovery temperature probe and hot wire velocity probe in the wake of the cylinder. The basic parts of the automation are a mounting setup, stepper motor, and motion controller. The mounting setup consists of a C shaped holder attached to the traverse and the stepper motor. A coupling is used to connect the motor shaft to the traverse shaft. A M063-FD09 model stepper motor from Superior Electric Inc. is used. It has a resolution of 200 steps per revolution or 1.8 deg per step. Combined with the traverse screw pitch of 1.27 mm (0.05 in.), the smallest displacement possible with this setup is 6.25 μm. A four-axis motion controller by Centroid operates the stepper motor. The Centroid motion controller connects to the computer (Linux workstation) by a RS-232 port. The automated traverse can span the entire width (203 mm) of the test section, but the motion is restricted to −96 mm to +70 mm with respect to the axis of the cylinder due to the structural constraints on the temperature probe. The probe is moved in steps of 2 mm, resulting in 84 measurements at each $x/D=-20$, 3, 5, 7, and 10 (Fig. 3(*a*)).

The recovery temperature probe is calibrated at different air speeds to assess its accuracy and consistency in measuring the recovery temperature in the flow. The recovery factor (defined in Eq. (2))

$$r = 1 + \frac{T_{r,00} - T_{t,\infty}}{U_{00}^2/2C_p} = 1 + \frac{T_{r,00} - T_{t,\infty}}{T_{d,00}} \tag{2}$$

is calculated by measuring the recovery temperature of the probe ($T_{r,00}$) for a known flow velocity (U_{00}) and total temperature ($T_{t,\infty}$). The recovery probe is placed in the wind tunnel in the absence of the cylinder during the calibration. A pitot tube is placed close to the probe to measure the freestream velocity. Note that the probe is calibrated in a uniform low turbulence (~0.25%) flow. The total temperature of the flow is measured with five K-type thermocouples at the entrance of the wind tunnel where the dynamic temperature is negligible. Four thermocouples are placed at the midpoints of the four sides of the inlet and one thermocouple is placed at the center of the inlet section (609×609 mm^2). The average temperature of the five inlet thermocouples is used as $T_{t,\infty}$ and the probe temperature is the recovery temperature $T_{r,00}$. Using these values of $T_{t,\infty}$ and $T_{r,00}$, the recovery factor for the probe is determined using Eq. (2). During the experiments, it is possible to maintain a standard deviation of 0.01°C between the five inlet thermocouple temperatures. Figure 5 shows the variation of recovery factor as a function of the freestream velocity. The recovery factor is found to be 0.735 ± 0.02, and is a constant for the velocity range studied (60–95 m/s).

Velocity and temperature measurements downstream of the cylinder are taken simultaneously with hotwire velocity and recovery temperature probes inserted through two slots (separated by 50 mm in spanwise direction) in the sidewall of the test section (Fig. 3(*a*)). Experiments are repeated with the probe positions interchanged. The flow is found to be two dimensional with no influence of the spanwise location. As the recovery temperature probe moves in the wake of cylinder, the total temperature of the flow measured at wind tunnel inlet is continuously monitored. This reference total temperature is used to calculate the energy separation factor at each location of the recovery temperature probe. Hot wire measurements are used to obtain the instantaneous velocity (U), which is used to calculate the time-averaged velocity ($\bar{U}$) and random fluctuations u' and v'.

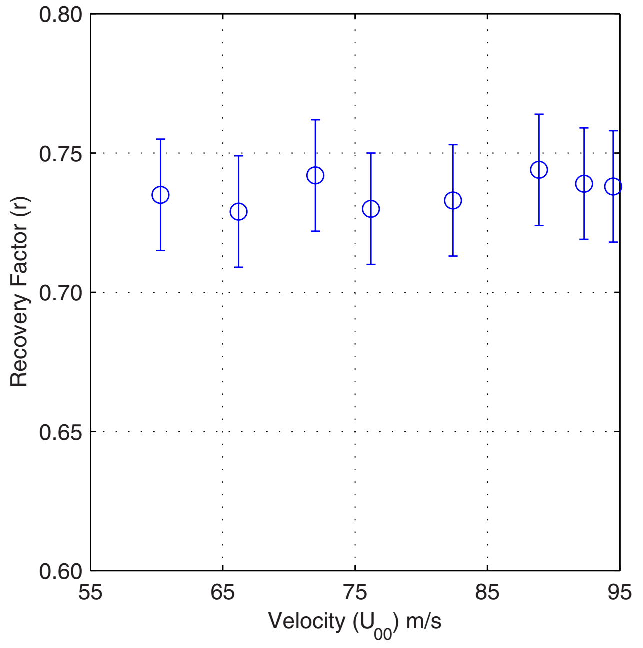

Fig. 5 Recovery factor calibration of recovery temperature probe

3 Results and Discussion

3.1 Data Reduction Procedure and Calculations. The time-averaged total temperature in the wake of the cylinder is normalized by the freestream dynamic temperature and expressed as an energy separation factor (S) (Eq. (3)).

$$S=\frac{T_t-T_{t,\infty}}{T_{d,\infty}}=\frac{T_r+(1-r)T_d-T_{t,\infty}}{T_{d,\infty}} \tag{3}$$

where

$$T_d=\frac{\overline{U^2}}{2C_p}=\frac{(\bar{U}^2+\overline{u'^2}+\overline{v'^2})}{2C_p} \tag{4}$$

The local average dynamic temperature given by Eq. (4) is obtained from the hot wire velocity measurement data for the particular cross stream (y/D) location. The hot wire is placed parallel to the cylinder axis $(Z$ direction), thus capturing both streamwise (u') and cross stream (v') velocity fluctuations. Velocity fluctuations (w') in the spanwise direction $(Z$ direction) along with v' are measured separately with the hot wire placed parallel to streamwise direction $(X$ direction) and found to be negligible $(w'/u' < 0.1)$. Thus, the local average energy separation factor, as calculated by Eq. (3), considers the local turbulent fluctuations, which are found to be significant in the wake region of the cylinder. Figure 6 shows normalized local dynamic temperature in the wake of the cylinder at $x/D=3$. Local dynamic temperatures obtained using the mean velocity alone and using Eq. (4) are normalized by the dynamic temperature using the freestream velocity. Turbulent fluctuations at this location are significant in affecting the energy separation factor. Figures 7 and 8 show the normalized velocity and turbulent intensity profiles upstream and at all four downstream locations. The turbulence intensity $((u'^2+v'^2)^{0.5}/\bar{U})$ upstream of the cylinder at $x/D=-20$ is $\sim 0.2\%$. The energy separation factor is calculated from the measurements of recovery temperature at all four downstream locations for the same freestream velocity (Fig. 9). The overall uncertainty in S is ± 0.021. The uncertainty is not expressed as percentage of typical value in this case because the typical value of S is close to 0.

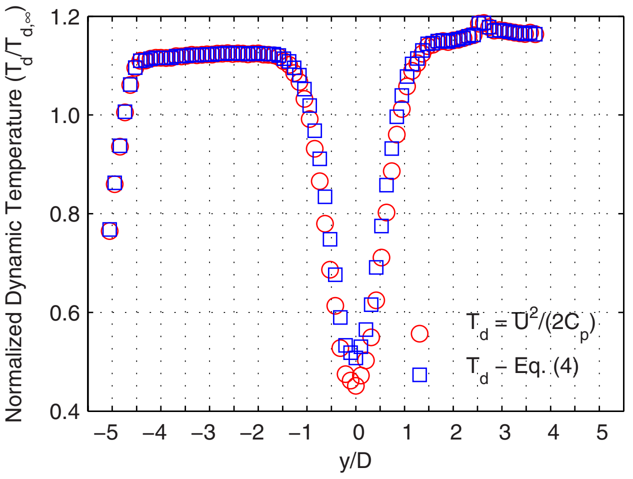

Fig. 6 Effect of turbulent fluctuations on measurement of local dynamic temperature $(x/D=3,\ \mathrm{Re}=9.2\times 10^4)$

3.2 Energy Balance Calculations. The measurement validity is checked by calculating the energy balance from the measured values of total enthalpy flow upstream (20 diameters from the cylinder (Fig. 3(*a*)), denoted by suffix 0 in Eq. (5)) and downstream of the cylinder. The total enthalpy difference between the upstream and downstream locations $(\Delta\dot{H}_t)$ is normalized by the enthalpy of the flowing mass with the dynamic temperature of the freestream $(\dot{H}_{d,\infty})$ as shown in

$$\begin{aligned}\frac{\Delta\dot{H}_t}{\dot{H}_{d,\infty}}&=\frac{\int\dot{m}_0C_p(T_{t,0}-T_{t,\infty})dy-\int\dot{m}C_p(T_t-T_{t,\infty})dy}{\int\dot{m}_0C_pT_{d,\infty}dy}\\&=\frac{\int\rho H\bar{U}_0C_p(T_{t,0}-T_{t,\infty})dy-\int\rho H\bar{U}C_p(T_t-T_{t,\infty})dy}{\int\rho H\bar{U}_0C_pT_{d,\infty}dy}\\&=\frac{1}{W}\left[\int\frac{\bar{U}_0}{U_\infty}S_0dy-\int\frac{\bar{U}}{U_\infty}Sdy\right]\end{aligned} \tag{5}$$

where

$$U_\infty=\frac{1}{W}\int_{-W/2}^{W/2}\bar{U}_0dy \tag{6}$$

The spatially averaged upstream velocity (U_∞) as defined by Eq. (6) is used to normalize the average upstream and downstream velocities and to calculate upstream dynamic temperature $(T_{d,\infty})$. The normalized enthalpy flux $(S\cdot\bar{U}/U_\infty)$ at all cross stream locations (y/D) is obtained both upstream and downstream of the cylinder with reference total temperature measured at the wind tunnel inlet $(T_{t,\infty})$. The normalized enthalpy flux $(S\cdot\bar{U}/U_\infty)$ is plotted at all cross stream locations (y/D) in Fig. 10. Since the profiles are symmetric in the Y direction, the normalized enthalpy flux is integrated over the half width of the tunnel $(-5.05\leqslant y/D \leqslant 0)$ and is used to verify the energy conservation. The value of energy separation factor upstream (S_0) is typically 0.

Figure 10 may give the impression that energy is not conserved in the energy separation process. Since S approaches, a value of 0 near the outer wake limits forcing the energy contribution of the accelerated flow region to be 0. However, the same data expressed in equivalent dimensional form (in terms of product of total temperature (°C) and normalized velocity, Fig. 11) show the positive energy content in the outer wake region explaining the apparent anomaly. The results are also summarized in Table 1. It shows the

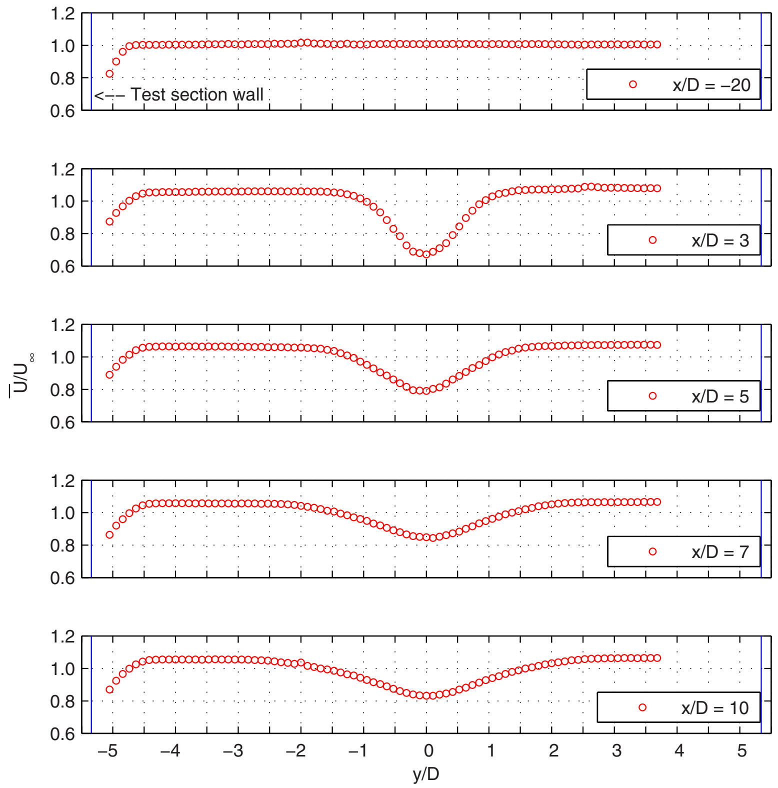

Fig. 7 Time-average velocity profile at $x/D=-20,3,5,7,10$ for $\mathrm{Re}=9.2\times 10^4$

spatially and temporally averaged streamwise velocity at every downstream location ($\langle\bar{U}\rangle$) (defined in Eq. (7)) normalized by spatially and temporally averaged upstream velocity (U_∞).

$$\langle\bar{U}\rangle=\frac{1}{W}\int_{-W/2}^{W/2}\bar{U}dy \tag{7}$$

This fraction is an indicator of the mass balance at various downstream locations and the results show mass balance within 1%. The energy balance is evaluated at all downstream locations and the results are within 10% of the flow enthalpy ($\dot{H}_{d,\infty}$) (Table 1). It is important to note that normalized enthalpy flux balance based on inlet flow enthalpy would result in an enthalpy balance of the order of a tenth of a percent due to the large enthalpy of the flow at room temperature. Also, the inlet flow enthalpy is not representative of the energy that is redistributed within the flow as a result of energy separation. Hence, an enthalpy associated with the dynamic temperature of the freestream is defined. This quantity represents the maximum energy that can be distributed within the fluid as a result of energy separation. Satisfactory values of mass and energy balance recorded in the study give authenticity to the experimental results.

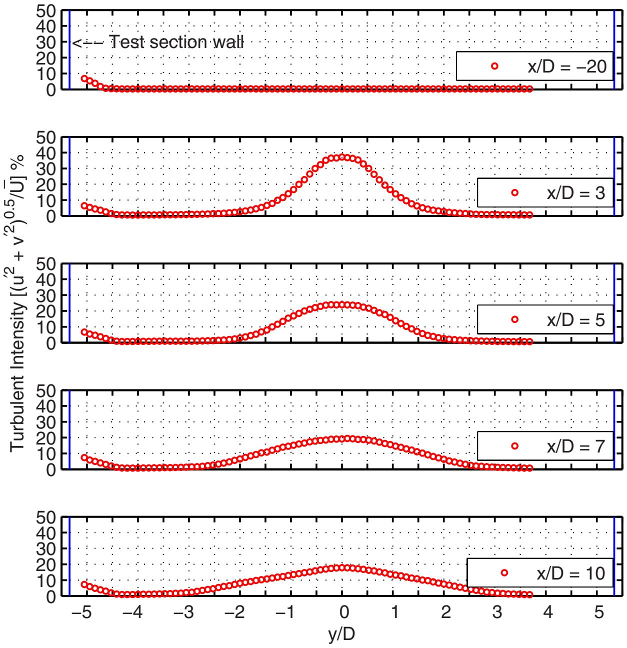

Fig. 8 Turbulent intensity profile at $x/D=-20,3,5,7,10$ for $\mathrm{Re}=9.2\times 10^4$

3.3 Effect of Downstream Location. Measurements are taken at 20 diameters upstream and 3, 5, 7, and 10 diameters downstream of the cylinder for $U_\infty \approx 76$ m/s corresponding to $\mathrm{Re}=9.2\times 10^4$.

There are several factors to be noted from these results:

1. The velocity profiles (Fig. 7) show a blockage effect due to the presence of the cylinder. The velocity outside the wake is higher than the corresponding upstream velocity (U_∞).
2. The profiles indicate a general increase in the size of the wake as flow moves downstream.
3. The turbulent intensity at the location $x/D=3$ is very high and contributes significantly in the determination of the recovery temperature and hence the energy separation factor.

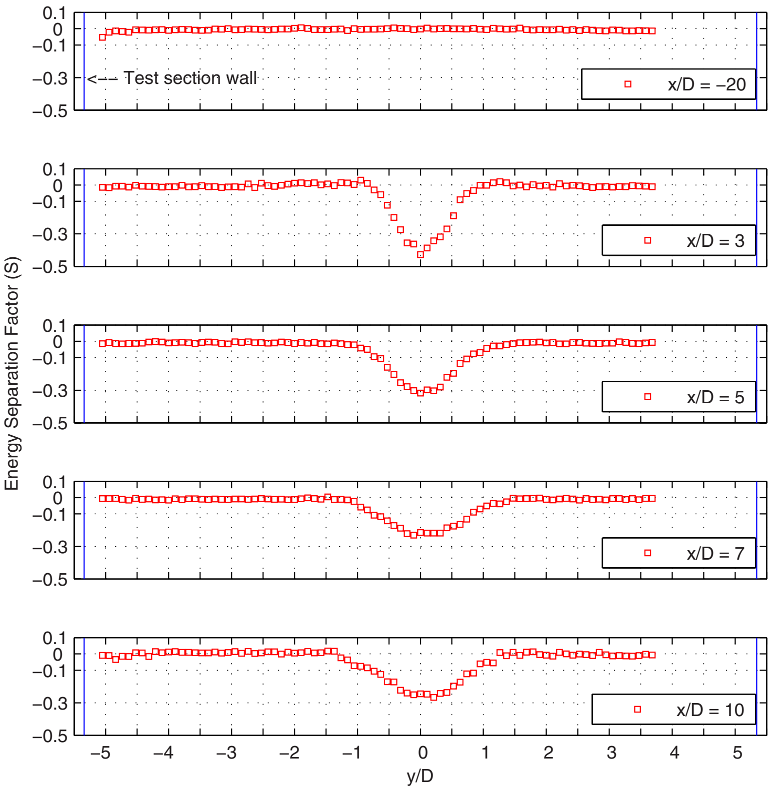

Fig. 9 Time-average energy separation factor profile at $x/D=-20,3,5,7,10$ for $Re=9.2\times10^4$

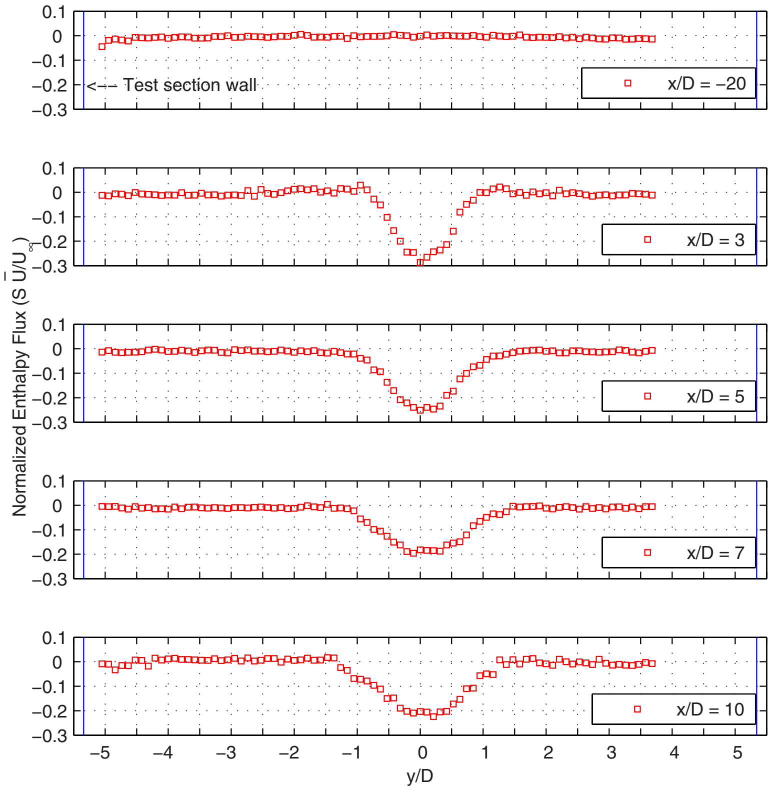

Fig. 10 Time-average normalized enthalpy flux profile at $x/D=-20,3,5,7,10$ for $Re=9.2\times10^4$

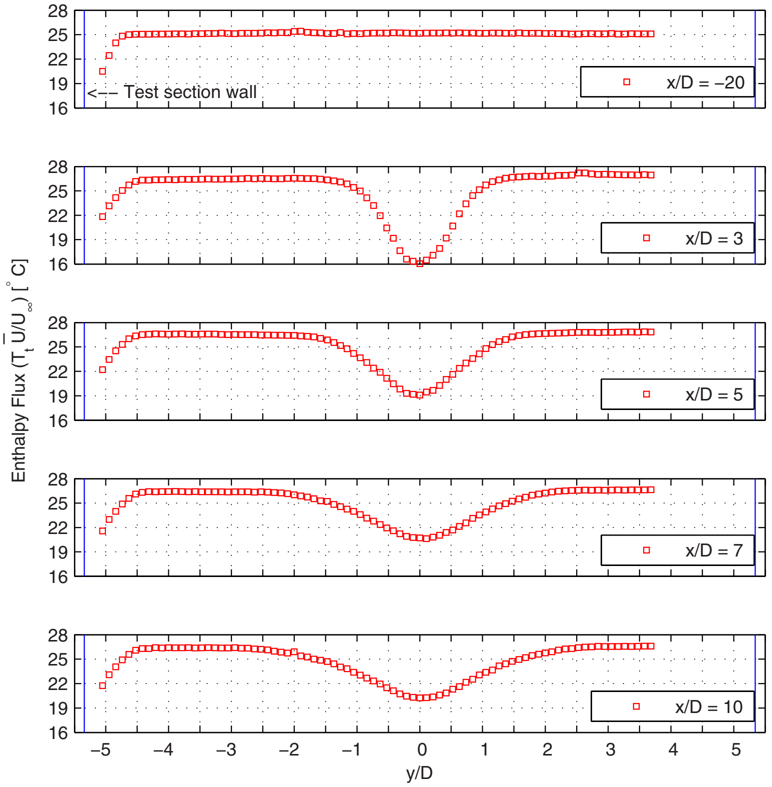

Fig. 11 Time-average enthalpy flux profile at $x/D=-20,3,5,7,10$ for Re $=9.2\times10^4$

This effect is clear from Fig. 6, which shows the effect of turbulence on the local dynamic temperature.

The recovery temperature is measured at the same locations and the data are reduced in the form of energy separation factor as calculated from Eq. (3) and plotted in Fig. 9. Some important factors can be noted from the results:

1. The profiles clearly indicate the existence of energy separation in the wake of the cylinder.
2. The energy separation factor is very close to zero outside the wake, thus indicating that the total energy of the fluid flowing in this region remains nearly constant.
3. The energy separation factor is negative near the centerline (e.g., $S=-0.427$ at $x/D=3$ and $y/D=0$) and positive near the wake limits (e.g., $S=0.020$ at $x/D=3$ and $y/D=1.26$), indicating lower total temperature near the wake centerline and higher total temperature in the outer wake. This behavior supports the energy separation mechanism discussed by Eckert [13] and Kurosaka et al.[14]. Also, the negative energy separation region on either side of the wake centerline increases away from the centerline as flow moves downstream, indicating slight vortex growth.

Table 1 Energy separation factor, mass balance, and enthalpy flux balance results (Re=9.2×10^4)

x/D	S centerline	$\frac{\langle\bar{U}\rangle}{U_\infty}$	$\frac{\Delta\dot{H}_t}{\dot{H}_{d,\infty}}$
3	−0.427	99.7%	5.95%
5	−0.318	100.4%	−0.70%
7	−0.230	100.1%	1.68%
10	−0.251	99.2%	9.98%

4. The magnitude of the energy separation decreases as the flow moves downstream. Thus, no significant positive energy separation in the outer wake limits is observed for $x/D=5,7,10$. Also, the average velocity in the outer wake is higher than that at the wake center resulting in a relatively small overshoot in total temperature. Kurosaka et al.[14] also report this lack of "hot spots" (their term) for time-averaged measurements in their numerical simulations. They suggest that flow along path lines of two particles—one similar to that described in Fig. 2 (bound to the vortex on one side of the cylinder) and the other crossing over from one vortex on the other side neutralize the hot spots. The present results support such an explanation. However, the measurement resolution at the modest velocities employed in addition to the weakening of energy separation effect may argue for the absence of the hot spots at $x/D=5$, 7, and 10.
5. Maximum negative energy separation occurs at the wake centerline. The magnitude of the energy separation decreases very slowly with x/D. This suggests that the vortices are convected downstream without significant change in strength. Nakagawa [23] suggests that $x/D\leqslant 3$ is the region for vortex growth and for $x/D>3$ the vortex is convected downstream without any significant decrease in its strength. Present results are in agreement with this mechanism for vortex shedding.
6. These results agree qualitatively with Ryan [25], though his measurements were at much higher Mach numbers (~2.5). The present study show that energy separation occurs even at relatively low (0.22) Mach number.

4 Conclusions

Time-averaged temperature and velocity measurements are performed to study energy separation in the vortex region behind a circular cylinder in cross flow. Measurements are carried out at various downstream locations for a fixed Reynolds number. The following conclusions can be drawn from the experimental results:

1. The measured energy separation factor (S) profiles clearly indicate the presence of energy separation in the wake of the cylinder even for low Mach number.
2. Large negative energy separation is observed near the wake centerline and a slight positive energy separation is observed in the outer wake. The energy separation decreases as the flow moves downstream. These observations indicate that the vortical structures are the cause of energy separation as proposed by Eckert [13] and Kurosaka et al. [14].
3. The energy separation profiles support the vortex shedding prediction by Nakagawa [23] that a vortex forming near the cylinder surface grows in size in the region $x/D \leqslant 3$ and is then carried further downstream without any appreciable increase in its size until $x/D=10$.
4. Time-averaged energy separation at the larger downstream locations ($x/D>3$) shows no significant positive energy separation regions in the outer wake supporting the hot spots neutralization mechanism of Kurosaka et al. [14].

Nomenclature

C_p = specific heat at constant pressure for the fluid (J/kg K)
D = diameter of circular cylinder (mm)
f = frequency of vortex shedding (Hz)
H = height of test section (mm)
$\dot{H}_{d,\infty}$ = enthalpy flow (Eq. (5)) (W)
$\Delta\dot{H}_t$ = difference in enthalpy flow between upstream and downstream of cylinder (W)
h_t = stagnation enthalpy per unit mass of fluid (J/kg)
M_∞ = freestream mach number
$\dot{m}$ = mass flow rate at downstream location ($x/D=3,6,5,7,10$) (kg/s)
$\dot{m}_0$ = mass flow rate at upstream location ($x/D=-20$) (kg/s)
ν = kinematic viscosity of fluid (m^2/s)
p = static pressure of fluid (Pa)
Re = Reynolds number ($=U_\infty D/\nu$)
r = recovery factor of temperature probe (Eq. (2))
ρ = fluid density ($\mathrm{kg/m}^3$)
S = energy separation factor (Eq. (3))
S_0 = energy separation factor at upstream location ($x/D=-20$)
St = Strouhal number
T_d = local dynamic temperature (Eq. (4)) (°C)
$T_{d,\infty}$ = dynamic temperature ($=U_\infty^2/2C_p$) (°C)
$T_{d,00}$ = dynamic temperature in the absence of cylinder ($=U_{00}^2/2C_p$) (°C)
T_r = recovery temperature measured by the probe (°C)
$T_{r,00}$ = recovery temperature measured by the probe in the absence of cylinder (°C)
T_t = total (stagnation) temperature (°C)
$T_{t,\infty}$ = total (stagnation) temperature at wind tunnel inlet (°C)
$T_{t,0}$ = total (stagnation) temperature at upstream location ($x/D=-20$) (°C)
t = time (s)
U = instantaneous streamwise velocity (m/s)
$\bar{U}$ = time-averaged streamwise velocity (m/s)
$\bar{U}_0$ = time-averaged streamwise velocity at upstream location ($x/D=-20$) (m/s)
U_{00} = streamwise velocity in the absence of cylinder (m/s)
U_∞ = spatially and temporally averaged flow velocity at upstream location ($x/D=-20$) (m/s)
$\langle\bar{U}\rangle$ = spatially and temporally averaged flow velocity (m/s)
u' = random fluctuations in streamwise velocity (X direction) (m/s)
V_0 = convective velocity of vortex (m/s)
V_w = swirling velocity of vortex (m/s)
v' = random fluctuations in cross stream velocity (Y direction) (m/s)
W = width of test section (mm)
w' = random fluctuations in spanwise velocity (Z direction) (m/s)
X = streamwise direction
x = distance in streamwise direction (mm)
Y = cross streamwise direction
y = distance in cross streamwise direction (mm)
Z = spanwise direction

References

[1] Ranque, G., 1933, "Experiences sur la d'etente giratoire avec productions simultan\ees d'un echappement d'air chaud et d'un echappement d'air froid," J. Phys. Radium, **4**, pp. 112–114.
[2] Eckert, E. R. G., 1986, "Energy Separation in Fluid Streams," Int. Commun. Heat Mass Transfer, **13**, pp. 127–143.
[3] Eckert, E. R. G., and Weise, W., 1940, "Messungn der Temperaturverteilung auf der Oberflache Schnell Angestromter umbeheizter korper," Jahrbuch 1940 der Deutschen Luftahrtforschung, **2**, pp. 25–31.
[4] Eckert, E. R. G., and Drewiz, O., 1941, "Die Berechnung des Temperaturfeldes in der laminaren Grenzschicht schnell angestromter, unbeheizter Korper," Luftfahrtforschung, **19**, pp. 189–196.
[5] Goldstein, R. J., Behbahani, A. I., and Heppelmann, K. K., 1986, "Streamwise Distribution of the Recovery Factor and the Local Heat Transfer Coefficient to an Impinging Circular Air Jet," Int. J. Heat Mass Transfer, **29**(8), pp. 1227–1235.
[6] Goldstein, R. J., Sobolik, K. A., and Seol, W. S., 1990, "Effect of Entrainment on the Heat Transfer to a Heated Circular Air Jet Impinging on a Flat Surface," ASME J. Heat Transfer, **112**, pp. 608–611.
[7] Fox, M., Kurosaka, M., and Hirano, K., 1990, "Total Temperature Separation in Jets," AIAA 21st Fluid Dynamics, Plasma Dynamics and Lasers Conference.
[8] Han, B., and Goldstein, R. J., 2003, "Instantaneous Energy Separation in a Free Jet. Part I. Flow Measurement and Visualization," Int. J. Heat Mass Transfer, **46**(21), pp. 3975–3981.
[9] Han, B., and Goldstein, R. J., 2003, "Instantaneous Energy Separation in a Free Jet. Part II. Total Temperature Measurement," Int. J. Heat Mass Transfer, **46**(21), pp. 3983–3990.
[10] Seol, W. S., and Goldstein, R. J., 1997, "Energy Separation in a Jet Flow," ASME J. Fluids Eng., **119**(1), pp. 74–82.
[11] Van Oudheusden, B. W., 2005, "Energy Separation in Steady Separated Wake Flow," ASME J. Fluids Eng., **127**(3), pp. 611–614.
[12] Goldstein, R. J., and He, B., 2001, "Energy Separation and Acoustic Interaction in Flow Across a Circular Cylinder," ASME J. Heat Transfer, **123**, pp. 682–687.
[13] Eckert, E. R. G., 1987, "Cross Transport of Energy in Fluid Streams," Waerme- Stoffuebertrag., **21**, pp. 73–81.
[14] Kurosaka, M., Gertz, J. B., Graham, J. E., Goodman, J. R., Sundaram, P., Ringer, W. C., Kuroda, H., and Hankey, W. L., 1987, "Energy Separation in a Vortex Street," J. Fluid Mech., **178**, pp. 1–29.
[15] Zdravkovich, M. M., 1997, *Flow Around Circular Cylinders: A Comprehensive Guide Through Flow Phenomena, Experiments, Applications, Mathematical Models and Computer Simulations*, Oxford Science, New York.
[16] Friehe, C. A., 1980, "Vortex Shedding From Cylinders at Low Reynolds Numbers," J. Fluid Mech., **100**, pp. 237–241.
[17] Cantwell, B., and Coles, D., 1983, "An Experimental Study of Entrainment and Transport in the Turbulent Near Wake of a Circular Cylinder," J. Fluid Mech., **136**, pp. 321–374.
[18] Ericsson, L. E., and Reding, J. P., 1979, "Criterion for Vortex Periodicity in Cylinder Wakes," AIAA J., **17**(9), pp. 1012–1013.
[19] Braza, M., Chassaing, P., and Minh, H. H., 1990, "Prediction of Large-Scale

Features in the Wake of a Circular Cylinder," Phys. Fluids A, **2**(8), pp. 1461–1471.

[20] Triantafyllou, G. S., Triantafyllou, M. S., and Chryssostomidis, C., 1986, "On the Formation of Vortex Streets Behind Stationary Cylinders," J. Fluid Mech., **170**, pp. 461–477.

[21] Bearman, P. W., 1969, "On Vortex Shedding From Circular Cylinder in the Critical Reynolds Number Regime," J. Fluid Mech., **37**, pp. 577–585.

[22] Roshko, A., 1960, "Experiments on the Flow Past a Circular Cylinder at Very High Reynolds Number," J. Fluid Mech., **10**, pp. 345–356.

[23] Nakagawa, T., 1986, "A Formation Mechanism of Alternating Vortices Behind a Circular Cylinder at High Reynolds Number," J. Wind. Eng. Ind. Aerodyn., **25**, pp. 113–129.

[24] Nakagawa, T., 1987, "Vortex Shedding Behind a Square Cylinder in Transonic Flows," J. Fluid Mech., **178**, pp. 303–323.

[25] Ryan, L. F., 1951, "Experiments in Aerodynamic Cooling," Ph.D. thesis, ETH, Zurich.

[26] Thomann, H., 1959, Technical Report No. FFA 84.

[27] Eber, G., 1941, "Experimental Research on Friction Temperature and Heat Transfer for Simple Bodies at Supersonic Velocities," German Archive Technical Report No. 66/57.

[28] Ng, W. F., Chakroun, W. M., and Kurosaka, M., 1990, "Time Resolved Measurements of Total Temperature and Pressure in the Vortex Street Behind a Cylinder," Phys. Fluids A, **2**(6), pp. 971–978.

[29] Terala, P., 2000, "Study of Energy Separation in the Wake of a Cylinder for High Speed Flow," M.S. thesis, University of Minnesota, Minneapolis.

[30] Hottel, H. C., and Kalitinsky, A., 1945, "Temperature Measurements in High Velocity Air Streams," ASME J. Appl. Mech., **67**, pp. A25–A32.

[31] Moffat, R. J., 1962, "Gas Temperature Measurement," *Temperature: its Measurement and Control in Science and Industry*, Reinhold, New York, pp. 553–571.

Investigation of Turbulent Flow and Heat Transfer in Periodic Wavy Channel of Internally Finned Tube With Blocked Core Tube

Qiu-Wang Wang[1]
e-mail: wangqw@mail.xtu.edu.cn

Mei Lin

Min Zeng

Lin Tian

State Key Laboratory of Multiphase Flow
in Power Engineering,
Xi'an Jiaotong University,
Xi'an 710049, China

Three-dimensional complex turbulent flow and heat transfer of internally longitudinally finned tube with blocked core tube and streamwise wavy fin are numerically investigated. The numerical method is validated by comparing the calculated results with corresponding experimental data. The effects of both wave height and wave distance on heat transfer performance are examined. The range of wave height to hydraulic diameter ratio is from 0.61 to 2.45, and that of wave distance to hydraulic diameter ratio is from 3.06 to 14.69, while that of Reynolds number is from 904 to 4520. The computational results demonstrate that the Nusselt number and friction factor increase with the increase of the wave height, while they decrease with the increase of the wave distance. Furthermore, general correlations are proposed to describe the performance of the wavy configuration for $904 \leq Re \leq 4520$, $0.61 \leq s/d_e \leq 2.45$, $6.12 \leq l/d_e \leq 11.02$, *with the mean deviations for heat transfer and friction factor correlations being* -2.8% *and* -1.9%, *respectively.*
[DOI: 10.1115/1.2891219]

Keywords: turbulent flow, periodic wavy channel, heat transfer, internally longitudinal finned tube

Introduction

Internally finned tubes have been widely applied in industry in order to enhance heat transfer inside tubes. Most of the relevant previous works have focused on the effects of fin number, fin length, and fin cross-sectional profile on heat transfer. Fabbri [1] studied the problem of optimizing heat transfer in an internally finned tube by varying the fin shape under the conditions of laminar flow and imposed heat flux on the tube wall. Afterwards, he investigated the effect of viscous dissipation on laminar forced convection under the optimized geometrical conditions [2]. Alam and Ghoshdastidar [3] numerically studied the steady, laminar flow and heat transfer in internally finned circular tubes having tapered lateral profiles subject to constant heat flux, and significant enhancement of heat transfer was found due to the internal fins. Zeitoun and Hegazy [4] conducted fully developed laminar convective heat transfer in a pipe provided with two groups of internally longitudinal fins having different heights. It was found that the fin heights affect greatly the flow and heat transfer characteristics for different pipe fin geometries. Saad et al. [5] performed an experiment to determine the detailed module-by-module pressure drop characteristics of turbulent flow inside circular finned tubes. The tubes were equipped with longitudinal fins interrupted in the streamwise direction by their arrangement in both a staggered and an inline manner. The results showed that, in the periodic fully developed region, the tube pressure drop with continuous fins is higher than that with inline arrangement fins and lower than that with staggered arrangement fins. Zhang and Faghri [6] presented the heat transfer enhancement in the latent heat thermal energy storage system by using an internally finned tube. They found that the heat conduction in the internal fins is an unsteady two-dimensional heat conduction problem and adding internal fins is an efficient way to enhance the heat transfer in thermal energy storage systems when a fluid with a low thermal conductivity is used as the transfer fluid. Yu et al. [7] conducted an experiment to determine the heat transfer and pressure drop characteristics in the entrance and fully developed regions of tubes with internally wave-like longitudinal fins. One tube with inner blocked tube and the other with inner unblocked tube were tested. It was found that the two finned tubes can significantly enhance the heat transfer, with the blocked one being superior. Huq et al. [8] found that the heat transfer coefficient of finned tube is large in the entrance region and the enhancement of heat transfer in the fully developed region is remarkable due to the fin effects. Campo and Chang [9] presented a unique combination of numerical and statistical results for the thermofluid dynamics of laminar viscous flows in contact with streamwise fins. They conducted empirical correlation equations for the asymptotic friction factor and the asymptotic Nusselt numbers as a function of the number of fins and fin height in the bundle. Dagtekin et al. [10] presented the entropy geometrician analysis in a circular duct with internal longitudinal fins of different fin shapes (thin, triangular, and V-shaped fins) for laminar flow. It was found that the number of fins and dimensionless length of the fins for both thin fins and triangular fins, and the fin angle for triangular and V-shaped fins have significant effects on both entropy generation and pumping power. Bhatia and Webb [11] numerically predicted single-phase heat transfer and friction losses for microfin tubes using the commercial CFD program, FLUENT. The predicted friction factors for five tube geometries were available, ranging from +13% to −9% of the experimental values. However, the Nusselt numbers were overpredicted, ranging from 29% to 55% as the Prandtl number was increased from 1 to 4. Liu and Jensen [12] performed numerically the turbulent flow and heat transfer in internally finned tubes. They investigated the fin profile (rectangular, triangular, and

---

[1] Corresponding author.

Contributed by the Heat Transfer Division for publication in the JOURNAL OF HEAT TRANSFER. Manuscript received January 8, 2007; final manuscript received July 26, 2007; published online April 23, 2008. Review conducted by Gautam Biswas.

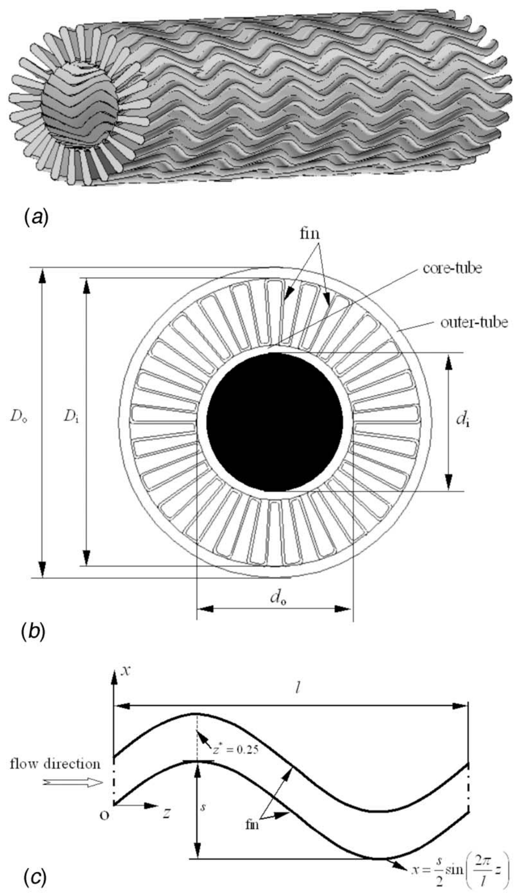

Fig. 1 Schematic of internally finned tube: (*a*) streamwise wavy fins (not to scale), (*b*) cross-sectional view of internally finned tube, and (*c*) one periodic streamwise wavy channel

round crest), fin numbers, fin width, fin height, and helix angle. It was found that the rectangular and triangular fins behave similarly: however, when the number of fins is large, the round crest fin can have larger friction factors. In our previous study [13], we numerically obtained the optimal ratio of blocked core-tube outside diameter to outer-tube inside diameter (d_o/D_i).

It can be seen that almost all the above literature studied the plain fin or round fin along the streamwise (longitudinal) direction in the tube. However, longitudinally wavy fin is one of the popular fin patterns to improve heat transfer, such as in the plate-and-fin heat exchangers. The wavy surface can change the flow direction of fluid and cause better mixing. Hence, higher heat transfer performance can be expected compared to the plain fin surfaces [14–17].

However, the effect of wavy fin along streamwise direction in internally finned tube with blocked core tube on the heat transfer characteristics does not appear to have been reported in the open literature. In this paper, we will focus on the effect of wave height, wave distance on the characteristics of momentum, and heat transfer, and the corresponding general correlations will be proposed to describe the performance of the wavy configuration. The range of wave height to hydraulic diameter ratio is from 0.61 to 2.45, and that of wave distance to hydraulic diameter ratio is from 3.06 to 14.69.

Physical Model and Numerical Method

Figure 1(*a*) shows a schematic view of the present wavy fins. Figure 1(*b*) shows a cross-sectional view of the internally wavy finned tube. The core tube has an inner diameter d_i and an outer diameter d_o. The outer tube has an inner diameter D_i and an outer diameter D_o. Figure 1(*c*) shows one periodic wavy axial channel, where s is the wave height and l is the wave distance. The expression of the wave in Fig. 1(*c*) is $x=(s/2)\sin((2\pi/l)z)$.

Usually, there are many waves located in both the transverse and streamwise directions, as shown in Fig. 1(*a*). The flow and heat transfer in the wavy channel can be regarded as fully periodically developed along both directions. The periodicities of the tube geometry in both the transverse and streamwise directions are exploited to obtain the smallest computational domain and to save computer memory. The computational cross section is simplified to be trapeze because there are usually more than 20 waves in the transverse section (see Fig. 1(*b*)). Figure 2 shows the complete details of the computational domain and the boundary conditions used in the simulation. The axial faces of the domain are set as translational periodic. A rotationally periodic boundary condition is imposed on the tangential faces. The conjugated heat transfer is considered, which means that the fins are located in the computational domain (see Fig. 2). The fin is regarded as "thin wall," which means the fin is only a surface with thickness of zero, and it is impermeable for "fluid." The temperature of the thin wall is obtained through coupling with the fluid flow field. A constant wall temperature boundary condition is imposed on the outer-tube surface.

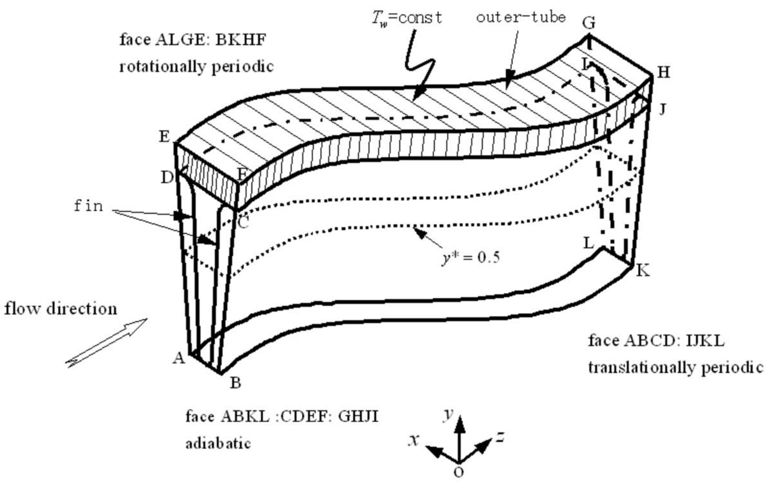

Fig. 2 Schematic of the computational domain

The fluid is assumed to be incompressible with constant thermal physical properties and the flow is assumed to be turbulent, steady, three dimensional with no viscous dissipation. The working fluid is dry air.

The governing equations as well as the detail expressions for different variables can be found in our previous study [13], and therefore are not shown here due to the space limitation.

The set of governing equations is solved by commercially available computer software (FLUENT 6.0). The pressure and velocity fields are linked by the semi-implicit method for pressure-linked equations consistent (SIMPLEC) algorithm described by Doormal and Raithby [18]. The convection terms are handled by the quadratic upwind interpolation of convective kinematics (QUICK) scheme. The diffusion terms are discretized with central differencing scheme. Besides the default quantities (such as velocity, temperature, turbulent kinetic energy, dissipation rate of turbulence energy, etc.) from FLUENT to control the convergence, the criteria of convergence in this study are judged by additionally monitoring other physical quantities, such as the variation of pressure gradient per unit length of channel and the bulk temperature ratio ($\theta = T_w - T_{\text{in}} / T_w - T_{\text{out}}$). The convergence criterion of

$$\left| \frac{R_\phi^n - R_\phi^{n-1}}{R_\phi^{n-1}} \right| \leq 10^{-4} \tag{1}$$

is applied for momentum and energy, where R_ϕ^n refers to the maximum residual value for variable ϕ (ϕ stands for velocity, temperature, turbulent kinetic energy, dissipation rate of turbulence energy, pressure gradient per unit length of channel, bulk temperature ratio, etc.) over all the computation cells after nth iteration.

The Reynolds number is defined as

$$\text{Re} = \frac{\rho u_m d_e}{\mu} \tag{2}$$

where u_m is the inlet average velocity. The hydraulic diameter d_e, is given by

$$d_e = \frac{4A_c}{P} = \frac{\pi(D_i^2 - d_o^2) - 4\delta_f l_f}{\pi(D_i + d_o) + 2l_f} \tag{3}$$

where δ_f is the fin thickness and l_f is the unfolded fin length at the tube cross section.

The Nusselt number is described as

$$\text{Nu} = \frac{hd_e}{\lambda} \tag{4}$$

where λ is the thermal conductivity of air and the heat transfer coefficient h is defined as

$$h = \frac{\Phi}{\Delta T \cdot A_f} \tag{5}$$

where Φ is the total heat transfer rate from fin surface, A_f is the area of fin surface (the fin efficiency is assumed to be 1, because it was made of copper with high thermal conductivity), and ΔT is the mean temperature difference between fin surface and air, which can be obtained for constant wall temperature as follows:

$$\Delta T = \frac{(T_{\text{in}} - T_w) - (T_{\text{out}} - T_w)}{\ln[(T_{\text{in}} - T_w)/(T_{\text{out}} - T_w)]} \tag{6}$$

The average Darcy friction factor is defined as

$$f = \frac{-(\Delta P/L)d_e}{\rho u_m^2/2} \tag{7}$$

where ΔP is the total pressure drop and L is the tube length with internal fins.

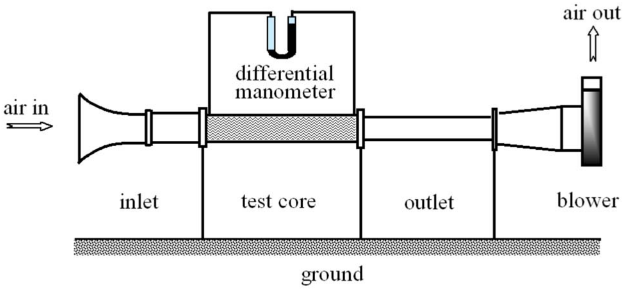

Fig. 3 Schematic of experimental system

Experimental Apparatus

The main objective of the present experimental study is to determine the friction factor and heat transfer performance of the turbulent flow through circular tube with internally longitudinal wavy fins in order to provide data to validate the numerical method and code. The experimental apparatus consist of four major components: (1) inlet section, (2) experimental section, (3) flow measuring section, and (4) fan assembly, as illustrated in Fig. 3.

Air is used as the working fluid in whole experimental measurement. It is sucked from the laboratory atmosphere and blown into the test finned tube. Air inside tube is heated by the electrical heater wrapped uniformly on the outside surface of the test tube.

Over the electrical heater, the outer tube are wound with mica sheet and insulation tape. A layer of plastic foam with thickness of 50 mm is used to insulate the test tube in order to minimize the heat loss. A motor-driven fan delivers air to the test finned tube through a trumpet-shaped entrance. The trumpet-shaped entrance gives nearly uniform velocity distribution at the test finned tube inlet. The airflow rate is measured by a rotameter. The control of airflow rate through the finned tube is performed by varying the motor's speed during the experiment process.

The test tube and fins are made of copper, whose detailed configuration is shown in Fig. 1. The detailed geometry of the tested internally longitudinal wavy finned tube is given in Table 1 (standard case). The static pressure taps are installed at the inlet and outlet of the test section to measure the pressure difference with a differential manometer.

The temperatures of the test tube surface are measured with the help of thermocouples nonuniformly distributed along the tube axis. At each cross section, three thermocouples are situated with equal degree along the outer surface. The thermocouples are made of copper-constantan wires and calibrated before installation. The thermocouple junctions between copper tube and thermocouple contact are soft soldered to grooves milled in the wall. They are installed to be flushed with the outer surface of the outer tube.

Table 1 Geometry of tested internally longitudinal wavy finned tube (standard case)

Variables	Values
Outer diameter of outer tube (D_o)	28 mm
Inner diameter of outer tube (D_i)	26 mm
Hydraulic diameter (d_e)	1.635 mm
Outer diameter of core tube (d_o)	14 mm
Tube length with fins (L)	372 mm
Wave distance (l)	13 mm
Unfolded fin length at tube cross section (l_f)	320 mm
Number of waves in cross section (N)	25
Wave mean height (s)	2.6 mm
Fin mean thickness (δ_f)	0.2 mm
Thermal conductivity of fin (copper) (λ)	398 W/(m K)

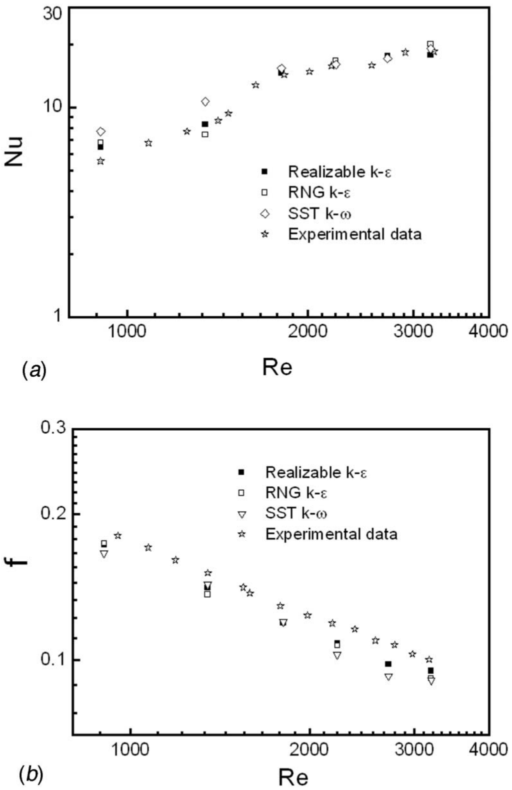

Fig. 4 Comparisons of Nusselt number and friction factor between experimental data and numerical predictions with various turbulence models: (*a*) Nu versus Re and (*b*) *f* versus Re

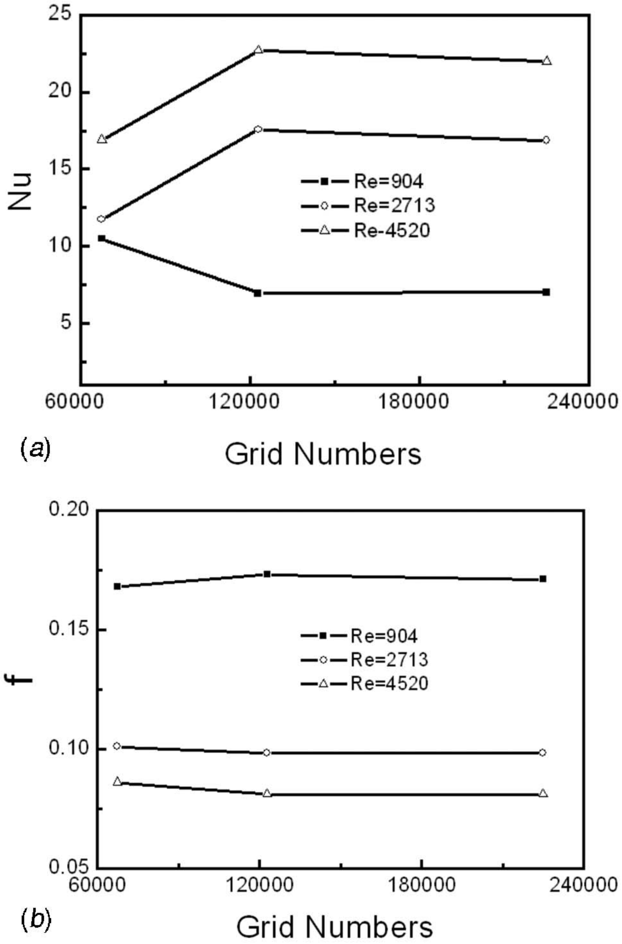

Fig. 5 Computational results for three meshes under different Reynolds number: (*a*) Nu versus grid nodes and (*b*) *f* versus grid nodes

The fluid bulk temperature at the inlet of the test section is measured using a thermometer located in the upstream of the test section inlet, while the bulk temperature at the outlet is measured by using thermocouples located at the outlet of the test section.

The investigated parameters in these experiments include inlet and outlet fluid bulk temperatures, wall temperature, mass flow rate, static pressure, and electric power. The accuracies of these measurements will be described as follows. The inlet air bulk temperature of the test section is read from thermometer with a resolution of 0.1°C, and accuracy of approximately ±0.2°C. The outer-tube wall temperatures as well as the outlet air bulk temperature are measured by calibrated copper-constantan thermocouples whose accuracy is about ±0.2°C as well. The airflow rate is determined by a rotameter with an accuracy of 2.5%. The static pressure difference is measured between the pressure at each location and atmosphere by an inclined manometer with an accuracy of 0.1 mm water column.

The atmospheric pressure is measured by a barometer with an accuracy of 0.03%. The electric power to the test section is measured by an electrodynameter with a full-scale accuracy of 0.25%. The heat balance error between the power input and enthalpy increase of air of all data are no more than 7%.

The method of experimental error analysis adopted is that recommended by Kline and McClintock [19]. The important parameters we concerned are the Nusselt number, friction factor, and Reynolds number, whose uncertainties at a moderate flow rate and average temperature are 7.8%, 8.4%, and 5.7%, respectively.

Code Validation and Grid Independence

Selection of an appropriate turbulence model for numerical simulation requires consideration of computational cost, anticipated flow phenomena. The key features of the flow in the inter-

Table 2 Parameters of numerical cases

Variables	Values	
Reynolds number	904, 1808, 2713, 3617, 4520 (for each geometrical dimension)	Number of Reynolds number: 5
$N=25$, $d_o=14$ mm	$s/d_e=0.61$, 0.80, 0.98, 1.22, 1.41, 1.59, 1.84, 2.02, 2.20, 2.45; $l/d_e=3.06$, 4.89, 6.12, 7.95, 9.18, 11.02, 12.85, 14.69	Number of geometrical dimension: 10*8+1+1=82
$N=20$, $d_o=14$ mm	$s/d_e=1.24$; $l/d_e=6.22$	
$N=20$, $d_o=12$ mm	$s/d_e=1.65$; $l/d_e=8.24$	
Total cases: 82×5=410		

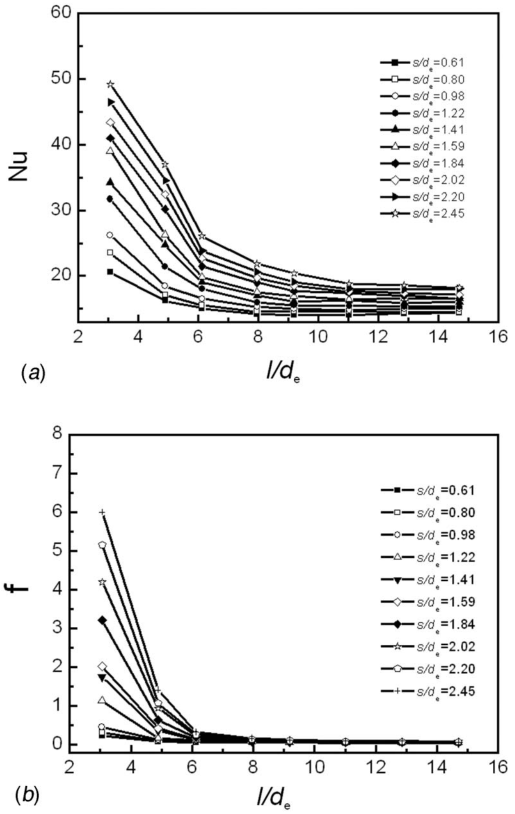

Fig. 6 Variation of Nusselt number and friction factor with wave distance under moderate Reynolds number (Re=2713): (*a*) Nu versus *l*/d_e and (*b*) *f* versus *l*/d_e

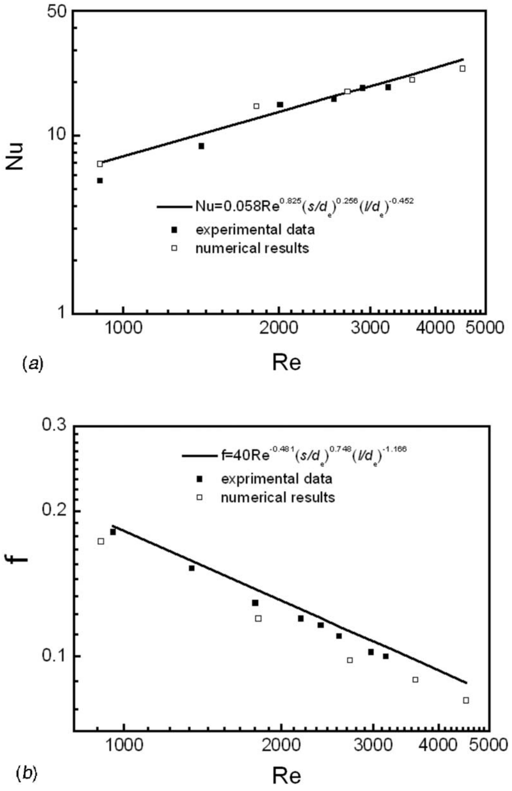

Fig. 7 Comparisons of Nusselt number and friction factor with Reynolds number among correlation, experimental data and numerical results: (*a*) Nu versus Re and (*b*) *f* versus Re

nally finned tube are separation, recirculation, and rotation. Therefore, the agreements between the calculated Nusselt number and friction factors and experimental data are the main criterion for selecting turbulent models. In the present study, three different turbulent models (the RNG k-ε model, the realizable k-ε model, and the SST k-ω model) are chosen to simulate the flow of the internally finned tube.

Figure 4 compares the experimentally obtained and the calculated average Nusselt number and friction factor at various Reynolds numbers with different turbulent models. From this figure, the realizable k-ε model fits the experiment better than the RNG k-ε and SST k-ω models. The maximum differences of Nu and f are −25% and −8%, respectively, for Reynolds number ranging from 904 to 4520. Hence, in this paper, the realizable k-ε turbulence model is selected.

To ensure the accuracy and validity of numerical results, a careful check for the grid independence of the numerical solutions has been made among three grid systems, (I) 44(40)×34×28 (67,390 nodes), (II) 44(40)×44×40 (122,804 nodes), (III) 44(40)×51×60 (208,261 nodes), as shown in Fig. 5. The nonuniform grid at the transverse direction and uniform grid along the longitudinal direction were used. It is found that in the range of studied Reynolds number (Re=904–4520), the relative deviations of both Nusselt numbers and friction factors between (II) and (III) are less than 5%. Hence, the mesh of 44(40)×44×40 (122,804 nodes) is selected as a reference mesh.

Results and Discussion

In the present study, a total of 410 cases are simulated, as shown in Table 2, with the main variables being Reynolds numbers, s/d_e, and l/d_e. The parameters for the standard case are the same, as shown in Table 1, that is, $s/d_e=1.59$ and $l/d_e=7.95$.

Figure 6 shows the variations of Nusselt number and friction factors with the dimensionless wave distance (l/d_e) at different dimensionless wave heights (s/d_e) at moderate Reynolds number (Re=2713). It can be seen that the Nusselt numbers, Nu, and the friction factors f increase with the increase of the dimensionless wave height at different dimensionless wave distance. The Nusselt numbers decrease remarkably with the increase of the dimensionless wave distance ($l/d_e \leqslant 11$) at different dimensionless wave heights, and reach a constant value at the condition of $l/d_e > 11$. The friction factors decrease also remarkably with the increase of the dimensionless wave distance ($l/d_e \leqslant 11$) at different dimensionless wave heights at moderate Reynolds number (Re=2713), and reach a constant value at the condition of $l/d_e > 11$. This is because when l/d_e increases, the channel becomes straighter even at the same s/d_e, and thus the strengths of separation and secondary flow become weak.

To summarize the relationships between the fully developed average friction factor and Nusselt number with Reynolds numbers, the corresponding correlations have been proposed for the wave number of 25, by the least square's method. The final expressions are shown as follows:

$$\mathrm{Nu} = 0.058\,\mathrm{Re}^{0.825}\left(\frac{s}{d_e}\right)^{0.256}\left(\frac{l}{d_e}\right)^{-0.452} \tag{8}$$

$$f = 40\,\mathrm{Re}^{-0.481}\left(\frac{s}{d_e}\right)^{0.748}\left(\frac{l}{d_e}\right)^{-1.166} \tag{9}$$

It should be noted that the ranges of dimensionless parameters for the above equations are $904 \leqslant \mathrm{Re} \leqslant 4520$, $0.61 \leqslant s/d_e \leqslant 2.45$, and $6.12 \leqslant l/d_e \leqslant 11.02$ (only part of the studied l/d_e). Equation (8) correlates 90% of the numerical data for 200 cases with maximum deviation of ±16% and mean deviation of −2.8%. Equation (9)

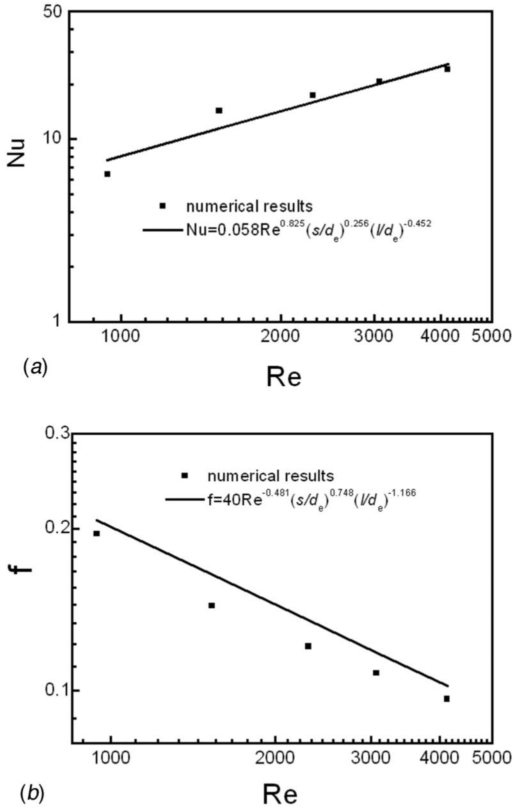

Fig. 8 Comparisons of Nusselt number and friction factor with Reynolds number between correlation and numerical results with different wave numbers (N=20): (a) Nu versus Re and (b) f versus Re

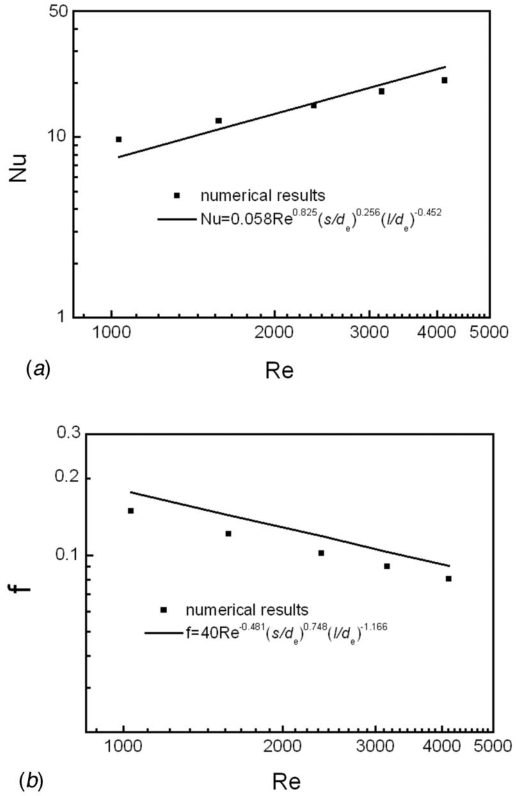

Fig. 9 Comparisons of Nusselt number and friction factor with Reynolds number between correlation and numerical results with different inner diameters (d_o=12 mm): (a) Nu versus Re and (b) f versus Re

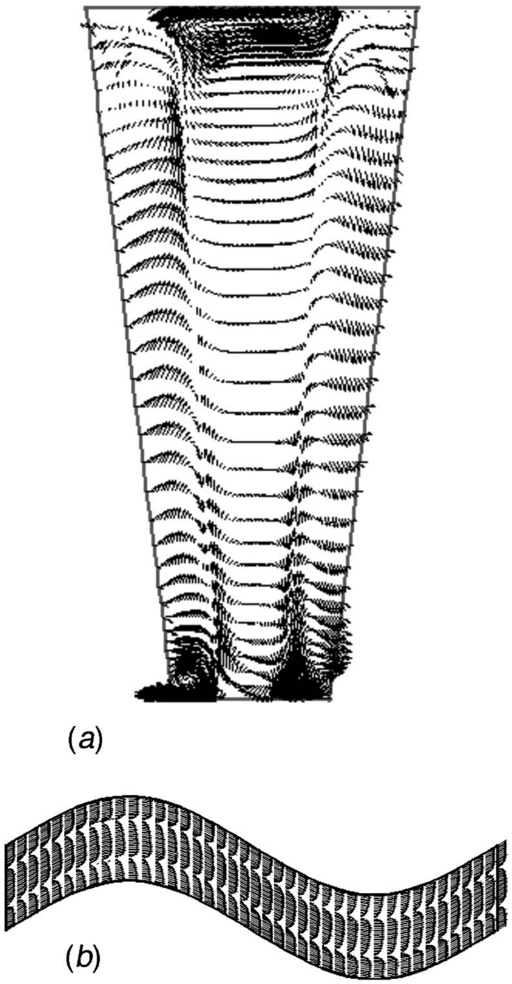

Fig. 10 Eddy formation at transverse and streamwise sections (Re=2713 and s/d_e=1.59, l/d_e=7.95): (a) transverse section (z^*=0.25) and (b) streamwise section (y^*=0.5)

correlates 90% of the numerical data for 200 cases with maximum deviation of ±20% and mean deviation of −1.9%.

Figure 7(a) demonstrates comparisons of Nusselt numbers between the experimental data and the numerical results from the correlation at the condition of the standard case (s/d_e=1.59 and l/d_e=7.95). The mean deviation of Nusselt number is 8.1%, and the maximum deviation is 26.3% at low Reynolds number Re =904, perhaps because the flow is in the transition region [20]. On the other hand, Fig. 7(b) demonstrates comparisons of the friction factor between the experimental data and the numerical data from correlation at the condition of the standard case (s/d_e=1.59 and l/d_e=7.95). The mean deviation of the friction factor is 4.4%, and the maximum deviation is 6.7% at low Reynolds number Re =904.

In order to validate the flexibility of Eqs. (8) and (9), the comparisons of Nusselt number and friction factor with Reynolds number between correlation and numerical results under different wave numbers and different inner diameter's are conducted in Figs. 8 and 9. Figure 8 shows the variations of Nusselt number and the friction factor for the internally longitudinal finned tube with different wave numbers (N=20), and the other geometrical parameters of the internally longitudinal finned tube are identical to the standard case (as shown in Table 1). From the figures, the numerical data are well satisfied with the correlations. The maximum deviations of the Nusselt number and the friction factor for the internally finned tube with 20 wave numbers are less than 20%

and 14.2%, respectively, while the corresponding mean deviations are −0.65% and 9.3%, respectively. Additionally, the maximum deviations of the Nusselt number and the friction factors for the internally finned tube with different inner diameters (d_o =12 mm) and the other geometrical parameters of the internally longitudinal finned tube being identical to the standard case are less than 19.6% and 18.4%, respectively, as illustrated in Fig. 9. The corresponding mean deviations are 0.32% and 16.1%, respectively.

The eddy formation may be developed in turbulent flow through a channel having periodic wavy wall due to the curvature effect, which may disturb the boundary layer and thus enhance the heat transfer. The typical results of eddy formation are shown in Fig. 10 for Re=2713 and s/d_e=1.59, l/d_e=7.95. Figure 10(*a*) shows the eddy formation at transverse section (z^*=0.25, as shown in Fig. 1(*c*)), while Fig. 10(*b*) shows that at streamwise section (y^*=0.5, as shown in Fig. 2). It can also be expected that the effect of eddy may increase with the increase of waviness.

Conclusions

The three-dimensional turbulent flow and convective heat transfer in wavy channel in internally longitudinal finned tube have been numerically studied. Both the Nusselt number and friction factor increase with the increase of the wave height, while they decrease with the increase of the wave distance. Furthermore, the correlations of Nusselt number and the friction factor with the Reynolds number and dimensionless fin wave height and wave distance are found from 200 cases in the ranges of $904 \leqslant \mathrm{Re} \leqslant 4520$, $0.61 \leqslant s/d_e \leqslant 2.45$, $6.12 \leqslant l/d_e \leqslant 11.02$, with the mean deviations being −2.8% and −1.9%, respectively.

Acknowledgment

This work was supported by Higher Academy Young Teacher Foundation Project of Fok Ying-Tung Education Foundation (Grant No. 91056) and NSFC Fund for Creative Research Groups (No. 50521604).

Nomenclature

A_c = area of flow, m^2
A_f = heat transfer surface area, m^2
D_i = inner diameter of outer tube, m
D_o = outer diameter of outer tube, m
d_e = hydraulic diameter, m
d_i = inner diameter of core tube, m
d_o = outer diameter of core tube, m
f = Darcy friction factor
h = average heat transfer coefficient, $\mathrm{W/(m^2\,K)}$
k = turbulent kinetic energy, $\mathrm{m^2/s^2}$
L = tube length, m
l = wave distance, m
l_f = unfolded periphery length of the wavy fin, m
N = number of waves
Nu = average Nusselt number
P = circumferential length, m
Re = Reynolds number
R_ϕ^n = maximum residual value for variable ϕ over all the computation cells after nth iteration
s = wave height, m
T_{in} = inlet air bulk temperature, K
T_{out} = outlet air bulk temperature, K
T_{w} = wall temperature of outer-tube, K
u_m = average inlet velocity, m/s
x, y, z = Cartesian coordinates
y^* = dimensionless coordinate in y direction (Fig. 2)
z^* = dimensionless coordinate in z direction (Fig. 1(*c*))

Greek Symbols

δ_f = fin thickness, m
Φ = heat transfer rate, W
ΔP = pressure drop between inlet and outlet, Pa
ΔT = temperature difference, K
ε = dissipation rate of turbulence energy, $\mathrm{m^2/s^3}$
λ = thermal conductivity, W/(m K)
μ = dynamic viscosity, Pa s
ρ = density, $\mathrm{kg/m^3}$

References

[1] Fabbri, G., 1998, “Heat Transfer Optimization in Internally Finned Tubes Under Laminar Flow Conditions,” Int. J. Heat Mass Transfer, **41**, pp. 1243–1253.
[2] Fabbri, G., 2004, “Effect of Viscous Dissipation on the Optimization of the Heat Transfer in Internally Finned Tubes,” Int. J. Heat Mass Transfer, **47**, pp. 3003–3015.
[3] Alam, I., and Ghoshdastidar, P. S., 2002, “A Study of Heat Transfer Effectiveness of Circular Tubes With Internal Longitudinal Fins Having Tapered Lateral Profiles,” Int. J. Heat Mass Transfer, **45**, pp. 1371–1376.
[4] Zeitoun, O., and Hegazy, A. S., 2004, “Heat Transfer for Laminar Flow in Internally Finned Pipes With Different Fin Heights and Uniform Wall Temperature,” Heat Mass Transfer, **40**, pp. 253–259.
[5] Saad, A. E., Sayed, A. E., Mohamed, E. A., and Mohamed, M. S., 1997, “Experimental Study of Turbulent Flow Inside a Circular Tube With Longitudinal Interrupted Fins in the Streamwise Direction,” Exp. Therm. Fluid Sci., **15**, pp. 1–15.
[6] Zhang, Y. M., and Faghri, A., 1996, “Heat Transfer Enhancement in Latent Heat Transfer Thermal Energy Storage System by Using the Internally Finned Tube,” Int. J. Heat Mass Transfer, **39**, pp. 3165–3173.
[7] Yu, B., Nie, J. H., Wang, Q. W., and Tao, W. Q., 1999, “Experimental Study on the Pressure Drop and Heat Transfer Characteristics of Tubes With Internal Wave-like Longitudinal Fins,” Heat Mass Transfer, **35**, pp. 65–73.
[8] Huq, M., and Huq, A. M. A., 1998, “Experimental Measurements of the Heat Transfer in an Internally Finned Tube,” Int. Commun. Heat Mass Transfer, **25**, pp. 619–630.
[9] Campo, A., and Chang, J., 1997, “Correlation Equations for Friction Factors and Convective Coefficients in Tubes Containing Bundles of Internal Longitudinal Fins,” Heat Mass Transfer, **33**, pp. 225–232.
[10] Dagtekin, I., Oztop, H. F., and Sahin, A. Z., 2005, “An Analysis of Entropy Generation through a Circular Duct With Different Shaped Longitudinal Fins for Laminar Flow,” Int. J. Heat Mass Transfer, **48**, pp. 171–181.
[11] Bhatia, R. S., and Webb, R. L., 2001, “Numerical Study of Turbulent Flow and Heat Transfer in Micro-Fin Tubes-Part1, Model Validation,” J. Enhanced Heat Transfer, **8**, pp. 291–304.
[12] Liu, X. Y., and Jensen, M. K., 1999, “Numerical Investigation of Turbulent Flow and Heat Transfer in Internally Finned Tubes,” J. Enhanced Heat Transfer, **6**, pp. 105–119.
[13] Wang, Q. W., Lin, M., and Zeng, M., 2008, “Effect of Blocked Core-Tube Diameter on Heat Transfer Performance of Internally Longitudinal Finned Tubes,” Heat Transfer Eng., **29**, pp. 107–115.
[14] Tsai, S. F., Sheu, T. W. H., and Lee, S. M., 1999, “Heat Transfer in a Conjugate Heat Exchanger With a Wavy Fin Surface,” Int. J. Heat Mass Transfer, **42**, pp. 1735–1745.
[15] Jang, J. Y., and Chen, L. K., 1997, “Numerical Analysis of Heat Transfer and Fluid Flow in a Three-Dimensional Wavy-Fin and Tube Heat Exchanger,” Int. J. Heat Mass Transfer, **40**, pp. 3981–3990.
[16] Lozzaa, G., and Merlob, U., 2001, “An Experimental Investigation of Heat Transfer and Friction Losses of Interrupted and Wavy Fins for Fin-and-Tube Heat Exchangers,” Int. J. Refrig., **24**, pp. 409–416.
[17] Leu, J. S., Liu, M. S., Liaw, J. S., and Wang, C. C., 2001, “A Numerical Investigation of Louvered Fin-and-Tube Heat Exchangers Having Circular and Oval Tube Configurations,” Int. J. Heat Mass Transfer, **44**, pp. 4235–4243.
[18] Doormal, J. P. V., and Raithby, G. G., 1984, “Enhancement of the SIMPLE Method for Predicting Incompressible Fluid Flows,” Numer. Heat Transfer, **7**, pp. 147–163.
[19] Kline, S. J., and McClintock, F. A., 1953, “Describing Uncertainties in Single-Sample Experiments,” Mech. Eng. (Am. Soc. Mech. Eng.), **75**, pp. 3–8.
[20] Webb, R. L., 1994, *Principles of Enhanced Heat Transfer*, Wiley, p. 210.

Jeremy Rice

Amir Faghri[1]
e-mail: amir.faghri@uconn.edu

Department of Mechanical Engineering,
University of Connecticut,
Storrs, CT 06269

Thermal and Start-Up Characteristics of a Miniature Passive Liquid Feed DMFC System, Including Continuous/Discontinuous Phase Limitations

The thermal and start-up characteristics of a passive direct methanol fuel cell system are simulated using a numerical model. The model captures both the thermal characteristics of the fuel cell and the passive fuel delivery system using a multifluid model approach. Since the fuel cell is run without any active temperature control, the temperature may rise until the convective and evaporative cooling effects balance the heat produced in the chemical reactions. The cell temperature can vary as much as 20°C, and it is vital to model the thermal effects for accurate results. The numerical model also includes continuous and discontinuous phase limitations, as well as a probabilistic spread of the porous properties. These added physical characteristics qualitatively portray the departure of carbon dioxide from the anode side of the fuel cell. [DOI: 10.1115/1.2891156]

Introduction

A passive direct methanol fuel cell (DMFC) [1–7] is an ideal candidate for many portable applications because of its capability to have an extended life for each refueling and its reduction in weight compared to a conventional battery. One of the leading benefits of a DMFC is that the methanol can be stored in its liquid state, and has the potential to be delivered by passive means, making all the power produced available for external work. One of the major issues encountered in designing a DMFC is controlling the amount of methanol crossover. Methanol crossover is methanol that diffuses through the membrane and reacts at the cathode catalyst layer. A dilute methanol solution is usually delivered to the anode in order to reduce the amount of crossover. The design of a DMFC entails a method to deliver this dilute solution.

Water and air management issues related to passive delivery were addressed recently [8]. There has also been substantial development of passively operated DMFCs that are air breathing. Casio, DuPont, Motorola, Samsung, Toshiba, Fujikura, and others have all undertaken research in their development.

A passive fuel delivery system that can deliver a dilute methanol solution to the anode from a pure methanol fuel source has been developed by Guo and Faghri [6–8]. This delivery system utilizes several porous layers, in which the methanol can transport, mainly through diffusion in the liquid phase, to the anode. In this system, only an initial supply of water is needed in the water storage layer. The additional water needed to dilute the methanol concentration at the anode comes from the by-products of the chemical reaction. This passive system, including a fuel cell, was modeled with a two-phase model that used a multifluid approach [9], but used an isothermal assumption.

There has been extensive development of other numerical models for fuel cells. García et al. [10] developed a semianalytical solution for a one-dimensional model for a DMFC. This model used a single phase approach, and omitted the thermal effects. Chen and Zhao [11] also developed a one-dimensional model for DMFC that included the thermal effects, but was still a single phase model. Nam and Kaviany [12] developed a one-dimensional model for a proton exchange membrane fuel cell (PEMFC) that included both multiphase transport effects and thermal effects.

There are also several multidimensional models in addition to Ref. [9]. Wang and Wang [13] used a mixture model to model the multiphase transport in a DMFC. They incorporated an isothermal assumption in their model. Pasaogullari and Wang [14,15] also used the multiphase mixture model to study PEMFCs, but incorporated an isothermal assumption. Hwang [16] developed a single phase model that included both thermal effects and Stefan–Maxwell diffusion in a PEMFC. Siegel et al. [17] as well as Wang and Wang [18] developed a multiphase model that included thermal effects in a PEMFC. There is a large body of fuel cell models that have been reviewed by Wang [19] and Faghri and Guo [20].

None of the aforementioned multiphase models take into account the local variability of porous properties or the irreducible saturation limits, presently called the continuous/discontinuous phase limitation, in the liquid and vapor phases. The continuous phase limitation is well documented in the open literature [21], as well as the local variability in pore properties [22]. The present simulations utilize a multifluid model approach to simulate the transport in the liquid and gas phases separately for the fuel cell and the fuel cell delivery system. A statistical distribution function is used to create the local pore properties, as well as the continuous phase limitation, which directly relates to connectivity of the pores. The model also employs the energy equation, which is important in passively operated fuel cells, since no forced convection effects are available to keep the cell operating at a nearly constant temperature.

Problem Formulation

The operation of a fuel cell is examined in two parts. First, the cell polarization is characterized when a dilute methanol solution is applied directly to the anode. The methanol solution is delivered to the fuel cell via natural convection, as presented in Fig. 1. Second, the fuel cell start-up characteristics of a passive fuel delivery system are examined. A schematic of the passive fuel de-

---

[1] Corresponding author.

Contributed by the Heat Transfer Division of ASME for publication in the JOURNAL OF HEAT TRANSFER. Manuscript received December 19, 2006; final manuscript received August 7, 2007; published online April 22, 2008. Review conducted by Yogendra Joshi.

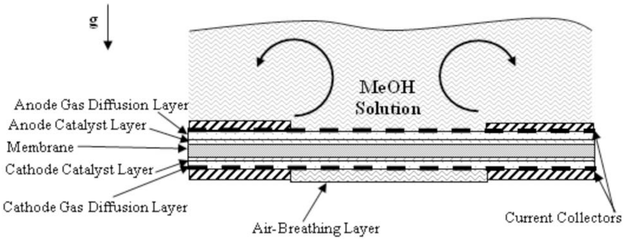

Fig. 1 Schematic of the setup for DMFC polarization tests

livery system and the membrane exchange assembly is presented in Fig. 2. There are eight layers shown. Each one of these layers has a function.

1. MeOH distribution layer: Methanol wets this region and water does not. This region prevents backdiffusion of water into the methanol storage media.
2. H_2O storage layer: Provides an initial water supply, and acts as an additional diffusion region for methanol to control the methanol concentration at the anode.

3 and 7. Gas diffusion layers: Electrically conductive and also an additional diffusion layer so that fuel and gas can transport under the ribs to the catalyst layers.

4–6. Membrane exchange assembly: Contains catalyst layers and proton exchange membrane; is where chemical reactions occur and hydrogen protons are separated from the electrons.

8. Air-breathing layer: A hydrophobic layer to prevent contaminants from entering the system. Also, since it is hydrophobic, water does not block the passage ways of oxygen.

The region above the ribs on the fuel cell and next to the water storage and methanol distribution layers is vacant. The purpose of this region is to provide a flow path for the gas produced in the oxidation reaction to be released from the cell. The closer to the cell the entry to this region is, the lower the methanol concentration, and therefore, the lower the methanol loss due to vaporization.

Governing Equations

Since all the regions modeled encompass a porous region (Regions 1–8), a volume average formulation is utilized from Faghri and Zhang [23]. Methanol and water are the only components considered in the liquid phase, while methanol, water, oxygen, carbon dioxide, and nitrogen are considered to exist in the gas phase. The continuity equations for the liquid and gas phases, in terms of the liquid saturation s and the intrinsic phase average velocities, are as follows:

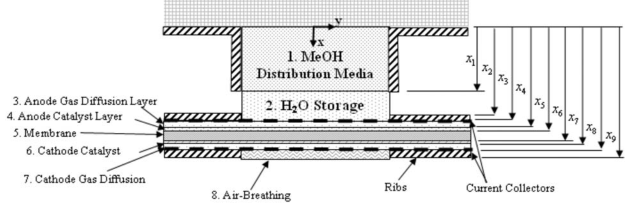

Fig. 2 Schematic of the DMFC fuel delivery system

$$\frac{\partial}{\partial t}(\varepsilon s \rho_l) + \nabla \cdot (\varepsilon s \rho_l \langle \mathbf{V}_l \rangle^l) = \dot{m}_l''' \tag{1}$$

$$\frac{\partial}{\partial t}(\varepsilon(1-s)\rho_g) + \nabla \cdot (\varepsilon(1-s)\rho_g \langle \mathbf{V}_g \rangle^g) = \dot{m}_g''' \tag{2}$$

The mass generation terms are a sum of the reaction rates (subscript R) and the mass transfer rates from the gas to the liquid phase (subscript T) of each component.

$$\dot{m}_l''' = \sum_i \dot{m}_{R,l,i}''' + \sum_i \dot{m}_{T,gl,i}''' \tag{3}$$

$$\dot{m}_g''' = \sum_i \dot{m}_{R,g,i}''' - \sum_i \dot{m}_{T,gl,i}''' \tag{4}$$

The momentum equations for both phases are satisfied by Darcy's law, with an electro-osmotic drag term in the liquid momentum equation [20].

In liquid momentum,

$$\varepsilon s \langle \mathbf{V}_l \rangle^l = -\frac{k_{rl}\mathbf{K}}{\mu_l}(\nabla p_l - \rho_l \mathbf{g}) + \frac{n_d M_l}{\rho_l}\frac{\mathbf{I}_p}{F}, \quad s > s_{ir,l}$$

$$\varepsilon s \langle \mathbf{V}_l \rangle^l = 0, \quad s \le s_{ir,l} \tag{5}$$

In gas momentum,

$$\varepsilon(1-s)\langle \mathbf{V}_g \rangle^g = -\frac{k_{rg}\mathbf{K}}{\mu_g}(\nabla p_g - \rho_g \mathbf{g}), \quad s < s_{ir,g}$$

$$\varepsilon(1-s)\langle \mathbf{V}_g \rangle^g = 0, \quad s \ge s_{ir,g} \tag{6}$$

The momentum equations account for an irreducible saturation limit in the liquid and gas phases. In the liquid phase, if the saturation is below the irreducible saturation limit, the liquid phase is no longer continuous; therefore, the velocity approaches zero. The same is true in the gas phase when the saturation is above the irreducible saturation limit. Since this value represents the continuous/discontinuous limit for a phase, it is henceforth called the continuous phase limitation. A schematic of a porous zone with continuous and discontinuous phase regions is presented in Fig. 3. Hysteric effects can be captured using this model, because the saturation of the porous material exhibits a history-dependent behavior. The increase in viscous resistance due to each void being partially filled with a particular phase is accounted for by the relative permeability.

$$k_{rl} = s^3 \tag{7}$$

$$k_{rg} = (1-s)^3 \tag{8}$$

The gas pressure and the liquid pressure are related by the capillary pressure.

$$p_c = p_g - p_l = \sigma \cos\theta \left(\frac{\varepsilon}{K}\right)^{1/2} J(s) \tag{9}$$

$$J(s) = \begin{cases} 1.417(1-s) - 2.120(1-s)^2 + 1.263(1-s)^3, & \theta < \pi/2.0 \\ 1.417s - 2.120s^2 + 1.263s^3, & \theta \ge \pi/2.0 \end{cases} \tag{10}$$

There are several species in an air-breathing DMFC system, including water, methanol, oxygen, carbon dioxide, and nitrogen. The species equations in the liquid and gas are as follows:

$$\frac{\partial}{\partial t}(\varepsilon s \rho_l \omega_{l,i}) + \nabla \cdot (\dot{\mathbf{m}}_{l,i}'') = \dot{m}_{l,i}''' \tag{11}$$

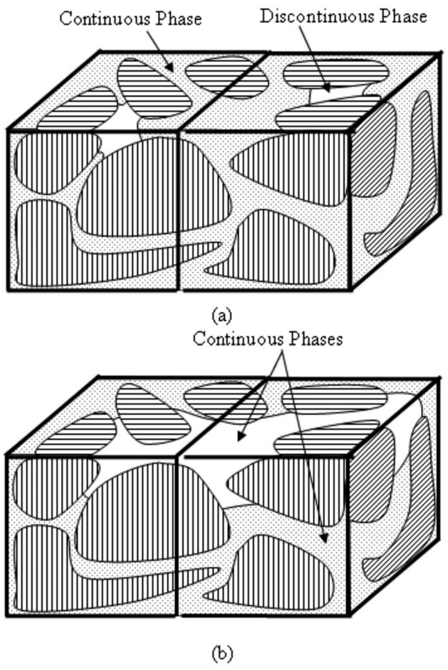

Fig. 3 Schematic of a porous zone with (*a*) one continuous phase and one discontinuous phase and (*b*) two continuous phases

$$\frac{\partial}{\partial t}(\varepsilon(1-s)\rho_g\omega_{g,i}) + \nabla\cdot(\dot{\mathbf{m}}''_{g,i}) = \dot{m}'''_{g,i} \tag{12}$$

The total mass flux (the sum of the advection and diffusion fluxes) of each species is represented by $\dot{\mathbf{m}}_{l,i}$ and $\dot{\mathbf{m}}_{g,i}$ in the liquid and gas phases, respectively.

Liquid species mass flux,

$$\dot{\mathbf{m}}''_{l,i} = \varepsilon s\rho_l\langle\mathbf{V}_l\rangle^l\omega_{l,i} - [\varepsilon s]^\tau\rho_l D_{l,12}\nabla\omega_{l,i}, \quad s > s_{ir,l}$$

$$\dot{\mathbf{m}}''_{l,i} = 0, \quad s \le s_{ir,l} \tag{13}$$

Gas species mass flux,

$$\dot{\mathbf{m}}''_{g,i} = \varepsilon(1-s)\rho_g\langle\mathbf{V}_g\rangle^g\omega_{g,i} - \sum_{j=1}^{N-1}[\varepsilon(1-s)]^\tau\rho_g D_{\mathrm{eff},ij}\nabla\omega_{g,j}, \quad s < s_{ir,g}$$

$$\dot{\mathbf{m}}''_{g,i} = 0, \quad s \ge s_{ir,g} \tag{14}$$

The effective diffusivity in the gas phase can be calculated from the Stefan–Maxwell equation after some mathematical manipulation [23].

$$[D_{\mathrm{eff},ij}] = \mathbf{A}^{-1}\mathbf{B} \tag{15}$$

$$A_{ii} = -\frac{\omega_{g,i}M_g^2}{D_{iN}M_NM_i} - \sum_{\substack{k=1\\k\neq i}}^{N}\frac{\omega_{g,k}M_g^2}{D_{ik}M_kM_i},$$

$$A_{ij} = \omega_{g,i}\frac{M_g^2}{M_i}\left(\frac{1}{D_{ij}M_j} - \frac{1}{D_{iN}M_N}\right), \quad i\neq j \tag{16}$$

$$B_{ii} = -\frac{M_g}{M_i}\left(1-\frac{M_g\omega_{g,i}}{M_i}\right) - \frac{M_g^2\omega_{g,i}}{M_iM_N},$$

$$B_{ij} = \frac{M_g^2\omega_{g,i}}{M_i}\left(\frac{1}{M_j} - \frac{1}{M_N}\right), \quad i\neq j \tag{17}$$

For the condensable gases, the liquid and vapor phases are considered to be in thermal dynamic equilibrium. Equilibrium is found using Raoult's law, where the saturation pressure is calculated by the Clausius–Clapeyron equation.

$$\omega_{g,i} = \beta_i\omega_{l,i}$$

$$\beta_i = \frac{M_lp_{\mathrm{ref}}}{M_gp_{\mathrm{op}}}\exp\left(\frac{h_{fg}M_i}{R}\left(\frac{1}{T_{\mathrm{ref}}} - \frac{1}{T}\right)\right) \tag{18}$$

The energy equation used in the fuel cell model is as follows:

$$\frac{\partial}{\partial t}(\varepsilon s\rho_lh_l + \varepsilon(1-s)\rho_gh_g + (1-\varepsilon)h_s) + \sum_i \nabla\cdot(\dot{\mathbf{m}}''_{l,i}h_{l,i} + \dot{\mathbf{m}}''_{g,i}h_{g,i})$$
$$= \nabla\cdot(k_{\mathrm{eff}}\nabla T) + \nabla\cdot(\phi_m\sigma_m\nabla\phi_m) + \nabla\cdot(\phi_c\sigma_c\nabla\phi_c) \tag{19}$$

where the enthalpy of each phase is as follows:

$$h_{l,i} = \int_{T_{\mathrm{ref}}}^{T} c_{p_{l,i}}dT + h_{l,i}^0 = \bar{h}_{l,i} + h_{l,i}^0 \tag{20}$$

$$h_{g,i} = \int_{T_{\mathrm{ref}}}^{T} c_{p_{g,i}}dT + h_{g,i}^0 = \bar{h}_{g,i} + h_{g,i}^0 \tag{21}$$

In the present simulations, the specific heat is considered to be constant. The enthalpy can be written as the sensible heat $\bar{h}$ plus the heat of formation, h^0. Taking the species mass balance into consideration, the energy equation can be rewritten in terms of the sensible heat transport and the heat generation terms that coincide with the reaction rates and phase change.

$$\frac{\partial}{\partial t}(\varepsilon s\rho_l\bar{h}_l + \varepsilon(1-s)\rho_g\bar{h}_g + (1-\varepsilon)\bar{h}_s) + \sum_i \nabla\cdot(\dot{\mathbf{m}}''_{l,i}\bar{h}_{l,i} + \dot{\mathbf{m}}''_{g,i}\bar{h}_{g,i})$$
$$= \nabla\cdot(k_{\mathrm{eff}}\nabla T) - \sum_i \dot{m}'''_{l,i}h_{l,i}^0 - \sum_i \dot{m}'''_{g,i}h_{g,i}^0 + \nabla\cdot(\phi_m\sigma_m\nabla\phi_m)$$
$$+ \nabla\cdot(\phi_c\sigma_c\nabla\phi_c) \tag{22}$$

The total sensible enthalpy in each phase is as follows:

$$\bar{h}_l = \sum_i \omega_{l,i}\bar{h}_{l,i} \tag{23}$$

$$\bar{h}_g = \sum_i \omega_{g,i}\bar{h}_{g,i} \tag{24}$$

The effective thermal conductivity is as follows:

$$k_{\mathrm{eff}} = \varepsilon sk_l + \varepsilon(1-s)k_g + (1-\varepsilon)k_s \tag{25}$$

The electrochemistry in the fuel cell is also modeled. The electric potentials of the carbon phase and the membrane phases are as follows:

$$\nabla\cdot(\sigma_c\nabla\phi_c) - R_{\mathrm{ox}} + R_{\mathrm{red}} = 0 \tag{26}$$

$$\nabla\cdot(\sigma_m\nabla\phi_m) + R_{\mathrm{ox}} - R_{\mathrm{red}} = 0 \tag{27}$$

The oxidation and reduction reaction rates are R_{ox} and R_{red}, respectively. The reaction rates are modeled from the expression developed by Meyers and Newman [25].

$$R_{\mathrm{ox}} = a_{\mathrm{ox}}I_{0,\mathrm{ref}}^{\mathrm{MeOH}}\frac{c_{\mathrm{MeOH}}}{c_{\mathrm{MeOH}} + \lambda\exp\left(\alpha_a\eta_a\frac{F}{R_uT}\right)}\exp\left(\alpha_a\eta_a\frac{F}{R_uT}\right) \tag{28}$$

$$R_{\mathrm{red}} = a_{\mathrm{red}} I_{0,\mathrm{ref}}^{\mathrm{O}_2} \frac{\omega_{\mathrm{O}_2}}{\omega_{\mathrm{O}_2,\mathrm{ref}}} \exp\left(-\alpha_c \eta_c \frac{F}{R_u T} \right) \tag{29}$$

The anode and cathode overpotentials are as follows:

$$\eta_a = \phi_c - \phi_m - U^{\mathrm{MeOH}} \tag{30}$$

$$\eta_c = \phi_c - \phi_m - U^{\mathrm{O}_2} \tag{31}$$

The reaction rates for the species equations are as follows: Liquid,

$$\dot{m}'''_{R,l,\mathrm{MeOH}} = -\frac{R_{\mathrm{ox}}}{6F} M_{\mathrm{MeOH}}, \quad \dot{m}'''_{R,l,\mathrm{H_2O}} = \left(-\frac{R_{\mathrm{ox}}}{6F} + \frac{R_{\mathrm{red}}}{2F} \right) M_{\mathrm{H_2O}} \tag{32}$$

Gas,

$$\dot{m}'''_{R,g,\mathrm{CO}_2} = \frac{R_{\mathrm{ox}}}{6F} M_{\mathrm{CO}_2}, \quad \dot{m}'''_{R,g,\mathrm{O}_2} = -\frac{R_{\mathrm{red}}}{4F} M_{\mathrm{O}_2} \tag{33}$$

Initial and Boundary Conditions

The phase saturation, temperature, and species mass fractions all need initialization. The phase saturation is initialized to a value, depending on what zone it is in, and the contact angle.

$$s = s_0, \quad \theta < \pi/2$$

$$s = 0, \quad \theta \geqslant \pi/2 \tag{34}$$

The initial saturation s_0 was assumed to be 0.98 in all the regions except the methanol distribution region, where it was assumed to be unity. The methanol distribution media are initially filled with pure methanol, while every other region contains only water.

$$\omega_{l,\mathrm{MeOH}} = 1, \quad x < x_1$$

$$\omega_{l,\mathrm{MeOH}} = 0, \quad x \geqslant x_1 \tag{35}$$

The initial mass fractions of water and methanol vapor are the saturated values if liquid is present, or equivalent to the ambient values if no liquid is present.

$$\omega_{g,i} = \omega_{g,i,\mathrm{sat}}, \quad s > 0$$

$$\omega_{g,i} = \omega_{g,i,\infty}, \quad s = 0 \tag{36}$$

The gas mass fraction for the rest of the components is broken into two regions.

$$\omega_{g,\mathrm{CO}_2} = 1 - \omega_{g,\mathrm{MeOH}} - \omega_{g,\mathrm{H_2O}}, \quad \omega_{g,\mathrm{O}_2} = \omega_{g,\mathrm{N}_2} = 0, \quad s > 0$$

$$\omega_{g,i} = \omega_{g,i,\infty}, \quad s = 0 \tag{37}$$

The initial temperature is equal to the ambient temperature.

The boundary conditions are as follows: At the symmetry $y=0$; at the top of the domain $y=y_1$ and $x<x_1$, $x_2<x<x_3$, $x>x_8$, or $y=y_2$, and $x_3<x<x_8$,

$$\nabla \Phi \cdot \mathbf{n} = 0, \quad \Phi = p_l, p_g, \omega_{l,i}, \omega_{g,i}, T, \phi_c, \phi_m \tag{38}$$

At gas release channel, $y=y_1$ and $x_1<x<x_2$,

$$\nabla \Phi \cdot \mathbf{n} = 0, \quad \Phi = p_l, \omega_{l,i}, \omega_{g,i}, T$$

$$p_g = 0 \tag{39}$$

At the entrance of the methanol distribution media, $x=0$,

$$\nabla \Phi \cdot \mathbf{n} = 0, \quad \Phi = p_g, \omega_{g,i}, T$$

$$p_l = 0$$

$$\omega_{l,\mathrm{MeOH}} = 1 \tag{40}$$

At the surface of the air-breathing layer, $x=x_9$,

$$p_g = 0$$

$$\langle \mathbf{V}_l \rangle^l \cdot \mathbf{n} = 0$$

$$-[\varepsilon(1-s)]^{\tau} \nabla \omega_{g,i} \cdot \mathbf{n} = h_m(\omega_{g,i} - \omega_{g,i,\infty})$$

$$-k_{\mathrm{eff}} \nabla T \cdot \mathbf{n} = h(T - T_{\mathrm{ref}}) + \sigma_{\mathrm{SB}}(T^4 - T_{\mathrm{ref}}^4) \tag{41}$$

The electric potential boundary conditions are as follows:

$$x = x_3, \quad \phi_c = 0$$

$$x = x_4, \quad x = x_7, \quad \nabla \phi_m \cdot \mathbf{n} = 0$$

$$x = x_5, \quad x = x_6, \quad \nabla \phi_c \cdot \mathbf{n} = 0$$

$$x = x_8, \quad \phi_c = V_{\mathrm{cell}} \tag{42}$$

When methanol is applied directly to the anode surface, the temperature of the solution is modeled using a lump capacitance method, while the methanol concentration is considered to be constant because the amount of methanol used is much less than the total initial mass of methanol. The temperature of the methanol solution is calculated by

$$\int \rho c_p \frac{dT_{\mathrm{fuel}}}{dt} dV = \int h(T_{\mathrm{AS}} - T_{\mathrm{fuel}}) dA \tag{43}$$

where the anode surface temperature at $x=x_4$ is denoted by T_{AS}. The heat leaving the anode surface is calculated by

$$-k_{\mathrm{eff}} \nabla T_{\mathrm{AS}} \cdot \mathbf{n} = h(T_{\mathrm{fuel}} - T_{\mathrm{AS}}) \tag{44}$$

The methanol mass transport is modeled by

$$\dot{\mathbf{m}}''_{l,i} = \varepsilon s \rho_l \langle \mathbf{V}_l \rangle^l \omega_{l,\mathrm{MeOH}} + h_m(\omega_{\mathrm{fuel,MeOH}} - \omega_{l,\mathrm{MeOH}}) \tag{45}$$

The heat and mass transfer coefficients are taken from the natural convection correlations on a horizontal surface facing up [19].

$$\mathrm{Nu} = 0.54(\mathrm{Gr}\,\mathrm{Pr})^{0.025}, \quad \mathrm{Nu} = \frac{hL}{k}$$

$$\mathrm{Sh} = 0.54(\mathrm{GrSc})^{0.025}, \quad \mathrm{Sh} = \frac{h_m L}{\rho D_{ij}} \tag{46}$$

where the Grashof number is

$$\mathrm{Gr} = \frac{g\rho|\Delta\rho|L^3}{\mu^2} \tag{47}$$

The heat and mass transfer coefficients at the surface of the air-breathing layer are calculated in a similar manner, but the coefficients are taken for a horizontal surface facing down.

$$\mathrm{Nu} = 0.27(\mathrm{Gr}\,\mathrm{Pr})^{0.025}, \quad \mathrm{Nu} = \frac{hL}{k}$$

$$\mathrm{Sh} = 0.27(\mathrm{GrSc})^{0.025}, \quad \mathrm{Sh} = \frac{h_m L}{\rho D_{ij}} \tag{48}$$

Numerical Methodology

In general, the governing equations are discretized using a finite volume formulation. A Gauss–Siedel-type solution procedure is used to solve for the flow variables. Since each phase may be discontinuous, there may be values of zero in the main diagonal of the coefficient matrix. Therefore, special consideration needs to be taken.

Calculation of Phase Saturation and Pressures. The liquid and gas phase continuity equations are solved in a coupled manner. Since a Gauss–Siedel solution procedure is used, the discretized continuity equations can be written as

$$a_{ls} s + a_{pl} p_l = b_l$$

Table 1 Significance of the diagonal values in coefficient matrix

Case	Significant coefficient	Physical meaning
1	$a_{pl}=0$	Liquid discontinuous in all directions
2	$a_{pg}=0$	Gas discontinuous in all directions
3	$a_{pl}\neq 0,\ a_{pg}\neq 0$	Liquid and gas are continuous in at least one direction

$$a_{gs}s + a_{pg}p_g = b_g \tag{49}$$

The solution can be solved in different ways depending on the coefficients in the matrix. There are three different possible cases that may arise. These cases may be solved in different fashions. The different cases are presented in Table 1. The calculation of the phase saturation, and the pressures in each phase, is slightly different for each case.

Case 1.

Step 1: Calculate phase saturation, $s=b_l/a_{ls}$

Step 2: Calculate gas pressure, $p_g(b_g-a_{gs}s)/a_{pg}$

Step 3: Calculate liquid pressure, $p_l=p_g-p_c$

Case 2.

Step 1: Calculate phase saturation, $s=b_g/a_{gs}$

Step 2: Calculate liquid pressure, $p_l(b_l-a_{ls}s)/a_{pl}$

Step 3: Calculate gas pressure, $p_g=p_c-p_l$

Case 3. Since the gas and liquid pressures are related to the capillary pressure, a saturation weighted pressure is solved for

$$\bar{p} = sp_l + (1-s)p_g \tag{50}$$

When this substitution is used, the liquid and gas pressures can be written as a function of the weighted pressure and the capillary pressure

$$p_l = \bar{p} - (1-s)p_c$$

$$p_g = \bar{p} + sp_c \tag{51}$$

This relationship can be inserted into the discretized equation and linearized with respect to the phase saturation.

$$\left(a_{ls} - a_{pl}\frac{\partial((1-s)p_c)^k}{\partial s}\right)s^{k+1} + a_{pl}\bar{p} = b_l - a_{pl}\left(-(1-s)p_c + \frac{\partial((1-s)p_c)}{\partial s}s\right)^k$$

$$\left(a_{gs} + a_{pg}\frac{\partial(sp_c)^k}{\partial s}\right)s^{k+1} + a_{pg}\bar{p} = b_g - a_{pg}\left(sp_c - \frac{\partial(sp_c)}{\partial s}s\right)^k \tag{52}$$

The solution steps for Case 3 are as follows:

Step 1: Calculate phase saturation, $s=\det\begin{bmatrix} b_l' & a_{pl}' \\ b_g' & a_{pg}' \end{bmatrix}/\det\begin{bmatrix} a_{ls}' & a_{pl}' \\ a_{gs}' & a_{pg}' \end{bmatrix}$

Step 2: Calculate liquid pressure, $p_l=(b_l-a_{ls}s)/a_{pl}$

Step 3: Calculate gas pressure, $p_g=(b_g-a_{gs}s)/a_{pg}$

Calculation of Mass Transfer Rates. Since the condensation rate is considered a flow variable, and the methanol mass fraction in the gas phase is a function of the methanol concentration in liquid phase, the discretized equations for methanol mass fraction are as follows:

$$a_l\omega_{l,\text{MeOH}} - \dot{m}'''_{gl,\text{MeOH}} = b_l$$

$$a_g\beta_{\text{MeOH}}\omega_{l,\text{MeOH}} + \dot{m}'''_{gl,\text{MeOH}} = b_g \tag{53}$$

Therefore, the mass fractions are solved by the following:

Step 1: Solve for $\omega_{l,\text{MeOH}}$, $\omega_{l,\text{MeOH}}=(b_l+b_g)/(a_l+a_g\beta_{\text{MeOH}})$

Step 2: Calculate $\omega_{g,\text{MeOH}}$, $\omega_{g,\text{MeOH}}=\beta_{\text{MeOH}}\omega_{l,\text{MeOH}}$

Step 3: Calculate $\dot{m}^{m}_{gl,\text{MeOH}}$, $\dot{m}^{m}_{gl,\text{MeOH}}=b_g-a_g\omega_{g,\text{MeOH}}$

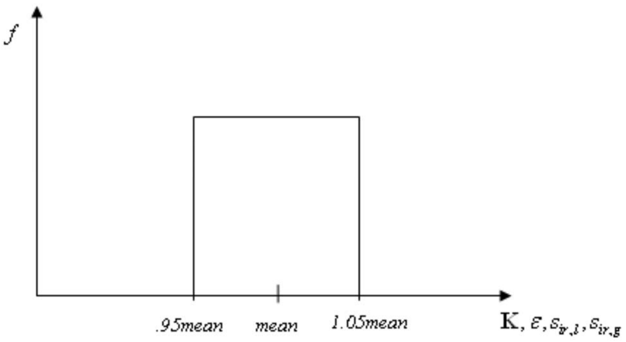

Fig. 4 Probability distribution function *f* for the porous properties

Since the water mass fraction in the liquid phase is determined by the balance of the mass fractions, the mass transfer rate of water cannot be solved in the same fashion as is done with the methanol. A check is performed, which compares the evaporation rate if enough liquid water is present, to the maximum liquid water that can be evaporated.

$$\dot{m}_1''' = b_g - a_g\beta_{\text{H}_2\text{O}}\omega_{l,\text{H}_2\text{O}}$$

$$\dot{m}_2''' = -(\varepsilon s\rho_l\omega_{l,\text{H}_2\text{O}})^n/\Delta t - \int \nabla\cdot\dot{\mathbf{m}}_{l,\text{H}_2\text{O}}dV_{\text{cell}} - \dot{m}'''_{R,l,\text{H}_2\text{O}} \tag{54}$$

The mass transfer rate from the gas phase to the liquid phase is the greater of the above two values.

$$\dot{m}_1''' > \dot{m}_2''', \quad \dot{m}'''_{gl,\text{H}_2\text{O}} = \dot{m}_1'''$$

$$\dot{m}_1''' \leqslant \dot{m}_2''', \quad \dot{m}'''_{gl,\text{H}_2\text{O}} = \dot{m}_2''' \tag{55}$$

This solution method exactly conserves water mass for every scenario.

Solution Procedure. The solution procedure is as follows:

1. solve electric potential, and update reaction kinetics
2. solve for saturation and liquid/gas pressure
3. solve species equations
4. solve energy equation
5. update properties
6. check convergence, repeat, or go to next time step

Porous Property Distribution

The pore properties of the porous materials used in a fuel cell can vary widely from one location to another. Holley and Faghri [22] reported as much deviation as 100% in Toray samples from one location to another. Therefore, using a constant value may give a false representation of the final solution. A random number generator is used by Stearns [26] to generate an evenly distributed spread of the porosity, permeability, and discontinuous phase saturation values within a certain percentage of a mean value. In the current simulations, the spread was chosen arbitrarily to be 5%. The distribution of the porous properties is assumed to be independent of each other; however, they may be better represented as a joint probability distribution function since the porous properties are not independent of each other. The probability distribution function, which represents the data range used in the presented simulations, is presented in Fig. 4.

Results

Before the bulk of the simulations was run, a grid study was performed for the 2*M* methanol feed concentration at an ambient temperature of 293 K. The anode and cathode gas diffusion layers, as well as the membrane, all had ten cells in the x-direction, while the anode and cathode catalyst layers were modeled with five cells in the x-direction. There were 15 cells used for the section of the fuel cell open to the methanol fuel, and 8 cells used for the section of the fuel cell covered by a rib in the y-direction. A polarization curve was made with this grid and compared to a grid with 50% more cells in every section. The cell current density was within 1% at every voltage; therefore, this is the mesh used for the bulk of the simulations. The physicochemical properties used for the simulations are presented in Table 2.

It was found that the cell polarization plots that included the continuous phase limitations were within 2% for the cases that did not include these limitations. However, the way in which CO_2 departed the cell varied dramatically. The continuous gas flow paths in the anode gas diffusion layer are presented in Fig. 5. These flow paths are compared to CO_2 departure sites that were found experimentally. When no continuous phase limitation is considered, CO_2 leaves nearly uniformly from the anode surface, and the entire anode gas diffusion layer is continuous in the gas phase. This results in a nonphysical solution, because CO_2 leaves from discrete locations in the experiment. When the continuous phase limitations are considered along with constant pore properties, carbon dioxide is predicted to leave from discrete locations. A similar result is found when a distributed set of pore properties is considered. However, when looking at a contour plot of CO_2, there is a variation between the constant porous properties and the varying porous properties, as seen in Fig. 6. When the pore properties are considered constant, CO_2 exists across a larger region than the continuous flow path. This observation indicates that the departure sites vary with time. When distributed porous properties are utilized, CO_2 only exists along the continuous flow paths, indicating that the location the CO_2 departs from remains the same. During experimentation, it is noted that CO_2 departure sites remain at the same discrete locations. Therefore, it can be concluded that simulating both the continuous phase limitation and the variation of porous properties yields the most qualitatively accurate result.

The numerical model is validated through a series of polarization curves. These curves were made by starting at a cell voltage of 0.8 V, and stepping down at an increment of 0.02 V. The solution is run for 15 s at each voltage. This approach is slightly different than the experimental approach by Guo and Faghri [6,7], because they operated the cell in constant current mode, but stepped the current from low to high current, which is analogous from stepping from high to low voltage. A comparison of the polarization curves for different methanol solution concentrations is presented in Fig. 7. The numerical results were run with ambient temperatures set to 293 K and 300 K for each methanol concentration. This is the typical temperature fluctuation in the testing environment. It can be seen that the numerical data bound the experimental data in this temperature range.

The mass transport limited reaction rate increases with increasing methanol feed concentration. It also increases with increasing ambient temperature, which results in a higher cell temperature. The current density increases because the reaction kinetics are improved with a temperature increase. It can also be noted that the maximum cell power density occurs at different current densities, depending on the methanol feed concentration. However, the maximum power density occurs in a more tightly bound region when looking at the cell voltage where it occurs. This voltage is between 0.2 V and 0.3 V.

Since the cell polarization simulations are made through a transient process, and the temperature of the cell is not actively controlled, the temperature of the cell is free to rise. The cell temperature rise above the ambient temperature for different methanol feed concentrations is compared to the experimental results in Fig. 8. The cell temperature rise increases with increasing methanol feed concentration. The temperature rise is greater because there is more methanol crossover, which produces more heat. When looking at the different ambient temperatures, the maximum cell temperature rise is slightly greater for the higher ambient temperatures. The increasing temperature increase is due to the enhanced reaction kinetics with increasing cell temperature.

The effects of the relative humidity of the ambient environment are also examined. The cell polarization and temperature rise of a $2M$ solution operating in dry air as well as 80% humidified air are presented in Fig. 9. The cell performs slightly better at the higher humidity, because there is less evaporative cooling, and the cell temperature increases as a result. The humidity of the air may not be significant for the shorter duration tests; however, in order for the operation of a system using only a pure methanol solution to be stable, the water evaporated must be less than or equal to the total water produced. To examine these rates, we introduce the usage ratio η for useful current, methanol evaporation, and water evaporation.

$$\eta_{\text{current}} = \frac{\mathbf{I}}{(\mathbf{I}+\mathbf{I}_c)}, \quad \eta_{\text{MeOH,evap}} = \frac{6F\int \dot{m}'''_{\text{MeOH},lv}dV}{M(\mathbf{I}+\mathbf{I}_c)A_{\text{cell}}},$$

$$\eta_{\text{current}} = \frac{\mathbf{I}}{(\mathbf{I}+\mathbf{I}_c)}, \quad \eta_{\text{MeOH,evap}} = \frac{6F\int \dot{m}'''_{\text{MeOH},lv}dV}{M(\mathbf{I}+\mathbf{I}_c)A_{\text{cell}}}, \tag{56}$$

It compares the fuel used to produce useful work, the fuel evaporated, and the water evaporated, compared to the total amount of fuel used in chemical reactions. The usage ratio is presented in Fig. 10 versus the current density for varying relative humidities and cell temperatures. The usage ratio of water is less than unity for all the operating conditions, except for the dry air at 300 K and low current density. This region is acceptable, because it is far from the ideal operating range. Another beneficial characteristic of the fuel cell is that the usage ratio of the useful current density is nearly maximum at the maximum power density. The methanol vapor carried out from the system with the release of CO_2 is approximately one-fifth the magnitude of the total methanol consumed in chemical reactions. Therefore, approximately as much methanol is wasted via crossover and evaporation as methanol used to produce work.

The cell start-up power density and temperature rise for a cell operated at constant voltages of 0.25 V and 0.35 V are presented in Fig. 11. The temperature is taken on the surface of the cathode catalyst layer along the centerline of the domain. The 0.35 V case, which is similar to the case run by Guo and Faghri [6,7], exhibits the same start-up characteristics. In the experimental work, it was noted that is took approximately 2 min for the cell to start to produce power, and approximately 5 min for the cell power density to reach a stable operating state, where the power density flattens out. Also, it was noted that the cell temperature rose for the first 35 min before the cell temperature reached an equilibrium state. The time scales of the experimental measurements and the numerical simulations are the same. However, the temperature rise of the numerical results is higher than the experiment. This may be due to convective-cooling losses from the side surfaces of the fuel cell, which are not modeled. While operating at a cell voltage of 0.25 V, the sustainable power density was approximately 7 mW/cm^2 higher than the power density achieved when operating the fuel cell at 0.35 V. This result is what would be expected based on the cell polarization. Therefore, the remaining results are from the 0.25 V cases.

The effects of the effective air-breathing thickness (L/ε) on the cell start-up are presented in Fig. 12. It can be noted that the stable power density is approximately equivalent for effective air-breathing thicknesses of 2.5–7.5 mm. However, when the effective thickness is increased to 12.5 mm, the power density decreases, because the oxygen transport is reduced. The methanol concentration at the surface of the anode gas diffusion layer was found to increase to a maximum value at 12–15 min. After this time, the methanol concentration decreased and asymptotically approached a steady value. The methanol concentration exhibits

Table 2 Physicochemical properties

Parameter		Value	Ref.
	$K/\varepsilon/\tau$ (m^2/unitless/unitless)	θ, $H_2O/MeOH$ (rad)	
MeOH distribution	$2.5E-13/0.3/1$	$1.33\pi/0$	Assumed
H_2O storage	$1E-10/0.9/1$	$0/0$	Assumed
agdl	$1E-11/0.7/1$	$0/0$	Assumed
acl	$2.5E-12/0.6/1.8$	$0/0$	Assumed
mem.	$1E-13/0.5/1.8$	$0/0$	Assumed
ccl	$2.5E-11/0.6/1.8$	$\frac{\pi}{3}/0$	Assumed
cgdl	$1E-10/0.7/1$	$1.33\pi/1.33\pi$	Assumed
Diffusivity, gas phase, $D_{ij}=D_{ji}$ (m^2/s)	O_2/CO_2 O_2/H_2O O_2/N_2 CO_2/H_2O CO_2/N_2 H_2O/N_2	$\left.\begin{matrix}0.159\times10^{-4}\\0.244\times10^{-4}\\0.202\times10^{-4}\\0.162\times10^{-4}\\0.160\times10^{-4}\\0.242\times10^{-4}\end{matrix}\right\}$ at 293 K, 101.325 kPa	Lide [27] for proportionality of form $D_{ij}\propto p^{-1}T^{3/2}$
	$\left.\begin{matrix}O_2/MeOH\\CO_2/MeOH\\H_2O/MeOH\\MeOH/N_2\end{matrix}\right\}$ Assumed	$\begin{pmatrix}-0.06954+\\4.5986\times10^{-4}T+\\9.4979\times10^{-7}T^2\end{pmatrix}\times10^{-4}$	Yaws [28]
Diffusivity, liquid phase (m^2/s)	$MeOH/H_2O$	$10^{(-5.4163-999.778/T)}$	Yaws [29]
Density, $\rho_{l,i}$ (kg/m^3)	H_2O	$\exp\begin{pmatrix}6.9094-2.0146\times10^{-5}(T-273)-\\5.9868\times10^{-6}(T-273)^2+2.5921\times10^{-8}(T-273)^3-\\9.3244\times10^{-11}(T-273)^4+1.2103\times10^{-13}(T-273)^5\end{pmatrix}$	Faghri and Zhang [23]
	MeOH	$244.4\times0.224^{(-(1-(T/513))^{2/7})}$	Yaws [29]
Electro-osmotic drag coefficient (mol/mol)	n_d	2.5	Ren et al. [24]
Electric conductivity (Ω^{-1} m^{-1})	σ_c σ_m	4000 3.4	Kulikovsky et al. [30]
Transfer coefficient	α_a α_c	0.82 0.76	Fit to data
Specific area (m^{-1})	a_{ax} a_{red}	17.8 43,478	Fit to data Assumed
Exchange current	$I_{0,\mathrm{ref}}^{\mathrm{MeOH}}$	$94.25\exp(35{,}570/R(1/353-1/T))$	Wang and Wang [13]
Density (A/m^2)	$I_{0,\mathrm{ref}}^{O_2}$	$0.04222\exp(732{,}000/R(1/353-1/T))$	
Oxidation constant (mol/cm^3)	λ	4.4×10^{-9}	Fit to data
Reduction reference mass fraction (kg/kg)	$m_{O_2,\mathrm{ref}}$	0.23	Wang and Wang [13]
Thermodynamic potential (V)	U^{MeOH}	-0.0229	Meyers and Newman [25]
	U^{O_2}	1.24	Wang and Wang [13]
Distance (m)	x_1 x_3-x_1 x_4-x_3 x_5-x_4 x_6-x_5 x_7-x_6 x_8-x_7 y_1 y_2	1×10^{-2} 1.2×10^{-3} 1.5×10^{-4} 2.3×10^{-5} 1.8×10^{-4} 2.3×10^{-5} 1.5×10^{-4} 3.25×10^{-3} 5×10^{-3}	

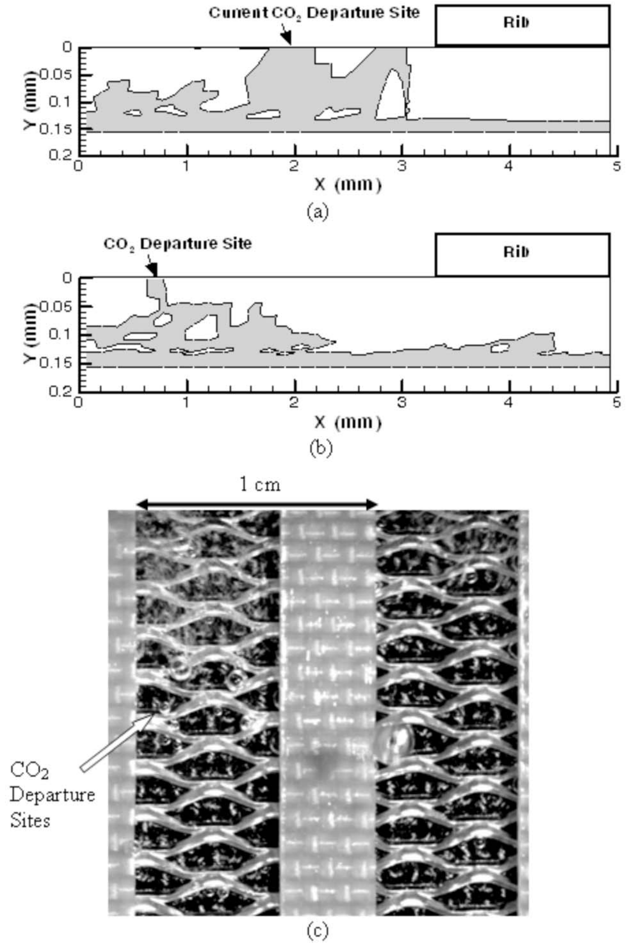

Fig. 5 Continuous phase flow paths of CO_2 with (*a*) constant pore properties and (*b*) distributed pore properties compared to the (*c*) distribution of CO_2 bubbles generated experimentally at the anode gas diffusion layer

this trend because the water production rate in the chemical reaction is greater than the water evaporation rate. Therefore, the methanol feed concentration at the anode becomes more dilute, until the production and generation rates of water reach equilibrium.

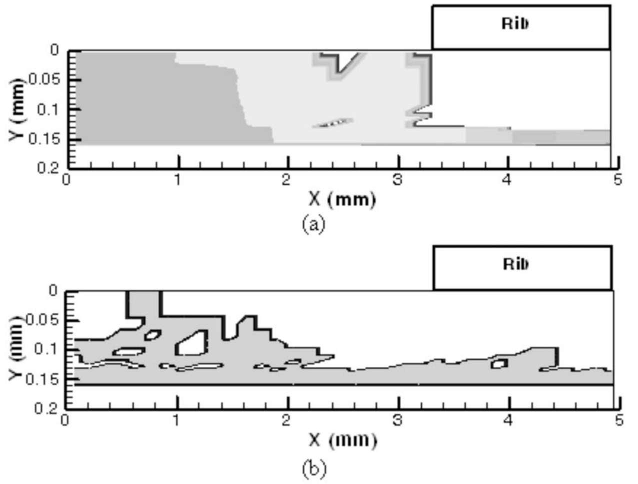

Fig. 6 Contour plots of CO_2 in the anode gas diffusion layer for (*a*) constant pore properties and (*b*) distributed pore properties

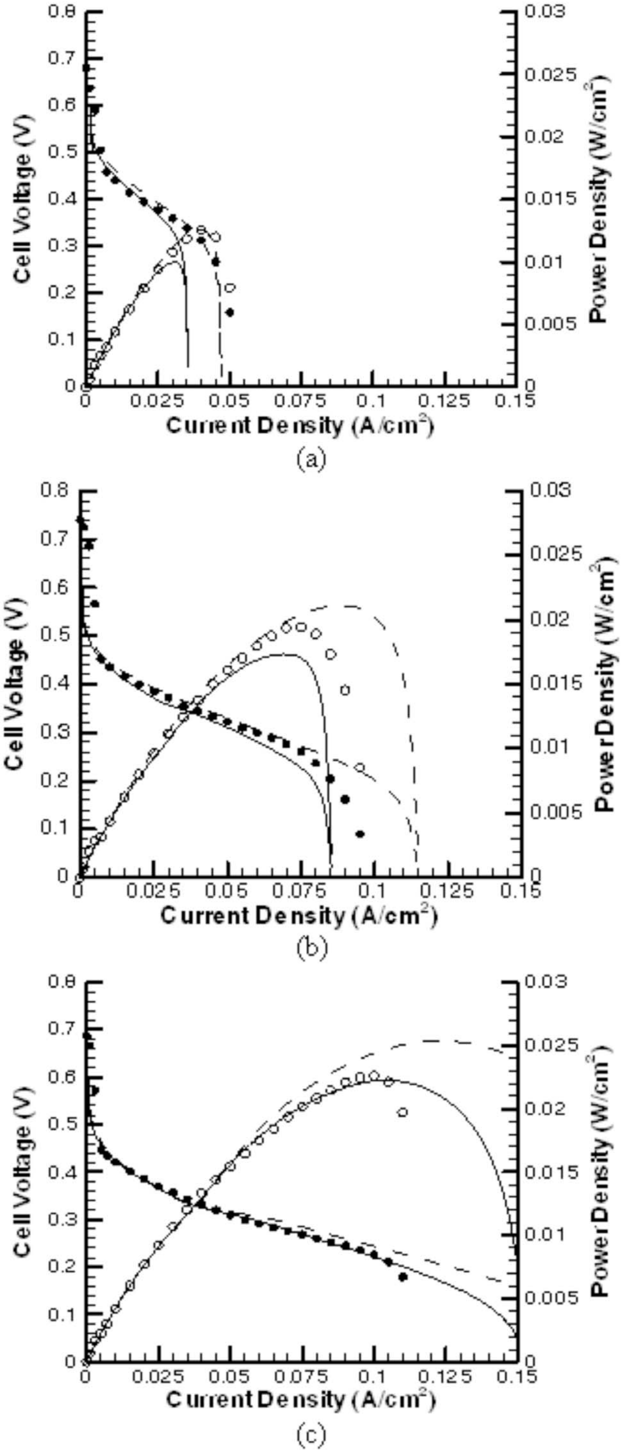

Fig. 7 Comparison of cell polarization and power density of numerical (lines, solid $T_{ref}=293$ K, dashed $T_{ref}=300$ K) and experimental results from Guo and Faghri [7] (symbols) for (*a*) 1*M*, (*b*) 2*M*, and (c) 3*M* methanol solutions

The water usage, η_{H_2O}, and the cell temperature rise are presented in Fig. 13 for different air-breathing effective thicknesses. It can be seen that the cell temperature increases with increasing air-breathing thickness because the evaporation rate of water decreases. For an effective air-breathing length of 2.5 mm, the water

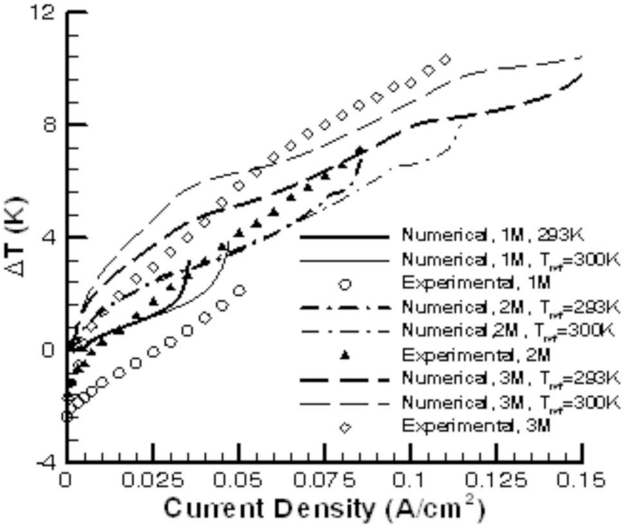

Fig. 8 Cell temperature rise, $\Delta T = T_{\mathrm{cathode}} - T_{\mathrm{ref}}$, versus current density for different methanol concentrations; experimental results from Guo and Faghri [7]

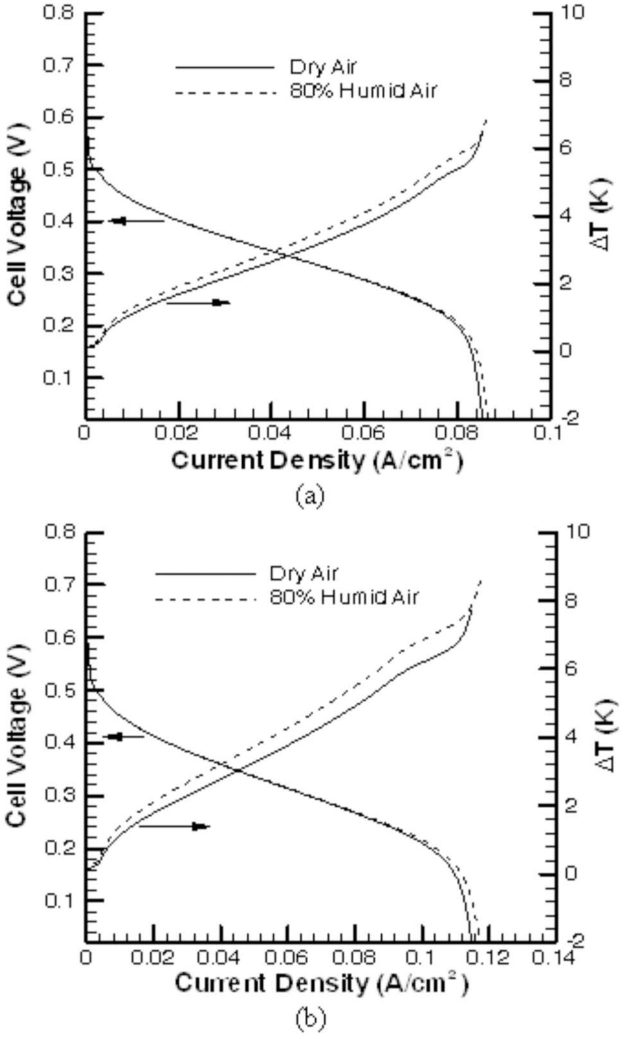

Fig. 9 Effect of relative humidity on cell polarization and temperature rise at ambient conditions of (*a*) 293 K and (*b*) 300 K

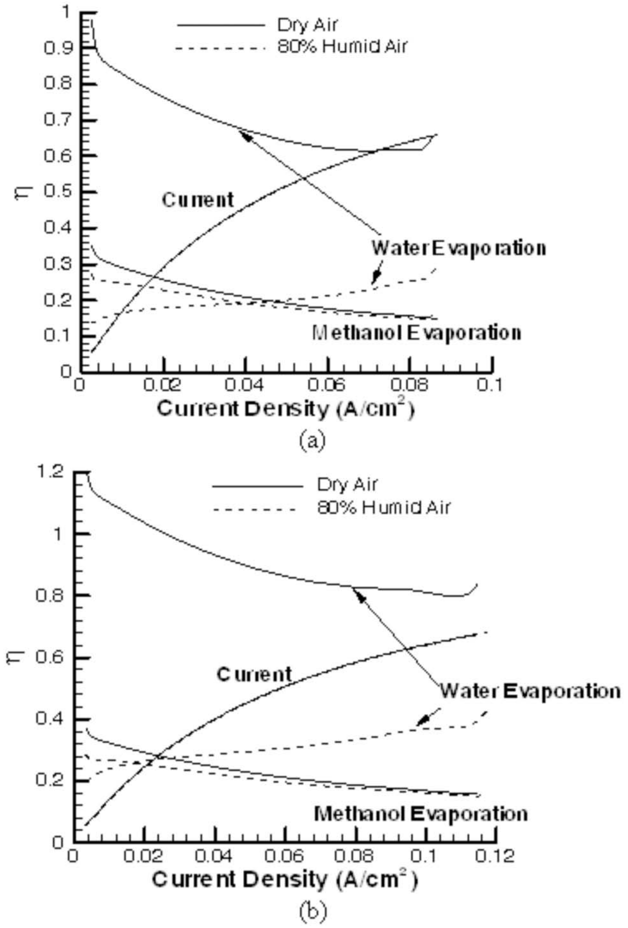

Fig. 10 Methanol crossover reaction, and methanol and water evaporation rates normalized by the stoichiometric coefficient and the sum of the cell current density and the crossover current for 2*M* methanol feed concentration with ambient temperatures of (*a*) 293 K and (*b*) 300 K

consumption ration rises slightly higher than 1. This indicates that the water produced is not enough to make up for the water loss due to evaporation. Therefore, in order for this system to run continuously, a water supply is needed for water makeup. When the air-breathing thickness is increased, the water consumption ratio is less than 1. However, if this value is too small, the water

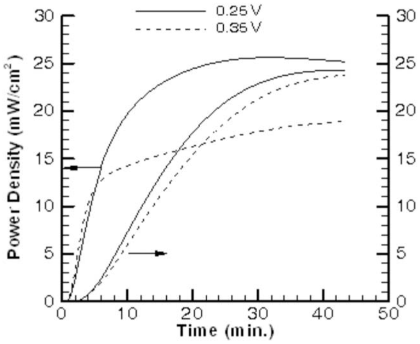

Fig. 11 Cell start-up with varying cell voltage and a water storage layer thickness and porosity of 1.2 mm and 0.9, respectively, a methanol distribution porosity of 0.3, and an effective air-breathing thickness of 5 mm at an ambient temperature of 293 K

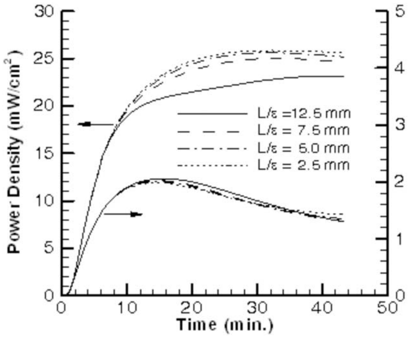

Fig. 12 Cell start-up with varying effective air-breathing lengths and a water storage layer thickness and porosity of 1.2 mm and 0.9, respectively, a methanol distribution porosity of 0.3, a cell voltage of 0.25 V, and an ambient temperature of 293 K

produced will eventually dilute the methanol concentration at the anode to a level where the cell performance begins to degrade. Nonetheless, the system will maintain its stability.

The methanol consumption ratio due to current that contributes to useful work and methanol evaporation are presented in Fig. 14. It can be noted that the consumption ratio of the methanol current decreases with increasing air-breathing thickness. However, increasing the air-breathing thickness decreases the evaporation rate of methanol, because less carbon dioxide is generated at the anode, thus carrying less methanol vapor with it.

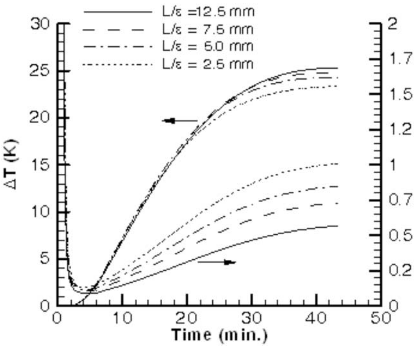

Fig. 13 Cell start-up temperature rise and water consumption ratio with a varying air-breathing effective length

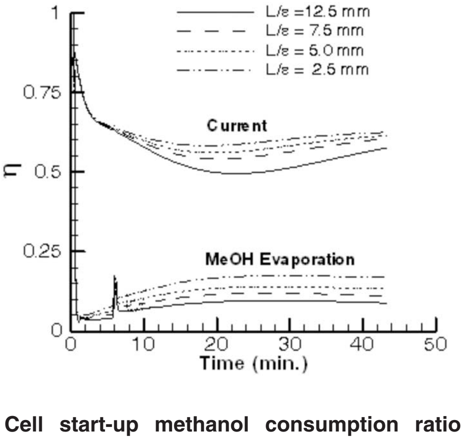

Fig. 14 Cell start-up methanol consumption ratio of the methanol used to produce useful work, and methanol evaporated

Conclusions

The temperature of a passive fuel cell was found to be a vital component of the numerical models, as the maximum cell power can substantially change with temperature. A numerical model is used, which captures both continuous and discontinuous phase regimes in a porous material. It was found that these limitations can capture the phenomena of CO_2 leaving from preferred sights, and not continuously from the entire domain. The start-up conditions of a passive fuel delivery system were characterized. Water management was found to be crucial to stable operation, and it was found that stability could be increased by increasing the air-breathing layer effective thickness.

Acknowledgment

This research was funded by the agreement with U.S. Army Communications-Electronics Command (CECOM) under Agreement No. DAAB07-03-3-K-415. The authors would also like to thank Brian Holley for photographs of the CO_2 bubbles.

Nomenclature

A = area of fuel cell (m^2)
$\mathbf{A}$ = Stefan–Maxwell flux coefficient matrix (s/m^2)
a = constant in coefficient matrix
a_{ox} = specific area for oxidation (m^{-1})
a_{red} = specific area for reduction (m^{-1})
b = element in solution matrix
$\mathbf{B}$ = mole fraction to mass fraction conversion matrix
c_{MeOH} = methanol concentration in liquid (mol/cm^3)
$c_{\mathrm{H_2O}}$ = water concentration in liquid (mol/cm^3)
c_p = specific heat (J/kg K)
d_g = characteristic length of gas phase (m)
D_{ij} = binary diffusivity (m^2/s)
$D_{\mathrm{eff},ij}$ = effective diffusivity of gas phase (m^2/s)
F = Faraday constant (C/mol)
$\mathbf{g}$ = gravity (m/s^2)
$\bar{h}$ = sensible heat (J/kg)
h^0 = heat of formation (J/kg)
h_m = mass transfer coefficient (kg/sm^2)
$I_{0,\mathrm{ref}}^{\mathrm{MeOH}}$ = oxidation exchange current density (A/m^2)
$I_{0,\mathrm{ref}}^{\mathrm{O_2}}$ = reduction exchange current density (A/m^2)
$\mathbf{I}$ = current density (A/m^2)
$\mathbf{I}_p$ = proton current density (proton/m^2 s)
$\mathbf{J}$ = mass flux (kg/m^2 s)
$J(s)$ = Leverette function
k = thermal conductivity (W/m K)
k_{rg} = relative permeability of gas phase
k_{rl} = relative permeability of liquid phase
$\mathbf{K}$ = permeability (m^{-2})
$\dot{m}'''$ = mass source (kg/m^3 s)
$\dot{\mathbf{m}}''$ = total species mass flux (kg/m^2 s)
M_i = molecular weight of component i (kg/mol)
M_g = molecular weight of gas (kg/mol)
M_l = molecular weight of liquid (kg/mol)
$\mathbf{n}$ = surface normal vector
n_d = electro-osmotic drag coeff. (mol/mol)
Nu = Nusselt number
p_c = capillary pressure (Pa)
p_l = liquid pressure (Pa)
p_g = gas pressure (Pa)
Pr = Prandtl number
R_u = ideal gas constant (J/mol K)
R_Ω = resistance (Ω)
R_{ox} = oxidation reaction rate (A/m^3)

R_{red} = reduction reaction rate ($\mathrm{A/m^3}$)
Re_ε = pore Reynolds number
t = time (s)
T = temperature (K)
s = liquid saturation
Sh = Sherwood number
$\langle \mathbf{V}_k \rangle^k$ = intrinsic phase velocity of phase k (m/s)
V = volume ($\mathrm{m^3}$)
x_{MeOH} = mole fraction of methanol in liquid (mol/mol)
x = distance in x-direction (m)
y = distance in y-direction (m)
α_l = liquid volume fraction
$\alpha_{l,\mathrm{MeOH}}$ = volume fraction of MeOH in liquid phase
α_a = anode transfer coefficient
α_c = cathode transfer coefficient
β = equilibrium constant in condensable phases
ε = porosity
ϕ = electric potential (V)
η = fuel consumption ratio
η_a = anodic overpotential (V)
η_c = cathodic overpotential (V)
λ = oxidation constant ($\mathrm{mol/cm^3}$)
μ = viscosity ($\mathrm{N\,s/m^2}$)
θ = contact angle between liquid and solid (rad)
σ = surface tension (N/m)
σ_c = electrical conductivity of carbon phase ($\Omega^{-1}\,\mathrm{m^{-1}}$)
σ_m = proton conductivity of membrane phase ($\Omega^{-1}\,\mathrm{m^{-1}}$)
ρ = density ($\mathrm{kg/m^3}$)
τ = tortuosity
$\omega_{g,i}$ = mass fraction of gas (kg/kg)
$\omega_{l,i}$ = mass fraction of liquid (kg/kg)
ζ = stoichiometric coefficient

Subscripts

acl = anode catalyst layer
agdl = anode gas diffusion layer
ccl = cathode catalyst layer
cgdl = cathode gas diffusion layer
e = entrance
g = gas
i = component i
j = component j
l = liquid
m = membrane
n = neighboring cells
ref = reference/ambient conditions
R = due to chemical reaction
T = due to mass transport (evaporation/condensation)

Superscripts

k = previous iteration
$k+1$ = next iteration

References

[1] Liu, J. G., Zhao, T. S., Chen, R., and Wong, C. W., 2005, "The Effect of Methanol Concentration on the Performance of a Passive DMFC," Electrochem. Commun., **7**, pp. 288–294.
[2] Kim, D., Cho, E. A., Hong, S. A., Oh, I. H., and Ha, H. Y., 2004, "Recent Progress in Passive Direct Methanol Fuel Cells at KIST," J. Power Sources, **130**, pp. 172–177.
[3] Faghri, A., and Guo, Z., 2005, "Thermal Fluids Management for Direct Methanol Fuel Cells," U.S. Patent Application No. 20060292412, pending.
[4] Faghri, A., and Guo, Z., 2005, "Planar Fuel Cell Stack and Method of Fabrication of the Same," U.S. Patent Application No. 20060286436, pending.
[5] Faghri, A., and Guo, Z., 2006, "Vapor Feed Fuel Cells With a Passive Thermal-Fluids Management System," U.S. Patent pending.
[6] Guo, Z., and Faghri, A., 2006, "Miniature DMFCs With Passive Thermal-Fluids Management Systems," J. Power Sources, **160**(2), pp. 1142–1155.
[7] Guo, Z., and Faghri, A., 2006, "Development of Planar Air Breathing Direct Methanol Fuel Cell Stacks," J. Power Sources, **160**(2), pp. 1183–1194.
[8] Jewett, G., Guo, Z., and Faghri, A., 2007, "Water and Air Management Systems for a Passive Direct Methanol Fuel Cell," J. Power Sources, **168**, pp. 434–446.
[9] Rice, J., and Faghri, A., 2006, "A Transient Multi-Phase and Multi-Component Model of a New Passive DMFC," Int. J. Heat Mass Transfer, **49**, pp. 4804–4820.
[10] García, B. L., Sethuraman, V. A., Weidner, J. W., White, R. E., and Dougal, R., 2004, "Mathematical Model of a Direct Methanol Fuel Cell," ASME J. Fuel Cell Sci. Technol., **1**, pp. 43–48.
[11] Chen, R., and Zhao, T. S., 2005, "Mathematical Modeling of a Passive-Feed DMFC With Heat Transfer Effect," J. Power Sources, **152**, pp. 122–130.
[12] Nam, J. H., and Kaviany, M., 2003, "Effective Diffusivity and Water-Saturation Distribution in Single- and Two-Layer PEMFC Diffusion Medium," Int. J. Heat Mass Transfer, **46**, pp. 4595–4611.
[13] Wang, Z. H., and Wang, C. Y., 2003, "Mathematical Modeling of Liquid-Feed Direct Methanol Fuel Cells," J. Electrochem. Soc., **150**(4), pp. A508–A519.
[14] Pasaogullari, U., and Wang, C. Y., 2004, "Liquid Water Transport in Gas Diffusion Layer of Polymer Electrolyte Fuel Cells," J. Electrochem. Soc., **151**(3), pp. A399–A406.
[15] Pasogullari, U., and Wang, C. Y., 2004, "Two-Phase Transport and the Role of Micro-Porous Layer in Polymer Electrolyte Fuel Cells," Electrochim. Acta, **48**, pp. 4359–4369.
[16] Hwang, J. J., 2006, "Thermal-Electrochemical Modeling of a Proton Exchange Membrane Fuel Cell," J. Electrochem. Soc., **153**(2), pp. A216–A224.
[17] Siegel, N. P., Ellis, M. W., Nelson, D. J., and von Spakovsky, M. R., 2003, "A Two-Dimensional Computational Model of a PEMFC With Liquid Water Transport," J. Power Sources, **128**, pp. 173–184.
[18] Wang, Y., and Wang, C. Y., 2006, "A Nonisothermal, Two-Phase Model for Polymer Electrolyte Fuel Cells," J. Electrochem. Soc., **153**, pp. A1193–A1200.
[19] Wang, C. Y., 2004, "Fundamental Models for Fuel Cell Engineering," Chem. Rev. (Washington, D.C.), **104**, pp. 4727–4766.
[20] Faghri, A., and Guo, Z., 2005, "Challenges and Opportunities of Thermal Management Issues Related to Fuel Cell Technology and Modeling," Int. J. Heat Mass Transfer, **48**, pp. 3891–3920.
[21] Kaviany, M., 1991, *Principles of Heat Transfer in Porous Media*, Springer-Verlag, Berlin.
[22] Holley, B., and Faghri, A., 2006, "Permeability and Effective Pore Radius Measurements for Heat Pipe and Fuel Cell Applications," Appl. Therm. Eng., **26**, pp. 448–462.
[23] Faghri, A., and Zhang, Y., 2006, *Transport Phenomena in Multiphase Systems*, Elsevier, New York.
[24] Ren, X., Springer, T. E., Zawodzinski, A., and Gottesfeld, S., 2000, "Methanol Transport Through Nafion Membranes, Electro-Osmotic Drag Effects on Potential Step Measurements," J. Electrochem. Soc., **147**(2), p. 466.
[25] Meyers, J. P., and Newman, J., 2002, "Simulation of the Direct Methanol Fuel Cell, Parts I-III," J. Electrochem. Soc., **149**(6), p. A718.
[26] Stearns, S. D., 1981, "A Portable Random Number Generator for Use in Signal Processing," Sandia National Laboratory, Technical Report.
[27] 2004, *Handbook of Chemistry and Physics*, 85th ed., D. R. Lide, ed., CRC, Boca Raton, FL.
[28] Yaws, C. L., 1995, *Handbook of Transport Property Data: Viscosity, Thermal Conductivity and Diffusion Coefficients of Liquids and Gases*, Gulf, Houston, TX.
[29] Yaws, C. L., 1992, *Thermodynamic and Physical Property Data*, Gulf, Houston, TX.
[30] Kulikovsky, A. A., Dvisek, J., and Kornyshev, A. A., 2000, "Two-Dimensional Simulation of Direct Methanol Fuel Cell, a New (Embedded) Type of Current Collector," J. Electrochem. Soc., **147**(3), p. 953.

Yogen Utturkar
Mehmet Arik

Thermal Systems Laboratory,
General Electric Global Research,
Niskayuna, NY 12309

Charles E. Seeley
Lifing Technologies Laboratory,
General Electric Global Research,
Niskayuna, NY 12309

Mustafa Gursoy
Pro Solutions USA, Inc.,
1223 Peoples Avenue,
Troy, NY 12180

An Experimental and Computational Heat Transfer Study of Pulsating Jets

Synthetic jets are meso or microscale fluidic devices, which operate on the "zero-net-mass-flux" principle. However, they impart a positive net momentum flux to the external environment and are able to produce the cooling effect of a fan sans its ducting, reliability issues, and oversized dimensions. The rate of heat removal from the thermal source is expected to depend on the location, orientation, strength, and shape of the jet. In the current study, we investigate the impact of jet location and orientation on the cooling performance via time-dependent numerical simulations and verify the same with experimental results. We firstly present the experimental study along with the findings. Secondly, we present the numerical models/results, which are compared with the experiments to gain the confidence in the computational methodology. Finally, a sensitivity evaluation has been performed by altering the position and alignment of the jet with respect to the heated surface. Two prime orientations of the jet have been considered, namely, perpendicular and cross jet impingement on the heater. It is found that if jet is placed at an optimum location in either impingement or cross flow position, it can provide similar enhancements. [DOI: 10.1115/1.2891158]

Keywords: synthetic jets, electronics cooling, thermal management, impingement, jet design

1 Introduction

Synthetic jets have been routinely investigated from the standpoint of flow control [1–4], thrust vectoring of jets [5], triggering turbulence in boundary layers [6,7], and heat transfer applications [8–10]. In the case of heat transfer applications, the cooling process can be facilitated either by direct impingement of vortex dipoles on heated surfaces [11,12] or via employing the jets to enhance the performance of existing cooling circuits [13]. In view of these applications, the jet performance can be assessed with various methodologies.

Integral analyses of the time and spatially dependent jet exit velocity profiles serve to effectively quantify the jet performance in terms of the net momentum/energy flux [4,14]. Gallas et al. [15] formulated accurate, low-dimensional models of the synthetic jet flow field to predict the impact of design changes on the losses in a jet orifice. Similarly, Raju et al. [16] developed a scaling relationship for the vorticity flux across the jet orifice. In addition, a semianalytical model for estimating the pressure loss across the orifice for oscillatory flows was also proposed. Holman et al. [10] derived a formation criterion for synthetic jets, which essentially stipulated a condition in terms of nondimensional parameters to prevent reentrainment of vortex dipoles into the jet cavity during the ingestion stroke. This criterion is particularly crucial for heat transfer applications since they heavily rely on the vortex dipole dynamics for their cooling performance.

To the best of our knowledge, the heat transfer behavior of synthetic jets was first observed by Yassour et al. [17]. Their experimental setup comprised an enclosed cavity with an orifice and a loudspeaker acting as flexible membrane. A heater was aligned in front of the orifice, and the heat transfer rates on its surface were recorded. The acoustic "puffs" emanating from the orifice produced a four times enhancement in the heat transfer. Coe et al. [18] generalized the above cooling concept by making use of actuation technologies (piezoelectric actuation) other than loudspeakers to create the synthetic jet action. Since then, active cooling with synthetic jet has been an active topic of research [8,9,11,12]. Garg et al. [19] performed an experimental study to characterize the cooling power of the jet by contrasting its heat transfer capability under a given temperature difference with that of natural convection with the aid of an enhancement factor (EF). Very recently, Utturkar et al. [20] investigated the sensitivity of synthetic cooling performance to its operating conditions and alignment by experimental and computational strategies.

Numerical simulations of synthetic jets have been greatly instrumental in distilling the flow physics from the standpoint of flow control [1,4] and heat transfer applications [10]. Numerical simulations are able to provide finer temporal and spatial resolutions of the flow domain, which could be a challenging proposition for experimental studies because of $O(10^{-3}-10^{-6})$ length scales. Especially, in the case of heat transfer applications, the cooling process is driven by impingement of vortex dipoles on the heated surface [12]. Consequently, a sound understanding of the vortex roll-up and dipole-forming mechanism and the interaction of vortex dipole with wall are imperative to enhance the jet design for heat transfer applications. This is possible via the approach of numerical simulations, which yield a detailed description of the flow field in space and time.

Recently, synthetic jet heat transfer research has attracted more scientists in the academia and industry. The effects of a small-scale rectangular synthetic air jet on the local convective heat transfer from flat heated surface test results were reported [21]. It was concluded that synthetic jets can lead to substantial enhancement of the local heat transfer from heated surfaces by strong mixing that disrupts the surface thermal boundary layer. The dependence of the local heat transfer coefficient on the primary parameters of jet motion is characterized over a range of operating conditions. Average Nusselt numbers were maximized when the dimensionless plate spacing was between 14 and 18. Furthermore, heat transfer rates were maximized when the jet frequency was close to the resonance frequency of the driver cavity. The effi-

---

Contributed by the Heat Transfer Division of ASME for publication in the JOURNAL OF HEAT TRANSFER. Manuscript received December 19, 2006; final manuscript received June 25, 2007; published online April 23, 2008. Review conducted by Jay M. Khodabadi.

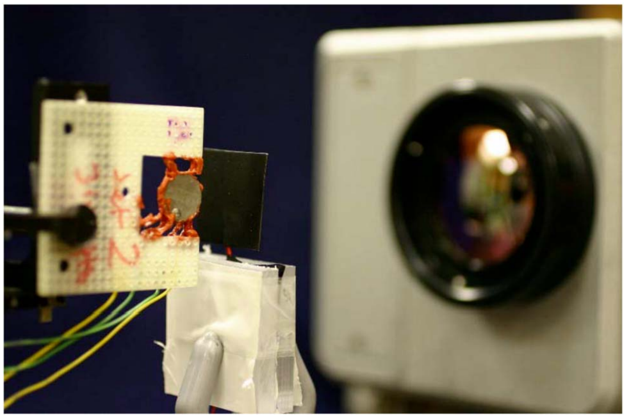

Fig. 1 Experimental setup

ciency and mechanisms of cooling a constant heat flux surface by impinging synthetic jets were investigated experimentally and compared to cooling with continuous jets [22]. Effects of jet formation frequency and Reynolds number at different nozzle-to-surface distances were investigated. High formation frequency (1200 Hz) synthetic jets were found to remove heat better than low frequency (420 Hz) ones. Moreover, synthetic jets are about three times more effective in cooling than continuous jets at the same Reynolds number. Using particle image velocimetry, it was shown that the higher formation frequency jets are associated with breakdown and merging of vortices before they impinge on the surface. Heat transfer and acoustic aspects of the small-scale synthetic jets are presented by Arik [23]. The synthetic jets designed and developed in this study provided peak air velocities of 90 m/s from a 1 mm hydraulic diameter rectangular orifice. The jets were driven by a sine wave with an operating frequency between 3 kHz and 4.5 kHz, providing the highest thermal performance for the current jets. It was found that the enhancement can be between four to ten times depending on the heater size, showing that smaller sizes provide the best jet effectiveness. It was also noted that jet noise can be as high as 73 dB, but possible abatement techniques can decrease this noise level to as low as 30 dB.

To the best of our knowledge, no study in the past has comprehensively investigated the heat transfer behavior of synthetic jets in conjunction with numerical models of the fluid flow and structural dynamics. Such a study would be needed in understanding the impact of the jet's flow physics and structural behavior on its heat transfer properties and would serve as a guideline in designing synthetic jets for electronics cooling applications. To address these needs, we employ numerical models along with the experimental data to understand the implications of the jet alignment/orientation with reference to the heater. Additionally, we also study the structural response of the jet to the excitation via modal analysis. This evaluation is expected to be a significant asset to the design of synthetic jet based cooling of electronic applications.

2 Experimental Study

An experimental test rig was designed and built to measure localized surface temperatures and the heat transfer to the ambient via synthetic jet cooling (see Fig. 1). A large Plexiglas enclosure was employed to minimize ambient air drifts to the experimental rig. Thin foil heaters sandwiched between thin aluminum backing plates (with 125 μm thickness) were used in the experimental study. Mapping the temperature profile of the localized points at the heater was critical, and thus the entire surface was made visible to an infrared (IR) camera. While the jet was impinging on one of the heater surface, the temperature measurements were performed from the back surface using the IR camera. It was ensured that a large fraction of the electrical power input to the heater was dissipated from the surface facing the jet, and the back surface heat transfer and electrical leads were assumed to contribute to the total heat losses. In our earlier experiments [19], we used a slightly different approach by attaching the heater to a Plexiglas frame. For the current study, we restricted the heater design by not considering its physical attachment to any fixture to avoid losses.

The heater temperature profile was first obtained under natural convection conditions. The front and back sides of the heater were tested at the same heater power condition. In this new procedure, a few critical experimental settings were ensured before the synthetic jet experiment was started. Firstly, the average temperature between the front and back heater surfaces was ascertained to vary by less than 1°C. Then, we obtained the natural convection heat loss curve based on the difference between the average surface temperature and ambient temperature. This curve was vital for the accuracy of our heat transfer enhancement calculations, as will be explained later.

In this study, the impingement heat transfer behavior of the synthetic jets was of interest. Accordingly, the jet was located at the desired location, and the flow streams impinged perpendicularly on the heater. The jet was mounted on a traverse system, enabling a precise placement and a 3D mobility of the jet. The jet was powered by means of a function generator with a time harmonic signal instrumented by a function generator and a power amplifier. An oscilloscope was placed in the power circuitry to precisely measure the frequency and driving voltage. The driving power to the heater was measured and the contribution of the backside natural convection was known (via the heat loss curve), the synthetic-jet-induced heat transfer could be determined. Electrical power was measured as the product of the current measured by a precision resistor and the voltage reading at the heater legs.

For accurate IR thermal imaging, the emissivity of the surface should be known with the highest accuracy. Heater surfaces were coated with known emissivity paint, and the emissivity (equal to 0.97) was measured by using the same methodology given in Garg et al. [19]. Steady state temperature profiles were captured by using an IR camera. A minimum pixel size of 300 μm was achieved via appropriate lenses. A typical temperature profile under natural conditions has been illustrated in Fig. 2(*a*). Similarly, Fig. 2(*b*) shows the influence of the jet on the heater temperature. It is seen that the average temperature in Fig. 2(*a*) is 71.2°C, while the maximum temperature difference between the hottest spot to the coolest spot (at the side) was 10°C. This difference is expected because of the heat dissipation from the heater sides.

2.1 Velocity Measurements.

The jet operates by the periodic ejection and the suction of the fluid. In order to capture both the suction and the ejection velocities, a hotwire probe was placed close to the jet orifice at a distance of approximately 0.5 mm (see Fig. 3(*a*)). The jet velocity is measured by means of a TSI IFA 100 hot wire anemometry system, which has 0.5 μm thick probe wire. A computer code was used to separately average the ejection and suction peaks. A typical velocity profile for the synthetic jet is shown in Fig. 3(*b*). The average exhaust and average suction velocities were calculated. Because of the single-wire probe type, no directional output can be obtained; we are thus able to tap only the local velocity magnitude.

The exhaust velocity was found to increase nonlinearly with the driving voltage, as illustrated in Fig. 4. Specifically, the peak exhaust jet velocity tends to increase at a lesser rate with driving voltage as the driving voltage is increased [19]. Though the cause for this behavior has not been studied in detail, we expect it to be because of either flow/structural nonlinearities or air leakages occurring at the high voltages due to an increase in strain. Figure 5 presents the trend between the jet exit velocity and the heat transfer enhancement. The driving voltage was kept at 50 V, while the harmonic signal was swept in the range of 2–5.5 kHz. The definition of an EF is given in [19]

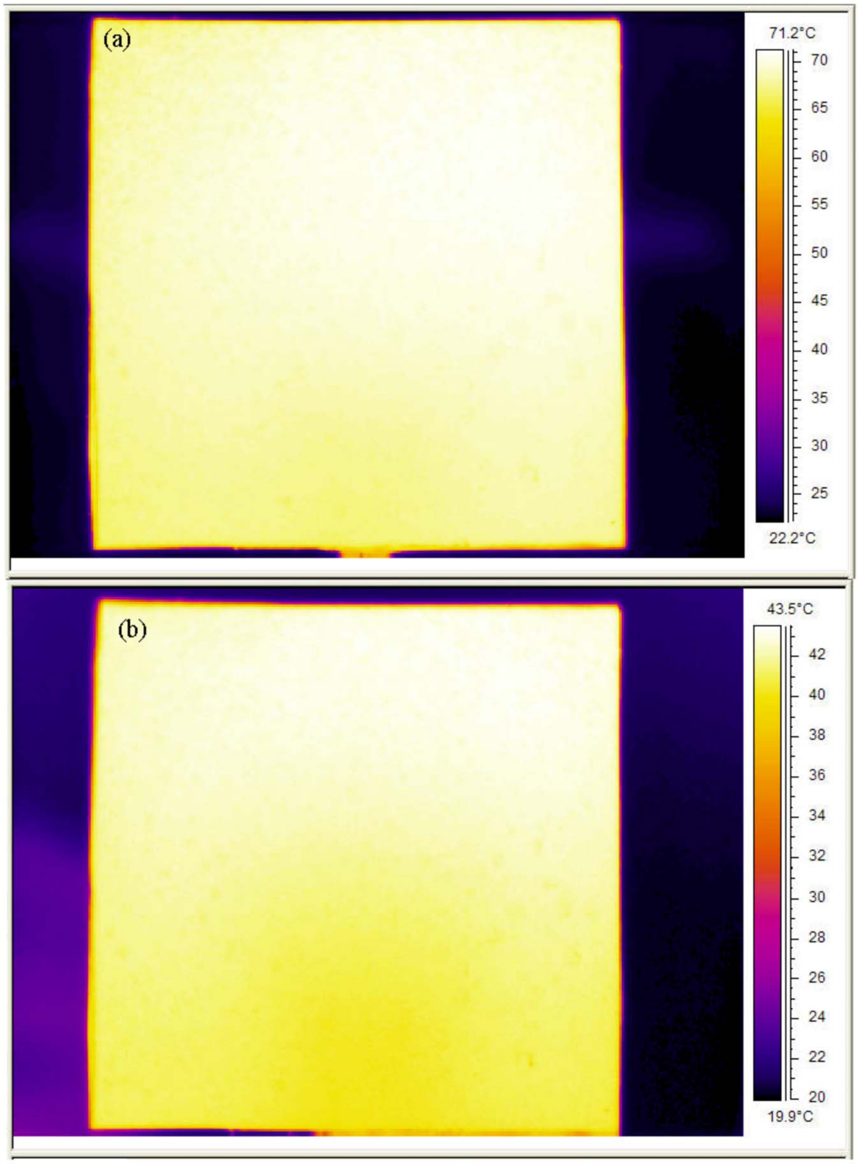

Fig. 2 Typical IR image showing heater temperature distribution. (*a*) Natural convection, 1.56 W heater power (maximum temperature=71.2°C). (*b*) Synthetic jet at 50 V_{rms} and 4500 Hz perpendicularly impinging on the heater center from a distance of 10 mm at 1.56 W heater power (maximum temperature=43.5°C).

$$\mathrm{EF}=\frac{h_{\mathrm{jet}}}{h_{\mathrm{nc}}}=\left.\frac{q_{\mathrm{jet}}}{q_{\mathrm{nc}}}\right|_{(T_s-T_{\mathrm{air}})} \tag{1}$$

As seen from the figure, an optimal air velocity of about 45 m/s is observed at 4.5 kHz, which is the natural frequency (or Helmholtz frequency) of the jet. Naturally, the best heat transfer performance (5.5 times based on Eq. (1)) is also obtained at that resonant frequency.

2.2 Power Measurements. Power consumption in an electronics cooling system is very important since it directly affects the coefficient of performance (COP) of the cooling solution. Therefore, a careful study was carried out to obtain the true power consumption of the synthetic jets. Figure 6 shows the synthetic jet power measurement setup. In addition to the basic synthetic jet heat transfer measurement setup, a 1 kΩ serial resistor was added to increase the accuracy of the current measurements. Voltage measurements were done before and after the resistance using a high-frequency differential probe (Tektronix 5205 100 Hz). By using a known resistance and voltage values, electrical current for the synthetic jet was calculated. Another high-frequency probe measured the exact driving voltage of the synthetic jets. During the experiments, the voltage, current, frequency, and phase were recorded by an oscilloscope.[1]

The effect of the driving voltage on the jet power consumption is depicted in Fig. 7. It is interesting to note the steady increase of power consumption over 30 V of the driving voltage. While the power consumption follows a steady trend, the jet exit velocity does not show the same steady trend over 30 V (as seen in Fig. 4). This indicates that the jet may be less efficient at higher voltages (greater than 30 V).

The effect of the driving frequency over the jet power con-

---

[1] LeCroy wave runner 6100.

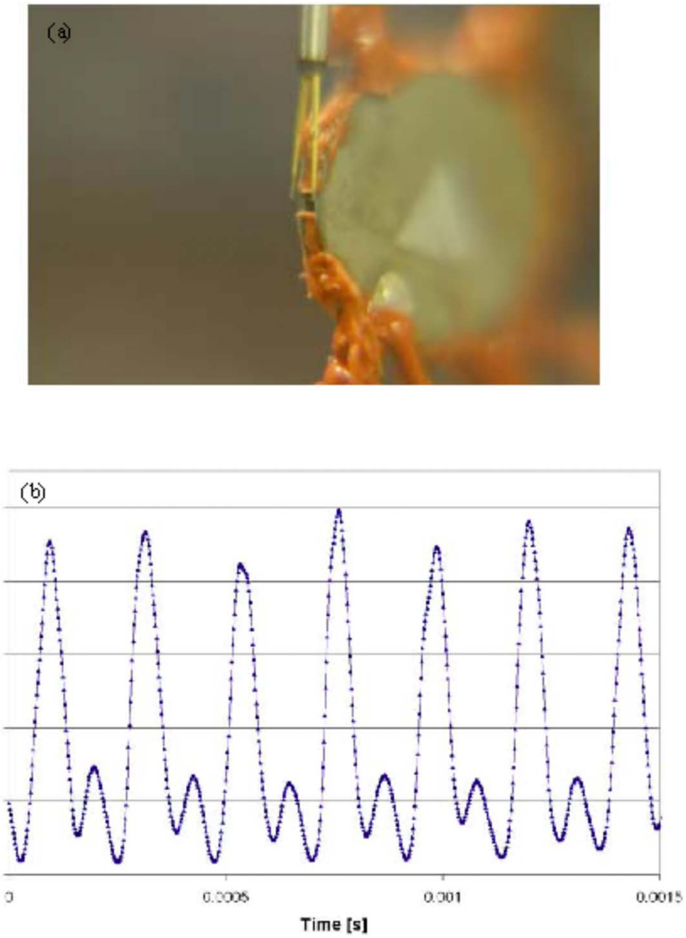

Fig. 3 (*a*) illustration of hotwire location near the jet exit. (*b*) Typical velocity response tapped by the hotwire (50 V_{rms} and 4500 Hz).

sumption is seen in Fig. 8. The jet was driven at 50 V constant voltage supply, and the frequency was swept between 2000 Hz and 6000 Hz. This range encompassed the structural and the Helmholtz natural frequencies of the jet. The jet showed maximum power consumption at the resonance frequency of 4500 Hz. Before and after the resonance frequency, it showed lower power consumption. This is particularly significant because of the capacitive effect and the fluid-structural coupling of the jet.

Power consumption is a very important design constraint for the application of synthetic jets in electronics cooling applications. From Figs. 5 and 8, we can comment that one can drive synthetic jets in the range of 40–100 mW and get about four to six times heat transfer enhancement. Furthermore, based on the consumed jet power and the measured heater input power, a COP of about 10 is estimated for the synthetic jet actuators in the present study.

2.3 Uncertainty Analysis. Standard techniques were followed to obtain the experimental uncertainty [24]. The basic uncertainty sources were temperature, power measurements, heat losses, and calibration errors. The uncertainty associated with

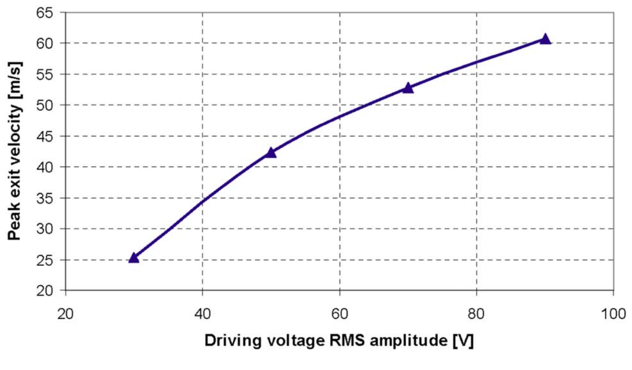

Fig. 4 Variation of peak jet exit velocity with driving voltage amplitude

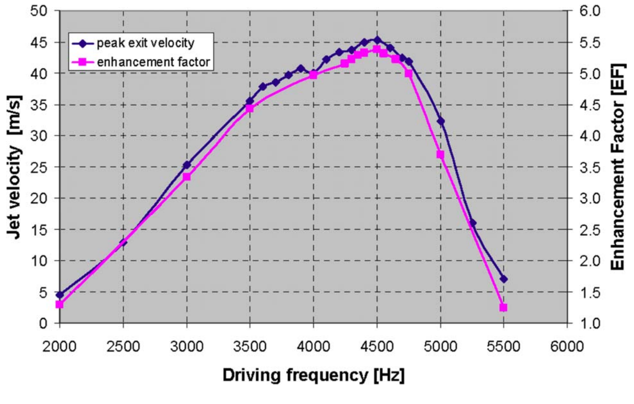

Fig. 5 Effect of driving frequency on heat transfer enhancement and peak jet exit velocity

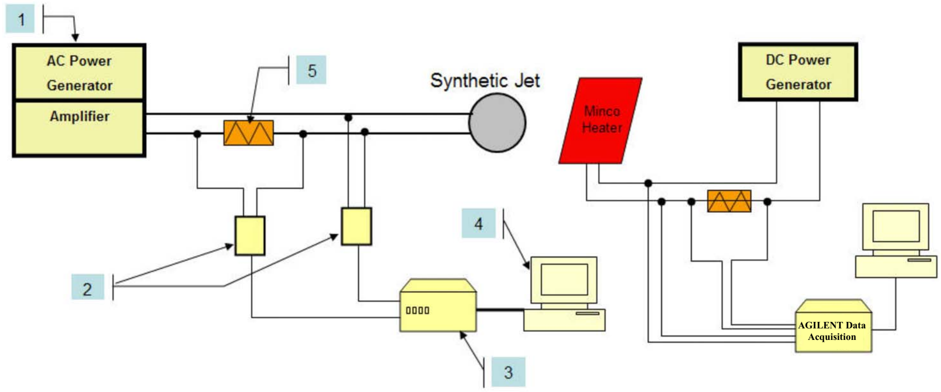

1. Power generator and amplifier, SRS DS345
2. Tektronix 5205 100mHz. High voltage differential probe
3. Tektronix 1103 Tekprobe power Supply
4. LaCroy waveRunner 6100, 1GHz, Oscilloscope
5. 1 kOhm resistor

Fig. 6 Experimental setup for power consumption measurements

temperature measurement using the *T*-type thermocouples was ±1°C. The error in temperature measurements using the IR camera is introduced due to the emissivity of the paint. The error in temperature measurements due to emissivity is ±0.5°C. It is interesting to note that most of this uncertainty was contributed by the thermocouple. A standard 0.1 Ω precision resistor was placed in the heater power circuit to measure the current. The total uncertainty in the heater power measurements was estimated to be approximately 0.05%.

3 Description of Computational Models

3.1 Fluid Flow Model. The schematic of the 2D synthetic jet model is depicted in Fig. 9. The jet is modeled, as shown, by a 23 mm tall cavity. The motion of the side diaphragms is suitably modeled by a spatially varying velocity profile, as shown below in Eqs. (2) and (3) and as illustrated in Fig. 9,

$$u_{\text{left}} = A/2[1 - \cos(2\pi y/D)]\sin(2\pi f t) \tag{2}$$

$$u_{\text{right}} = A/2[1 - \cos(2\pi y/D)]\sin(2\pi f t + \pi) \tag{3}$$

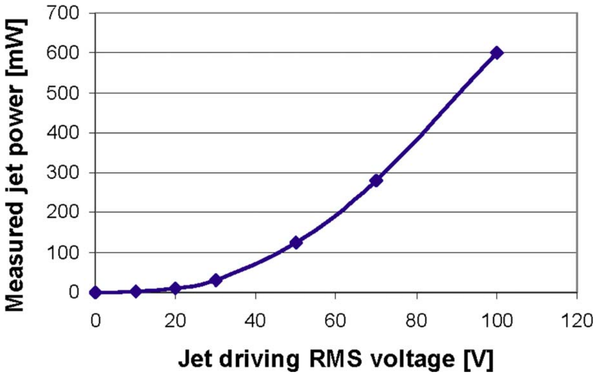

Fig. 7 Synthetic power consumption with driving voltage

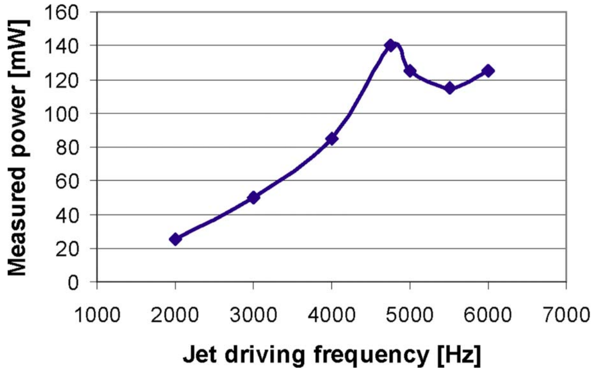

Fig. 8 Synthetic jet power consumption with frequency

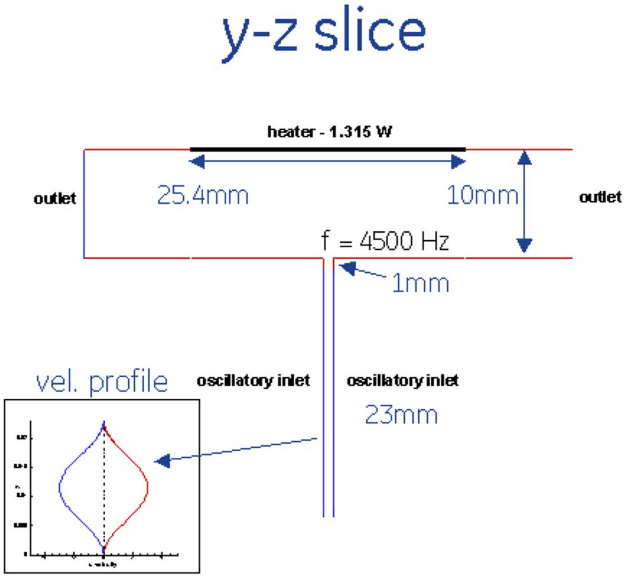

Fig. 9 Schematic of a 2D synthetic jet model

Here, A is the velocity amplitude, D is the diaphragm height, and f is the operating frequency. In the present study, we assign $A=3$ m/s and $f=4500$ Hz. The above profiles, besides yielding zero u velocity, also produce a zero u velocity gradient at the ends to imitate the clamping effect of the diaphragm (refer to Refs. [4] and [14]). The width and height of the jet orifice are 1 mm. The chamber comprises a 1 in. long heater, which is modeled as a "thin" aluminum wall emitting 1.32 W of heat. All other walls are at 20.8°C (ambient). The distance of the heater from the jet orifice is chosen to be 10 mm based on a previously reported sensitivity analysis [19]. All of the above specifications are consistent with the experimental setup shown in Fig. 1, and the simulation inputs are based on the experimental case corresponding to the peak performance point, as shown in Fig. 5.

A commercial computational fluid dynamics (CFD) software (FLUENT©, Release 6.2.16) is employed to perform two-dimensional, incompressible, time-dependent Navier–Stokes computations on the above geometry. The second-order upwind scheme is employed for the convective terms, and central differencing is used for the viscous terms. The energy equation is solved in addition to the mass (continuity) and momentum equations. Time stepping is performed via the first-order implicit Euler discretization. The commonly used noniterative operator-splitting technique pressure-based implicit splitting of operators (PISO) [25] is selected for pressure-velocity coupling to expedite the computational time without sacrificing the formal accuracy.

The Reynolds number (Re) for the simulation, based on time-averaged mean velocity at the jet exit, is 2012. The Stokes number (S), which is a nondimensional form of the forcing frequency, is 42. The definitions of Re and S are mentioned below alongside other relevant parameters.

$$\mathrm{Re} = \frac{V_{\mathrm{inv}}^{\mathrm{av}} d}{\nu} \tag{4}$$

$$S = \sqrt{\frac{2\pi f d^2}{\nu}} \tag{5}$$

In the above equations, $V_{\mathrm{inv}}^{\mathrm{av}}$ represents the time-averaged (over half a cycle) and spatially averaged velocity in the jet orifice. Recently performed direct numerical simulations have demonstrated turbulent flow transitions for synthetic jets operating around $\mathrm{Re}=1150$ and $S=17$ [26]. They also indicated the tendency of the flow to stabilize to a laminar regime in the jet orifice. Thus, the flow regimes for synthetic jet actuators could range from being laminar in the orifice to turbulent in the external environment. Though the use of Reynolds averaged Navier Stokes (RANS) -based turbulence models appears as an intuitive option, the resultant high effective viscosity is expected to damp the small vorticity scales in the jet orifices and blur the flow physics. Considering this fact, we choose to perform laminar simulations in this study in conjunction with the use of a finer mesh near the orifice vicinity (22 mesh points across the orifice).

3.2 Structural Model. The structural design of the synthetic jet has a significant impact on its cooling ability. Piezoelectric materials were used as actuators to deform the synthetic jet structure at a high frequency, resulting in rapid changes to the enclosed volume of air to alternately ingest and expel air through the orifice creating the pulsating jet that impinges on the surface to be cooled. A structural dynamics model was developed to understand the mechanical behavior of the cooling device and to perform parametric studies for future improvements. The model is based on a Ritz approach that assumes polynomial displacement functions. These functions are combined with the geometric and material properties to determine the potential and kinetic energy of the structure indicated. Minimization of the total energy indicated the equations of motion below,

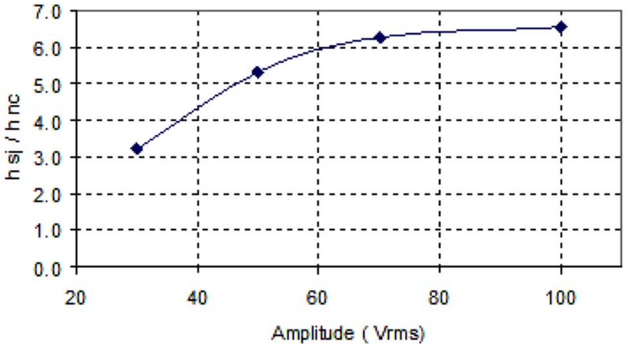

Fig. 10 Effect of driving voltage on heat transfer enhancement

$$\begin{bmatrix} M_{SS} & 0 \\ 0 & M_{FF} \end{bmatrix} \begin{bmatrix} \ddot{U}_S \\ \ddot{U}_F \end{bmatrix} + \begin{bmatrix} C_{SS} & C_{SF} \\ C_{FS} & C_{FF} \end{bmatrix} \begin{bmatrix} \dot{U}_S \\ \dot{U}_F \end{bmatrix} + \begin{bmatrix} K_S + K_F & K_{SF} \\ K_{SF} & K_F \end{bmatrix} \times \begin{bmatrix} U_S \\ U_F \end{bmatrix} = \begin{bmatrix} F_S \\ 0 \end{bmatrix} \tag{6}$$

Note that the stiffness matrix is highly coupled between the structure and the fluid since the volume of enclosed air acts like a spring that is driven from the piezoelectric structure. The damping matrix is also coupled as viscous forces through the orifice and tends to resist the flow of air that is coupled to the structure. The structural component of the damping matrix is determined by assuming Rayleigh damping where the structural damping is assumed to be proportional to the stiffness and mass matrices. The mass matrix is uncoupled, and there are no external fluid forces.

4 Results and Discussions

4.1 Experimental Results. The impacts of the driving frequency, voltage, and jet-to-heater spacing on the heat transfer and jet power consumption were studied. The resonance frequency (4.5 kHz) was previously determined from laser vibrometer measurements.

In the first set of heat transfer augmentation experiments conducted, the power to the heater was set to such a level that the heater temperature was in the vicinity of 80°C. The total power input to the heater for this setting was 1.56 W. The IR image of the heater under natural convection conditions is shown in Fig. 2(*a*). After the system reached a steady state under natural convection conditions, the temperature distributions were recorded. The axial distance between the jet and the heater was set to the desired location. The synthetic jet was turned on with the desired driving frequency and voltage. The axial distance was varied between 5 mm and 50 mm.

In Eq. (1), T_s is the average heater temperature and q_{jet} is the heat flux dissipated from the surface of the heater facing the synthetic jet. As a result, q_{jet} was not equal to the total heat input to the heater, as there was a finite heat loss from the back side of the heater due to natural convection to ambient. Figures 10 and 11 present the effect of the driving voltage and the axial distance over the heat transfer. As seen from the figure, the increased driving voltage does not increase the heat transfer at the same rate as the jet power consumption. This is particularly important because it might cause degradation of COP (i.e., COP) and might coarsen the advantage of the higher EFs obtained at higher voltages.

An optimum placement of the jet from the heater is important. In an ideal system, the jet should not consume a large footprint area and volume. Therefore, it should be placed as close as possible. As given in Fig. 11, the jet can be placed as close as 5 mm with little performance degradation, though it gives a better performance at 10 mm. There are several reasons for an optimum spacing to provide a better heat transfer performance. First of all,

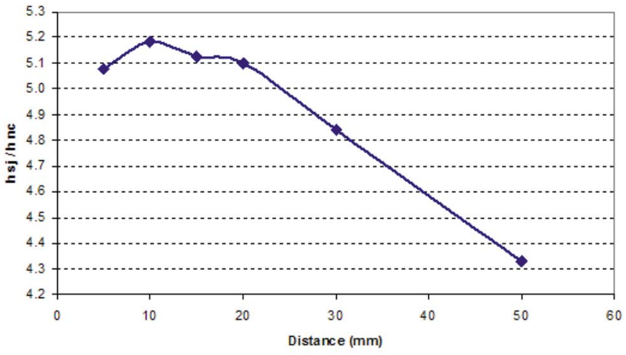

Fig. 11 Effect of axial distance on heat transfer enhancement

at low spacing, the area of the heater being cooled by impingement is much smaller. This implies that the region of high heat transfer coefficient is smaller at smaller spacing, leading to a lower overall heat transfer coefficient. This, in turn, leads to a higher average heater temperature. Another important aspect is the air temperature. The air exiting the jet during the exhaust cycle is hotter than the ambient, mainly because of the heat generated within the jet itself. When the jet is placed very close to the heat source, the temperature of the impinging air is close to the temperature of the air exiting from the jet. When the distance between the jet and the heater is increased, ambient air gets entrained, causing the temperature of the air impinging upon the heater to decrease substantially (Garg et al. [19]).

4.2 Flow Simulation Results. In this section, the experimental data were employed to develop and assess the computational model and extend the computational model/tool to predict the behavior of the jet under different alignment conditions.

The sensitivity of the model illustrated in Fig. 9 is investigated by two grids: 16,300 nodes (40 across the orifice) and 26,800 nodes (60 across the orifice). The heater in the simulations is modeled by a constant heat flux boundary patch. Accounting the measured heat loss of 0.25 W for the given heater power of 1.56 W, a net heat flux of 1.32 W is applied over the 25.4 mm long heater patch. Since the hotwire location, dimensions, and measurements are known, we extracted and averaged the velocity magnitude from the grid points at the hotwire location. The uncertainty in the hotwire length and location is within ±0.25 mm. The time-dependent results in Fig. 12 not only show that they are fairly grid independent, but also illustrate a reasonable match with the experimental measurements in Fig. 3(*b*) (given the above hotwire uncertainties) for both mesh densities. This agreement instills confidence in the computational procedure.

Table 1 Comparison between CFD and experiments (T_0 =20.8°C)

Variable	Expt.	CFD	Difference (%)
T_{av}, °C	42.1	41.0	2.6
h_{av}, $\mathrm{W/m^2\,K}$	95.6	100.0	4.6

The steady state heater temperature is averaged and compared with the average temperature on the 25.4 mm heat flux patch in the CFD model. For instance, the experimental heater average temperature mentioned in Table 1 is extracted from Fig. 2(*b*). As seen from the table, the average temperatures and average heat transfer coefficients, which are likewise calculated, agree within 5% between the experiments and simulations. While the computational study only solved for the fluid flow and heat transfer from the heater surface, it did not consider the internal conduction effects in the thin aluminum plate. We assume that they are negligible.

Our natural convection heat loss experiment yielded a natural convection heat transfer coefficient equal to 18 $\mathrm{W/m^2\,K}$ (it includes both natural convection and radiation) at a 40°C heater temperature. Using this value, we could extract the EF (Eq. (1)) variation over the heater surface. Figure 13 depicts that though the overall enhancement on the heater is about five times (as indicated by the average heat transfer coefficient in Table 1), the middle portion of the heater is subjected to a 14 times enhanced heat transfer. Furthermore, an almost eight jet diameter wide area on the heater experiences at least 10 times heat transfer. This information is highly useful in sizing the complete thermal system. For instance, for a given jet size, we could decide the maximum area that can be cooled with the jet, and, vice versa, for a given heater size it can indicate the minimum size of the jet to be used.

The instantaneous vorticity plots in Fig. 14 reveal the relation between the heat transfer variation and the flow field. As observed, the jet periodically emanates vortex dipoles, which impinge on the central part of the heater and convect heat away from the heater surface. Thus, we obtain the maximum cooling power at the exact impingement locations. The temperature difference plots in the same figure indicate the formation of hotspots at the heater ends, which agrees with the previous discussion. The in-

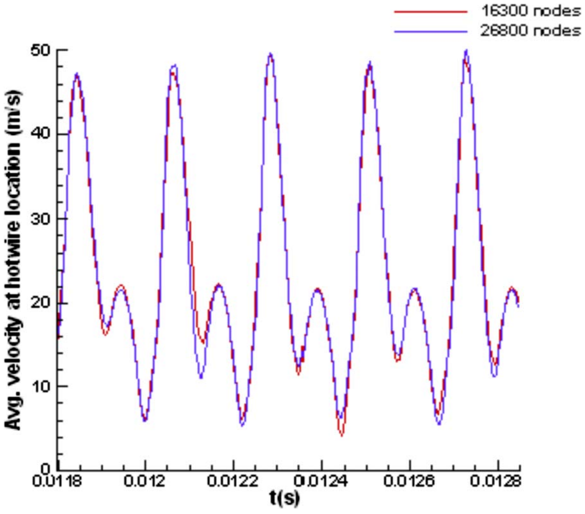

Fig. 12 Time-dependent velocity magnitude extracted from the computational domain at the hotwire location

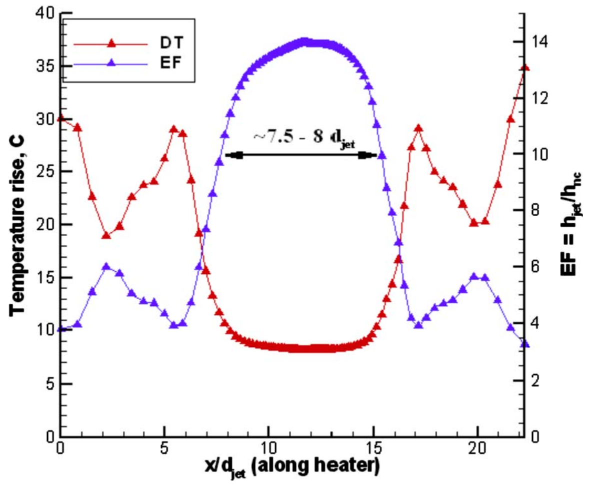

Fig. 13 Variation of temperature rise and heat transfer enhancement along the heater surface

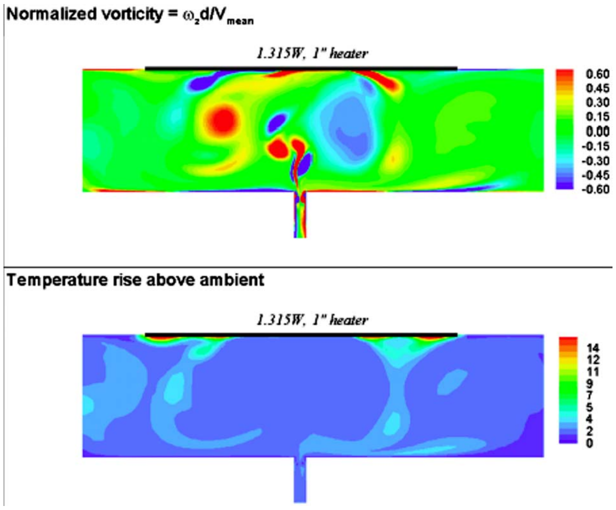

Fig. 14 Normalized vorticity and temperature rise at the beginning of the expulsion phase of the jet

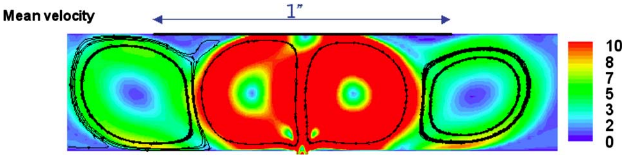

Fig. 15 Time-averaged streamlines and synthetic jet velocity field

stantaneous vorticity plots are not able to clearly explain the formation of these hotspots though they justify the heat transfer behavior at the heater center. As a result, we portray the time-averaged velocity field in Fig. 15 that may be viewed from the perspective of a steady jet. The flow field is characterized by a perpendicular impingement of the jet with a stagnation point at the heater center. In a time-averaged sense, the jet induces recirculation currents, which seemingly scale with the distance between the heater and the jet. Between two adjacent recirculation zones, there exist smaller secondary recirculation zones near the heater surface. Interestingly, the hotspots seen in Figs. 13 and 14 develop near the location of these secondary vortices. This could be due to the fact that the secondary vortices stagnate the fluid within a smaller region and thus restrict the heat transfer. Furthermore, the velocity contours depict an upward jet movement at about 10 m/s. This value, which is the velocity actually facilitating the heat transfer, is fairly lower than the peak hotwire measurement (50 m/s). As a result, we believe that the hotwire measurement may be inadequate in terms of gauging the heat transfer, and time-averaged results may be more valuable for this matter.

We finally alter the jet alignment from the perpendicular impingement position to the cross flow orientation. This is motivated by packaging restrictions, which may arise due to space limitations between two circuit boards. Figure 16 shows the computational domain. Note that we just change the jet angle from 90 deg to 0 deg, holding other computational parameters constant. Figure 17 compares the temperature rise on the heater surface between the perpendicular and cross flow positions. Though the heater temperature in the cross flow case is asymmetrical, its average value over the heater surface is within 0.1°C of the average value in the perpendicular case. Thus, the cross flow position works as good as the perpendicular impingement position. In the case of the cross flow alignment, the heat transfer is facilitated through a boundary layer flow, as opposed to the perpendicular impingement. Though the flow structure near the heater surface is different in each case, the heat transfer is less affected by it.

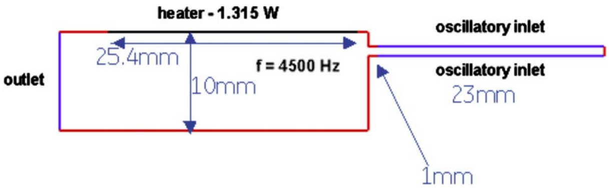

Fig. 16 Schematic of computational domain in the cross flow alignment

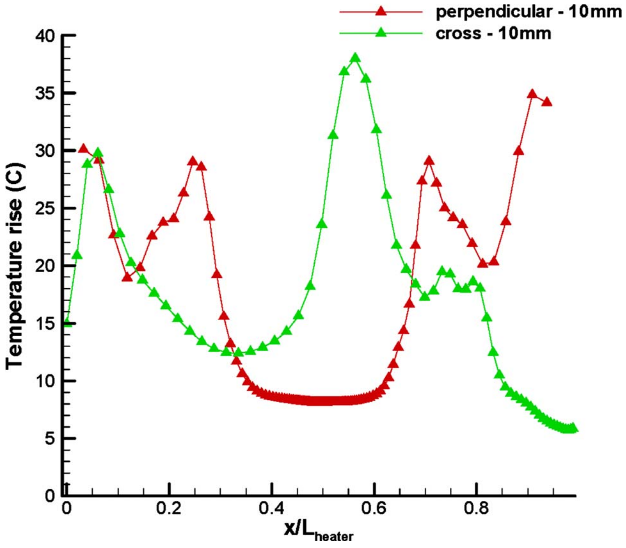

Fig. 17 Temperature variation on the heater surface for the two flow alignments

4.3 Structural Dynamics. The calculated mode shapes shown in Fig. 18 indicate the shape of the deformed structure at its resonance frequencies and give a good indication of how the structure behaves at its operating frequency. The modes are found by calculating the eigenvectors of the equations of motion pre-

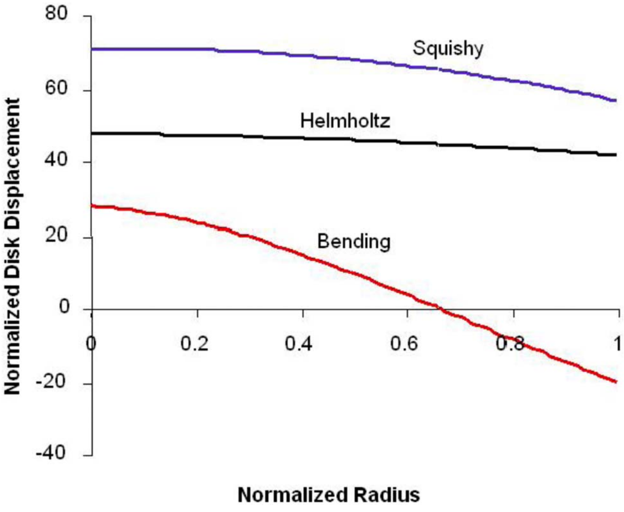

Fig. 18 Synthetic jet mode shapes. The squishy and Helmholtz modes are the dominant modes at lower frequencies. The bending mode occurs at higher frequencies. This mode simultaneously compresses and expands the volume of enclosed air, resulting in minimal flow.

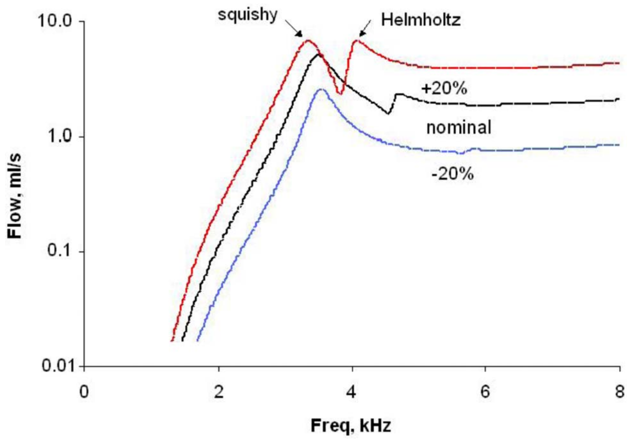

Fig. 19 Flow versus frequency. The flow increases with frequency up to the first resident point.

sented above. In this figure, the modal displacements are plotted as a function of the normalized radius of the synthetic jet device. The "squishy" mode is the near rigid body motion of the pair of plates moving in and out, which compress the enclosed volume of air. It is normally the lowest frequency mode. The next highest frequency mode is typically the Helmholtz mode. This is the acoustic mode that results in the greatest air flow through the orifice. The volume of enclosed air acts as a compressible spring, while the volume of air in the orifice acts as an incompressible slug with a particular mass. When the driving frequency is such that these two volumes act in phase, an amplification effect occurs and this is known as the Helmholtz resonance. This acoustic Helmholtz mode also tended to influence the structural displacements from a feedback process through a fluid-structure interaction. The first bending mode occurs at a higher frequency. This mode refers to the bending of the plates that compress the enclosed volume of air. Note that this bending mode simultaneously compresses and expands the volume of enclosed air depending on the radius resulting in a cancellation of the change in pressure across the entire enclosed volume, thus reducing the air that is forced through the orifice.

The model is also useful to perform parametric studies of various synthetic jet parameters. A good metric of the jet's cooling performance is the volumetric flow rate Q found as follows:

$$Q=\frac{1}{3}R^2V_Cf \tag{7}$$

In Fig. 19, the volumetric flow rate is plotted as a function of driving frequency for three cases. In the first case, the flow is calculated for a nominal disk radius of 5 mm. In cases 2 and 3, the flow is calculated at a radius 20% less than nominal (4 mm) and 20% greater than nominal (6 mm), respectively. The first resonance frequency (squishy mode) is not nearly as sensitive to geometric changes compared to the second resonance frequency at the Helmholtz mode. This is because the Helmholtz frequency depends explicitly on the geometry, and not on the material characteristics. The squishy mode depends on both the geometry and the material characteristics. As the synthetic jet grows in diameter, the mass of the disks increases, but the amount of material holding them in place also increases. The net result is that the stiffness and mass increase roughly in proportion, thus reducing the sensitivity of the squishy mode frequency to geometric changes. The trend of increased flow with larger jets is clear. This indicates that larger synthetic jets produce more flow and, thus, better cooling performance. Practical geometric constraints in a particular cooling application will limit the size of the synthetic jet and, thus, the cooling capability.

5 Summary and Conclusions

The current study presented experimental and computational results on the performance of synthetic jets under various operating conditions. Hotwire velocity measurements and IR thermal measurements are used to measure the jet exit velocity and heat transfer augmentation, respectively. The computational model, based on the experimental setup, is validated using the experimental measurements. The match between the two studies is within 5%.

The enhancement caused by synthetic jet is dependent on the operating frequency. Naturally, the best performance is obtained at the resonance frequency. Furthermore, the enhancement increases with the jet driving voltage due to an increase in the disk amplitude. However, at higher voltages, the jet consumes power at a much higher rate and, consequently, loses its COP. The power measurements in this study indicate a high COP of approximately 10 for the synthetic jet, which underscores its high cooling efficacy.

The computational model reveals the variation of heat transfer over the heater surface. In general, the local performance of the jet at the impingement locations may be two to three times its overall performance. This variation of heat transfer behavior unveiled by CFD would also assist in sizing the jet orifice for a given electronic component. The cooling performance of the synthetic jet is strongly dependent on the time-averaged flow structure of the jet, while instantaneous velocity values/measurements may be misleading and less conservative. The structural models reveal the key mode shapes of the jet, namely, the acoustic mode and the squishy mode. While the acoustic mode produces high heat transfer rates, it is a noisy mode of the jet operation. In contrast, the squishy mode is able to deliver a comparable level of cooling enhancements at much lower noise levels (less than or equal to 40 dB).

Lastly, the numerical simulations justify that synthetic jets may be equally effective in cross flow alignment and may be conveniently packaged between two closely spaced circuit boards. Overall, the present study significantly contributes to maturing different aspects of synthetic jet design and is expected to be an asset to transitioning synthetic jets from exploratory devices in laboratories to a robust electronics cooling solution.

Acknowledgment

The authors would like to acknowledge insightful discussions with Jim Petroski (GE-Lumination) and Todd Wetzel (General Electric Global Research Center) during the course of this work.

Nomenclature

x, y, and t = coordinate axes and time
M, C, and K = mass, damping, and stiffness matrices
U = degrees of freedom (overdots represent derivative with respect to time)
F = piezoelectric force vector
R = inner radius of the jet enclosed volume
Q = volumetric flow rate
u = x-velocity component
ω = vorticity
A = amplitude of the velocity profile
D = length/height of the diaphragm
f = operating frequency
d = orifice diameter
Re = Reynolds number
S = Stokes number
V = velocity scale
T = period of oscillation or temperature
ν = kinematic viscosity
μ = dynamic viscosity
ρ = density
h = heat transfer coefficient

q = heat flux

Subscripts

av = time averaged over half cycle
inv = equivalent of an inviscid profile
0 = ambient
rms = root mean square
s = surface
nc = natural convection
jet = side of the heater facing the jet
S = structural property
F = fluid property
C = jet disk center

References

[1] Mittal, R., and Rampunggoon, P., 2002, "On Virtual Aero-Shaping Effect of Synthetic Jets," Phys. Fluids, **14**(4), pp. 1533–1536.
[2] Smith, D., Amitay, M., Kibens, V., Parekh, D., and Glezer, A., 1998, "Modification of Lifting Body Aerodynamics Using Synthetic Jet Actuators," AIAA Paper No. 1998-0209.
[3] Crook, A., Sadri, A. M., and Wood, N. J., 1999, "The Development and Implementation of Synthetic Jets for the Control of Separated Flow," AIAA Paper No. 1999-3176.
[4] Mittal, R., Rampunggoon, P., and Udaykumar, H. S., 2001, "Interaction of a Synthetic Jet With a Flat Plate Boundary Layer," AIAA Paper No. 2001-2773.
[5] Smith, B. L., and Glezer, A., 2002, "Jet Vectoring Using Synthetic Jets," J. Fluid Mech., **458**, pp. 1–34.
[6] Rathnasingham, R., and Breur, K. S., 1997, "System Identifcation and Control of Turbulent Boundary Layer," Phys. Fluids, **9**(7), pp. 1867–1869.
[7] Lee, C. Y., and Glodstein, D. B., 2001, "DNS of Microjets for Turbulent Boundary Layer Control," AIAA Paper No. 2001-1013.
[8] Mahalingam, R., Rumigny, N., and Glezer, A., 2004, "Thermal Management Using Synthetic Jet Ejectors," IEEE Trans. Compon. Packag. Technol., **27**(3), pp. 439–444.
[9] Mahalingam, R., and Glezer, A., 2005, "Design and Thermal Characteristics of a Synthetic Jet Ejector Heat Sink," J. Electron. Packag., **127**, pp. 172–177.
[10] Holman, R., Utturkar, Y., Mittal, R., Smith, B., and Cattafesta, L., 2005, "Formation Criterion for Synthetic Jets," AIAA J., **43**(10), pp. 2110–2116.
[11] Li, S., 2005, "A Numerical Study of Micro Synthetic Jet and Its Applications in Thermal Management," Ph.D. thesis, Georgia Institute of Technology.
[12] Erbas, N., Koklu, M., and Baysal, O., 2005, "Synthetic Jets for Thermal Management of Microelectronic Chips," *Proceedings of IMECE*, Paper No. IMECE 2005-81419.
[13] Timchenko, V., Reizes, J., and Leonardi, E., 2004, "A Numerical Study of Enhanced Micro-Channel Cooling Using a Synthetic Jet Actuator," 15th Australian Fluid Mechanics Conference, Sydney Australia.
[14] Utturkar, Y., Mittal, R., Rampunggoon, P., and Cattafesta, L., 2003, "Sensitivity of Synthetic Jets to the Design of the Jet Cavity," AIAA Paper No. 2002-0214.
[15] Gallas, Q., Holman, R., Raju, R., Mittal, R., Sheplak, M., and Cattafesta, L., 2004, "Low Dimensional Modeling of Zero-Net-Mass-Flux Actuators," AIAA Paper No. 2004-2413.
[16] Raju, R., Mittal, R., Gallas, Q., and Cattafesta, L., 2005, "Scaling of Vorticity Flux and Entrance Length Effects in Zero-Net-Mass-Flux Devices," AIAA Paper No. 2005-4751.
[17] Yassour, Y., Stricker, J., and Wolfshtein, M., 1986, "Heat Transfer From a Small Pulsating Jet," *Proceedings of the Eighth International Conference*, San Francisco, CA, Aug. 17–22, Vol. 3, pp. 1183–1186.
[18] Coe, D. J., Allen, M. G., Trautman, M. A., and Glezer, A., 1994, "Micromachined Jet for Manipulation of Macro Flow," Solid-State Sensor and Actuation Workshop, Hilton Head Island, SC, Jun 13–16.
[19] Garg, J., Arik, M., Weaver, S., Wetzel, T., and Saddoughi, S., 2005, "Meso Pulsating Jet for Electronics Cooling," ASME J. Electron. Packag., **127**(4), pp. 503–551.
[20] Utturkar, Y., Arik, M., and Gursoy, M., 2006, "An Experimental and Computational Sensitivity Analysis of Synthetic Jet Cooling Performance," ASME International Mechanical Engineering Congress and Exposition, Chicago, IL, Nov. 5-10.
[21] Gillespie, M. B., Black, W. Z., Rinehart, C., and Glezer, A., 2006, "Local Convective Heat Transfer from a Constant Heat Flux Flat Plate Cooled by Synthetic Air Jets," ASME J. Heat Transfer, **128**, pp. 990–1000.
[22] Pavlova, A., and Amitay, M., 2006, "Electronic Cooling Using Synthetic Jet Impingement," ASME J. Heat Transfer, **128**, (9), pp. 897–907.
[23] Arik, M., 2007, "An Investigation Into Feasibility of Impingement Heat Transfer and Acoustic Abatement of Meso Scale Synthetic Jets," Appl. Therm. Eng., **27**, pp. 1483–1494.
[24] Moffat, R. J., 1988, "Describing the Uncertainties in Experimental Results," Exp. Therm. Fluid Sci., **1**, pp. 3–17.
[25] Issa, R., 1985, "Solution of the Implicitly Discretized Fluid Flow Equations by Operator-Splitting," J. Comput. Phys., **62**, pp. 40–65.
[26] Kotapati, R. B., and Mittal, R., 2005, "Time-Accurate Three-Dimensional Simulations of Synthetic Jets in Quiescent Air," AIAA Paper No. 2005-0103.

An Interfacial Tracking Method for Ultrashort Pulse Laser Melting and Resolidification of a Thin Metal Film

Yuwen Zhang[1]
Associate Professor
Fellow ASME
e-mail: zhangyu@missouri.edu

J. K. Chen
William and Nancy Thompson Professor
Mem. ASME

Department of Mechanical and Aerospace Engineering,
University of Missouri-Columbia,
Columbia, MO 65211

An interfacial tracking method was developed to model rapid melting and resolidification of a freestanding metal film subject to an ultrashort laser pulse. The laser energy was deposited to the electrons near thin film surface, and subsequently diffused into a deeper part of the electron gas and transferred to the lattice. The energy equations for the electron and lattice were coupled through an electron-lattice coupling factor. Melting and resolidification were modeled by considering the interfacial energy balance and nucleation dynamics. An iterative solution procedure was employed to determine the elevated melting temperature and depressed solidification temperature in the ultrafast phase-change processes. The predicted surface lattice temperature, interfacial location, interfacial temperature, and interfacial velocity were compared with those obtained by an explicit enthalpy model. The effects of the electron thermal conductivity models, ballistic range, and laser fluence on the melting and resolidification were also investigated.

[DOI: 10.1115/1.2891159]

Keywords: heat transfer, laser, melting, solidification, microscale

Introduction

Microscale heat transfer has drawn the attention of many researchers due to its importance in many advanced manufacturing and materials processing. The traditional phenomenological laws, such as Fourier's law of heat conduction, are challenged in the microscale regime because (1) the characteristic lengths of the various heat carriers are comparable to each other and to the characteristic length of the system considered, and/or (2) the characteristic times of the various heat carriers are comparable to the characteristic energy excitation time [1]. Thus, microscale heat transfer can be referred to as heat transfer occurring on both the micro-length- and micro-time-scales. Microscale heat transfer finds applications in thin film (micro-length-scale) as well as ultrashort-pulsed laser processing (micro-time-scale).

Ultrafast laser material processing has received significant attention due to a growing need for the fabrication of miniaturized devices at micro- and nanoscales. When the laser pulse is reduced to a nanosecond (10^{-9} s) or less, the heat flux of the laser beam can be as high as 10^{12} W/m^2. For femtosecond pulse lasers, the laser intensity can even be up to 10^{21} W/m^2. Compared to long-pulsed laser processing, short-pulsed laser processing enables users to precisely control the size of the heat-affected zone, the heat rate, and the interfacial velocity. Griffith et al. [2] investigated femtosecond laser machining of steel and developed the femtosecond laser micro-fabrication capability in the microscale regime. Klein-Wiele et al. [3] introduced a new technology of laser processing via ablation for nanofabrication of solid materials with femtosecond laser. Heat-affected zone of metals ablated with femtosecond laser was investigated by Hirayama and Obara [4].

During laser-metal interaction, the laser energy is first deposited into electrons on the metal surface, where two competing processes occur [5]. One is ballistic motion of the excited electrons into deeper parts of the metal with velocity close to the Fermi velocity ($\sim 10^6$ m/s). Another process is collision between the excited electrons and electrons around the Fermi level—an electron temperature is defined upon establishment of equilibrium among hot electrons. These hot electrons are then diffused into deeper part of the electron gas at a speed ($< 10^4$ m/s) much lower than that of the ballistic motion. Meanwhile, the hot electrons are cooled by transferring their energy to the lattice through electron-phonon coupling. The nonequilibrium between electrons and lattice has been observed experimentally [6,7] and can be described by the two-temperature model, which was originally proposed by Anisimov et al. [8] and rigorously derived by Qiu and Tien [9] from the Boltzmann transport equation. The nonequilibrium electron and lattice temperature model can also be derived using the dual-phase-lag model by considering lagging behavior of different energy carrier [10,11]. Jiang and Tsai extended the existing two-temperature model to high electron temperatures by using full-run quantum treatments [12]. Chen et al. proposed a semiclassical two-step heating model to investigate thermal transport in metals caused by ultrashort laser heating [13].

Most existing two-temperature models dealt with the case that lattice temperature is well below the melting point and only pure conduction is considered. Under higher laser fluence and/or short pulse, the lattice temperature can exceed the melting point and melting takes place. The liquid phase will be resolidified when the lattice is cooled by conducting heat away. Short-pulsed laser melting of thin film involves the following three steps [14]: (1) absorption of photon energy by free electrons, (2) energy transfer between the free electrons and the lattice, and (3) phase change of the lattice due to the propagation of energy. The rapid phase-change phenomena induced by ultrashort pulse laser are controlled by nucleation dynamics at the interface, not by interfacial energy balance [15]. The solid-liquid interface can be heated well above the melting point during a rapid melting process, in which case the solid becomes superheated. Similarly, the solid-liquid interface can be cooled far below the melting point in the rapid solidification process, in which case the liquid becomes undercooled. Both superheated solid and undercooled liquid are ther-

---

[1] Corresponding author.

Contributed by the Heat Transfer Division of ASME for publication in the JOURNAL OF HEAT TRANSFER. Manuscript received December 29, 2006; final manuscript received September 10, 2007; published online April 23, 2008. Review conducted by Ben Q. Li..

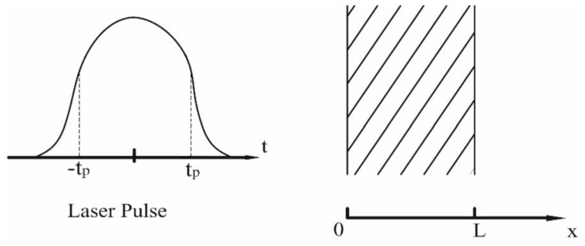

Fig. 1 Laser melting of thin film

modynamically metastable states. Once phase change is triggered in a superheated solid or undercooled liquid, the solid-liquid interface can move at an extremely high velocity (on the order of $10-10^3$ m/s). When the laser fluence is sufficiently high [16] or when the laser pulse width is in the order of femtosecond [17], the liquid surface temperature may exceed the saturation temperature and vaporization may take place.

Many numerical models for melting and solidification of various phase-change materials (PCMs) have been developed. The numerical models can be divided into two groups [18]: *deforming grid schemes* (or strong numerical solutions) and *fixed grid schemes* (or weak numerical solutions). Deforming grid schemes transform solid and liquid phases into fixed regions by using a coordinate transformation technique. The governing equations and boundary conditions are complicated due to the transformation. However, the disadvantage of deforming grid schemes is that it requires a significant amount of computational time. On the contrary, the fixed grid schemes use one set of governing equations for the whole computational domain including both liquid and solid phases, and solid-liquid interface is later determined from the temperature distribution. This simplicity makes the computation much faster than deforming grid schemes, while it still provides reasonably accurate results [19]. There are two main methods in the fixed grid schemes: the enthalpy method and the equivalent heat capacity method. The enthalpy method [20] can solve heat transfer in the mushy zone but has difficulty with temperature oscillation, while the equivalent heat capacity method [21,22] requires a large enough temperature range in the mushy zone to obtain a converged solution. Cao and Faghri [23] combined the advantages of both enthalpy and equivalent heat capacity methods and proposed a temperature transforming model (TTM) that could also account for natural convection.

The energy equation for electrons was solved using a semi-implicit Crank–Nicholson scheme, while the energy equation and phase change for lattices were solved using an explicit enthalpy model in Refs. [14,17]. While an explicit scheme is very easy to apply, a very small time step is required to ensure stability. Development of an implicit scheme for enthalpy model that can outperform an explicit scheme is numerically challenging [18]. The TTM[23] and the enthalpy linearization model [24] are two very efficient models that can be easily discretized using an implicit scheme. These two models assume that phase change occurs in a range of temperature near the melting point, which prevents an inclusion of superheat in solid in the melting stage and undercooling of liquid in the solidification stage. In this paper, a fixed grid interfacial tracking method is proposed to solve kinetics controlled rapid melting and resolidification during an ultrashort pulse laser interaction with a freestanding metal film. Effects of electron thermal conductivity model, ballistic range, and laser fluence on the phase-change processes are investigated.

Physical Model

The physical model of the problem under consideration is shown in Fig. 1. A metal film with a thickness of L and an initial temperature of T_i is subjected to a temporal Gaussian laser pulse with a full width at half maximum (FWHM) pulse width of t_p and fluence of $J(J/\mathrm{m}^2)$ from the left surface ($x=0$). The problem can be approximated to be one dimensional because the radius of the laser beam is significantly larger than the metal film thickness. The energy equation of the free electrons is

$$C_e \frac{\partial T_e}{\partial t} = \frac{\partial}{\partial x}\left(k_e \frac{\partial T_e}{\partial x}\right) - G(T_e - T_l) + S \tag{1}$$

which is valid in the entire computational domain. The energy equation for the lattice is

$$C_l \frac{\partial T_l}{\partial t} = \frac{\partial}{\partial x}\left(k_l \frac{\partial T_l}{\partial x}\right) + G(T_e - T_l) \tag{2}$$

which is valid in both solid and liquid phases but not at the solid-liquid interface. The heat capacity of electron is proportional to the electron temperature, i.e.,

$$C_e = B_e T_e \tag{3}$$

The bulk thermal conductivity of metal measured at equilibrium k_{eq} is the sum of the electron thermal conductivity k_e and the lattice thermal conductivity k_l. Since the mechanism for heat conduction in metal is diffusion of free electron, k_e is usually dominated. For gold, k_e is 99% of k_{eq}, while k_l only contributes to 1% of k_{eq} [25]. At a nonequilibrium condition, thermal conductivity of the electrons depends on the temperatures of both electrons and lattice [14], i.e.,

$$k_e = k_{\mathrm{eq}}\left(\frac{T_e}{T_l}\right) \tag{4}$$

where $k_{\mathrm{eq}}(T)$ is the thermal conductivity of the electron when the electrons and lattice are in thermal equilibrium. Equation (4) is valid when the electron temperature is much lower than the Fermi temperature T_F, which is 6.42×10^4 K for gold. If the electron temperature is comparable to the Fermi temperature, the electron temperature can be calculated by [26]

$$k_e = \chi \frac{(\vartheta_e^2 + 0.16)^{5/4}(\vartheta_e^2 + 0.44)\vartheta_e}{(\vartheta_e^2 + 0.092)^{1/2}(\vartheta_e^2 + \eta\vartheta_l)} \tag{5}$$

where $\vartheta_e = T_e/T_F$ and $\vartheta_l = T_l/T_F$. The two constants in Eq. (5) are $\chi = 353$ W/m K and $\eta = 0.16$ for gold. For high electron temperature, $\vartheta_e \gg 1$, Eq. (5) results in the well-known dependence $k_e \sim T_e^{5/2}$ that is the characteristics of low-density plasma. On the other hand, Eq. (5) will reduce to Eq. (4) under low electron temperature limit, $\vartheta_e \ll 1$. The difference between the results obtained by using thermal conductivities will be discussed later. The electron-lattice coupling factor G for liquid is 20% higher than that of the solid, because electrons collide more frequently with liquid atoms than with the atoms in the solid crystals [14].

The source terms in Eq. (1) can be described by the following equation:

$$S = 0.94 \frac{1-R}{t_p \delta} J \exp\left(\frac{x}{\delta} - 2.77\left(\frac{t}{t_p}\right)^2\right) \tag{6}$$

where R is the reflectivity of the thin film, t_p is the laser pulse duration (s), δ is the optical penetration depth (m), and J is the laser pulse fluence ($\mathrm{J/m^2}$). While Eq. (6) is widely used in many existing works, Wellershoff et al. [27] and Hohlfeld et al. [5] suggested that the ballistic motion and diffusion of the hot electrons spread the absorbed laser energy into a much greater depth of electrons, especially for the s/p-band metals. This hot electron bath should be initially localized within either the ballistic range (for s/p-band metals) or the optical penetration depth. Therefore, it is necessary to incorporate the effect of the ballistic motion and hot electron diffusion by adding the ballistic range δ_b to the optical penetration depth in Eq. (6), i.e.,

$$S = 0.94\frac{1-R}{t_p(\delta+\delta_b)[1-e^{-L/(\delta+\delta_b)}]}J\exp\left(\frac{x}{\delta+\delta_b}-2.77\left(\frac{t}{t_p}\right)^2\right) \tag{7}$$

where $[1-e^{-L/(\delta+\delta_b)}]$ is to correct the film thickness effect. The effect of ballistic motion on the ultrafast melting and resolidification will be discussed later.

The lattice thermal conductivity k_ℓ is taken as 1% of the thermal conductivity of bulk metal, k_{eq}, since the mechanism of heat conduction in metal is mainly by electrons [14,25], i.e.,

$$k_l = 0.01k_{\text{eq}} \tag{8}$$

While many researchers suggested that the conduction term in Eq. (2) be negligible (e.g., Refs. [9,12]), Chen and Beraun [28] showed that inclusion of a lattice conduction resulted in a more accurate thermal response than the models without a lattice conduction. As will become evident later, large lattice temperature gradients in solid and liquid phases exist near the solid-liquid interface during ultrashort pulse laser induced melting and resolidification and therefore, lattice conduction is included in this work.

While the energy equation for electrons, Eq. (1), is valid for both solid and liquid phases, the coupling factor for solid and liquid phases is different. For the energy equation of lattice, Eq. (2) is valid for both solid and liquid phases, but not at the interface. The energy balance at the solid-liquid interface is [29]

$$k_{l,s}\frac{\partial T_{l,s}}{\partial x} - k_{l,\ell}\frac{\partial T_{l,\ell}}{\partial x} = \rho_\ell h_m u_s, \quad x = s(t) \tag{9}$$

where the additional interfacial velocity due to the density change during melting and solidification has been considered.

For the conventional melting process, the velocity of the solid-liquid interface is obtained by the energy balance, as specified by Eq. (9). However, this is not the case for rapid melting/solidification processes, because the velocity of the interface is dominated by nucleation dynamics. For short-pulsed laser melting of gold, the velocity of the solid-liquid interface is described by [14]

$$u_s = V_0\left[1-\exp\left(-\frac{h_m}{R_g T_m}\frac{T_{l,I}-T_m}{T_{l,I}}\right)\right] \tag{10}$$

where V_0 is the maximum interface velocity, R_g is the gas constant for the metal, and $T_{l,I}$ is the interfacial temperature. The interfacial temperature $T_{l,I}$ is higher than the melting point T_m during melting and lower than the melting point during solidification.

The time $t=0$ is defined as the time when the peak of a laser pulse reaches the film surface. Therefore, the initial conditions of the problem are

$$T_e(x,-2t_p) = T_l(x,-2t_p) = T_i \tag{11}$$

The boundary conditions of the problem can be specified by assuming that the heat loss from the film surface can be neglected, i.e.,

$$\left.\frac{\partial T_e}{\partial x}\right|_{x=0} = \left.\frac{\partial T_e}{\partial x}\right|_{x=L} = \left.\frac{\partial T_l}{\partial x}\right|_{x=0} = \left.\frac{\partial T_l}{\partial x}\right|_{x=L} = 0 \tag{12}$$

Numerical Solution and Interfacial Tracking

Discretization of the Governing Equations. The computational domain (0, L) is discretized using a nonuniform grid. The implicit finite difference equations are obtained by integrating Eqs. (1) and (2) in each control volume and time step [30]. The electron temperature can be obtained by

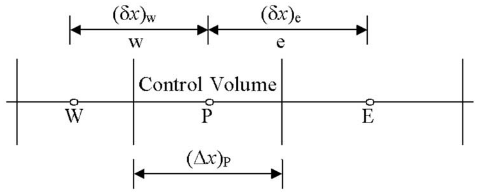

(a) Single phase control volume

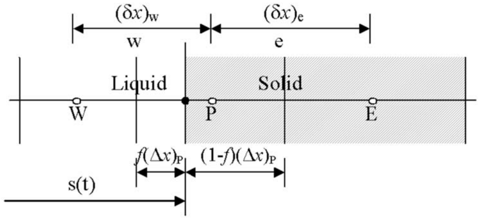

(b) Control volume with interface

Fig. 2 Grid system

$$a_{e,P}T_{e,P} = a_{e,W}T_{e,W} + a_{e,E}T_{e,E} + b_e \tag{13}$$

where $T_{e,P}$, $T_{e,W}$, and $T_{e,E}$ are, respectively, electron temperatures at Grids P, W, and E at the current time step (see Fig. 2). The coefficients in Eq. (13) are as follows:

$$a_{e,W} = \frac{k_{e,w}}{(\delta x)_w} \tag{14}$$

$$a_{e,E} = \frac{k_{e,e}}{(\delta x)_e} \tag{15}$$

$$b_e = a_{e,P}^0 T_{e,P}^0 + (G_P T_{l,P} + S_P)(\Delta x)_P \tag{16}$$

$$a_{e,P}^0 = \frac{C_{e,P}(\Delta x)_P}{\Delta t} \tag{17}$$

$$a_{e,P} = a_{e,P}^0 + a_{e,W} + a_{e,E} + G_P(\Delta x)_P \tag{18}$$

where $k_{e,w}$ and $k_{e,e}$ are electron conductivities at the faces of the control volume, e and w, and they are obtained by harmonic averaging the thermal conductivities at the two control volumes [30]. $T_{e,P}^0$ is the electron temperature at Grid Point P for the previous time step, $T_{l,P}$ is the lattice temperature at Grid Point P for the current time step, and S_P is the intensity of the heat source at Grid Point P.

For a control volume that contains only one phase, the lattice temperature can be obtained by integrating Eq. (2) in the control volume P, i.e.,

$$a_{l,P}T_{l,P} = a_{l,W}T_{l,W} + a_{l,E}T_{l,E} + b_l \tag{19}$$

where $T_{l,P}$, $T_{l,W}$, and $T_{l,E}$ are, respectively, electron temperatures at Grids P, W, and E at the current time. The coefficients in Eq. (19) are as follows:

$$a_{l,W} = \frac{k_{l,w}}{(\delta x)_w} \tag{20}$$

$$a_{l,E} = \frac{k_{l,e}}{(\delta x)_e} \tag{21}$$

$$b_l = a_{l,P}^0 T_{l,P}^0 + G_P T_{e,P}(\Delta x)_P \tag{22}$$

$$a_{l,P}^0 = \frac{C_{l,P}(\Delta x)_P}{\Delta t} \tag{23}$$

Table 1 Thermophysical properties of gold [14]

Properties	Solid (s)	Liquid (l)
Coefficient for electron heat capacity, B_e (J/m^3 K)	70	
Electron-lattice coupling factor, G (W/m^3 K)	2.6×10^{16}	3.1×10^{16}
Density, ρ (kg/m^3)	19.30×10^3	17.28×10^3
Specific heat, c_p (J/kg K)[a]	$105.1+0.2914T_l-8.713\times10^{-4}T_l^2$ $+1.187\times10^{-6}T_l^3-7.051\times10^{-10}T_l^4$ $+1.538\times10^{-13}T_l^5$	163.205
Thermal conductivity at equilibrium, k_{eq} (W/m K)[a]	$320.973-0.0111T_l-2.747$ $\times10^{-5}T_l^2-4.048\times10^{-9}T_l^3$	$37.72+0.0711T_l-1.721$ $\times10^{-5}T_l^2+1.064\times10^{-9}T_l^3$
Reflectivity, R	0.6	
Optical penetration depth, δ (nm)	20.6	
Melting point, T_m (K)	1336	
Latent heat of fusion, h_m (J/kg)	6.373×10^4	
Limit velocity, V_0 (m/s)	1300	
Gas constant for gold, R_g (J/kg K)	42.21	

[a] Correlations were obtained by curve-fitting data in Ref. [14].

$$a_{l,P}=a^0_{l,P}+a_{l,W}+a_{l,E}+G_P(\Delta x)_P \tag{24}$$

where the lattice conductivities at the faces of the control volume are obtained by harmonic averaging the thermal conductivities at two control volumes, and $T^0_{l,P}$ is the lattice temperature at Grid P for the previous time step.

Interfacial Tracking Method. Wang and Matthys [31] proposed an effective interface-tracking method by introducing an addition node at the interface, which divides the control volume containing interface into two control volumes. This approach could accurately account for energy balance at the interface because the solid-liquid interface is always between two small control volumes. In this paper, an alternative approach that does not require dividing the control volume containing interface but can still accurately account for energy balance at the interface will be developed. For the control volume that contains a solid-liquid interface, the lattice temperature $T_{l,P}$ is numerically set as interfacial temperature $T_{l,I}$ by letting

$$a_{l,P}=10^{20} \quad \text{and} \quad b_l=T_{l,I}\times10^{20} \tag{25}$$

in Eq. (19). This treatment will yield an accurate result when the solid-liquid interface is exactly at Grid Point P. When the interfacial location is not at Grid Point P (see Fig. 2(*b*)), a modified thermal conductivity, $\hat{k}_{l,w}$, at the face of the control volume w is introduced by equating the actual heat flux across the face of the control volume w, based on the position and temperature of the solid-liquid interface, to the heat flux at face w based on the position and temperature of the main grid point, P [32], i.e.,

$$\frac{k_{l,w}(T_{l,W}-T_{l,I})}{(\delta x)_w-(0.5-f_P)(\Delta x)_P}=\frac{\hat{k}_{l,w}(T_{l,W}-T_{l,P})}{(\delta x)_w} \tag{26}$$

Considering $T_{l,P}=T_{l,I}$, Eq. (26) becomes

$$\hat{k}_{l,w}=\frac{(\delta x)_w}{(\delta x)_w-(0.5-f_P)(\Delta x)_P}k_{l,w} \tag{27}$$

Similarly, a modified thermal conductivity at face e of the control volume can be obtained as

$$\hat{k}_{l,e}=\frac{(\delta x)_e}{(\delta x)_e+(0.5-f_P)(\Delta x)_P}k_{l,e} \tag{28}$$

The modified thermal conductivities defined by Eqs. (27) and (28) are used to obtain the coefficients for Grid Points W and E, which allows the temperature at the main grid (P) to be used in the computation, regardless of the location of the interface within the control volume. To determine the interfacial location and the interfacial temperature, the energy balance at the interface, Eq. (9), and the nucleation dynamics, Eq. (10), must be employed. The energy equation for the control volume that contains a solid-liquid interface can be written in the enthalpy form

$$\frac{\partial H_l}{\partial t}=\frac{\partial}{\partial x}\left(k_l\frac{\partial T_l}{\partial x}\right)+G(T_e-T_l) \tag{29}$$

The volumetric enthalpy can be expressed as

$$H_l=\int_0^{T_{l,I}}C_{l,s}(T_l)dT_l+f\rho_\ell h_m \tag{30}$$

where the first term is the enthalpy of the solid phase at the interfacial temperature, and the second term is the latent heat due to partial melting. Substituting Eq. (30) into Eq. (29), one obtains

$$C_{l,s}(T_{l,I})\frac{\partial T_{l,I}}{\partial t}+\rho_\ell h_m\frac{\partial f}{\partial t}=\frac{\partial}{\partial x}\left(k_l\frac{\partial T_l}{\partial x}\right)+G(T_e-T_l) \tag{31}$$

which is applicable in the control volume that contains a solid-liquid interface. The liquid fraction f is related to the location of the solid-liquid interface by (see Fig. 2(*b*))

$$\frac{\partial f}{\partial t}=\frac{1}{(\Delta x)_P}\frac{ds}{dt}=\frac{u_s}{(\Delta x)_P} \tag{32}$$

Substituting Eq. (32) into Eq. (31) and integrating the resulting equation in the control volume that contains a solid-liquid interface, the solid-liquid interfacial velocity can be obtained as

$$u_s=\frac{1}{\rho_\ell h_m}\left[\frac{k_{l,w}(T_{l,W}-T_{l,I})}{(\delta x)_w-(0.5-f_P)(\Delta x)_P}-\frac{k_{l,e}(T_{l,I}-T_{l,E})}{(\delta x)_e+(0.5-f_P)(\Delta x)_P}\right.$$
$$\left.+G_P(T_{e,P}-T_{l,P})(\Delta x)_P-C_{l,s}(T_{l,I})(T_{l,I}-T^0_{l,I})\frac{(\Delta x)_P}{\Delta t}\right] \tag{33}$$

where $T^0_{l,I}$ is the solid-liquid interfacial temperature at the previous time step. The third and fourth terms in the bracket at the right-hand side of Eq. (33) represent the effects of the electron-lattice interaction and change of the interfacial temperature on the solid-liquid interfacial temperature. Equation (33) can be rewritten in a more compact form by considering Eqs. (27) and (28), i.e.,

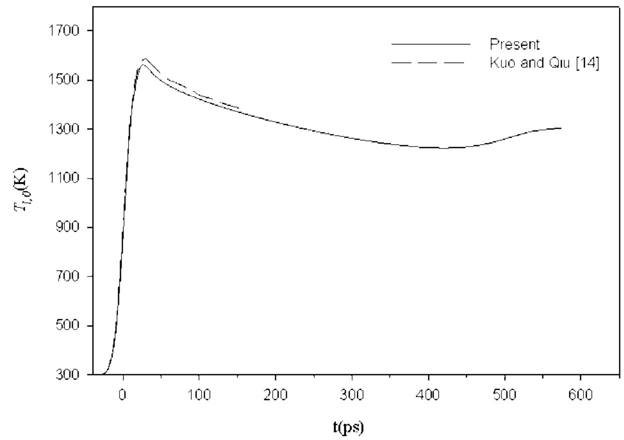

(a) Surface lattice temperature

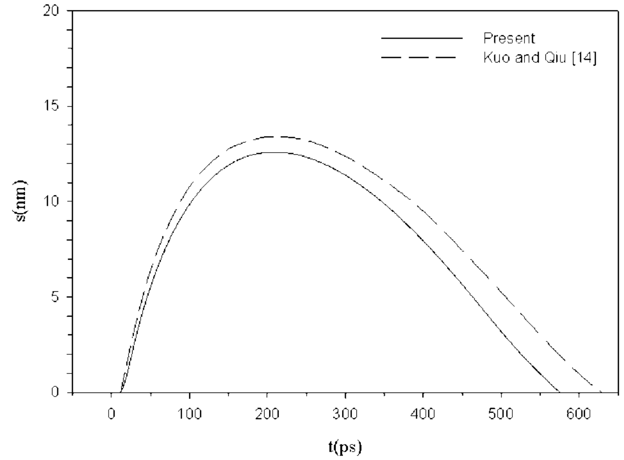

(b) Interfacial location

Fig. 3 Comparison of surface lattice temperatures and interfacial locations

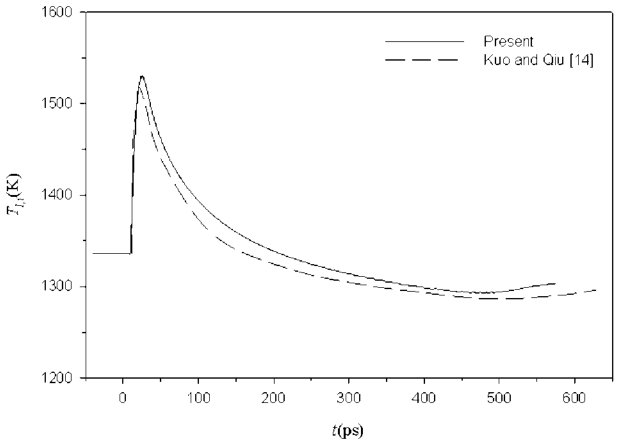

(a) Interfacial temperature

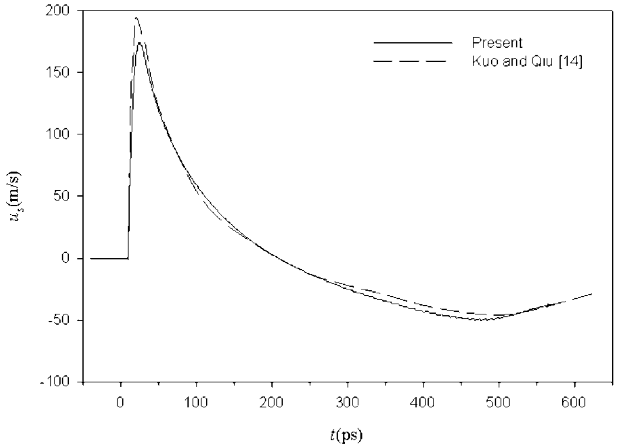

(b) Interfacial velocity

Fig. 4 Comparison of interfacial temperatures and velocities

$$u_s = \frac{1}{\rho_\ell h_m}\left[\frac{\hat{k}_{l,w}(T_{l,W}-T_{l,P})}{(\delta x)_w} - \frac{\hat{k}_{l,e}(T_{l,P}-T_{l,E})}{(\delta x)_e} + G_P(T_{e,P}-T_{l,P})(\Delta x)_P - C_{l,s}(T_{l,I})(T_{l,I}-T^0_{l,I})\frac{(\Delta x)_P}{\Delta t}\right] \tag{34}$$

which will be used together with Eq. (10) to determine the solid-liquid phase interfacial velocity and the temperature. The interfacial location is then determined using

$$s = s^0 + u_s\Delta t \tag{35}$$

and the liquid fraction in the control volume that contain interface is

$$f = \frac{s - x_P - (\Delta x)_P/2}{(\Delta x)_P} \tag{36}$$

Numerical Solution Procedure. The numerical solution starts from time $t=-2t_p$, and the initial temperatures of electrons and lattice are given by Eq. (11). Before the onset of melting, the electron and lattice temperatures are obtained by solving Eqs. (13) and (19) simultaneously. Once the lattice temperature at the first control volume from the heated surface obtained from Eq. (19) (without phase change accounted for) exceeds the melting point, the lattice temperature of the first control volume sets at the melting point using Eq. (25) and phase change will be modeled. Since rapid melting and resolidification are controlled by nucleation dynamics, the interfacial temperature $T_{l,I}$ is unknown and it is related to the interfacial velocity by Eq. (10). After melting is initiated, the following iterative procedure is employed to solve for the interfacial temperature and the interfacial location at each time step.

(1) The solid-liquid interfacial temperature $T_{l,I}$ is assumed and Eq. (34) is used to determine the solid-liquid phase interfacial velocity. The location of the interface is determined using Eq. (35) and the liquid fraction in the first control volume is determined using Eq. (36).
(2) The interfacial velocity from the nucleation dynamics is obtained from Eq. (10) and compared with the interfacial velocity obtained from Eq. (34) in Step (1). If the interfacial velocity obtained from Eq. (34) is higher than that from Eq. (10), the interfacial temperature will be increased; otherwise, the interfacial temperature is decreased.
(3) Equations (13) and (19) ($a_{l,P}$ and b_l at the control volume that contains interface are altered using Eq. (25)) are solved simultaneously to obtain the electron and lattice temperature distributions.
(4) Steps 1–3 are repeated until the difference between the interfacial velocities obtained from Eqs. (33) and (10) is less than 10^{-6} m/s.

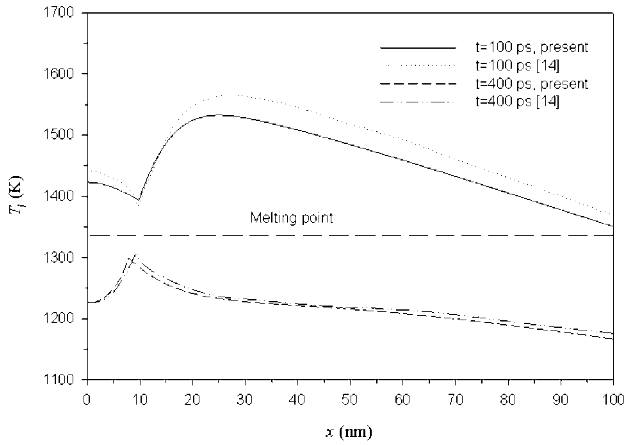

Fig. 5 Comparison of lattice temperature distributions

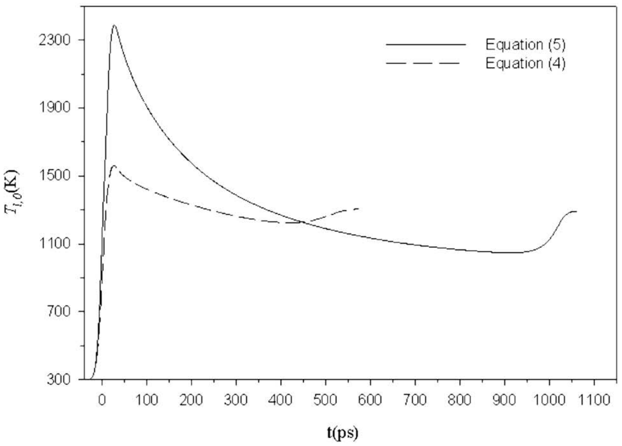

(a) Surface lattice temperature

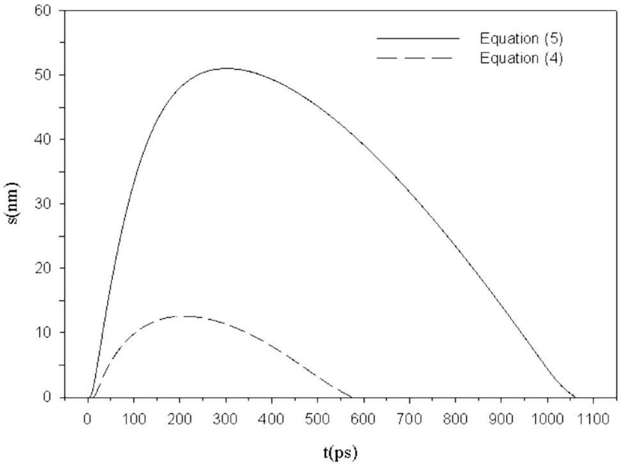

(b) Interfacial location

Fig. 6 Effect of electron thermal conductivities on the surface lattice temperatures and the interfacial locations

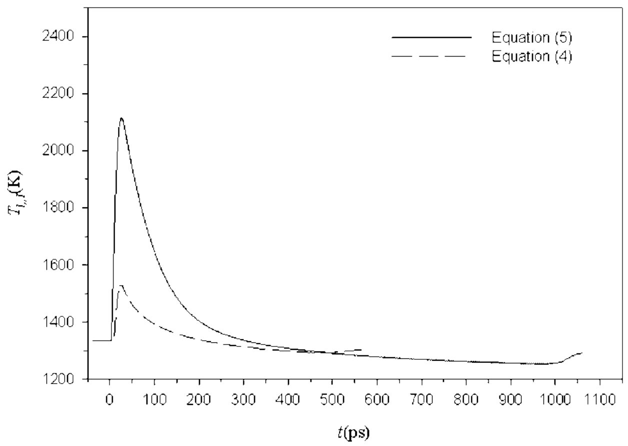

(a) Interfacial temperature

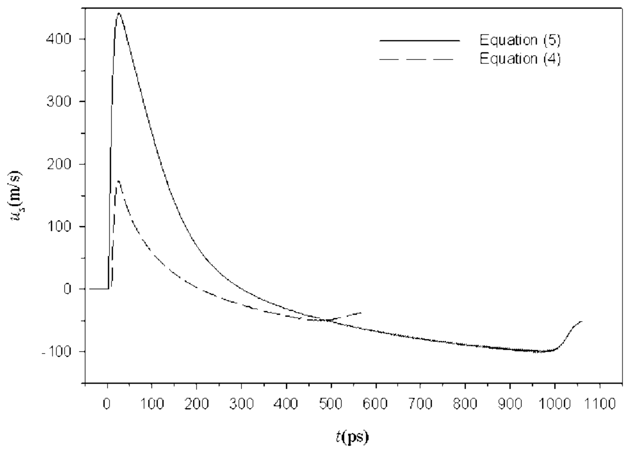

(b) Interfacial velocity

Fig. 7 Effect of electron thermal conductivities on the interfacial temperatures and velocities

Results and Discussions

Picosecond laser melting and resolidification of a freestanding pure gold film are simulated. In order to compare the results obtained by the present interfacial tracking method and those obtained by the explicit enthalpy method in Ref. [14], the thermophysical properties of the gold in the present study are exactly the same as those used in Ref. [14]. The thermophysical properties of the gold listed in Table 1 are for solid below the melting point and for liquid above the melting point only. The properties for the superheated solid and undercooled liquid are taken as those at the melting point because of lack of properties for these nonequilibrium states.

Figure 3 shows a comparison of the surface lattice temperature and interfacial location for a 1000 nm gold film under irradiation of a laser pulse with a fluence of $J=0.3\ \mathrm{J/cm^2}$ and a pulse width of $t_p=20$ ps. Under the assumption that the electron temperature is much lower than the Fermi temperature and neglecting the effect of ballistic motion, the electron thermal conductivity was calculated from Eq. (4) and the source term in Eq. (1) was obtained from Eq. (6). The grid number is 2502 and the time step is $\Delta t=0.05$ ps. The peak surface lattice temperature is 1562 K and occurs at $t=27$ ps, while the maximum melting depth is 12.59 nm and occurs at $t=209$ ps. The peak temperature and the maximum melting depth obtained in the present paper are 1.4% and 6% lower than those obtained by Kuo and Qiu [14]. The duration of phase change in the present paper is 9% shorter than that obtained by Kuo and Qiu [14].

The interfacial temperature and velocity during the picosecond laser pulse and gold film interaction are shown in Fig. 4. Strong superheating in the melting stage and undercooling in the solidi-

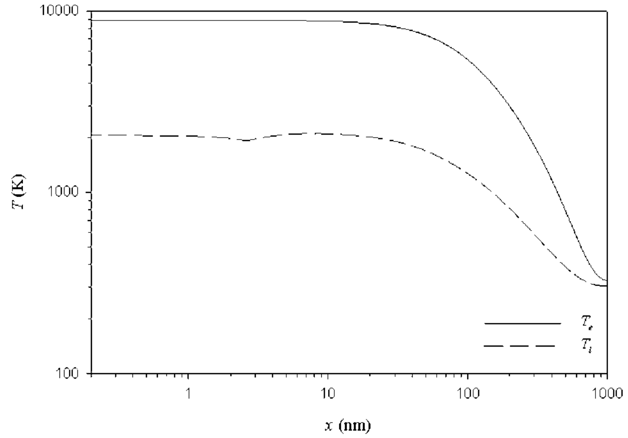

(a) Electron and lattice temperatures

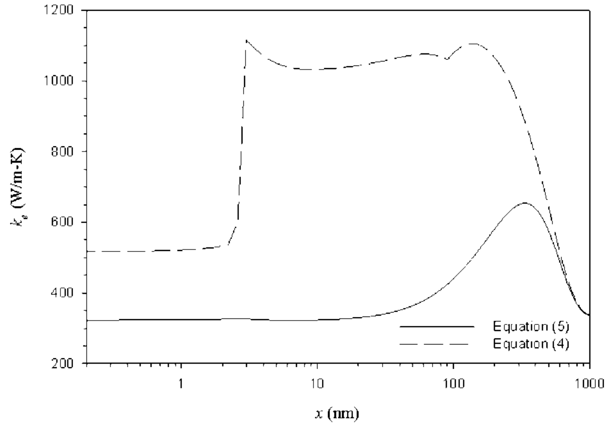

(b) Electron thermal conductivity

Fig. 8 Temperature and electron thermal conductivity distributions (t=15 ps)

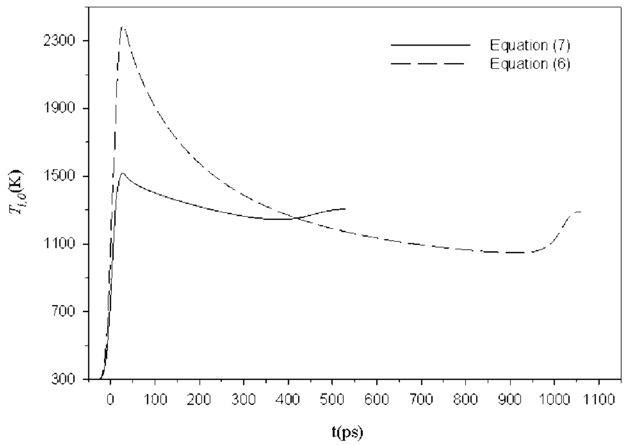

(a) Surface lattice temperature

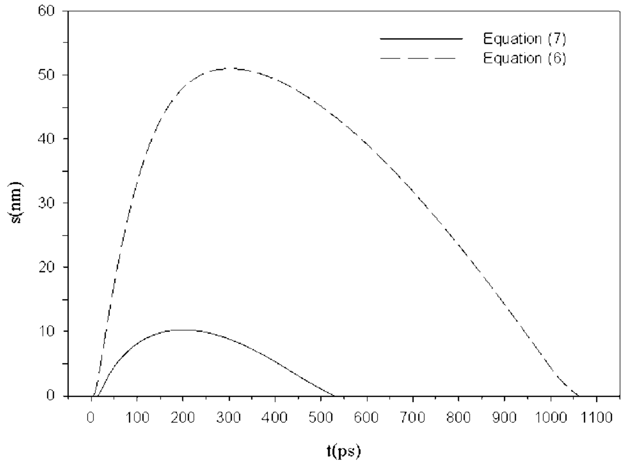

(b) Interfacial location

Fig. 9 Effect of ballistic range on the surface lattice temperatures and the interfacial locations

fication stage can be observed in Fig. 4(a), although the degrees of superheating and undercooling in the present paper are slightly lower than that in Ref. [14]. The peak interfacial velocity in the present paper is lower than that in Ref. [14], which is consistent with the result in Fig. 3(b). The interfacial velocity reached its peak at a very early stage of phase change (t=23.5 ps), and the phase change continues until t=575 ps. Since the interfacial velocity decreases in most parts of phase-change process (23.5 ps $<t<$575 ps), the melting depth obtained by the present implicit scheme is smaller than that obtained by the explicit scheme.

Figure 5 shows a comparison between the lattice temperatures obtained by using the present model and those obtained by Kuo and Qiu [14]. Strong superheating of solid in the melting stage (t=100 ps) and undercooling of the liquid phase in the resolidification stage (t=400 ps) can be successfully predicted using the proposed interfacial tracking model. The slopes of temperature curves near the interface obtained by the present paper are slightly lower than those obtained by Kuo and Qiu's [14] explicit enthalpy model, which is consistent with results shown in Figs. 3 and 4.

Numerical simulation is then performed using the electron thermal conductivity obtained from Eq. (5) while all parameters are the same as those in Figs. 3 and 4. A comparison of the surface lattice temperature and the interfacial location obtained by using different thermal conductivities is shown in Fig. 6. The peak surface lattice temperature obtained using Eq. (5) is 2388 K occurring at t=28 ps, while the maximum melting depth is 60 nm occurring at t=302 ps. They are 53% and 377%, respectively, higher than those obtained using Eq. (4). The duration of phase change obtained using Eq. (5) is 88% longer than that obtained using Eq. (4). Comparison of the interfacial temperature and velocity obtained using different thermal conductivities is shown in Fig. 7. The maximum interfacial temperature in the melting stage obtained using Eq. (5) is 2115 K, which is much higher than 1531 K obtained using Eq. (4). The interfacial velocity obtained using Eq. (5) peaks at 443 m/s as oppose to 174 m/s obtained using Eq. (4). The results presented in Figs. 6 and 7 indicated that different models of the electron thermal conductivity have significant effects on the results of ultrashort pulse laser interaction with metal film. The electron and temperature distributions at t=15 ps obtained using Eq. (5) are shown in Fig. 8(a), and the corresponding electron thermal conductivity is shown in Fig. 8(b) as the solid line. The thermal conductivity using Eq. (4) with temperatures in Fig. 8(a) is also plotted in Fig. 8(b) for comparison. When both electron and lattice temperatures are low, the thermal conductivity obtained from Eq. (4) agreed with that obtained from Eq. (5) very well. At higher electron and lattice temperature, however, the thermal conductivity obtained from Eq. (4) is several times higher than that obtained from Eq. (5). The differences between the results obtained using different thermal conductivities can be explained by the strong deviation of thermal conductivity models, as shown in Fig. 8(b).

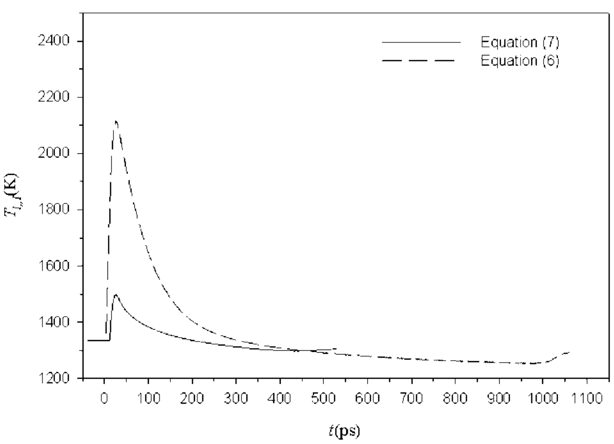

(a) Interfacial temperature

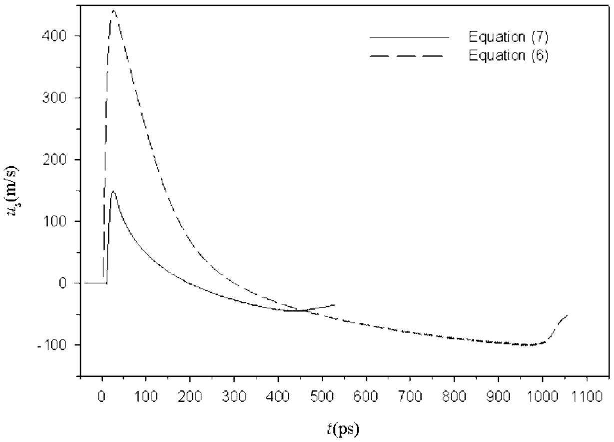

(b) Interfacial velocity

Fig. 10 Effect of ballistic range on the interfacial temperatures and velocities

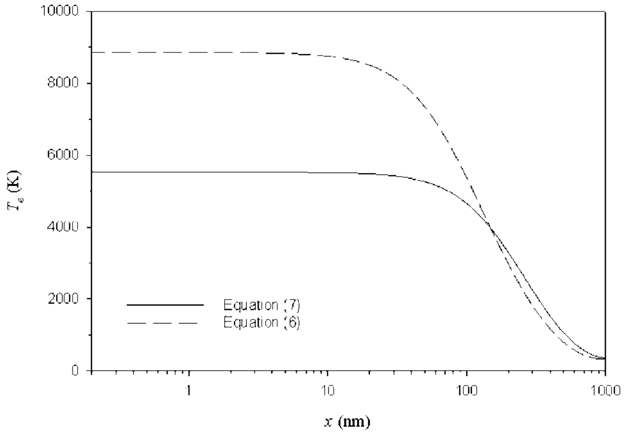

(a) Electron temperatures

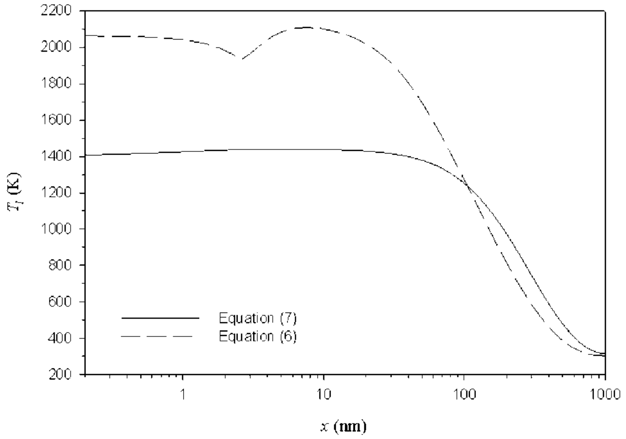

(b) Lattice temperature

Fig. 11 Effect of ballistic range on the electron and lattice temperature distributions (t=15 ps)

To investigate the effects of electron ballistic motion on the ultrashort laser melting and resolidification of metal film, simulation is carried out using the internal heat source defined in Eq. (7). The ballistic motion range of the electrons is δ_b=105 nm, as recommended in Ref. [27]. A comparison of the surface lattice temperatures and the interfacial locations obtained by using different heat sources is shown in Fig. 9. The peak surface lattice temperature obtained using Eq. (7) is 1518 K occurring at t=27.5 ps, while the maximum melting depth is 10.28 nm occurring at t =199 ps. They are, respectively, 36% and 83% lower than those obtained with δ_b=0. The duration of phase change obtained using Eq. (7) is 52% shorter than that obtained with δ_b=0. Figure 10 shows a comparison of the interfacial temperature and velocity obtained using the different heat sources. The maximum interfacial temperature in the melting stage is reduced from 2115 K to 1499 K when the ballistic motion of electrons is considered. The peak interfacial velocity is decreased from 443 m/s to 151 m/s due to the effect of the ballistic motion. Figure 11 shows the effects of the ballistic range on the electron and lattice temperature distributions. It can be seen that both electron and lattice temperatures in the region near the irradiated surface are lower when the ballistic range is considered. This is attributed to the fact that the laser energy penetrates to deeper parts of the metal film when the effect of the ballistic range is taken into account. The magnitudes of the results with the electron thermal conductivity from Eq. (5) and the heat source from Eq. (7) are comparable with those obtained using the simple electron conductivity model, Eq. (4), and the heat source without ballistic range, Eq. (6).

Figure 12 shows the surface lattice temperatures and the interfacial locations at different laser fluences while the laser pulse width is kept at t_p=20 ps. It can be seen that the surface lattice temperature increases significantly with increasing laser fluence. The time at which peak temperature occurs is slightly delayed with increasing laser fluence. The maximum melting depth is increased by 7.2 times when the laser fluence is increased from 0.3 J/cm^2 to 0.45 J/cm^2. The peak time at which a maximum melting depth is reached significantly delays with increasing laser fluence. The duration of phase change is doubled when the laser fluence is increased from 0.3 J/cm^2 to 0.45 J/cm^2. Effects of laser fluence on the interfacial temperature and velocity are shown in Fig. 13. While the peak interfacial temperature during the melting stage increases significantly—from 1499 K for J =0.3 J/cm^2 to 2216 K for J=0.45 J/cm^2—with increasing laser fluence, the minimum interfacial temperature during the solidification stage is almost unaffected by the laser fluence. Similarly, the peak interfacial velocity is increased from 151 m/s for J =0.3 J/cm^2 to 403 m/s for J=0.45 J/cm^2, while the effect of the laser fluence on the interfacial velocity during the solidification stage is insignificant.

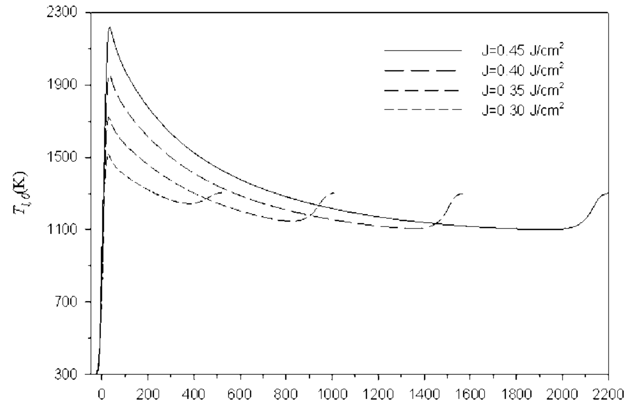

(a) Surface lattice temperature

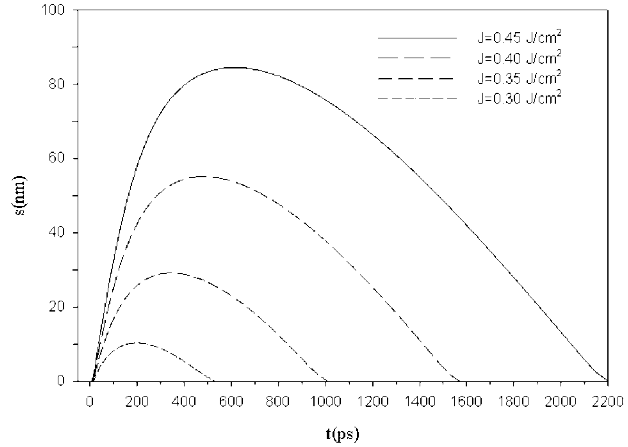

(b) Interfacial location

Fig. 12 Effect of laser fluence on the surface lattice temperatures and the interfacial locations (t_p=20 ps)

Conclusions

An interfacial tracking method was developed to model ultrashort laser melting and resolidification of the metal film. The interfacial velocity and temperature were obtained by considering interfacial energy balance and nucleation dynamics. For the case with a simple electron thermal conductivity model, Eq. (4), and without the electron ballistic motion, the results agreed with the existing results in the literature. When the more sophisticated electron thermal conductivity model, Eq. (5), was employed, the interfacial velocity and temperature were significantly increased due to the strong deviation between the two thermal conductivity models at high temperatures. Consideration of the ballistic range of electron motion resulted in the penetration of laser energy into deeper parts of the metal film and thus lowers the interfacial velocity and temperature. The maximum melting depth, peak interfacial temperature, and velocity during the melting stage significantly increase with increasing laser fluence.

Acknowledgment

Support for this work by the University of Missouri System Research Board and the College of Engineering at University of Missouri-Columbia is gratefully acknowledged.

Nomenclature

B_e = coefficient for electron heat capacity ($\mathrm{J/m^3\,K^2}$)

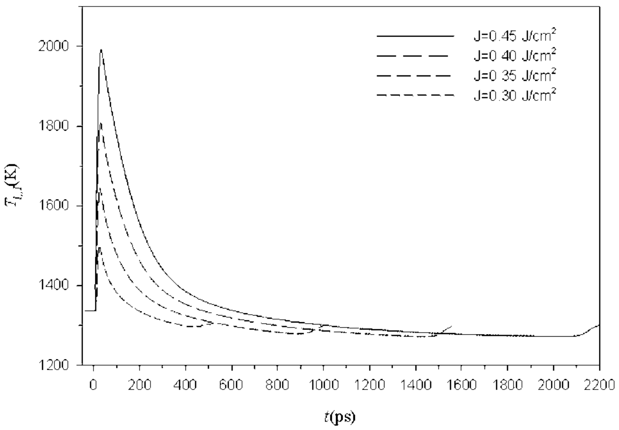

(a) Interfacial temperature

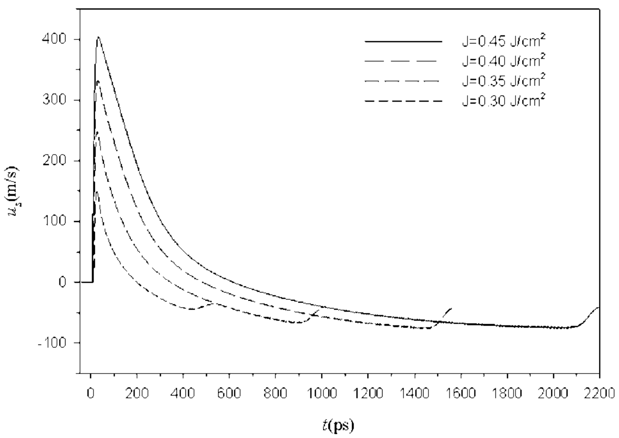

(b) Interfacial velocity

Fig. 13 Effect of laser fluence on the interfacial temperatures and velocities (t_p=20 ps)

C = heat capacity ($\mathrm{J/m^3\,K}$)
c_p = specific heat (J/kg K)
f = liquid fraction
G = electron-lattice coupling coefficient ($\mathrm{W/m^3\,K}$)
H_l = enthalpy of lattice per unit volume ($\mathrm{J/m^3}$)
h_m = latent heat of fusion (J/kg)
J = heat source fluence ($\mathrm{J/m^2}$)
k = thermal conductivity (W/m K)
L = thickness of the metal film (m)
M = molar mass (kg/kmol)
R = reflectivity
R_g = gas constant (J/kg K)
s = solid-liquid interfacial location (m)
S = intensity of the internal heat source ($\mathrm{W/m^3}$)
t = time (s)
t_p = FWHM pulse width (s)
T = temperature (K)
T_m = melting point (K)
$T_{l,I}$ = lattice temperature at solid-liquid interface (K)
u_s = solid-liquid interfacial velocity (m/s)
V_0 = interfacial velocity factor (m/s)
x = coordinate (m)

Greek Symbols

δ = optical penetration depth (m)
δ_b = ballistic range (m)

ρ = density (kg/m^3)

Subscripts

e = electron
i = initial
l = lattice
ℓ = liquid
s = solid

References

[1] Wang, G. X., and Prasad, V., 2000, "Microscale Heat and Mass Transfer and Non-Equilibrium Phase Change in Rapid Solidification," Mater. Sci. Eng., A, **292**, pp. 142–148.
[2] Griffith, M. L., Ensz, M. T., and Reckaway, D. E., 2003, "Femtosecond Laser Machining of Steel," Proc. SPIE, **4977**, pp. 118–122.
[3] Klein-Wiele, J., Bekesi, J., Ihlemann, J., and Simon, P., 2003, "Nanofabrication of Solid Materials With Ultraviolet Femtosecond Pulses," Proc. SPIE, **5399**, pp. 139–146.
[4] Hirayama, Y., and Obara, M., 2003, "Heat Affected Zone of Metals Ablated With Femtosecond Laser Pulses," Proc. SPIE, **4977**, pp. 417–425.
[5] Hohlfeld, J., Wellershoff, S. S., Gudde, J., Conrad, U., Jahnke, V., and Matthias, E., 2000, "Electron and Lattice Dynamics Following Optical Excitation of Metals," Chem. Phys., **251**, pp. 237–258.
[6] Eesley, G. L., 1986, "Generation of Non-Equilibrium Electron and Lattice Temperatures in Copper by Picosecond Laser Pulses," Phys. Rev. B, **33**, pp. 2144–2155.
[7] Elsayed-Ali, H. E., Norris, T. B., Pessot, M. A., and Mourou, G. A., 1987, "Time-Resolved Observation of Electron-Phonon Relaxation in Copper," Phys. Rev. Lett., **58**, pp. 1212–1215.
[8] Anisimov, S. I., Kapeliovich, B. L., and Perel'man, T. L., 1974, "Electron Emission From Metal Surface Exposed to Ultrashort Laser Pulses," Sov. Phys. JETP, **39**, pp. 375–377.
[9] Qiu, T. Q., and Tien, C. L., 1993, "Heat Transfer Mechanisms During Short-Pulse Laser Heating of Metals," ASME J. Heat Transfer, **115**, pp. 835–837.
[10] Tzou, D. Y., 1997, *Macro- to Microscale Heat Transfer*, Taylor & Francis, Washington, DC.
[11] Tzou, D. Y., 2006, "Computational Techniques for Microscale Heat Transfer," *Handbook of Numerical Heat Transfer*, 2nd ed., W. J. Minkowycz, E. M. Sparrow, and J. Y. Murthy, eds., Wiley, Hoboken, NJ.
[12] Jiang, L., and Tsai, H. L., 2005, "Improved Two-Temperature Model and Its Application in Ultrashort Laser Heating of Metal Films," J. Heat Transfer, **127**, pp. 1167–1173.
[13] Chen, J. K., Beraun, J. E., and Tzou, D. Y., 2006, "A Semiclassical Two-Temperature Model for Ultrasfast Laser Heating," Int. J. Heat Mass Transfer, **49**, pp. 307–316.
[14] Kuo, L. S., and Qiu, T., 1996, "Microscale Energy Transfer During Picosecond Laser Melting of Metal Films," ASME National Heat Transfer Conference, Vol. 1, pp. 149–157.
[15] Von Der Linde, D., Fabricius, N., Danielzik, B., and Bonkhofer, T., 1987, "Solid Phase Superheating During Picoseond Laser Melting," Mater. Res. Soc. Symp. Proc., **74**, pp. 103–108.
[16] Shi, Y., Zhang, Y., and Konrad, C., 2007, "Solid-Liquid and Liquid-Vapor Phase Change Induced by a Nanosecond Laser in Selective Laser Sintering," Nanoscale Microscale Thermophys. Eng., **11**, pp. 301–318.
[17] Chowdhury, I. H., and Xu, X., 2003, "Heat Transfer in Femtosecond Laser Processing of Metal," Numer. Heat Transfer, Part A, **44**, pp. 219–232.
[18] Voller, V. R., 1997, "An Overview of Numerical Methods for Solving Phase Change Problems," *Advances in Numerical Heat Transfer*, Vol. 1, W. J. Minkowycz and E. M. Sparrow, eds., Taylor & Francis, Basingstoke.
[19] Sasaguchi, K., Ishihara, A., and Zhang, H., 1996, "Numerical Study on Utilization of Melting of Phase Change Material for Cooling of a Heated Surface at a Constant Rate," Numer. Heat Transfer, Part A, **29**, pp. 19–31.
[20] Binet, B., and Lacroix, M., 2000, "Melting From Heat Sources Flush Mounted on a Conducting Vertical Wall," Int. J. Numer. Methods Heat Fluid Flow, **10**, pp. 286–306.
[21] Morgan, K., 1981, "A Numerical Analysis of Freezing and Melting With Convection," Comput. Methods Appl. Mech. Eng., **28**, pp. 275–284.
[22] Hsiao, J. S., 1984, "An Efficient Algorithm for Finite Difference Analysis of Heat Transfer With Melting and Solidification," ASME Paper No. 84-WA/HT-42.
[23] Cao, Y., and Faghri, A., 1990, "A Numerical Analysis of Phase Change Problem Including Natural Convection," ASME J. Heat Transfer, **112**, 812–815.
[24] Swaminathan, C. R., and Voller, V. R., 1993, "On the Enthalpy Method," Int. J. Heat Fluid Flow, **3**, pp. 233–234.
[25] Klemens, P. G., and Williams, R. K., 1986, "Thermal Conductivity of Metals and Alloys," Int. Met. Rev., **31**, pp. 197–215.
[26] Anisimov, S. I., and Rethfeld, B., 1997, "On the Theory of Ultrashort Laser Pulse Interaction With a Metal," Proc. SPIE, **3093**, pp. 192–202.
[27] Wellershoff, S., Hohlfeld, J., Güdde, J., and Matthias, E., 1999, "The Role of Electron-Phonon Coupling in Femtosecond Laser Damage of Metals," Appl. Phys. A: Mater. Sci. Process., **69**, pp. 99–107.
[28] Chen, J. K., and Beraun, J. E., 2001, "Numerical Study of Ultrashort Laser Pulse Interactions With Metal Films," Numer. Heat Transfer, Part A, **40**, pp. 1–20.
[29] Faghri, A., and Zhang, Y., 2006, *Transport Phenomena in Multiphase Systems*, Elsevier, Burlington, MA.
[30] Patankar, S. V., 1980, *Numerical Heat Transfer and Fluid Flow*, McGraw-Hill, New York.
[31] Wang, G. X., and Matthys, E. F., 1992, "Numerical Modeling of Phase Change and Heat Transfer During Rapid Solidification Processes: Use of Control Volume Integral With Element Subdivision," Int. J. Heat Mass Transfer, **35**, pp. 141–153.
[32] Olsson, E. D., and Bergman, T. L., 1990, "Reduction of Numerical Fluctuations in Fixed Grid Solidification Simulations," HTD (Am. Soc. Mech. Eng.), **130**, pp. 130–140.

Patrick E. Hopkins

Pamela M. Norris[1]
e-mail: pamela@virginia.edu

Department of Mechanical and Aerospace Engineering,
University of Virginia,
P.O. Box 400746,
Charlottesville, VA 22904-4746

Robert J. Stevens
Department of Mechanical Engineering,
Rochester Institute of Technology,
76 Lomb Memorial Drive,
Rochester, NY 14623-5604

Thomas E. Beechem

Samuel Graham

GW Woodruff School of Mechanical Engineering,
Georgia Institute of Technology,
771 Ferst Drive NE,
Atlanta, GA 30332

Influence of Interfacial Mixing on Thermal Boundary Conductance Across a Chromium/Silicon Interface

The thermal conductance at solid-solid interfaces is becoming increasingly important in thermal considerations dealing with devices on nanometer length scales. Specifically, interdiffusion or mixing around the interface, which is generally ignored, must be taken into account when the characteristic lengths of the devices are on the order of the thickness of this mixing region. To study the effect of this interfacial mixing on thermal conductance, a series of Cr films is grown on Si substrates subject to various deposition conditions to control the growth around the Cr/Si boundary. The Cr/Si interfaces are characterized with Auger electron spectroscopy. The thermal boundary conductance (h_{BD}) is measured with the transient thermoreflectance technique. Values of h_{BD} are found to vary with both the thickness of the mixing region and the rate of compositional change in the mixing region. The effects of the varying mixing regions in each sample on h_{BD} are discussed, and the results are compared to the diffuse mismatch model (DMM) and the virtual crystal DMM (VCDMM), which takes into account the effects of a two-phase region of finite thickness around the interface on h_{BD}. An excellent agreement is shown between the measured h_{BD} and that predicted by the VCDMM for a change in thickness of the two-phase region around the interface. [DOI: 10.1115/1.2897344]

Keywords: thermal boundary conductance, nanoscale, solid-solid interfaces, material diffusion, Auger electron spectroscopy, elemental characterization, diffuse scattering, pump-probe transient thermoreflectance technique

Introduction

Thermal management has played a critical role in the development of micro- and optoelectronic devices over the past several decades. Much of the theory used in thermal management design has relied on macroscopic principles where feature sizes and times are larger than the mean free path and scattering time of the energy carriers. Only recently, with the advent of smaller devices and structures, have we had to develop models and theories based on microscopic principles. This is particularly the case with the growing interest in nanoscale and superlattice devices. For this reason, there has been a growing interest in the determination of the thermophysical properties, but perhaps more critical to thermal transport in nanoscale and superlattice devices is the thermal boundary conductance (h_{BD}), which is frequently approximated or neglected, leading to significant uncertainties in design and performance. The thermal boundary conductance between materials is becoming increasingly critical to both the design and selection of innovative materials. Indeed, as the nanorevolution continues, our focus turns toward the manipulation of material systems to enhance/restrict thermal transport, but much fundamental work remains before significant advances can be made in the area of interface engineering.

Heat conduction across solid-solid interfaces is a controlling factor for thermal transport in thermoelectrics [1,2], thin-film high temperature superconductors [3,4], vertical cavity surface emitting lasers [5], and optical data storage media [6]. The properties of the interfaces in these devices lead to varying levels of h_{BD}, creating a temperature difference between the two solids. Kapitza was the first to observe a finite temperature drop across an interface between two different materials [7]. This work was at low temperatures where the mean free paths of the primary energy carriers (acoustic phonons) are large. Unlike at low temperatures, at room temperature, the energy carriers' mean free paths are quite small ($\sim 10-100$ nm) and h_{BD} is typically neglected. With the advent of nanoscale devices with dimensions on the order of the mean free paths, h_{BD} has become significant in thermal management at room temperature. This is especially the case for devices with multiple interfaces, such as superlattices [8] and very large scale integrated (VLSI) circuits [8].

Thermal boundary conductance across nanomaterial interfaces has been the focus of several computational and experimental studies. An extensive review of thermal boundary conductance experiments and theory until 1989 is presented by Swartz and Pohl [9]. Since then, much progress has been made in numerical studies of h_{BD} [10]. Several groups have numerically examined the effects that lattice mismatch and the type of phonon scattering—elastic, inelastic, specular, or diffuse—have on h_{BD} [11–22]. The dependence of h_{BD} on lattice mismatch and phonon scattering has also been examined experimentally [23–26]. These analyses have mainly focused on perfect interfaces between nanomaterials (i.e., no interatomic mixing or disorder around the interface). However, in realistic nanodevices, pronounced interdiffusion or reactions can occur on the order of the characteristic length of the device, even at room temperature [27]. This interdiffusion results in the presence of a disordered and two-phase region at the interface of two materials, which contributes to the

---

[1] Corresponding author.

Contributed by the Heat Transfer Division of ASME for publication in the JOURNAL OF HEAT TRANSFER. Manuscript received January 30, 2007; final manuscript received November 21, 2007; published online April 23, 2008. Review conducted by Jayathi Murthy.

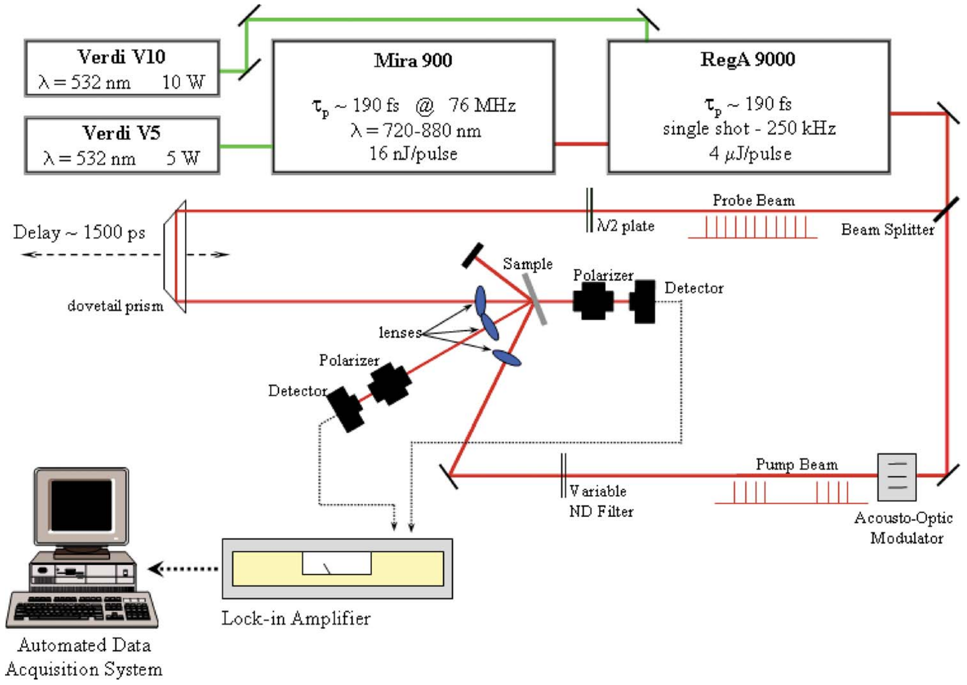

Fig. 1 TTR experimental setup used in this study

overall h_{BD} [9]. The effects of disorder or a two-phase region on h_{BD} has been the focus of many numerical studies [28–32] but, experimentally, has only been qualitatively observed [33]. The lack of experimental observation has led to conflicting theoretical results for h_{BD} as a result of multiphase and diffusion regions. For example, the scattering-mediated acoustic mismatch model (SMAMM) predicts a decrease in h_{BD} [20], while calculations by Kozorezov et al. indicate an increase [34]. However, these results are based on purely theoretical calculations, and, as previously mentioned, there have not been many experimental studies on the effects of interfacial mixing on h_{BD}; clearly, an in-depth experimental examination of interfacial diffusion effects on h_{BD} in thin-film systems would make a large contribution to the current understanding of h_{BD}.

This study examines h_{BD} at the interfaces of Cr films on Si substrates fabricated by various deposition procedures in an attempt to systematically vary the properties of the Cr/Si interface. Chromium is of particular interest since Cr films are often used as adhesion layers for more conductive materials in interconnects [35,36], in metal-dielectric mixtures (cermets) [37], and in high powered laser systems [38]. The thermal boundary conductance in the Cr/Si systems is measured with the transient thermoreflectance (TTR) technique. In the TTR technique, a short-pulsed laser beam is used to heat a thin metal film. The transient reflectance of the thin metal film is then probed with a weaker laser pulse after a known time delay. This technique has been used by several groups to measure h_{BD} at metal-dielectric interfaces [23,24,39]. The change in elemental composition near the interfaces is characterized with Auger electron spectroscopy (AES). Since this study is focused on the elemental change of Cr and Si in the interfacial region, AES is sufficient to resolve the major constituents. The experimental results show an excellent agreement with the virtual crystal diffuse mismatch model (VCDMM) [40,41], a model based on the diffuse mismatch model (DMM) [9] that takes into account the effect of mixing around the interface of two materials on h_{BD}.

Experimental Setup

The TTR data were taken with the pump-probe experimental setup shown in Fig. 1. The primary output of the laser system emanates from a Coherent RegA 9000 amplifier operating at a 250 kHz repetition rate with about 4 μJ/pulse and a 150 fs pulse width at 800 nm. The pulses were split at a 9:1 pump to probe ratio. The pump beam, modulated at 125 kHz, was focused down to a 100 μm radius spot size to achieve a 10 J m^{-2} fluence. The radii of the pump and probe beams were measured with a sweeping knife edge [42]. Although the low repetition rate of the RegA system and the "one shot on–one shot off" modulation rate of the pump beam ensures minimal residual heating between pump pulses, the phase of the signal must still be taken into account. The phase correction was performed by the procedures for signal phase adjustment outlined by Stevens et al. [42].

For long scans, the alignment of the pump and probe spots may become an issue [24,43]. To avoid misalignment problems, the probe beam was collimated before the probe delay stage and was profiled with a sweeping knife edge at all time delays. In this study, a pump to probe radius ratio of 10:1 was used, and the probe was aligned with the delay stage, resulting in less than 1.5 μm and 4.0 μm drift along the horizontal and vertical axes perpendicular to the surface, respectively. These spot characteristics result in less than 1% error due to misalignment of the beams [42].

The TTR technique produces some excitation of the metal film followed by a cooling of the film due to the film's thermal connection to the substrate. To simplify data reduction, the temperature response is ideally influenced only by conductance across the interface and not by diffusion within the metal film. If the film is too thick or has a low thermal conductivity, however, there will be two free parameters (film thermal conductivity k_f and h_{BD}) when fitting experimental data to a thermal model. To avoid this situation, the Biot number Bi for the interface should be significantly less than 1 (typically less than 0.1), so that the film can be treated as a lumped thermal capacitance [44]. Therefore, the film thickness should be restricted to

$$\mathrm{Bi} = \frac{h_{\mathrm{BD}} d}{k_f} < 0.1 \Rightarrow d < \frac{0.1 k_f}{h_{\mathrm{BD}}} \tag{1}$$

where d is the film thickness. For Cr/Si interfaces, $h_{\mathrm{BD}} \sim 2.0 \times 10^8$ W m^{-2} K^{-1} and $k_f = 94$ W m^{-1} K^{-1} [24,45]. Therefore, the film thickness should be no more than 50 nm. This is a reasonable thickness from the microscopic prospective since it is approximately three times larger than the mean free path, therefore reducing the probability of ballistic electron scattering at the interface [46,47].

For the case when the metal film is treated as a lumped capacitance, the thermal model for the film and substrate system is

$$\rho d C_f \frac{dT_f(t)}{dt} = h_{\mathrm{BD}}[T_s(0,t) - T_f(t)] \tag{2}$$

$$\frac{\partial T_s(x,t)}{\partial t} = \alpha_s \frac{\partial^2 T_s(x,t)}{\partial x^2} \tag{3}$$

where T_f is the temperature of the film that is measured using the TTR technique, T_s is the substrate temperature and is a function of time and space, and ρ, C_f, and α_s are the film density, film specific heat, and substrate diffusivity, respectively. Radiative and convective losses at the front of the film surface are negligible compared to typical interface conductances of 10^6–10^8 W m^{-2} K^{-1} and are therefore neglected. The temperature in Eqs. (2) and (3) can be nondimensionalized by

$$\varphi_{f,s} = \frac{T_{f,s} - T_0}{T_f(0) - T_0} \tag{4}$$

where T_0 is the ambient temperature and $T_f(0)$ is the temperature of the film immediately after excitation. Therefore, the thermal model can be expressed as

$$\frac{d\varphi_f(t)}{dt} = \frac{h_{\mathrm{BD}}}{\rho d C_f}[\varphi_s(0,t) - \varphi_f(t)] \tag{5}$$

$$\frac{\partial \varphi_s(x,t)}{\partial t} = \alpha_s \frac{\partial^2 \varphi_s(x,t)}{\partial x^2} \tag{6}$$

subject to the following initial conditions:

$$\varphi_f(0) = 1 \tag{7}$$

$$\varphi_s(x,0) = 0 \tag{8}$$

and the following boundary conditions:

$$-k_s \frac{\partial \varphi_s(0,t)}{\partial x} = h_{\mathrm{BD}}[\varphi_f(t) - \varphi_s(0,t)] \tag{9}$$

$$\frac{\partial \varphi_s(\infty,t)}{\partial x} = 0 \tag{10}$$

The semi-infinite assumption made in Eq. (10) is reasonable for the time scale of interest, ~1–5 ns. The thermal penetration depth for most substrates at this time scale is $(\alpha_s t)^{1/2} < 1$ μm, which is significantly less than the thickness of the Si substrate used in this study.

Table 1 Thermophysical parameters used in the study [56]

Lattice heat capacity of Cr film, C_f	3.3×10^6 J m^{-3} K^{-1}
Lattice heat capacity of Si substrate, C_s	1.65×10^6 J m^{-3} K^{-1}
Thermal conductivity of Si substrate, k_s	148 W m^{-1} K^{-1}
Ambient temperature, T_0	300 K

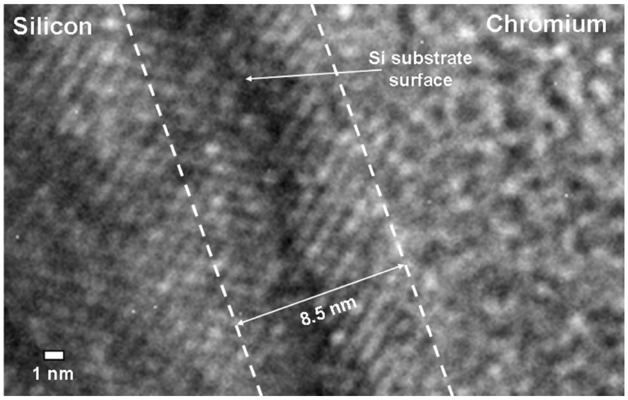

Fig. 2 TEM image of the Cr/Si interface. The observable mixing from the TEM analysis is based on the Si crystallographic planes, yielding a 8.5 nm mixing layer. However, the actual Cr/Si elemental mixing may not be completely crystalline; therefore, AES is used for interfacial chemical analysis.

Equations (5) and (6) subject to Eqs. (7)–(10) were numerically solved using the Crank–Nicolson method, which has only a second order truncation error in both time and space. The thermal boundary conductance was determined by fitting the TTR data to the model using the material constants listed in Table 1. The specifics of the fitting procedure are discussed in a later section.

Sample Preparation and Interface Characterization

The purpose of changing the conditions during deposition was to try to control the amount of interdiffusion between the Cr and Si. When in contact with Si at room temperature, Cr has been shown to form an intermixed region ~10 ML thick [48]. However, when in contact with thick oxide layers (such as SiO_2, an oxide layer that naturally forms on Si), Cr will develop a strong adhesive bond to the oxide, creating a diffusion barrier for further reaction between the Cr and SiO_2 [36]. In addition, Cr is known to form silicides on oxide-free surfaces at elevated temperatures ($CrSi_2$ at 720 K) [49]. An example of Cr/Si mixing is shown in the transmission electron micrograph in Fig. 2, which is focused on the interface between the Cr film and the Si substrate of sample Cr-4 (see Tables 1 and 2). The surface of the Si substrate exhibits some degree of roughness, which is apparent by the dark region labeled “Si substrate surface” in Fig. 2. Note that the thickness of interatomic mixing determined from the transmission electron microscopy (TEM) analysis was quantified by examining the interference lines from the Si[110] crystallographic planes. Therefore, the mixing region, which is determined from the TEM as 8.5 nm

Table 2 Fabrication details of Cr/Si samples

Sample ID	Backsputter etch (min)	Heat treatment prior to deposition	Deposition notes
Cr-1	None	None	50 cm Cr at 300 K
Cr-2	5	None	50 nm Cr at 300 K
Cr-3	5	20 min at 873 K	50 nm Cr at 300 K
Cr-4	5	50 min at 873 K	50 nm Cr at 300 K
Cr-5	5	20 min at 873 K	50 nm Cr at 573 K
Cr-6	5	None	10 nm Cr at 300 K; Heat treatment to 770 K; deposition of 40 nm Cr at 300 K

thick, only represents the Cr/Si mixing when the Si diamond structure is still present. There is still some atomic mixing between the Cr/Si that results in a noncrystalline structure; therefore, the chemical mixing between Cr and Si could be slightly larger than the structural quantification from the TEM image. This elucidates the importance of a chemical analysis for an accurate determination of Cr/Si elemental mixing.

The Cr films were grown on Si ⟨100⟩ substrates in a multisource, high vacuum thin-film sputter deposition system, a Supersystem III manufactured by the Kurt J. Lesker company capable of pumping down to 10^{-7} Torr. This specific system is equipped with a chamber heater capable of reaching temperatures greater than 900 K and a vibrating quartz crystal to monitor deposition rate. The Cr deposition rate is about 17 nm/min with 37 SCCM Ar flow rate and 300 W power to the target gun. All substrates were spin cleaned with reagent alcohol (90.7% ethyl alcohol, 4.8% isopropyl alcohol, 4.5% methyl alcohol, and 0.12% water), trichloroethylene, and methanol, and were then subsequently baked for 5 min at 400 K to remove any residual water that may have formed at the substrate surface as a result of spin cleaning. Once in the chamber, various in situ deposition procedures were performed including backsputter etching followed by chamber heating up to 873 K before deposition. While fabricating some samples, the chamber temperature was elevated during or after Cr deposition. During any type of chamber heating, a ramp rate of 20 K/min was maintained until the target temperature was reached. Therefore, if a certain deposition requires the chamber to maintain 873 K for 20 min, the chamber is actually at an elevated temperature for a much longer time due to the slow temperature rise to reach the target temperature and the slow radiative cooling processes of the vacuum chamber back to room temperature. The procedures used during fabrication for each of the 50 nm Cr/Si samples are summarized in Table 2. A total of 50 nm of Cr was deposited during any given deposition and was verified with the in situ vibrating quartz crystal. Films of this thickness ensure that h_{BD} across the Cr/Si interface can be accurately resolved, given the 1.5 ns maximum delay of the probe path in the TTR experimental setup [24].

A number of differently composed interface regions were expected, as the Cr/Si fabrication parameters were systematically modified. The interfaces were characterized by AES, used in conjunction with an argon ion beam to provide quantitative compositional information as a function of depth into the material. Data were taken on a commercial X-ray photoemission spectroscopy (XPS)/scanning Auger system (Physical Electronics 560), equipped with a double-pass, cylindrical mirror electron energy analyzer (CMA). To minimize the adsorption of contaminants on the sample surface, the chamber is maintained at ultrahigh vacuum (at a base pressure of 10^{-9} Torr) with a 200 Hz ion pump, assisted by a small sublimation pump. These pumps allow the vacuum chamber to remain virtually free of hydrocarbon contamination. The electron gun is mounted coaxially inside the electron energy analyzer for efficient data collection and to reduce shadowing effects. A 3 keV electron beam was used for AES analysis, and depth profiling was conducted by atomically sputtering away the material using a 240 nA Ar ion beam current and a 2×2 mm^2 raster, which resulted in a Cr sputtering yield of 4.12 nm/min. A typical AES depth profile of the Cr/Si samples is shown in Fig. 3. It should be noted that the vacuum in the sputtering chamber during Cr deposition was low (10^{-6} Torr), so the relatively low levels of O_2 and C contamination found in the films is expected. Also, note that the O_2 and C percentages in the Cr film depth are slightly higher than the actual composition since contaminants from the film surface are pushed into the depth of the film as a result of the Ar ion bombardment for the depth profile. The beginning and end of the Cr/Si mixing region is defined as the depth at which Si reaches 10% of the total film composition and Cr reaches 10% of the film composition, respectively. This threshold was chosen since C levels were slightly less than 10% of the total film composition near the interface.

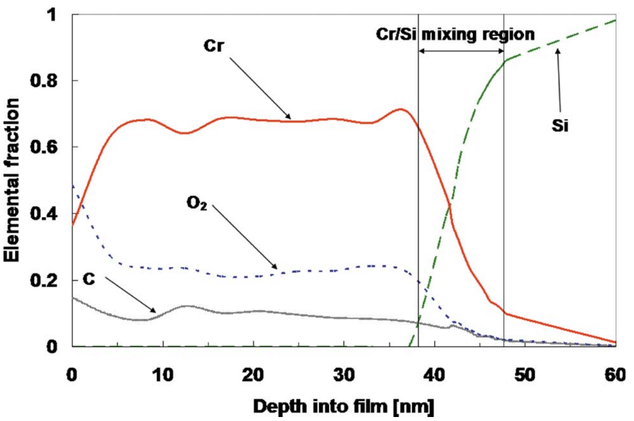

Fig. 3 Example of a full AES spectrum of one of the Cr/Si films examined, Cr-1. Note the relatively high concentrations of O_2 and C at the sample surface, about 100% more than those in the film. These elements were sputtered away from the surface with the ion gun during the depth profiling procedure. The mixing layer is depicted by the vertical lines at the 10% mark of the Si and Cr.

The AES spectra around the mixing region for all six samples are shown in the Appendix. The ID's of each sample corresponding to the ID's in Table 2 are shown in the upper left of each plot. The line types in the Appendix represent different elements and correspond to the same designation as in Fig. 3. Due to the controlled deposition conditions, varying mixing layer thicknesses and spatial gradients are expected at the sample interfaces. Since Cr is expected to form a diffusion barrier when in contact with an oxide layer, the O_2 levels at the beginning of the mixing layer must also be considered to explain the different compositional changes among the samples. The O_2 levels at the beginning of the defined mixing layer range from 12% to 21%. Examining only the samples that were deposited at room temperature (Cr-1–Cr-4), Cr-1 has about 19% O_2 at the beginning of the mixing layer while the other room temperature samples have about 14%. The backsputter etch procedure performed on Cr-2–Cr-4 is most likely responsible for this since bombarding the substrate with Ar atoms prior to deposition is a common method to remove the native oxide layer.

Substrate etching can physically roughen the substrate, which could lead to Cr atoms being deposited into craters beneath the substrate surface introduced by the backsputter process. This is evident from the differing mixing layer thicknesses among the samples deposited at room temperature. In an attempt to smooth the substrate surface after backsputtering, the chamber temperature was increased to 873 K prior to Cr deposition. When only backsputtered (Cr-2), the mixing layer depth is almost 15 nm compared to a 9.5 nm two-phase region seen in Cr-1, which was not backsputtered prior to deposition (however, since only ETM spin cleaning was performed on Cr-1, it is assumed that the surface was relatively smooth from factory polishing and the oxide layer). The annealing for different times (20 min and 50 min for Cr-3 and Cr-4, respectively) results in a smaller mixing layer depth with increased annealing times. Notice that annealing for 50 min (Cr-4) results in a two-phase region of 10 nm, almost the same thickness as Cr-1 (9.5 nm) in which there was no in situ substrate preparation.

The thermal model used in this study is extremely sensitive to film thickness [24]. Although 50 nm of Cr was deposited during fabrication due to the varying levels of Cr/Si mixing, the portion of the film that can be modeled with the Cr heat capacity is actually less than 50 nm. To accurately model this system, the thick-

Table 3 Summary of results from the AES and TTR data

Sample ID	Cr film thickness (nm)	Mixing layer (nm)	O_2 (%)	Slope of Si in mixing layer (%/nm)	Av. h_{BD} ($GW\,m^{-2}\,K^{-1}$)
Cr-1	38	9.5	19	9.7	0.178
Cr-2	37	14.8	14	16.4	0.113
Cr-3	35	11.5	14.2	16.6	0.139
Cr-4	35	10.1	14.6	7.4	0.15
Cr-5	39	5.8	21.5	24.1	0.134
Cr-6	45	7	12.3	28.1	0.124

ness used in Eq. (5) was determined from the AES scans, and the thickness of the film in this study is defined as the distance from the film surface to the beginning of the mixing layer. The thicknesses used for each film are listed in Table 3.

To quantify the spatial change of the elements in the mixing layer, the Si data points in the first ~3 nm after the beginning of the mixing layer were fitted with a linear trend. The slope of this line represents the rate of change of the Si concentration during the first few nanometers of Cr/Si mixing. Since the elemental concentrations of Cr, C, and O_2 all decrease as Si increases, monitoring the change in Si with distance into the mixing layer gives a good indication of the spatial gradient in the mixing region. As previously mentioned, a total of 50 nm of Cr was deposited during the fabrication of each sample. The defined mixing layers all terminate at or before 50 nm in the AES profiles, indicating that Si diffusion into the deposited Cr is the primary diffusion element causing the two-phase mixing layer. Again, examining the room temperature depositions, Cr-1 and Cr-4 have similar Si gradients and Cr-2 and Cr-3 have similar gradients. This is probably a result of different interdiffusion rates of the Cr and Si during deposition, resulting from O_2 layers or various degrees of roughness on the substrate surface. The higher O_2 levels on the surface of Cr-1 limited interdiffusion, resulting in a slower diffusion of the Si into the Cr. This is consistent with past studies indicating that Cr and O_2 form a diffusion barrier [36]. However, we see the same type of gradient in Cr-4, indicating that the Si diffusion could be dictated by the smoothness of the surface. Substrate roughening is assumed in Cr-2 from the backsputter procedure, and perhaps a similar degree of roughness is present in Cr-3 since the attempt to anneal the substrate only lasted for 20 min, as opposed to Cr-4, which maintained a high chamber temperature for 50 min. A summary of the mixing layer depth, O_2 concentration at the beginning of the interfacial mixing layer, and slopes of the Si in the AES profiles is given in Table 3.

Samples Cr-5 and Cr-6 were subjected to higher deposition temperatures. 50 nm of Cr was deposited on a backsputtered and annealed substrate at 573 K in Cr-5. Notice that the Si diffusion is much smoother throughout the mixing layer, and the defined mixing layer is much thinner than the room temperature samples. The higher temperature and smooth surface probably resulted in much faster Si diffusion, which would lead to the thinner mixing layer. This also explains the profile for Cr-6, which exhibits the same thin mixing layer. This sample was only backsputtered before 10 nm of Cr was deposited; then, the chamber was heated above the $CrSi_2$ formation temperature. This explains the mixing layer ending slightly after 50 nm from the Cr film surface (similar to Cr-2). However, the chamber was heated and maintained above the $CrSi_2$ formation temperature for 5 min. So, theoretically, this could have resulted in silicide formation that would not have been detected in the AES depth profile presented in the Appendix. This sample (Cr-6) was additionally characterized with XPS [50], and no evidence of Cr silicide formation was detected.

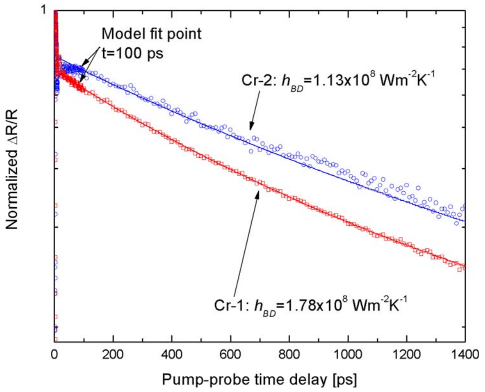

Fig. 4 TTR data of Cr-1 and Cr-2 fits with the model described with Eqs. (5)–(10). A 40% decrease in the best fit h_{BD} from Cr-1 to Cr-2 is observed, with the only change in the experiment occurring in the deposition conditions (see Table 1).

Thermal Boundary Conductance at Various Cr/Si Interfaces

Several TTR scans were taken on each sample, and the average of the resulting h_{BD} for these scans is reported in Table 3. A consistent deviation of less than 7% from the mean was calculated for all the data on each sample. The thermal boundary conductance of each was determined by scaling the model (Eqs. (5)–(10)) to the TTR data at 100 ps and fitting the model to the data [24]. This method assumes that the reflectance varies linearly with temperature [24,39,51]. At 100 ps, the temperature gradient in the metal film is negligible, and the electrons and lattice are in thermal equilibrium. The thermal boundary conductance was treated as a free parameter and was adjusted to minimize the sum of squares between the thermal model and the TTR data. Minimization was performed using an inverse parabolic interpolation technique, which normally required less then ten iterations to converge.

To ensure that the TTR data taken with the $10\ J\,m^{-2}$ pump can be linearly related to electron temperature, h_{BD} of Cr-3 was measured at a variety of pump fluences ranging from $0.5\ J\,m^{-2}$ to $10\ J\,m^{-2}$. The average h_{BD} measured with varying pump fluence was $0.139\ GW\,m^{-2}\,K^{-1}$, which is the same h_{BD} determined from the various measurements on Cr-3 with $10\ J\,m^{-2}$. The deviation among the measurements was less than 4% from the mean, which is less than the ~7% deviation among the samples from repeated measurements at one fluence, as previously mentioned. This indicates that for the fluence used in this study ($10\ J\,m^{-2}$), the assumption that the reflectance varies linearly with temperature is valid.

Figure 4 shows the normalized TTR data taken on Cr-1 and Cr-2 and the best fit of the thermal model to the data using the thermophysical constants listed in Table 1 and h_{BD} as the fitting parameter. A best fit h_{BD} of $0.178\ GW\,m^{-2}\,K^{-1}$ was found for Cr-1, where Cr-2 showed a 40% reduction in h_{BD} with $0.113\ GW\,m^{-2}\,K^{-1}$. Examining the corresponding AES profiles of Cr-1 and Cr-2 (Appendix), it is apparent that the thickness of the mixing layer and spatial change of the Si content in the mixing layer can both contribute to varying levels of h_{BD}.

The thermal boundary conductance measured in Cr-1 is consistent with the $0.2\ GW\,m^{-2}\,K^{-1}$ h_{BD} measurement of a 30 nm Cr film deposited on a lightly backsputtered Si substrate by Stevens et al. [24]. However, Cr-1 was not subject to backsputtering, where Cr-2 was deposited after backsputtering at relatively high powers for a long time. This is evidence of the extreme sensitivity

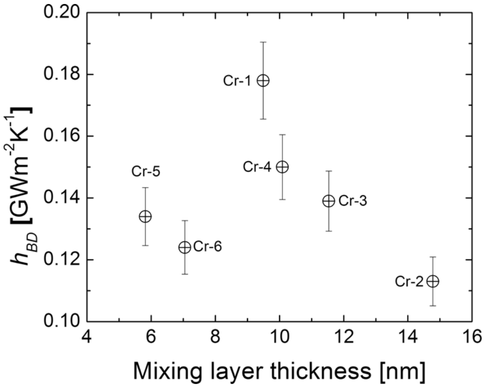

Fig. 5 Average of the measured h_{BD} of each sample as a function of mixing layer thickness. The room temperature samples display a linear decrease in h_{BD} with increasing mixing layer thickness. The samples deposited at higher temperatures (Cr-5 and Cr-6) do not follow this trend, which could be due to defects of a change in the microstructure relative to the room temperature deposited samples. The error bars represent the 7% deviation from the mean calculated from the data from each sample, which are the calculated errors associated with the repeatability of the data from the experiment.

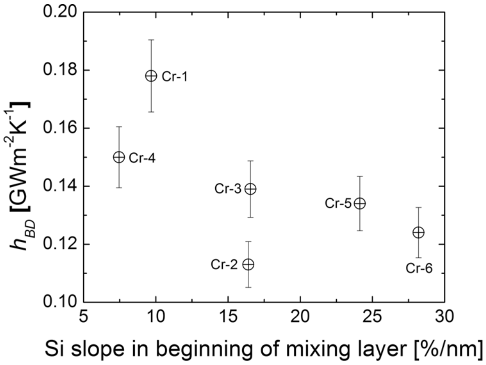

Fig. 6 Average of the measured h_{BD} of each sample as a function of rate of Si increase at the beginning of the interfacial layer. An increase in h_{BD} is observed as the Si spatial change in the film becomes more gradual. The error bars represent the 7% deviation from the mean calculated from the data from each sample, which are the calculated errors associated with the repeatability of the data from the experiment.

of h_{BD} to interfacial conditions and is indicative of the variability in the fabrication processes.

The sensitivity of the model to film thickness also needs to be considered. Since the model assumes a lumped capacitance, a change in film thickness would change the thermal mass of the system, affecting the predicted change in temperature. For example, assuming that the Cr film thicknesses were actually 50 nm, the amount of Cr deposited onto the Si substrates during deposition, the values of h_{BD} determined from the fitting routine could increase as much as 50%. However, this increase would be common on all samples maintaining the same trends reported in this study. As previously mentioned, the Cr film thicknesses were determined from the AES profiles and are listed in Table 3. This thickness sensitivity also gives more evidence of the effect of fabrication variability and interfacial conditions on the measured thermal boundary conductance since h_{BD} measured by Stevens et al. was slightly higher for a thinner film.

Figure 5 shows the measured h_{BD} of the six Cr samples as a function of mixing layer thickness. The thermal boundary conductance in the room temperature samples (Cr-1–Cr-4) decreased with increasing mixing layer thickness. In these samples, the h_{BD} ranged from 0.178 GW m^{-2} K^{-1} in the sample with a 9.5 nm mixing thickness to 0.113 GW m^{-2} K^{-1} in the sample with 14.8 nm of mixing. In these room temperature samples, the smallest amount of mixing occurred in Cr-1, which was not subject to any in situ substrate cleaning. The other room temperature samples, Cr-2–Cr-4, were subject to backsputter etching, which reduced the oxygen on the Si surface from ~19% to ~14% (see Table 3) and also roughened the substrate prior to Cr deposition. The largest mixing layer thickness and lowest h_{BD} were measured in Cr-2, which could be a result of the Si substrate being rougher than the other room temperature samples. When the substrate was heated after etching, presumably smoothing the surface and reducing surface defects before room temperature Cr deposition (Cr-3 and Cr-4), the mixing layer thickness decreased, resulting in a linear increase in h_{BD}. The measured h_{BD} in Cr-1 deviated from the linear trend in Cr-2–Cr-4, which could be partly due to the increased O_2 concentration.

The samples that were subject to non-room-temperature depositions, Cr-5 and Cr-6, did not demonstrate the same relationship between h_{BD} and mixing layer. Both samples had much smaller mixing layer thicknesses. The elevated temperatures imposed on the Cr during deposition could have introduced impurities or changed the material structure around the interface or in the film that was not detectable by AES, therefore introducing another variable between the high temperature deposited samples and the room temperature deposited samples.

Figure 6 shows the relationship between measured h_{BD} and the interface "abruptness" (the slope of the Si content changes with depth, as previously described). Note that the slope of the spatial increase of Si is quantified by only considering the first 3 nm in the mixing layer defined in the AES data. In addition, a very abrupt interface does not necessarily relate to a small mixing layer thickness. The apparent trend is a decrease in h_{BD} with an increasingly abrupt interface. The highest h_{BD} values in the room temperature samples (Cr-1–Cr-4) are measured on the samples in which the Cr was deposited on a smooth Si surface, which created a more gradual increase in Si content near the interface compared to the samples in which Cr was deposited at elevated temperatures (Cr-5 and Cr-6). Chromium and Si represent acoustically matched materials with nearly identical Debye temperatures ($\Theta_{D\_\mathrm{Cr}}=630$ K and $\Theta_{D\_\mathrm{Si}}=640$ K) and, therefore, have similar Debye cutoff frequencies [45]. By calculating the phonon radiation limit (PRL) of the Cr/Si system, an upper limit of the h_{BD} is established as 1.38 GW m^{-2} K^{-1} [23,52]. Any contribution to thermal boundary conductance by phonons resulting in a value above this limit would indicate occurring inelastic phonon scattering processes [25,26]. The calculated PRL is higher than the measured h_{BD}; so, elastic scattering is assumed in this analysis.

The DMM, which assumes elastic phonon scattering [9], can therefore be applied to the system. In its simplest form, the DMM can be calculated with

$$h_{\mathrm{BD}} = h_{1\rightarrow 2} = \frac{1}{4}\sum_{j} \nu_{1,j}\int_{0}^{\omega_{\max}} \tau_{1\rightarrow 2}\hbar\omega\frac{\partial N_{1,j}}{\partial T}d\omega \tag{11}$$

where $\nu_{1,j}$ is the speed of phonon mode j (longitudinal or transverse) in side 1 (acoustically softer material—here, the Cr film), $\tau_{1\rightarrow 2}$ is the probability of phonon transmission from side 1 into side 2, and $N_{1,j}$ is the product of the phonon occupation function and density of states of mode j on side 1. Assuming that the diffuse scattering from the rough boundary equilibrates the phonon system, the Bose-Einstein distribution function can be implemented and h_{BD} of 0.855 GW m^{-2} K^{-1} is calculated using a Debye approximation. The DMM, like the PRL, also overpredicts the measured h_{BD}. This has often been associated with poor interface quality and substrate damage [9,23,24,33]. As shown in this study, this could result in varying degrees of mixing, which is most likely the direct cause for differences between the measured h_{BD} and that calculated from the DMM. The DMM does not take into account an interfacial mixing layer. Although the SMAMM has been proposed to partially account for this [20], it is not applied in this study since it assumes specular phonon reflection, which is clearly not a valid assumption in this case since the interfacial region is shown to be significantly disordered [4].

At an ideal interface with no mixing, a phonon from the Cr film scatters at the Cr/Si interface and is either transmitted into the Si or reflected back into the Cr. Assuming diffuse scattering and using equations in the references based on the phonon speeds of the different modes (longitudinal and transverse), the phonon transmission probability can be calculated [9]. For a Cr/Si interface, the phonon transmission probability is $\alpha_{\mathrm{Cr-Si}}=37\%$ under the Debye solid model, meaning that at the ideal interface, 37% of the phonons are transmitted from the Cr side to the Si side (or from Si to Cr since the phonon loses its "memory" when it is scattered). This transmission can be assumed constant over the energy spectrum if we assume that Cr and Si are isotropic Debye solids, an assumption that is made in the derivation of the form of the DMM and PRL that is used in this study [9]. This scattering can also be explained as 37% of the incident phonon energy is transmitted into the substrate.

In the event of interfacial mixing, the phonons must propagate across a finite amount of space to conduct energy into the substrate. When these phonons scatter with Si at the beginning of the mixing layer, a certain percentage is transmitted deeper into the mixing layer. As the thickness of interfacial mixing layer increases, the probability that a phonon will scatter more than once increases, thereby decreasing h_{BD}, which is expected with increased diffuse scattering in well matched materials [9]. Reduced transmission can also occur from defects or a change in the microstructure around the interface, which could explain the further reduction of h_{BD} observed in Cr-5 and Cr-6, assuming that the elevated temperature during deposition changed the microstructure of the two-phase region compared to the room temperature deposited samples.

Table 4 Comparison of VCDMM to DMM and experimental data on samples deposited at room temperature

Sample ID	Measured h_{BD} (GW/m^2 K)	VCDMM (GW/m^2 K)	DMM (GW/m^2 K)
Cr-1	0.178	0.147	0.855
Cr-2	0.113	0.118	0.855
Cr-3	0.139	0.146	0.855
Cr-4	0.15	0.131	0.855

VCDMM to Predict h_{BD} as a Function of Mixing Region Thickness

The functionality of h_{BD} with mixing region thickness and composition can be predicted with the VCDMM [40,41]. This model introduces a simple correction to the DMM through the use of a virtual crystal to account for the manner by which energy propagates through the interfacial region. In this manner, multiple scattering events occurring at the interface can be quantified, allowing for a more accurate prediction of h_{BD} as well as insight into the effect of interfacial quality on an overall heat transfer.

In calculations of the traditional DMM (Eq. (11)), the estimation of a perfect interface is assumed; however, as shown in the previous sections, interfacial thickness indeed affects h_{BD}. To account for this thickness, the VCDMM replaces the interfacial region with a third material, the virtual crystal, which has properties that are a blend of the bulk materials [53] and a thickness equal to the length of disorder. Incorporating the virtual crystal modifies the DMM by necessitating the need to account for both the interaction between each of the bulk materials and interface as well as the now finite thickness of the interface.

The interaction between the two materials and the disordered region is investigated by estimating the h_{BD} between each of the bulk materials and the virtual crystal. This is accomplished using Eq. (11) for each of the now two interfaces with a modification of the transmission coefficient α to account for the virtual crystal. This modification is shown below where the subscript i designates the bulk material of interest, and VC the virtual crystal,

$$\tau_{i\rightarrow \mathrm{VC}}=\frac{\sum_{j}\nu_{\mathrm{VC},j}^{-2}}{\sum_{j}(\nu_{i,j}^{-2}+\nu_{\mathrm{VC},j}^{-2})} \tag{12}$$

Again, this calculation treats all solids as Debye solids. To calculate the phonon propagation speed in the virtual crystal, a rule of mixture estimation is used where b_1 is the percentage by mass of material 1 in the disordered region,

$$\nu_{\mathrm{VC},j}=b_1\nu_{1,j}+(1-b_1)\nu_{2,j} \tag{13}$$

To accurately calculate the percentage b_1 for the Cr/Si interfaces presented here, the depth profiles of Cr-1–Cr-4 were analyzed. These interfaces were chosen for this analysis because the temperature of these samples during Cr deposition was consistent. Therefore, any interfacial structural changes occurring from heat treatments to the Cr/Si system post-Cr deposition do not have to be taken into account, and only the effects of the mixing layer on h_{BD} can be examined. By fitting a functional form using shape preserving interpolants through the silicon profile, a mean value of the elemental percentage was obtained. This value was then used to calculate the virtual crystal properties and hence the h_{BD} for the two interface system according to

$$h_{\mathrm{BD}}=\left[\left\{\sum_{j}h_{1\rightarrow \mathrm{VC},j}\right\}^{-1}+\left\{\sum_{j}h_{2\rightarrow \mathrm{VC},j}\right\}^{-1}\right]^{-1} \tag{14}$$

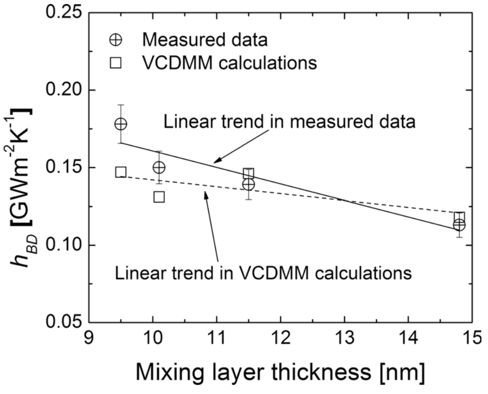

Fig. 7 Comparison of the VCDMM to the experimental data on samples Cr-1–Cr-4. Added electron-phonon coupling resistance is taken into account in these calculations since Cr and Si are acoustically matched solids. Where as the DMM predicts h_{BD} that is almost eight times larger than that measured on the samples with no dependence on mixing layer thickness or compositions, the VCDMM calculations are within 18% of the measured values and show similar trends with mixing layer thickness when taking into account the change in Si composition in the mixing region.

The above relation accounts for only the efficiency by which

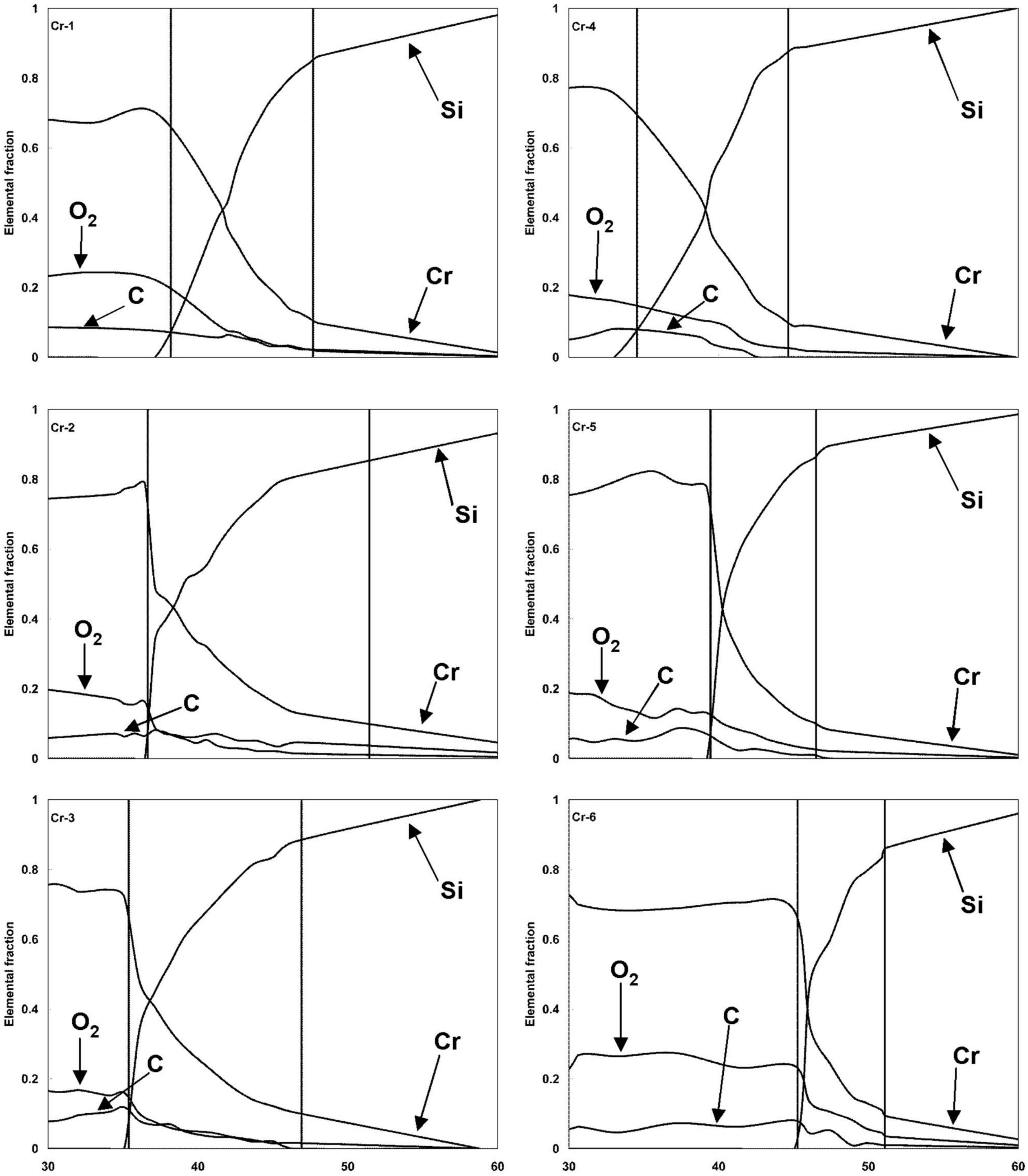

Fig. 8 Auger electron spectroscopy depth profiles

energy transfers from the bulk to the interface but does not analyze the ease by which energy propagates through the interfacial region. To examine this effect, the results of Eq. (14) are scaled according to the depth factor δ, which is a ratio of the interfacial thickness D to the mean free path of the virtual crystal Λ_{VC}. Using kinetic theory to estimate the mean free path along with the measured thickness of the Cr/Si interface, the depth factor was calculated, allowing for the estimation of the h_{BD} from the VCDMM approach, as shown in

$$h_{\mathrm{BD}} = \left[\left\{ \frac{\sum_j h_{1\to \mathrm{VC},j}}{\delta_j} \right\}^{-1} + \left\{ \frac{\sum_j h_{2\to \mathrm{VC},j}}{\delta_j} \right\}^{-1} \right]^{-1} \quad (15)$$

Finally, to completely model the system, the electron-phonon coupling was incorporated by using the value reported by Hostetler et al. [54] for chromium and the methodology of Majumdar and Reddy [55] in order to obtain the final prediction for h_{BD}.

Table 4 and Fig. 7 show a comparison of the virtual crystal model to the experimental data. The virtual crystal approach is within 18% of the measured values, whereas the predicted h_{BD} of the DMM is about eight times these values. In both prediction and measurement, there is a distinct trend of decreasing thermal boundary conductance with increasing interfacial thickness. This results from the additional scattering, which occurs as the phonons must propagate through the disordered region. The additional scattering, reduces the rate at which energy flows, thus decreasing the overall conductance and illuminating the role of interfacial quality on performance.

Conclusions

The thermal boundary conductance at the Cr/Si interface was studied for a variety of interfacial conditions. The deposition conditions for the 50 nm Cr films were systematically varied to change various aspects of the Cr/Si mixing, and h_{BD} was measured with the TTR technique. The range of h_{BD} values across the six Cr/Si interfaces show that slight changes in interfacial properties can significantly affect thermal boundary conductance. By different in situ substrate preparation techniques, h_{BD} was reduced by as much as 40%. Results showed a dependence of h_{BD} on both mixing layer thickness and the abruptness of Si change at the interface. The trend in h_{BD} values follows with diffuse scattering assumptions, and it is apparent that in well matched systems such as Cr/Si, phonons that scatter more than once can decrease h_{BD}, which is not taken into account in traditional models such as the DMM. A recently developed model, the VCDMM, was applied to the room temperature deposited data, and a close agreement in both value and trend with mixing layer thickness was observed, offering new insight into the dependence of thermal boundary conductance on disorder around solid interfaces.

Acknowledgment

This work would not have been possible without financial support from NSF Grant No. CTS-0536744 (P.M.N.) and the NSF CAREER program through Grant No. CTS-0448795 (S.G.). The authors greatly appreciate additional funding through the NSF Graduate Research Fellowship Program (P.E.H.). The authors thank Mike Klopf of Jefferson Lab and Richard Salaway, Jenni Simmons, and Jes Sheehan of the University of Virginia for their helpful insight, discussions, and critical reading of this manuscript, and Cathy Dukes for assistance with AES and XPS measurements.

Nomenclature

b = percentage by mass
Bi = Biot number
C = heat capacity, J m^{-3} K^{-1}
d = film thickness, m
h_{BD} = thermal boundary conductance, W m^{-2} K^{-1}
k = thermal conductivity, W m^{-1} K^{-1}
N = total number of phonons per frequency per volume at temperature T, m^{-3}(s^{-1})$^{-1}$
T = temperature, K
v = phonon velocity, m s^{-1}

Greek Symbols

α = thermal diffusivity, m^2 s^{-1}
δ = depth factor in virtual crystal
φ = nondimensionalized temperature
Θ_D = Debye temperature, K
ρ = mass density, kg m^{-3}
τ = probability of phonon transmission across the interface

Subscripts

f = film
$i\rightarrow 2$ = from side i to the virtual crystal
j = phonon mode (longitudinal or transverse)
s = substrate
VC = virtual crystal
0 = initial
1 = material on side 1
2 = material on side 2
$1\rightarrow 2$ = from side 1 to side 2

Appendix

The Auger electron spectroscopy depth profiles of the six Cr/Si samples are shown in Fig. 8. Note the variation among samples of the mixing layer thickness, Si rate of change at the beginning of the mixing layer, and O_2 concentrations, which are summarized in Table 3.

References

[1] Da Silva, L. W., and Kaviany, M., 2004, “Micro-Thermoelectric Cooler: Interfacial Effects on Thermal and Electrical Transport,” Int. J. Heat Mass Transfer, **47**, pp. 2417–2435.
[2] Mahan, G. D., and Woods, L. M., 1998, “Multilayer Thermionic Refrigeration,” Phys. Rev. Lett., **80**, pp. 4016–4019.
[3] Phelan, P. E., Song, Y., Nakabeppu, O., Ito, K., Hijikata, K., Ohmori, T., and Torikoshi, K., 1994, “Film/Substrate Thermal Boundary Resistance for an Er-Ba-Cu-O High-Tc Thin Film,” ASME J. Heat Transfer, **116**, pp. 1038–1041.
[4] Phelan, P. E., 1998, “Application of Diffuse Mismatch Theory to the Prediction of Thermal Boundary Resistance in Thin-Film High-Tc Superconductors,” ASME J. Heat Transfer, **120**, pp. 37–43.
[5] Chen, G., Tien, C. L., Wu, X., and Smith, J. S., 1994, “Thermal Diffusivity Measurement of GaAs/AlGaAs Thin-Film Structures,” ASME J. Heat Transfer, **116**, pp. 325–331.
[6] Kim, E.-K., Kwun, S.-I., Lee, S.-M., Seo, H., and Yoon, J.-G., 2000, “Thermal Boundary Resistance at $Ge_2Sb_2Te_5/ZnS:SiO_2$ Interface,” Appl. Phys. Lett., **76**, pp. 3864–3866.
[7] Kapitza, P. L., 1941, “The Study of Heat Transfer in Helium II,” Zh. Eksp. Teor. Fiz., **11**, pp. 1–31.
[8] Cahill, D. G., Bullen, A., and Lee, S.-M., 2000, “Interface Thermal Conductance and the Thermal Conductivity of Multilayer Thin Films,” High Temp. - High Press., **32**, pp. 135–142.
[9] Swartz, E. T., and Pohl, R. O., 1989, “Thermal Boundary Resistance,” Rev. Mod. Phys., **61**, pp. 605–668.
[10] Cahill, D. G., Ford, W. K., Goodson, K. E., Mahan, G. D., Majumdar, A., Maris, H. J., Merlin, R., and Phillpot, S. R., 2003, “Nanoscale Thermal Transport,” J. Appl. Phys., **93**, pp. 793–818.
[11] Hopkins, P. E., and Norris, P. M., 2007, “Effects of Joint Vibrational States on Thermal Boundary Conductance,” Nanoscale Microscale Thermophys. Eng., **11**, pp. 247–257.
[12] Chen, G., 1998, “Thermal Conductivity and Ballistic-Phonon Transport in the Cross-Plane Direction of Superlattices,” Phys. Rev. B, **57**, pp. 14958–14973.
[13] Chen, G., and Neagu, M., 1997, “Thermal Conductivity and Heat Transfer in Superlattices,” Appl. Phys. Lett., **71**, pp. 2761–2763.
[14] Daly, B. C., Maris, H. J., Imamura, K., and Tamura, S., 2002, “Molecular Dynamics Calculation of the Thermal Conductivity of Superlattices,” Phys. Rev. B, **66**, p. 024301.
[15] Kosevich, Y. A., 1995, “Fluctuation Subharmonic and Multiharmonic Phonon Transmission and Kapitza Conductance Between Crystals With Very Different Vibrational Spectra,” Phys. Rev. B, **52**, pp. 1017–1024.
[16] Pettersson, S., and Mahan, G. D., 1990, “Theory of the Thermal Boundary Resistance Between Dissimilar Lattices,” Phys. Rev. B, **42**, pp. 7386–7390.
[17] Yang, B., and Chen, G., 2003, “Partially Coherent Phonon Heat Conduction in Superlattices,” Phys. Rev. B, **67**, p. 195311.
[18] Yang, R., and Chen, G., 2004, “Thermal Conductivity Modeling of Periodic Two-Dimensional Nanocomposites,” Phys. Rev. B, **69**, p. 195316.
[19] Zeng, T., and Chen, G., 2001, “Phonon Heat Conduction in Thin Films: Impacts of Thermal Boundary Resistance and Internal Heat Generation,” ASME J. Heat Transfer, **123**, pp. 340–347.
[20] Prasher, R. S., and Phelan, P. E., 2001, “A Scattering-Mediated Acoustic Mismatch Model for the Prediction of Thermal Boundary Resistance,” ASME J. Heat Transfer, **123**, pp. 105–1121.
[21] Chen, G., and Zeng, T., 2001, “Nonequilibrium Phonon and Electron Transport in Heterostructures and Superlattices,” Microscale Thermophys. Eng., **5**, pp. 71–88.
[22] Chen, Y., Li, D., Yang, J., Wu, Y., Lukes, J., and Majumdar, A., 2004, “Molecular Dynamics Study of the Lattice Thermal Conductivity of Kr/Ar Superlattice Nanowires,” Physica B, **349**, pp. 270–280.
[23] Stoner, R. J., and Maris, H. J., 1993, “Kapitza Conductance and Heat Flow Between Solids at Temperatures From 50 to 300 K,” Phys. Rev. B, **48**, pp. 16373–16387.
[24] Stevens, R. J., Smith, A. N., and Norris, P. M., 2005, “Measurement of Thermal Boundary Conductance of a Series of Metal-Dielectric Interfaces by the Transient Thermoreflectance Technique,” ASME J. Heat Transfer, **127**, pp.

315–322.

[25] Lyeo, H.-K., and Cahill, D. G., 2006, "Thermal Conductance of Interfaces Between Highly Dissimilar Materials," Phys. Rev. B, **73**, p. 144301.

[26] Hopkins, P. E., Stevens, R. J., and Norris, P. M., 2008, "Influence of Inelastic Scattering at Metal-Dielectric Interfaces," ASME J. Heat Transfer, **130**, p. 022401.

[27] Poate, J. M., Tu, K. N., and Mayer, J. W., 1978, *Thin Films: Interdiffusion and Reactions*, Wiley, New York.

[28] Beechem, T. E., Graham, S., Hopkins, P. E., and Norris, P. M., 2007, "The Role of Interface Disorder on Thermal Boundary Conductance Using a Virtual Crystal Approach," Appl. Phys. Lett., **90**, p. 054104.

[29] Kechrakos, D., 1991, "The Role of Interface Disorder in the Thermal Boundary Conductivity Between Two Crystals," J. Phys.: Condens. Matter, **3**, pp. 1443–1452.

[30] Ren, S.-F., Cheng, W., and Chen, G., 2006, "Lattice Dynamics Investigations of Phonon Thermal Conductivity of Si/Ge Superlattices With Rough Interfaces," J. Appl. Phys., **100**, p. 103505.

[31] Stevens, R. J., Zhigilei, L. V., and Norris, P. M., 2007, "Effects of Temperature and Disorder on Thermal Boundary Conductance at Solid-Solid Interfaces: Nonequilibrium Molecular Dynamics Simulations," Int. J. Heat Mass Transfer, **50**, pp. 3977–3989.

[32] Kechrakos, D., 1990, "The Phonon Boundary Scattering Cross Section at Disordered Crystalline Interfaces: A Simple Model," J. Phys.: Condens. Matter, **2**, pp. 2637–2652.

[33] Swartz, E. T., and Pohl, R. O., 1987, "Thermal Resistances at Interfaces," Appl. Phys. Lett., **51**, pp. 2200–2202.

[34] Kozorezov, A. G., Wigmore, J. K., Erd, C., Peacock, A., and Poelaert, A., 1998, "Scattering-Mediated Transmission and Reflection of High-Frequency Phonons at a Nonideal Solid-Solid Interface," Phys. Rev. B, **57**, pp. 7411–7414.

[35] Mattox, D. M., 1973, "Thin Film Metallization of Oxides in Microelectronics," Thin Solid Films, **18**, pp. 173–186.

[36] Tu, K. N., and Mayer, J. W., 1978, *Thin Films: Interdiffusion and Reactions*, Wiley, New York.

[37] Chopra, K., 1969, *Thin Film Phenomena*, McGraw-Hill, New York.

[38] Qiu, T. Q., Juhasz, T., Suarez, C., Bron, W. E., and Tien, C. L., 1994, "Femtosecond Laser Heating of Multi-Layer Metals. II. Experiments," Int. J. Heat Mass Transfer, **37**, pp. 2799–2808.

[39] Costescu, R. M., Wall, M. A., and Cahill, D. G., 2003, "Thermal Conductance of Epitaxial Interfaces," Phys. Rev. B, **67**, p. 054302.

[40] Beechem, T., and Graham, S., 2006, "Estimating the Effects of Interface Disorder on the Thermal Boundary Resistance Using a Virtual Crystal Approximation," *Proceedings of the 2006 ASME International Mechanical Engineering Congress*, Anaheim, CA, Paper No. IMECE2006-14161.

[41] Beechem, T. E., Graham, S., Hopkins, P. E., and Norris, P. M., 2007, "The Role of Interface Disorder on Thermal Boundary Resistance Using a Virtual Crystal Approach," Appl. Phys. Lett., **90**, p. 054104.

[42] Stevens, R. J., Smith, A. N., and Norris, P. M., 2006, "Signal Analysis and Characterization of Experimental Setup for the Transient Thermoreflectance Technique," Rev. Sci. Instrum., **77**, p. 084901.

[43] Capinski, W. S., and Maris, H. J., 1996, "Improved Apparatus for Picosecond Pump-and-Probe Optical Measurements," Rev. Sci. Instrum., **67**, pp. 2720–2726.

[44] Ozisik, M. N., 1993, *Heat Conduction*, Wiley, New York.

[45] Gray, D. E., 1972, *American Institute of Physics Handbook*, McGraw-Hill, New York.

[46] Hohlfeld, J., Wellershoff, S.-S., Gudde, J., Conrad, U., Jahnke, V., and Matthias, E., 2000, "Electron and Lattice Dynamics Following Optical Excitation of Metals," Chem. Phys., **251**, pp. 237–258.

[47] Ashcroft, N. W., and Mermin, N. D., 1976, *Solid State Physics*, Saunders College, Fort Worth.

[48] Franciosi, A., Peterman, D. J., Weaver, J. H., and Moruzzi, V. L., 1982, "Structural Morphology and Electronic Properties of the Si-Cr Interface," Phys. Rev. B, **25**, pp. 4981–4993.

[49] Bower, R. W., and Mayer, J. W., 1972, "Growth Kinetics Observed in the Formation of Metal Silicides on Silicon," Appl. Phys. Lett., **20**, pp. 359–361.

[50] Cattaruzza, E., Mattei, G., Mazzoldi, P., Bertoncello, R., Battaglin, G., and Mirenghi, L., 1995, "Formation of Amorphous Silicide Nanoclusters in Chromium- and Titanium-Implanted Silica," Appl. Phys. Lett., **67**, pp. 2884–2886.

[51] Capinski, W. S., Maris, H. J., Ruf, T., Cardona, M., Ploog, K., and Katzer, D. S., 1999, "Thermal-Conductivity Measurements of GaAs/AlAs Superlattices Using a Picosecond Optical Pump-and-Probe Technique," Phys. Rev. B, **59**, pp. 8105–8113.

[52] Snyder, N. S., 1970, "Heat Transport Through Helium II: Kapitza Conductance," Cryogenics, **10**, pp. 89–95.

[53] Abeles, B., 1963, "Lattice Thermal Conductivity of Disordered Semiconductor Alloys at High Temperatures," Phys. Rev., **131**, pp. 1906–1911.

[54] Hostetler, J. L., Smith, A. N., Czajkowsky, D. M., and Norris, P. M., 1999, "Measurement of the Electron-Phonon Coupling Factor Dependence on Film Thickness and Grain Size in Au, Cr, and Al," Appl. Opt., **38**, pp. 3614–3620.

[55] Majumdar, A., and Reddy, P., 2004, "Role of Electron-Phonon Coupling in Thermal Conductance of Metal-Nonmetal Interfaces," Appl. Phys. Lett., **84**, pp. 4768–4770.

[56] Incropera, F., and Dewitt, D. P., 1996, *Fundamentals of Heat and Mass Transfer*, Wiley, New York.

A Nonequilibrium Thermal Model for Rapid Heating and Pyrolysis of Organic Composites

Jianhua Zhou
Postdoctoral Fellow
Mem. ASME

Yuwen Zhang[1]
Associate Professor
Fellow ASME
e-mail: zhangyu@missouri.edu

J. K. Chen
William & Nancy Thompson Professor
Mem. ASME

D. E. Smith
Associate Professor
Mem. ASME

Department of Mechanical and Aerospace Engineering,
University of Missouri-Columbia,
Columbia, MO 65211

A nonequilibrium thermal model is developed to predict the through-thickness transient temperature variation in organic composites subjected to intensive heating. In addition to heat conduction, the model incorporates four important mechanisms: rate-dependent pyrolysis, pyrolysis by-product outgassing, irradiance-dependent convection heat loss, and radiation heat lose. Both the shape of the gas flow channel and the gas addition velocity from the channel wall are evaluated based on the decomposition reaction rate. The through-thickness temperature transients, the continually changing gas channel, and the pressure distribution in the decomposition gas are obtained and discussed.
[DOI: 10.1115/1.2897337]

Keywords: composite, heat transfer, laser, pyrolysis

Introduction

Advanced composites are a material in which two (or more) constituents are engineered to produce properties that would not be attained by conventional means [1]. Laser machining offers the advantages of high machining rates, no tool wear, no contact forces, and relatively high precision [2]. The effectiveness of laser machining depends primarily on the thermal and structural behaviors of the composite materials. Knowing the through-thickness transient temperature variation is a prerequisite for the subsequent laser ablation. Reed and Rice [3] developed a rate-dependent pyrolysis model to characterize the heat transfer in decomposing material. Chen et al. [4] used a modified Crank–Nicholson finite difference scheme to model the heat transfer process in laser-irradiated composites, but the cooling effect arising from the decomposition reaction outgassing was not accounted for. Recently, Zhou et al. [5] developed a two-dimensional model to investigate the coupled compressible gas flow and heat transfer in a microchannel surrounded by solid media, but the gas addition velocity and the microchannel shape are assumed and not based on the pyrolysis reaction.

To overcome the drawbacks of the existing models, a new numerical model is developed in this work. The heat conduction in the solid part is considered to be one dimensional, and the pyrolysis gas flow is treated as a two-dimensional axisymmetric compressible flow in a microchannel with varying cross-section area, which is determined according to the decomposition reaction rate. To the authors' knowledge, no work has been done to calculate the gas channel size based on the pyrolysis reaction as did in the present study.

Model Description

The physical model is shown in Fig. 1 for a fiber composite material subjected to a localized heat flux q'', with a thickness of L and an initial temperature of T_i. Figure 1(*a*) is a schematic of the composite before heating. The black regions represent fibers; the gray denotes the matrix. Figure 1(*b*) shows the composite material after a heat flux is imposed on the top surface. Once the material is pyrolyzed, the pyrolyzed products are ejected as the gas flows outward from the pyrolysis zone toward the heated surface (the white regions in Fig. 1(*b*) represent the gas flow channels). Each gas flow channel, together with its surrounding material, constitutes an element (shown in the dash-line box of Fig. 1(*b*), as zoomed out in Fig. 1(*c*)).

Assuming a constant heat flux is specified at the top boundary (Fig. 1), the one-dimensional heat conduction in the solid part of the composite is governed by

$$\rho_s c_{ps}\frac{\partial T_s}{\partial t}=\frac{\partial}{\partial x}\left(k_s\frac{\partial T_s}{\partial x}\right)+\dot{Q}_{\mathrm{pyro}}H(t-t_{\mathrm{pyro}}) + \frac{h_{\mathrm{gas}}(T_g-T_s)}{R_f^2(1-\alpha)/2R_c}H(t-t_{\mathrm{pyro}}) \tag{1}$$

where T_s and T_g are solid and gas temperatures, respectively. The heat capacity of the solid $\rho_s c_{ps}$ is

$$\rho_s c_{ps}=(1-\alpha_{\max})(\rho_s c_{ps})_f+\alpha_{\max}(\rho_s c_{ps})_m \quad \text{in nonpyrolysis region} \tag{2}$$

$$\rho_s c_{ps}=(1-\alpha_{\max})(\rho_s c_{ps})_f+(\alpha_{\max}-\alpha)(\rho_s c_{ps})_m \quad \text{in pyrolysis region} \tag{3}$$

where α is the fraction of the decomposed material with a maximum value of $\alpha_{\max}$. The subscripts f and m denote the fiber and matrix, respectively. The thermal conductivity k_s is temperature dependent and will change as pyrolysis takes place. The thermal conductivity used in Ref. [4], with both temperature dependence and effect of pyrolysis accounted for, is used in this work.

The pyrolysis is a rate-dependent process and the heat source term $\dot{Q}_{\mathrm{pyro}}$ in Eq. (1) is calculated by

$$\dot{Q}_{\mathrm{pyro}}=-\frac{\rho_s\Delta H\cdot\dfrac{d\alpha}{dt}}{1-\alpha}=-\rho_s\Delta H\cdot A\cdot e^{B/T-M\cdot\int_{t_{\mathrm{pyro}}}^{t}Ae^{B/T}dt}/(1-\alpha) \tag{4}$$

where ΔH is the chemical reaction heat, A is the frequency factor, B is activation energy, and M is the molar mass (kg/mol). The Heaviside step function, $H(t-t_{\mathrm{pyro}})$, is zero before pyrolysis ($t<t_{\mathrm{pyro}}$) and one after pyrolysis ($t>t_{\mathrm{pyro}}$). The convection heat exchange coefficient h_{gas} between the gas and the solid structure is evaluated based on the gas temperature gradient at channel wall, which can be calculated by the simulation results of the gas flow.

The front surface ($x=0$) is heated by the localized heat flux q'' and is cooled by convection and radiation. The rear surface (x

---

[1] Corresponding author.

Contributed by the Heat Transfer Division of ASME for publication in the JOURNAL OF HEAT TRANSFER. Manuscript received January 18, 2007; final manuscript received August 16, 2007; published online April 23, 2008. Review conducted by Walter W. Yuen.

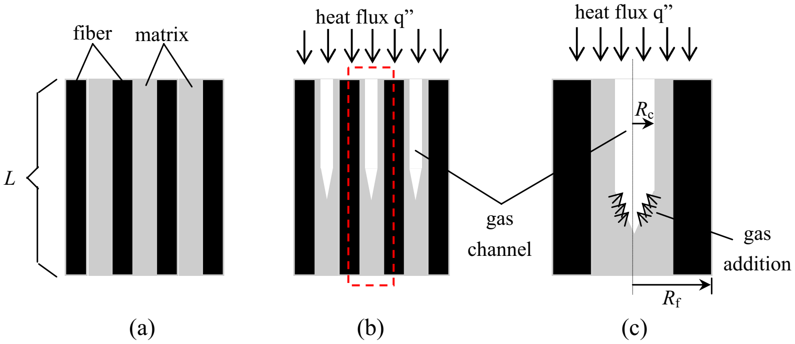

Fig. 1 Physical model: (*a*) before heating: (*b*) after the commencement of heating: (*c*) zoom-out of a fiber-matrix element

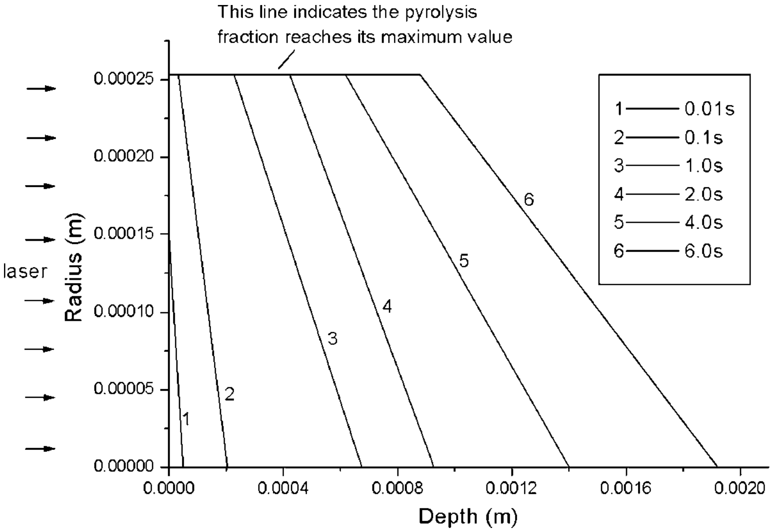

Fig. 2 Progression of the pyrolysis front with time

$=L$) is cooled by radiation and natural convection. The convection heat transfer coefficient at the front surface depends on the surface heat flux [6].

To obtain the gas temperature in Eq. (1), it is necessary to solve the fluid flow and heat transfer in the gas region. The 2D gas flow is assumed to be laminar and compressible. The governing equations and solution procedure of the gas flow in channel can be found in Ref. [5].

The radius of the gas flow channel is not a constant and is determined by the fraction of the decomposition reaction:

$$R_c = \sqrt{\alpha} \cdot R_{\text{fiber}} \tag{5}$$

where the fraction of the decomposed material, α, is evaluated based on the rate equation:

$$\frac{d\alpha}{dt} = A(1-\alpha)^M e^{B/T} \tag{6}$$

where the constant B is determined by the activation energy and the universal gas constant.

The gas addition from the channel wall is determined by considering conservation of mass at the gas-solid interface, i.e.,

$$V_{\text{add}} = -\frac{1}{2}\frac{R_f^2}{R_c}\frac{\rho_s}{\rho_g}\frac{d\alpha}{dt} \tag{7}$$

where the minus sign is a result of the fact that the gas is added in the negative radial coordinate.

In the early stage of heating, the channel is very narrow and thus the Knudsen number for the gas flow is very large, where the traditional Navier–Stokes equation will break down [7]. Therefore, in this stage, the gas flow effect is approximated based on the energy conservation principle at the gas-solid interface.

The governing Navier–Stokes equations are solved with the finite volume method (FVM) based on the SIMPLE algorithm [8].

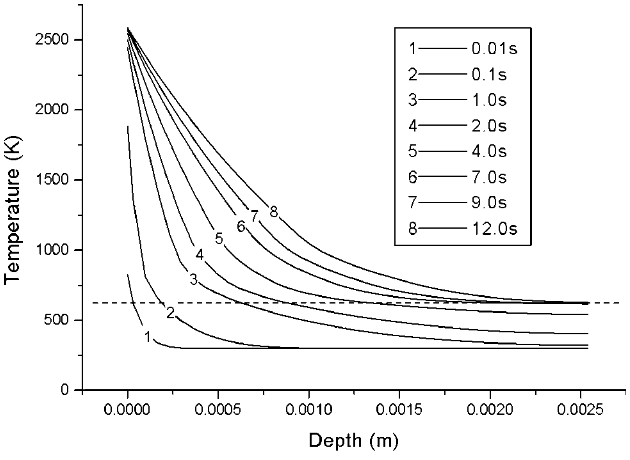

Fig. 3 Spatial distribution of the temperature at different times

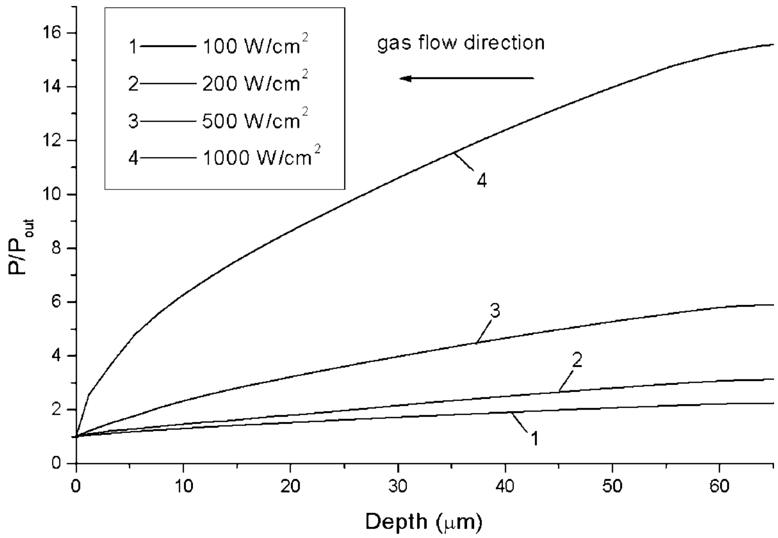

Fig. 4 Centerline normalized pressure distribution for different heating fluxes

The extension of the traditional SIMPLE method to a compressible one can be found in Refs. [9–13]. The body-fitted mesh is generated using the multisurface technique [14].

Results and Discussion

A composite medium with 2.54 mm thickness is considered. The outer radius of the unit cell R_f is 400 μm. The material is initially at a uniform temperature, $T_i=300$ K. For time $t>0$, a constant heat flux of $q''=5$ MW/m^2 is impinged on the surface. After a grid convergence study, a 64×26 mesh is employed in the 2D compressible gas flow and 41 grid points are used in the 1D heat conduction simulation of the solid part. The numerical solution started from time $t=0$ with a varying time step Δt (a small time step is used in the initial stage since the temperature change during this stage is very drastic). The thermophysical properties of the solid composite used in the simulations are $(\rho_s)_f=1200$ kg/m^3, $(c_{ps})_f=1500$ J/(kg K), $(\rho_s)_m=800$ kg/m^3, $(c_{ps})_m=1100$ J/(kg K). The physical properties of the gaseous byproducts are $M=28.97\times 10^{-3}$ kg/mol, $c_{pg}=1005$ J/(kg K), Pr $=0.7$, $\mu=1.81\times 10^{-6}$ kg/(m s), $\gamma=1.4$. Other data are as follows: The ambient temperature is $T_\infty=300$ K. The surface radiation emissivity is $\varepsilon_{\text{surf}}=0.92$. The convection coefficient between the solid material and the ambient is $h=5$ W/(m^2 K) before onset of the pyrolysis reaction. The pyrolysis onset temperature is $T_{\text{pyro}}=625$ K. The decomposition reaction heat is $\Delta H=2\times 10^6$ J/kg. The order of the decomposition reaction is $M=1$. The maximum decomposition fraction $\alpha_{\max}$ is 0.4. The frequency factor in the rate equation is $A=1.243\times 10^7$. The constant B in the rate equation is $B=-1.17\times 10^4$ K.

Figure 2 shows the progression of the pyrolysis front as a function of time. It is clearly seen that the pyrolysis reaction front penetrates deeper and deeper into the composite as the heating proceeds. The horizontal line in Fig. 2 indicates that the fraction of the decomposed material reaches its maximum value. This leads to a straight gas channel section that has a constant cross-section area.

The spatial distributions of the temperatures at different times are plotted in Fig. 3. The decomposition reaction front is the intersection point between the temperature curve and the dashed line of the pyrolysis onset temperature. As time elapses, the decomposition reaction front penetrates deeper and deeper into the composite.

Figure 4 presents the centerline normalized pressure distribution for different heating fluxes at $t=10.6$ s. It is seen from this figure that the pressure decreases gradually from the pyrolysis front to the heated surface. The higher the input heat flux, the larger the pressure difference from the pyrolysis front to the heated surface. This is because a higher heating flux causes a much more violent decomposition reaction, which, in turn, results in a higher gas addition velocity along the gas channel wall.

Conclusions

A nonequilibrium heat transfer model is developed to calculate the temperature transients in composites exposed to high heating flux. Besides the convection and radiation heat loss effects at surface, the pyrolysis gas flow effect is included into the model. Compared to previous studies, the most striking improvement of the present model is that both the shape of the gas flow channel and the gas addition velocity from the channel wall are evaluated based on the decomposition reaction rate. Transient temperature and pressure distributions are obtained and analyzed.

Acknowledgment

The work presented in this article was funded by the Laser Effects Research Branch of Air Force Research Laboratory in Kirtland Air Force Base through Ball Aerospace, Inc.

References

[1] Agarwal, B. D., and Broutman, L. J., 1990, *Analysis and Performance of Fiber Composites*, 2nd ed., Wiley, New York.
[2] dell'Erba, M., Galantucci, L. M., and Miglietta, S., 1992, "An Experimental Study on Laser Drilling and Cutting of Composite Materials for the Aerospace Industry Using Excimer and CO_2 Sources," Compos. Manuf., **3**(1), pp. 14–19.
[3] Reed, H. E., and Rice, M. H., 1993, "Failure of Solid Rocket Engines due to Laser Radiation Exposure," Cubed Report No. SSS-DFR-93-14222.
[4] Chen, J. K., Perea, A., and Allahdadi, F. A., 1995, "A Study of Laser/Composite Material Interactions," Compos. Sci. Technol., **54**, pp. 35–44.
[5] Zhou, J., Zhang, Y., and Chen, J. K., 2007, "Numerical Simulation of Compressible Gas Flow and Heat Transfer in a Microchannel Surrounded by Solid Media," Int. J. Heat Fluid Flow, **28**(6), pp. 1484–1491.
[6] Smith, D. E., Zhang, Y., and Chen, J. K., 2006, *HELVAMP: Laser/Composite Interaction Research Project*, Final Technical Report Submitted to Air Force Research Laboratory/Ball Aerospace.
[7] Harley, J. C., Huang, Y., Bau, H. H., and Zemel, J. N., 1995, "Gas Flow in Micro-Channels," J. Fluid Mech., **284**, pp. 257–274.
[8] Patankar, S. V., 1980, *Numerical Heat Transfer and Fluid Flow*, Hemisphere, New York.
[9] Karki, K. C., and Patankar, S. V., 1989, "Pressure Based Calculation Procedure for Viscous Flows at All Speeds in Arbitrary Configurations," AIAA J., **27**(9), pp. 1167–1174.

[10] Demirdzic, I., Lilek, Z., and Peric, M., 1993, “A Collocated Finite Volume Method for Predicting Flows at All Speeds,” Int. J. Numer. Methods Fluids, **16**, pp. 1029–1050.

[11] Rincon, J., and Elder, R., 1997, “A High-Resolution Pressure-Based Method for Compressible Flows,” Comput. Fluids, **26**(3), pp. 217–231.

[12] Date, A. W., 1998, “Solution of Navier-Stokes Equations on Nonstaggered Grid at All Speeds,” Numer. Heat Transfer, Part B, **33**, pp. 451–467.

[13] Rhie, C. M., and Chow, W. L., 1983, “Numerical Study of the Turbulent Flow Past an Airfoil With Trailing Edge Separation,” AIAA J., **21**(11), pp. 1525–1532.

[14] Eiseman, P. R., 1985, “Grid Generation for Fluid Mechanics Computations,” Annu. Rev. Fluid Mech., **17**, pp. 487–522.

Tube Transverse Pitch Effect on Heat/Mass Transfer Characteristics of Flat Tube Bank Fin Mounted With Vortex Generators

Song Liu

Liangbi Wang[1]
e-mail: lbwang@mail.lzjtu.cn

Jufang Fan

Yongheng Zhang

Yuanxin Dong

Kewei Song

Department of Mechanical Engineering,
Lanzhou Jiaotong University,
Lanzhou, Gansu 730070, P.R. China

For one heat exchanger model of three-row flat tube bank fin mounted with vortex generators (VGs), the effect of transversal tube pitch on heat/mass transfer performance was investigated by the experimental method of naphthalene sublimation. For the same arrangement of VGs around the tube, it is found that the larger the transversal tube pitch, the larger the heat transfer enhancement because of less interactions of vortices generated from different VGs. Interaction of vortices decreases the heat transfer enhancement on the fin surfaces with and without VGs for the case with small transversal tube pitch. For isothermal condition, two correlated equations of average Nusselt number and friction factor considering the fin spacing, the attack angle of VG, the height of VG, the ratio of transversal tube pitch, and Reynolds number are reported. [DOI: 10.1115/1.2897339]

Keywords: heat transfer enhancement, vortex generator, finned flat tube bank, heat exchanger

Introduction

The finned flat tube bank fin heat exchangers have many applications especially on vehicles such as radiators of Diesel locomotive. Vortex generators (VGs) can generate swirl of the flow and flow destabilization [1,2]. The local and average heat transfer over a finned three-row flat tube bank with four/tube and six/tube delta winglet VGs with an aspect ratio of 2 was reported in Refs. [3,4]. In these studies, several types of surfaces involved in heat transfer process were considered. The optimal fin spacing [5], angle [6], position of VGs [7], and height of VGs [8] were investigated considering no uniform fin temperature. Recent study shows that vortices generated upstream will interact with vortices generated downstream, depending on the rotation direction of vortex; such interaction will increase or decrease the intensity vortices and effect heat transfer enhancement [9]. For tube bank fin heat exchanger, the transversal pitch of tube is an important parameter, especially for tube bank fin heat exchanger with VGs. The transversal pitch of tube determines the relative location of VGs and hence affects the intensity of interactions of vortices.

The objective of this paper is to evaluate the effects of transversal tube pitch effect on heat transfer performance of flat tube bank fin mounted VGs on fin surface without considering the changes of heat transfer characteristics in tube side. Evaluations were performed through the local and average heat/mass transfer data obtained by the naphthalene sublimation technique.

Experimental Model

The geometry of experimental setup is based on a typical locomotive radiator. In order to do experiment, we enlarged the geometry of locomotive radiator with a factor of 2.5. The flat tube fin geometries and positions of VGs are presented in Fig. 1. The geometric parameters are $S_2=55$ mm, $b=46.3$ mm, and $a=6.3$ mm. The leading points of first VG pair are on the line tangent to the flat tube and two tube widths apart. Figure 1(*a*) presents the arrangements of VG pair. The geometry of VG is presented in Fig. 1(*b*), and the aspect ratio was selected as 2. The detail information of experimental setup can be obtained in Ref. [7].

For average Nu_a and f_a, measurements were carried out for three different S_1's (32 mm, 40 mm, 53 mm), three θ's (25 deg, 35 deg, 45 deg), three H's (3 mm, 4 mm, 5 mm), and three T_p's (4 mm, 5 mm, 6 mm). Seven Reynolds numbers were conducted for each combination of above parameters. There are some impossible combinations, for example, $T_p=4$ mm and $H=5$ mm, excluding such cases, a total of 72 sets of data were obtained. The local measurement of Nu was carried on three types of tube transversal pitch $S_1=32$ mm, 40 mm, 53 mm at $\theta=35$ deg, $T_p=5$ mm, and $H=4$ mm conditions. The Re is selected from the working condition of a typical locomotive radiator. This type of radiator has a working velocity about 10 m/s of air, and flat tube with a width of 2.5 mm, in this condition the Re_a is about 1300 (using the characteristic length of flat tube width).

The same data reduction method as reported in Ref. [8] is used. The experimental uncertainty was estimated using the same method presented in Refs. [3,8], although several years have passed after the publication of Refs. [3,8]. From the results conducted recently, it is found that the repeatability of experiments for the local results of $S_1/S_2=0.727$ is considerably good.

Results and Discussion

Effect of S_1/S_2 on Local Nu_a Distribution. The local Nu_a distributions on Surface II (the surface without VGs) for three different S_1/S_2 are presented in Figs. 2(*a*)–2(*c*), respectively. These figures reveal that ahead of the second row of VGs, Nu_a is small. This characteristic means that vortices generated by the first row of VGs mounted on Surface I (the surface mounted with VGs) will need space to develop. These vortices can reach the fin Surface II and have some effect on Nu_a of Surface II. Starting from the second row of VGs, there is a region with large Nu_a around the tube. This indicates that the vortices near Surface II is intensified by the second row VGs. The streamwise axis of the core of vortices is nearly in line with the second row of tube for case of $S_1/S_2=0.582$, the region with large Nu_a is broken by this tube, see Fig. 2(*a*). Nu_a on Surface II is small around the second row of tube indicts that the interactions of vortices generated by the tube and VGs of first and second rows decrease the heat transfer enhancement around this tube for the case of $S_1/S_2=0.582$. For this configuration, heat transfer enhancement is deteriorated around the third row tube due to the intensified unfavorable interactions of the vortices generated by VGs, the tubes upstream, and the VGs downstream. Here the interactions between vortices mean that the vortices generated at different positions increase or decrease the amplitude of the same velocity component in a given point. If more rigorous definition is used, interactions mean the increase or decrease of the cross-averaged absolute vortex flux in

---

[1] Corresponding author.

Contributed by the Heat Transfer Division for publication in the JOURNAL OF HEAT TRANSFER. Manuscript received January 28, 2007; final manuscript received September 19, 2007; published online April 23, 2008. Review conducted by S. A. Sherif.

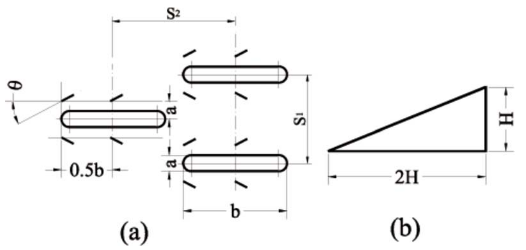

Fig. 1 Flat tube bank parameters and positions of VGs: (*a*) configuration; (*b*) shape of VG

main flow direction. Unfavorable interactions of vortices mean they decrease the amplitude of velocity components. It is found that unlike for the case of $S_1/S_2=0.582$, for cases of $S_1/S_2=0.969$ and $S_1/S_2=0.727$, starting from the second row VGs, there are clear regions with large Nu_a beside the tubes, see Figs. 2(*b*) and 2(*c*). The width of the region with large Nu_a is increased with increasing S_1/S_2.

As shown in Figs. 3(*a*)–3(*c*), on fin Surface I, the heat transfer enhancement is appreciable, especially around the tube. The heat transfer enhancement becomes weak in the region far from the tube for $S_1/S_2=0.969$. The distributions of Nu_a around the first tube row are similar for the three cases of S_1/S_2. In the region of the second tube row, it is found that effect of the vortices generated upstream on Nu_a can penetrate far downstream. It is found that the vortices generated by VGs located around the first tube row have counter-rotation direction compared to the vortices generated by the VGs located around the second tube row. If the tube centerlines in main flow direction of the first tube row and the second tube row are too close, the interactions of these vortices with counter-rotation direction reduce the amplitude of velocity components and hence deteriorate heat transfer enhancement. Due to the increasing intensity of vortice interactions with counter-rotation direction for small S_1/S_2, there is no clear region with large Nu_a near the end of the third tube row. For large S_1/S_2, for example, $S_1/S_2=0.969$, with less interactions of vortices, two clear regions in which the Nu_a is enhanced are observed.

Effect of S_1/S_2 on Span-Averaged Nu_a Distribution. At different S_1/S_2, the comparison of span-averaged Nu_a distribution in the stream direction on fin Surfaces I and II is presented in Fig. 4. In this experiment, we used the same size of VG, considering the fin with different S_1/S_2 will have different areas of heat transfer. In this figure, we added the span-averaged Nu_a of smooth fin for reference. The heat transfer enhancement can be compared with these reference data. As shown in Fig. 4(*a*), for $S_1/S_2=0.582$, it is clear that VGs can enhance heat transfer efficiently. In most regions, Nu_a on Surface I is larger than that on Surface II. When

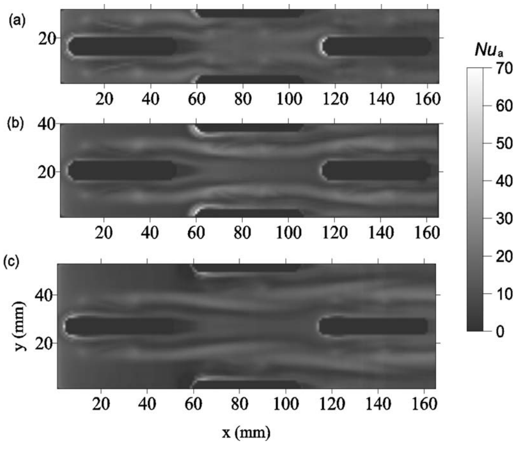

Fig. 2 Comparison of local Nu_a distribution on fin Surface II: (*a*) $\mathrm{Re}_a=1119$, $S_1/S_2=0.528$; (*b*) $\mathrm{Re}_a=1121$, $S_1/S_2=0.727$; (*c*) $\mathrm{Re}_a=1090$, $S_1/S_2=0.969$

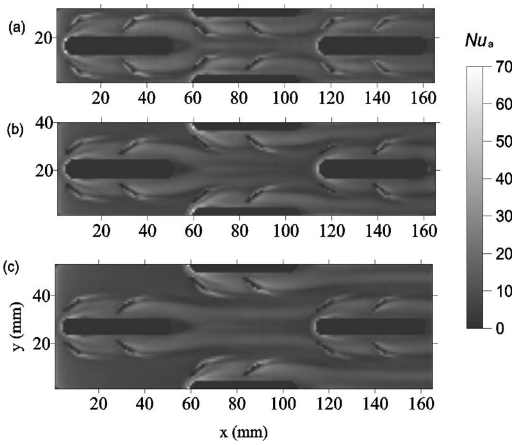

Fig. 3 Comparison of local Nu_a distribution on fin Surface I; (*a*) $\mathrm{Re}_a=1119$, $S_1/S_2=0.528$; (*b*) $\mathrm{Re}_a=1121$, $S_1/S_2=0.727$; (*c*) $\mathrm{Re}_a=1090$, $S_1/S_2=0.969$

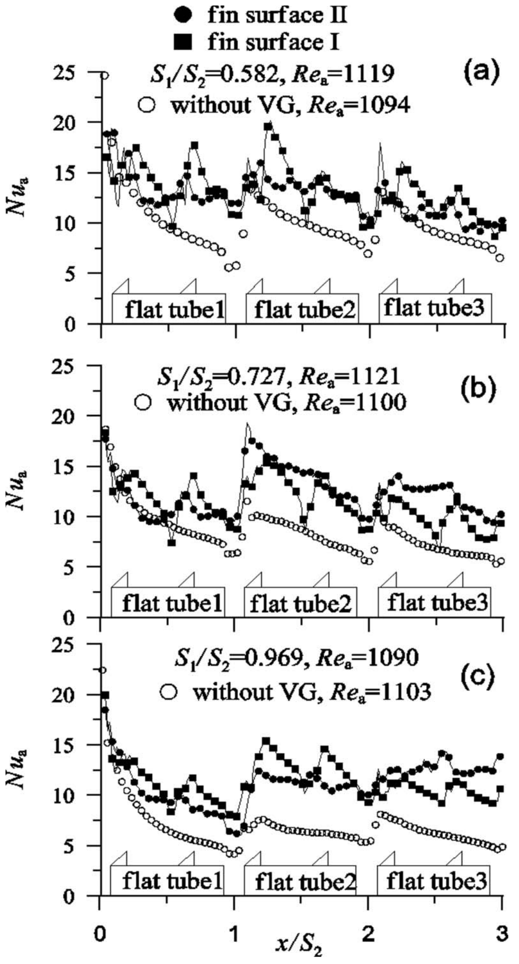

Fig. 4 Comparison of span-averaged Nu_a on the fin Surfaces I and II for different S_1/S_2

S_1/S_2=0.727, within a relative large region, Nu_a on II is larger than Nu_a on I around the first and the second tube rows. However, when S_1/S_2=0.969, Nu_a on II is larger than Nu_a on I around the third tube row.

Interactions of vortices will decrease heat transfer enhancement for small S_1/S_2 the case. For case of S_1/S_2=0.969, there is enough space for vortices generated upstream to develop, and there is less intensity of vortice interactions; Nu_a on II has a larger value than Nu_a on I downstream. If we refer to Fig. 2(*c*), because the centerlines in main flow direction of the first tube row and the second tube row are far away, it is clear that the vortices generated by VGs around the first row is unlikely interacted with vortices generated by VGs around the second row tube. Compared with the reference data, from Fig. 4, it is found that the heat transfer enhancement by VGs is different for the three cases studied. The larger heat transfer enhancement comes from the case of S_1/S_2 =0.969. The smaller heat transfer enhancement occurred for case of S_1/S_2=0.582. These results can be explained by the interactions of vortices generated by VGs explained above. The interactions of vortices affect the heat transfer on surfaces with and without VGs.

Effect of S_1/S_2 on Average Nu_a and f_a. All of data obtained by the experiments are correlated considering T_p, θ, H, and S_1/S_2; the following equations can be obtained:

$$\mathrm{Nu}_a = 0.282\,\mathrm{Re}_a^{0.631}\left(\frac{T_p}{a}\right)^{0.527}\left(\frac{H}{T_p}\right)^{0.241}\left(\frac{\theta}{45\ \mathrm{deg}}\right)^{0.180}\left(\frac{S_1}{S_2}\right)^{0.871} \tag{1}$$

$$f_a = 8.482\,\mathrm{Re}_a^{-0.515}\left(\frac{T_p}{a}\right)^{0.527}\left(\frac{H}{T_p}\right)^{0.647}\left(\frac{\theta}{45}\right)^{0.319}\left(\frac{S_1}{S_2}\right)^{-0.592} \tag{2}$$

$$500 < \mathrm{Re}_a < 4100, \quad 25\ \mathrm{deg} \le \theta \le 45\ \mathrm{deg}$$

$$0.528 \le T_p/a \le 0.952$$

The maximum deviation of data is 12.3%.

Conclusions

The effects of transversal tube pitch on local and average heat transfer of flat tube bank fin with VGs are studied. For isothermal condition, considering fin spacing, parameters of VG such as attack angle and height, transversal tube pitch, two correlated equations for Nu and f based on the 72 set of experimental data were provided. For the same arrangement of VGs around the tube, it is found that the larger the transversal tube pitch, the larger the enhancement of heat transfer because of less interactions of vortices generated from different VGs located at upstream. Interaction of vortices decreases the heat transfer enhancement on fin surfaces with and without VGs for configuration with small transversal tube pitch. The experimental results indicate that for small transversal tube pitch, if VGs are used to enhance heat transfer, the method to avoid interactions of vortices must be considered.

Nomenclature

a = width of flat tube (m)
b = length of flat tube (m)
f = friction factor
H = height of winglet type vortex generators (m)
Nu = Nusselt number
Re = Reynolds number
S_1 = transversal pitch between flat tubes (m)
S_2 = longitudinal pitch between flat tubes (m)
T_p = fin spacing (m)

Greek Symbol

θ = attack angle of vortex generator (deg)

Subscript

a = with reference to tube width

References

[1] Fiebig, M., 1995, "Embedded Vortices in Internal Flow: Heat Transfer and Pressure Loss Enhancement," Int. J. Heat Fluid Flow, **16**, pp. 376–388.

[2] Joardar, A., and Jacob, A. M., 2005, "Impact of Leading Edge Delta-Wing Vortex Generators on the Thermal Performance of a Flat Tube, Louvered-Fin Compact Heat Exchanger," Int. J. Heat Mass Transfer, **48**, pp. 1480–1493.

[3] Wang, L. B., Ke, F., Gao, S. D., and Mei, Y. G., 2002, "Local and Average Characteristics of Heat/Mass Transfer Over Flat Tube Bank Fin With Four Vortex Generators Per Tube," ASME J. Heat Transfer, **124**, pp. 546–552.

[4] Wang, L. B., Zhang, Y. H., Su, Y. X., and Gao, S. D., 2002, "Local and Average Heat/Mass Transfer Over Flat Tube Bank Fin Mounted In-Line Vortex Generators With Small Longitudinal Spacing," J. Enhanced Heat Transfer, **9**, pp. 77–87.

[5] Shi, B. Z., Wang, L. B., Gen, F., and Zhang, Y. H., 2006, "The Optimal Fin Spacing for Three-Row Flat Tube Bank Fin Mounted With Vortex Generators," Heat Mass Transfer, **43**, pp. 91–101.

[6] Ke, F., Wang, L. B., Hua, L., Gao, S. D., and Su, Y. X., 2006, "The Optimum Angle of Attack of Delta Winglet Vortex Generators on Heat Transfer Performance of Finned Flat Tube Bank With Considering No Uniform Fin Temperature," Exp. Heat Transfer, **19**, pp. 227–249.

[7] Zhang, Y. H., Wang, L. B., Su, Y. X., and Gao, S. D., 2004, "Effects of Span Position of Winglet Vortex Generator on Local Heat/Mass Transfer Over a Three-Row Flat Tube Bank Fin," Heat Mass Transfer, **40**, pp. 881–891.

[8] Gao, S. D., Wang, L. B., Zhang, Y. H., and Ke, F., 2003, "The Optimum Height of Winglet Vortex Generators Mounted on Three-Row Flat Tube Bank Fin," ASME J. Heat Transfer, **125**, pp. 1007–1016.

[9] Zhu, C. L., Hua, L., Sun, D. L., Wang, L. B., and Zhang, Y. H., 2006, "Numerical Study of Interactions of Vortices Generated by Vortex Generators and Their Effects on Heat Transfer Enhancement," Numer. Heat Transfer, Part A, **50**, pp. 353–368.

Bipolar Plate Thermal Response to PEM Fuel Cell Stack Compressive Load

N. Fekrazad

T. L. Bergman
e-mail: tberg@engr.uconn.edu

Department of Mechanical Engineering,
University of Connecticut,
191 Auditorium Road, Unit 3139,
Storrs, CT 06269

This technical brief reports new findings regarding the strong relationship between the temperature of the bipolar plates of a proton exchange membrane fuel cell stack and thermal conditions within the membranes of the stack. The unique feature of the study is the notion that bipolar plate temperature might be used as an indicator to identify optimal stack clamping pressures that lead to nearly isothermal conditions inside the stack. Uniform thermal (and humidity) conditions are expected to enhance fuel cell durability and reliability. [DOI: 10.1115/1.2897928]

Keywords: fuel cell, contact resistance

Introduction

Considerable progress has been made in developing comprehensive heat and mass transfer models of proton exchange membrane (PEM) fuel cells. For the most part, interest has been in the prediction of detailed stack thermal, humidity, and electron and proton distributions. Less attention has been paid to manufacturing issues, such as the impact of fuel cell stack assembly (individual fuel cells are usually assembled in series, forming a compact fuel cell stack) on fuel cell performance and behavior.

A recent study [1] reports the development of a two-dimensional model to discern detailed behavior within a fuel cell stack. An important feature of the model is its incorporation of both electrical and thermal contact resistances that exist at the interface between a bipolar plate (BP) and the gas diffusion layer (GDL) within a typical fuel cell stack. In addition, variation in the GDL permeability with compressive load applied to the stack is accounted for. Specifically, the dependence of the contact resistances (as well as GDL permeability) to the compressive force applied to the stack was taken from recently reported experimental results [2], and the contact resistance variation with pressure for Sigracet GDL material is shown in Fig. 1.

Figure 2, taken from Ref. [1], illustrates a fuel cell stack (Fig. 2(*a*)) that arbitrarily consists of five membranes and six current collectors (BPs). An oxidant (humidified air) flows on the cathode side of the membrane and fuel (humidified H_2) is supplied to the anode side, as shown in Fig. 2(*b*). A compressive force is used to assemble and hold the stack together. In practice, the compression is controlled by placing the stack within a yoke and squeezing the yoke with all-threaded rods equipped with springs or Belville washers as shown schematically. From the transport phenomenon point of view, the compressive force will alter *both* the electrical and thermal contact resistances that develop at the interface between the GDLs of Fig. 2(*b*) and the adjacent BPs. The permeabilities of the porous GDLs will also be reduced as the compressive force is increased.

The governing equations and boundary conditions used to predict the various steady-state distributions within the fuel cell stack are very lengthy, are described in detail in Ref. [1], and will not be repeated here. Suffice it to state that conservation of energy, species, and electron and ion charge principles are all applied to the computational domain indicated by the dashed lines in Fig. 2(*b*), which is an expanded view of a repetitive fuel cell stack element shown in Fig. 2(*a*). The periodicity of the stack structure is exploited to simplify the computation. Various constitutive relations, listed and described in detail in Ref. [1], complete the formulation of the model, which is ultimately capable of predicting both the fuel cell power output and the detailed two-dimensional spatial distributions of various quantities within the stack. The model's predictions, in terms of the sensitivity of the fuel cell power output to clamping pressure, were validated through quantitative comparison with experimental measurement [1] and are in qualitative agreement with recently reported experimental measurements [3] and numerical predictions [4] that show an increase in the fuel cell power output with increasing clamping pressure as the clamping pressure is increased from very low values.

Knowledge of the internal temperature and humidity *distributions* is important for a variety of reasons. A critical issue is enhancement of the durability and lifetime (reduction in cost) of PEM fuel cell stacks and, as noted in the literature [5–8], it is highly desirable to minimize spatial temperature variations within the delicate polymer material that forms the membrane electrode assembly (MEA, Fig. 2(*b*)) consisting of a very thin Nafion sheet sandwiched between two catalyst layers (shown as the two dark vertical lines in Fig. 2(*b*)). In general, minimization of spatial temperature differences within the GDLs and MEA will promote uniform humidity conditions, decreasing the chance of membrane dry-out that can lead to the formation of "pinholes" through the MEA and, in turn, mixing of the cathode and anode gases that will ultimately lead to failure of the entire fuel cell stack. Also, minimization of spatial temperature differences (and, in general, promotion of uniform humidity conditions) will minimize stresses within the membrane material that is clamped between the BPs. A thorough description of the detailed failure mechanisms is available in Ref. [8].

An unanticipated discovery, discussed in Ref. [1], is that thermal conditions within the MEA might be made nearly uniform by carefully adjusting the compressive force (or pressure) used to assemble the stack. For example, much of Fig. 3 is replicated from Ref. [1] and shows the maximum temperature difference along the vertical centerline of the membrane (see Fig. 2(*b*)) for various operating conditions and for various clamping pressures. For a very wide range of conditions and BP geometries (See Tables 1

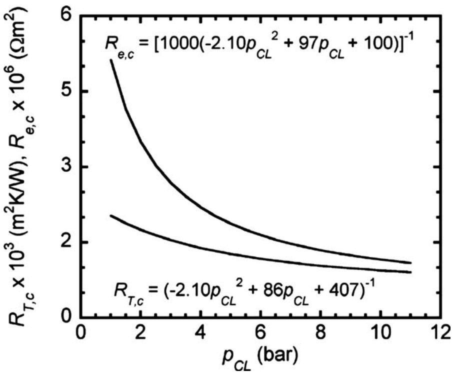

Fig. 1 Electrical and thermal contact resistance dependences upon clamping pressure for Sigracet GDL material. The curve fits are to the experimental data of Ref. [2].

Contributed by the Heat Transfer Division for publication in the JOURNAL OF HEAT TRANSFER. Manuscript received February 16, 2007; final manuscript received October 9, 2007; published online May 7, 2008. Review conducted by Ben Q. Li.

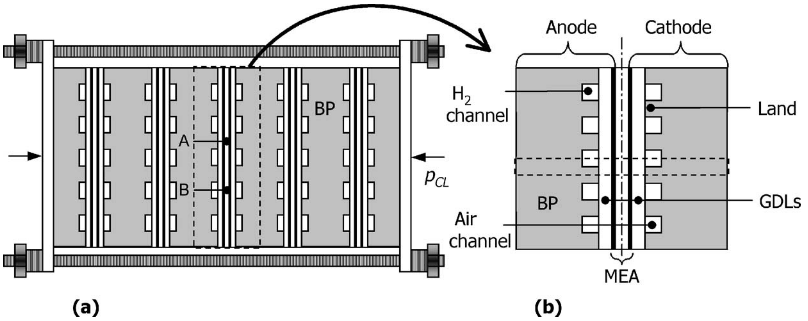

Fig. 2 **Schematic diagram of (*a*) a fuel cell stack and (*b*) a single cell within the stack**

and 2 as well as Figs. 8–10 of Ref. [1]), it was found that nearly isothermal conditions tend to group around a compressive pressure (defined as force per unit active area of MEA) of $p_{\mathrm{cl}} \approx 2$ bars. The two large circles that identify minimum values of ΔT will be discussed shortly.

As noted in Ref. [1], minimization of spatial temperature differences in the MEA corresponds to a sudden *shift* in maximum local membrane temperatures from the middle of a BP land (Location "A" of Fig. 2(*a*)) to the middle of a gas channel (Location "B" of Fig. 2(*a*)) in response to a complex interplay involving reductions in both the electrical and thermal contact resistances associated with increased clamping pressures and conjugate heat transfer associated with the relatively high thermal conductivity BP (65 W/m K) and its role in redistributing heat transfer rates between the hot membrane and the cool gases. The fuel cell stack power output is only modestly affected by changes in the clamping pressure.

Since minimization of internal temperature differences is desirable and can be controlled by varying the clamping pressure applied to the stack, it would be useful to somehow identify and subsequently apply optimal clamping pressures. Unfortunately, local nonintrusive measurement of any quantity within the MEA is extremely difficult in the warm, moist, and electrically active environment experienced by the delicate, low thermal conductivity membrane materials. Recognizing this practical limitation, an opportunity presents itself to further examine (beyond the investigation of Ref. [1]) the predicted stack behavior and its sensitivity to clamping pressure, in an effort to identify other features that might correspond to desirable internal distributions inside the fuel cell and, in turn, be used to optimize clamping forces.

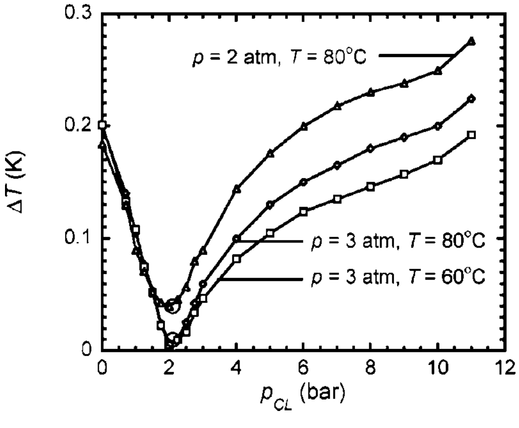

Fig. 3 **Maximum temperature difference along the centerline of the membrane of Fig. 2(*b*) as a function of the clamping pressure for $V_{\mathrm{cell}}=0.6$ V. Gas pressure and temperature are as indicated. The circles indicate clamping pressures associated with the BP thermal shift of Fig. 4.**

Results and Conclusions

Figure 4 shows the predicted local BP temperature associated with a very wide variety of operating conditions and flow channel geometries (Table 1) as a function of the clamping pressure applied to the fuel cell stack. The results presented in Fig. 4 are a compilation of predicted BP temperatures for 136 individual simulations; none of which has been previously reported. No numerical predictions associated with any operating condition have been excluded from Fig. 4. Half of the simulations are associated with specification of constant cell voltage, while the other half are associated with a specified cell current density; two different conditions that depend on the electrical characteristics of the actual fuel cell load; both conditions of which can be incorporated in the model [1]. All of the simulations are associated with the Sigracet GDLs of Refs. [1,2].

Relative to any other thermal feature associated with a fuel cell stack, the temperature of a BP is easy to measure using a variety of standard techniques because of its thickness, strength, high thermal conductivity, and high emissivity. For each case considered here, the BP temperatures are spatially uniform to within ±0.05°C; in essence a unique temperature is associated with the BP for any condition. Also, the spatially averaged BP temperature increases as the clamping pressure is increased. The results of Fig. 4 are associated with BP temperature variations ($T_{b,\max}$-$T_{b,\min}$) of approximately 1°C–2.5°C over clamping pressures ranging from $p_{\mathrm{cl,min}}=1$ bar to $p_{\mathrm{cl,max}}=4$ bars associated with the cases of Table 1.

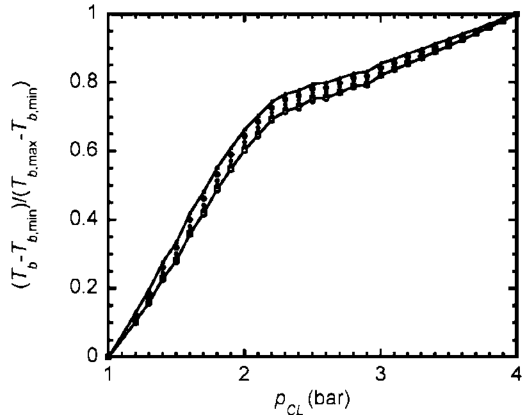

Fig. 4 **Dimensionless BP temperature versus clamping pressure for the conditions of Table 1.**

Table 1 Operating conditions and channel dimensions. Parameters shown are the average gas temperatures (T), gas pressures (p), channel half-width (w_{ch}), and land half-width (w_L). The channel height is 0.5 mm in all cases.

Constant cell potential (V_{cell}=0.6 V)	Constant current density (I=7050 A/m^2)
T=80°C, p=3 atm, w_{ch}=4 mm, w_L=3 mm	T=80°C, p=3 atm, w_{ch}=4 mm, w_L=3 mm
T=60°C, p=3 atm, w_{ch}=4 mm, w_L=3 mm	T=60°C, p=3 atm, w_{ch}=4 mm, w_L=3 mm
T=80°C, p=2 atm, w_{ch}=4 mm, w_L=3 mm	T=80°C, p=2 atm, w_{ch}=4 mm, w_L=3 mm
T=80°C, p=3 atm, w_{ch}=3 mm, w_L=4 mm	T=80°C, p=3 atm, w_{ch}=3 mm, w_L=4 mm

For the entire range of operating conditions and BP geometries considered here, the BP temperature exhibits a clear shift in behavior at $p_{cl} \approx 2$ bars. The shift occurs in direct response to the conjugate heat transfer associated with the BP and how this is affected by the clamping pressure through variations in the contact resistances (and to a very minor degree, the GDL permeability [1]).

To illustrate how the BP temperature dependence upon p_{cl} might be exploited, the clamping pressure associated with the change in slope of the BP temperature versus clamping pressure behavior may first be determined from Fig. 4 (or from associated experimental measurements on a fuel cell stack). The corresponding p_{cl} values are marked with circles in Fig. 3, clearly identifying these as optimal clamping pressures in terms of promoting uniform thermal conditions in the membrane. The same robust relationship between the BP thermal shift and achievement of nearly isothermal internal conditions is noted for all cases of Table 1. Hence, the BP temperature dependence on the clamping pressure might be exploited for purposes of identifying desirable clamping pressures for improving the durability of fuel cell stacks.

Acknowledgment

The authors acknowledge support of this research by the Army Power Division, U.S. Army Research, Development & Engineering Command under Contract No. DAAB07-03-3-K-415.

Nomenclature

I = current density, A/m^2
p_{cl} = clamping pressure, bar or atm
$R_{e,c}$ = electric contact resistance, Ω m^2
$R_{T,c}$ = thermal contact resistance, m^2 K/W
T = gas or membrane temperature, K
T_b = BP temperature, K
V_{cell} = single cell voltage, V
w_{ch} = channel half-width, m
w_L = land half-width, m

References

[1] Fekrazad, N., and Bergman, T. L., 2007 "The Effect of Compressive Load on PEM Fuel Cell Stack Performance and Behavior," ASME J. Heat Transfer, **129**, pp. 1004–1013.
[2] Ihonen, J., Mikkola, M., and Lindbergh, G., 2004 "Flooding of Gas Diffusion Backing in PEFCs," J. Electrochem. Soc., **151**(8), pp. A1152–A1161.
[3] Chang, W. R., Hwang, J. J., Weng, F. B., and Chan, S. H., 2007 "Effect of Clamping Pressure on the Performance of a PEM Fuel Cell," J. Power Sources, **166**, pp. 149–154.
[4] Zhou, P., and Wu, C. W., 2007 "Numerical Study on the Compression Effect of Gas Diffusion Layer on PEMFC Performance," J. Power Sources, **170**, pp. 93–100.
[5] Hyunchul, J., Meng, H., and Wang, C.-Y., 2005, "A Single-Phase, Non-Isothermal Model for PEM Fuel Cells," Int. J. Heat Mass Transfer, **48**, pp. 1303–1315.
[6] Hottinen, T., and Himanen, O., 2007 "PEMFC Temperature Distribution Caused by Inhomogeneous Compression of GDL," Electrochem. Commun., **9**, pp. 1047–1052.
[7] Al-Baghdadi, M. A. R. S., and Al-Janabi, H. A. K. S., 2007, "Influence of the Design Parameters in a Proton Exchange Membrane (PEM) Fuel Cell on the Mechanical Behavior of the Polymer Membrane," Energy Fuels, **21**, pp. 2258—2267.
[8] Solasi, R., Zou, Y., Huang, X., Reifsnider, K., and Condit, D., 2007, "On Mechanical Behavior and In-Plane Modeling of Constrained PEM Fuel Cell Membranes Subjected to Hydration and Temperature Cycles," J. Power Sources, **167**, pp. 366–377.